



Notre Dame, Indiana, USA

**Proceedings of the
Second International Workshop
on
Model Reduction in Reacting Flows**

This workshop received support from the Center for Applied Mathematics – University of Notre Dame and the National Science Foundation.

This material is based upon work supported by the National Science Foundation under Grant No. 0902504.

Any opinions, findings, and conclusions or recommendations expressed in this material are those of the author(s) and do not necessarily reflect the views of the National Science Foundation

Edited by:

**S. Paolucci (University of Notre Dame)
J. M. Powers (University of Notre Dame)
A. J. Sommes (University of Notre Dame)**

March 30 – April 1, 2009

ABOUT

The Second International Workshop on Model Reduction in Reacting Flow is hosted by the University of Notre Dame, Notre Dame, Indiana, USA. This is the continuation of the first workshop held at the University of Rome "La Sapienza" in 2007.

The meeting is held at the Center for Continuing Education on the University of Notre Dame campus.

The Workshop's main areas of interest are:

- Theoretical foundations of model reduction including definitions of slow, fast, invariant manifolds and related subjects
- Chemical kinetic mechanism simplification
- Model reduction in ODE's and PDE's
- Model reduction in systems with non trivial asymptotic dynamics
- Computational tools to analyze numerically generated reacting flow

The objective of the Workshop is to provide a forum for:

- exploring relationships among different methods,
- exploring capabilities and limitations of different methods, and
- reporting on new developments, in the area of model reduction in reacting flow.

SCIENTIFIC COMMITTEE

M. Giona (University of Rome "La Sapienza")
D. Goussis (University of Athens)
H. Najm (Sandia National Laboratories, Livermore)
S. Paolucci (University of Notre Dame)
J. M. Powers (University of Notre Dame)
A. J. Sommes (University of Notre Dame)
M. Valorani (University of Rome "La Sapienza")

LOCAL ORGANIZING COMMITTEE

S. Paolucci (University of Notre Dame)
J. M. Powers (University of Notre Dame)
A. J. Sommes (University of Notre Dame)

PROGRAM

DAY ONE – Monday, March 30, 2009

- 8:00 – 8:30 Registration
- 8:30 – 8:45 Opening Remarks
- 8:45 – 9:35 Linda Petzold, University of California – Santa Barbara; *Sensitivity Analysis, Model Reduction, and Circadian Oscillators*; page 89.
- 9:35 – 9:45 Break
- 9:45 – 10:10 Khachik Sargsyan, Bert Debuschere, and Habib Najm; Sandia National Laboratories, *Spectral Representation and Reduced Order for Modeling of Stochastic Reaction Networks*, page 105.
- 10:10 – 10:35 Xiaolong Gou, Wenting Sun, Zheng Chen, and Yiguang Ju; Princeton University; *An Efficient Multi-time Scale (MTS) Method for Combustion Modeling with Reduced and Detailed Kinetic Mechanisms*, page 43.
- 10:35 – 10:50 Break
- 10:50 – 11:15 Michael Davis, Argonne National Laboratory; *Phase Space Structure of Complex Chemical-kinetic Mechanisms: Low-dimensional Manifolds for Homogeneous Chemical Kinetics and 1-d Premixed Flames*, page 21.
- 11:15 – 11:40 Stephen Pope, Zhuyin Ren, and Varun Hiremath; Cornell University and ANSYS, Inc.; *Dimension Reduction and Tabulation of Combustion Chemistry using ICE-PIC and ISAT*, page 91.
- 11:40 – 1:10 Lunch
- 1:10 – 2:00 Benjamin Sonday, Amit Singer, and Ioannis Kevrekidis; Princeton University; *Diffusion Maps for Model Reduction: Exploiting Data Mining to Accelerate Simulation*, page 47.
- 2:00 – 2:10 Break
- 2:10 – 2:35 Samuel Paolucci and Mauro Valorani, University of Notre Dame and University di Roma “La Sapienza”; *Adaptive Model Reduction and the G-Scheme*, page 71.
- 2:35 – 3:00 Mauro Valorani and Samuel Paolucci, University di Roma “La Sapienza” and University of Notre Dame; *Application of the G-Scheme to Reactive Systems*, page 77.
- 3:00 – 3:25 Tibor Nagy and Tamas Turanyi, Eötvös University; *Mechanism Reduction Based on Simulation Error Minimization*, page 115.
- 3:25 – 3:40 Break
- 3:40 – 4:05 Dirk Lebedez, Volkmar Reinhardt, and Jochen Siehr; University of Freiburg and University of Heidelberg; *Geometric Criteria for Model Reduction in Chemical Kinetics via Optimization of Trajectories*, page 111.
- 4:05 – 4:30 Ashraf Al-Khateeb, Joseph Powers, Samuel Paolucci, Andrew Sommesse, Jeffrey Diller, and Jonathan Hauenstein; University of Notre Dame; *Projective Space Method for Slow Invariant Manifolds of Reactive Systems*, page 7.

DAY TWO – Tuesday, March 31, 2009

- 8:00 – 8:30 Registration
- 8:30 – 9:20 James Rawlings, University of Wisconsin; *Extending the Tools of Chemical Reaction Engineering to the Molecular Scale*, page 103.
- 9:20 – 9:30 Break
- 9:30 – 9:55 Jesus Izaguirre and Christopher Sweet, University of Notre Dame; *Adaptive Dimensionality Reduction of Stochastic Differential Equations for Protein Dynamics*, page 37.
- 9:55 – 10:20 Ovidiu Radulescu and Alexander Gorban, University of Rennes and University of Leicester; *Limitation and Averaging for Deterministic and Stochastic Biochemical Reaction Networks*, page 95.
- 10:20 – 10:35 Break
- 10:35 – 11:00 Panayotis Kourdis, Ralf Steur, and Dimitris Goussis; National Technical University – Athens and University of Manchester; *Analysis of a Stiff Limit Cycle: Glycolysis in Saccharomyces Cerevisiae*, page 33.
- 11:00 – 11:25 Dimitris Diamantis, Dimitris Kyritsis, and Dimitris Goussis; University of Illinois and University of Athens; *Two Stage Ignition of n-heptane: Identifying the Chemistry Setting the Explosive Time Scales*, page 49.
- 11:25 – 12:55 Lunch
- 12:55 – 1:45 Henry Curran, National University of Ireland; *Validation of Detailed Chemical Kinetic Models*, page 19.
- 1:45 – 1:55 Break
- 1:55 – 2:20 Ashraf Al-Khateeb, Joseph Powers, Samuel Paolucci, Andrew Sommesse, Jeffrey Diller, and Joshua Mengers; University of Notre Dame; *On the Relation between Reaction Dynamics and Thermodynamics in Closed Systems*, page 11.
- 2:20 – 2:45 Geoffrey Oxberry, Alexander Mitsos, Paul Barton, and William Green; MIT; *Range-Constrained Simultaneous Reaction and Species Elimination in Kinetic Mechanisms*, page 63.
- 2:45 – 3:10 Mauro Valorani, Samuel Paolucci, and Habib Najm; University di Roma “La Sapienza”, University of Notre Dame, and Sandia National Laboratories; *Sensitivity Indices Based on the G-Scheme*, page 83.
- 3:10 – 3:25 Break
- 3:25 – 3:50 David Sheen, Terese Lovas, and Hai Wang, University of Southern California and University of Tromsø; *Reduction of Detailed Chemical Models with Controlled Uncertainty*, page 109.
- 3:50 – 4:15 Erkut Aykutluğ and Kenneth Mease, University of California – Irvine; *Finite-Time Lyapunov Analysis and Optimal Control*, page 53.
- 4:45 Bus Pick Up at McKenna Hall
- 5:15 Tour of Studebaker National Museum
- 6:30 Dinner at Tippecanoe Place

DAY THREE – Wednesday, April 1, 2009

- 9:00 – 9:25 Charles Westbrook, William Pitz, and Marco Mehl; Lawrence Livermore National Laboratory; *Recent Developments in Detailed Chemical Kinetic Mechanisms*, page 119.
- 9:25 – 9:50 Youssef Marzouk, Bert Debusschere, Habib Najm, Dimitris Goussis, Mauro Valorani, and Michael Frenklach; MIT, Sandia National Laboratories, National Technical University of Athens, University di Roma “La Sapienza”, University of California – Berkeley; *Time Integration of Reacting Flows with CSP Tabulation*, page 25.
- 9:50 – 10:15 Eliodoro Chiavazzo, Ilya Karlin, Alexander Gorban, and Konstantinos Boulouchos; Swiss Federal Institute of Technology, University of Southampton, and University of Leicester; *Invariant Grids and Lattice Boltzmann Method for Combustion*, page 15.
- 10:15 – 10:30 Break
- 10:30 – 10:55 Geoffrey Oxberry, William Green, and Paul Barton; MIT; *Affine Lumping Formalism for Comparison of Model Reduction Techniques*, page 67.
- 10:55 – 11:20 Bill Goodwine and Baoyang Deng, University of Notre Dame; *Reduction and Equivalence of Nonlinear Distributed Symmetric Control Systems*, page 29.
- 11:20 – 12:50 Lunch
- 12:50 – 1:15 Hans Kaper, Tasso Kaper, and Antonios Zagaris; Boston University, Argonne National Laboratory, and University of Amsterdam; *Analysis of Reduction Methods for ODEs*, page 45.
- 1:15 – 1:40 W.J.S. Ramaekers, J.A. van Oijen, and L.P.H. de Goey; Eindhoven University of Technology; *Flamelet Generated Manifolds for Chemistry Representation in Partially-Premixed Flames*, page 99.
- 1:40 – 2:05 H.N. Najm, M. Valorani, D. Goussis; Sandia National Laboratories, University di Roma “La Sapienza”, National Technical University of Athens; *Analysis of Methane-Air Edge Flame Structure using CSP*, page 57.
- 2:05 – 2:20 Break
- 3:30 CAM Nieuwland Lecturer, Charles Westbrook, Lawrence Livermore National Laboratory; *The Role of Combustion in Future Energy Scenarios*, page 123.

Projective Space Method for Slow Invariant Manifolds of Reactive Systems

A. N. Al-Khateeb*, J. M. Powers*, S. Paolucci*, A. J. Sommesè†, J. A. Diller†, J. D. Hauenstein†

*University of Notre Dame, Department of Aerospace and Mechanical Engineering, Notre Dame, Indiana, USA

†University of Notre Dame, Department of Mathematics, Notre Dame, Indiana, USA

Abstract—One dimensional slow invariant manifolds for dynamical systems arising from modeling isothermal, spatially homogeneous, closed reactive systems are calculated. The technique is based on global analysis of the composition space of the reactive system. The identification of all the system’s finite and infinite critical points plays a major role in calculating the system’s slow invariant manifold. The slow invariant manifolds are constructed by calculating heteroclinic orbits which connect appropriate critical points to the unique stable physical equilibrium point. The technique is applied to small and large detailed kinetics mechanisms.

I. INTRODUCTION

In detailed kinetics models, the presence of a wide range of scales induces a large computational cost when calculations are fully resolved. Because direct numerical simulation (DNS) is not feasible for many practical flows, the main challenge in modeling is to simplify the problem without significant loss of accuracy. One of the major approaches employs lower dimensional manifolds, which are based on a reduction in the composition space dimension.

For spatially homogeneous systems, reaction dynamics are described by a set of ordinary differential equations (ODEs). The solutions of this set of ODEs are represented by trajectories in the species composition space. Each trajectory represents the reactive system’s evolution with time for a specific initial condition. The evolved trajectories seem to quickly be attracted to a special trajectory and stay exponentially close to it until they reach equilibrium in infinite time [1]. The reactive system’s slow modes are the only active ones on this special trajectory. Thus, identifying this slow invariant manifold (SIM) for a reactive system will make it possible to reduce the computational cost by filtering the system’s fast modes. For each reactive system there are SIMs of different dimensions; this work focuses on the construction of only one-dimensional (1-D) SIMs.

Here, 1-D SIMs for unsteady spatially homogeneous mixtures of calorically imperfect ideal gases described by detailed kinetics are calculated. While such construction has been done for small two-dimensional systems [2], the present work offers the first construction of SIMs for realistic detailed kinetics systems of dimension greater than 2-D. The SIM is constructed by a global analysis over the entire composition space. By finding all equilibria and connecting them via heteroclinic orbits, it is easy to identify the system’s actual SIM. Zel’dovich nitric oxide system and a detailed hydrogen-air kinetic system

will be the mechanisms we focus in this paper. The second system is of interest since it is intrinsic to common combustion applications, included in the combustion of all hydrocarbons, and is well-known and widely accepted.

In comparison to other dimension reduction techniques that obtain approximate SIMs, such as the intrinsic low-dimensional manifold (ILDM) [3], the computational singular perturbation (CSP) [4], the invariant constrained equilibrium edge preimage curve method (ICE-PIC) [5], minimal entropy production trajectories (MEPT) [6], and iterative methods [7], the technique presented here identifies the actual SIMs. In the first section, the governing ODEs for closed, isothermal, reactive system are presented. This is followed by a reduction of the ODEs into a system of differential algebraic equations (DAEs) which describes the system’s evolution within the reduced composition space. Following a brief description of how we identify and examine all the system’s finite and infinite equilibria, the numerical method to construct the SIMs is presented. Once the difficult task of identifying all of the equilibria is complete, it is seen that constructing the actual SIMs is easy and computationally efficient. The main results of this study are the construction of the 1-D SIMs for realistic detailed kinetics isothermal reactive systems.

II. MATHEMATICAL MODEL

A. Governing Equations

We consider a mixture of total mass M confined in a volume V containing N gas phase species composed of L atomic elements that undergo J reversible reactions. The evolution of the species with time t is obtained from the following set of ODEs:

$$\frac{dn_i}{dt} = V \sum_{j=1}^J \nu_{ij} r_j, \quad i = 1, \dots, N. \quad (1)$$

Here, the dependent variables are the species’ number of moles n_i . Also, for the j^{th} reaction r_j and ν_{ij} are, respectively, the reaction rate given by the law of mass action and the net stoichiometric matrix. In general, ν_{ij} is a non-square matrix of dimensions $N \times J$, and it is of rank $R \leq (N - L)$; commonly $R = (N - L)$.

B. Reduced System

Equation (1), defines an N -dimensional composition space. The dimensionality of this space is reduced to R

as a consequence of the conservation of elements, and any additional constraints that can possibly arise. The elements constraints are enforced by

$$\sum_{i=1}^N \phi_{li} n_i = \sum_{i=1}^N \phi_{li} n_i^*, \quad l = 1, \dots, L, \quad (2)$$

where ϕ_{li} is the element index matrix and quantities with superscript (*) are at the initial state. Here, the n_i 's are linearly dependent composition variables, which implies that (2) is underconstrained and solutions of the following form

$$n_i = n_i^* + M \sum_{k=1}^R \mathcal{D}_{ik} z_k, \quad i = 1, \dots, N, \quad (3)$$

can be found. Here, z_k is a reduced composition variable, which physically represents the number of moles of species k in M . \mathcal{D}_{ik} is a dimensionless constant matrix of size $N \times R$ and has full rank R . Each column vector of \mathcal{D}_{ik} is linearly independent of the remaining column vectors. However, \mathcal{D}_{ik} is not unique, and it can be constructed in several ways.

As a result, the reactive system described by (1) is recast as an autonomous standard dynamical system of the form

$$\frac{dz}{dt} = \mathbf{f}(\mathbf{z}), \quad \mathbf{z} \in \mathbb{R}^R, \quad (4)$$

where \mathbf{f} is a set of R non-linear coupled polynomials of degree d connected with a given reaction mechanism. From a geometric point of view, \mathbf{z} is a vector in the Euclidian composition space \mathbb{R}^R . Thus, reactive system solutions are trajectories that move on the reduced composition space \mathbb{R}^R , which is a subspace of the full composition space \mathbb{R}^N . Full details are given by [8].

III. METHODOLOGY

A. Equilibria

The proposed construction method of a reactive system's SIM is based on identifying all the equilibria of (4). In general, the set of equilibria of such a function is complex, and contains finite and infinite equilibria [9]. Moreover, the equilibria can be positive dimensional continua [10]. In this work, only the system's real isolated finite and infinite equilibria are considered.

To obtain the dynamical system's finite equilibria, we find all the \mathbf{z}^e that satisfy $\mathbf{f}(\mathbf{z}^e) = \mathbf{0}$. One of the finite equilibria is of special interest; it is the unique critical point located inside the physically accessible domain [11].

The next step is to identify the system's infinite equilibria. To do so, the projective space method is employed [10]. This technique maps the infinite critical points onto the finite domain, and is realized by the following relations

$$Z_k = \frac{1}{z_k}, \quad k \in \{1, \dots, R\}, \quad (5)$$

$$Z_i = \frac{z_i}{z_k}, \quad i \neq k, \quad i = 1, \dots, R, \quad (6)$$

where z_k is any arbitrarily selected dependent variable, and \mathbf{Z} are the state variables in the projective space.

By employing the projective space mapping, the original dynamical system is recast in the following form

$$\frac{d\mathbf{Z}}{d\tau} = \mathbf{F}(\mathbf{Z}), \quad \mathbf{Z} \in \mathbb{R}^R, \quad (7)$$

where \mathbf{F} is a set of R non-linear functions that correspond to the non-linear functions \mathbf{f} in the projective space, and τ is the transformed time in the projective space which is related to t by the following relation, $dt/d\tau = (Z_k)^{d-1}$. The finite equilibria of the resulting dynamical system, \mathbf{Z}^e that satisfy $\mathbf{F}(\mathbf{Z}^e) = \mathbf{0}$, represent the infinite equilibria of the original system (4).

Next, the dynamic behavior of the system in the neighborhood of each finite and infinite equilibrium is investigated by employing standard linearization techniques. The stability of each critical point is determined by examining the eigenvalue spectrum of its local Jacobian and the corresponding eigenvectors. At the physical equilibrium point, the eigenvector associated with the smallest eigenvalue represents the systems slowest mode.

B. Construction Method

We start the process of SIM construction by generating a heteroclinic orbit from the finite equilibrium which has the least positive eigenvalue. Then, we check whether the generated orbit approaches the the physical equilibrium point in the direction of its slowest mode. After that, another orbit is generated starting from the finite equilibrium which has the second lowest positive eigenvalue. If the two generated orbits approach the the physical equilibrium point in the direction of its slowest mode, then these are the SIM's two branches. Otherwise, we generate a new heteroclinic orbit from the finite equilibrium which has the third lowest eigenvalue, and so on. After checking all finite equilibria, we follow the same procedure with the infinite equilibria. During this procedure, any time we obtain two heteroclinic orbits that approach the physical equilibrium point in the direction of its slowest mode, there is no need to consider the remaining equilibria.

C. Computational Method

The kinetic rates and the thermodynamic properties are calculated using the public domain edition of the Chemkin package [12]. The typical computational time to construct a 1-D SIM is less than one minute on a 2.16 GHz MacPro machine. All the calculations have been performed to high precision. However, all the listed results are rounded to three significant digits. Integers indicate that the reported numbers are exact. Also, Bertini [13], a C-code based on homotopy continuation, is used to obtain the system's equilibria to any desired accuracy. Lastly, all trajectories are obtained by numerical integration of the species evolution equations using a computationally inexpensive explicit fourth-order Runge-Kutta scheme.

IV. RESULTS

A. Zel'dovich mechanism

In this section, the strategy to construct a 1-D SIM is illustrated using a simple but realistic reactive system;

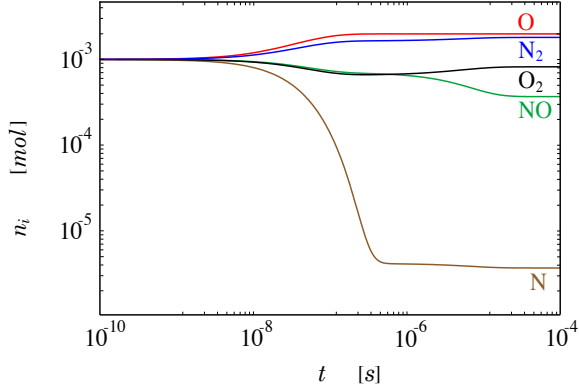


Fig. 1. The time evolution of species for the Zel'dovich model problem.

the Zel'dovich mechanism of nitric oxide formation. This mechanism contains $N = 5$ species, $L = 2$ elements, and $J = 2$ reversible reactions, and the kinetic data have been adopted from Baulch *et al.* [14]. A special case in which the system is isochoric will be considered, and the assigned mixture temperature and volume are $T = 4000 \text{ K}$ and $V = 10^3 \text{ cm}^3$, respectively. For convenience, the assigned initial number of moles of all species are $n_i^* = 10^{-3} \text{ mol}$, where $i = \{1, 2, 3, 4, 5\}$ corresponds to the species $\{NO, N, O, O_2, N_2\}$, respectively. The multi-scale nature of this system is clearly shown in Fig. 1, where the full dynamics of the evolution of the species are presented.

In this system, the total number of moles remain constant, as a consequence of the fact that the kinetics mechanism includes only bimolecular reactions. Consequently, one algebraic constraint, in addition to element conservation, exists in the system. Thus, this model problem is described in the $R = 2$ dimensional reactive composition space [8],

$$\frac{dz}{dt} = \dot{\mathbf{w}} \equiv \mathbf{f}(\mathbf{z}), \quad \{\mathbf{z}, \dot{\mathbf{w}}\} \in \mathbb{R}^R, \quad (8)$$

where

$$\dot{w}_k = \frac{1}{\rho} \sum_{j=1}^R \left[\left(\sum_{i=1}^N \mathcal{D}_{ik} \mathcal{D}_{ij} \right)^{-1} \left(\sum_{i=1}^N \mathcal{D}_{ij} \dot{\omega}_i \right) \right], \quad (9)$$

and $d = 2$.

By equilibrating the right hand side of (8) and using Bertini to obtain all \mathbf{z}^e that satisfy $\mathbf{f}(\mathbf{z}^e) = \mathbf{0}$, we find the following finite isolated equilibria,

$$\begin{aligned} R_1 &\equiv (\mathbf{z}^e) = (-1.78 \times 10^{-5}, -1.67 \times 10^{-2}) \text{ mol/g}, \\ R_2 &\equiv (\mathbf{z}^e) = (-4.20 \times 10^{-3}, -2.66 \times 10^{-5}) \text{ mol/g}, \\ R_3 &\equiv (\mathbf{z}^e) = (3.05 \times 10^{-3}, 2.94 \times 10^{-5}) \text{ mol/g}, \end{aligned}$$

where the rest of the species are recast using (3). It is clear that R_1 and R_2 are non-physical equilibria, while R_3 is the reactive systems unique physical equilibrium point.

The dynamical behavior analysis within the neighborhood of each critical point reveals that R_1 is a source, R_2 is saddle with one unstable mode, and R_3 is a sink.

In addition to the systems finite equilibria, (8) has three infinite equilibria. They are obtained using the projective space method, in which we select $k = 1$ arbitrarily. These equilibria are:

$$\begin{aligned} I_1 &\equiv (\mathbf{Z}^e) = (0, 0), \\ I_2 &\equiv (\mathbf{Z}^e) = (0, 1.01), \\ I_3 &\equiv (\mathbf{Z}^e) = (0, 2.60), \end{aligned}$$

The dynamical behavior analysis within the neighborhood of each critical point reveals that I_2 is a source, I_3 is a saddle with one positive eigenvalue, and I_1 is a non-hyperbolic critical point. Using the normal form theory [9], it is found that I_1 is a saddle-node, which consists of two hyperbolic sectors, one parabolic sector, and three separatrices. Only one of these separatrices is unstable.

Now, following our 1-D SIM construction procedure, these three points are ordered as follows: R_2, I_1, I_3 . So, starting from the unstable direction of R_2 , (8) are numerically integrated to generate a heteroclinic orbit. This orbit approaches R_3 along its slowest mode. So, the generated orbit represents the first branch of the 1-D SIM. Then, starting from the unstable direction of I_1 , another heteroclinic orbit is numerically generated. Also, this orbit approaches R_3 along its slowest mode. So, it represents the second and last branch of the reactive systems 1-D SIM. Subsequently, there is no need to check the third critical point, I_3 . In Fig. 2, part of the systems finite phase space and the SIM are presented. The attractiveness of the SIM is revealed by visually examining the relaxation of several trajectories onto it.

B. Detailed Hydrogen-Air Mechanism

In this section, the 1-D SIM for a detailed kinetics hydrogen-air reactive system is constructed using the previously discussed technique. The reaction mechanism used is extracted from Miller *et al.* [15], and consists of $J = 19$ reversible reactions that describe how $N = 9$ species composed of $L = 3$ elements react. The

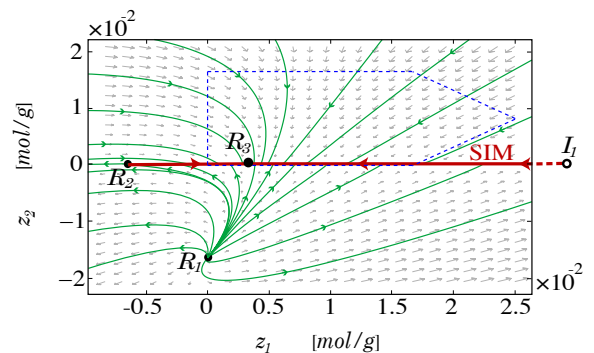


Fig. 2. A region of the finite phase space for the Zel'dovich mechanism. The solid dots represent finite critical points, the open circle represents an infinite critical point, the arrows indicate the flow direction, and the dashed simplex represents the physically accessible domain of the system. The SIM is illustrated as a thick line, the thin lines represent trajectories, and R_3 represents the system's physical equilibrium state.

stoichiometric hydrogen-air mixture is initially at $p = 10^7$ dyne/cm² and the chosen mixture temperature is $T = 1500$ K. The full dynamics of the species evolution is presented in Fig. 3. Here, the dependent variables are $\{z_{H_2}, z_{O_2}, z_H, z_O, z_{OH}, z_{H_2O}\}$, which correspond to $\{z_1, z_2, z_3, z_4, z_5, z_6\}$, respectively.

Using the procedure discussed earlier, 326 finite and infinite equilibria are found. One of these critical points represents the physical equilibrium state. This point is

$$R_{19} \equiv (\mathbf{z}^e) = (1.98 \times 10^{-6}, 9.00 \times 10^{-7}, 1.72 \times 10^{-9}, 2.67 \times 10^{-10}, 3.66 \times 10^{-7}, 1.44 \times 10^{-2}) \text{ mol/g.}$$

Then, the dynamical character of each of the real finite and infinite critical points is determined. It is found that among them there are only 14 critical points which have eigenvalue spectra that contain only one unstable direction. All of these 14 equilibria are finite. Finally by examining all trajectories that emanate from these 14 equilibria, only two of them are connected with R_{19} along its slowest mode via heteroclinic orbits. These two critical points are R_{74} and R_{79} . Fig. 4 shows a 3-D projection of the 1-D SIM embedded inside the 6-D reduced composition space. Since only the slow modes are present on the SIM, this 1-D manifold is the best description of the system's slowest dynamics.

V. CONCLUSION

Actual 1-D SIMs for closed, spatially homogenous, isothermal, reactive systems described by detailed kinetics are obtained. The construction method is based on a geometrical approach that relies upon finding and examining the dynamical behavior of all the system's critical points. It has been shown that the construction of the 1-D SIMs are algorithmically easy and computationally efficient. The resulting procedure provides a useful tool to significantly reduce the computational cost associated with modeling reactive systems.

ACKNOWLEDGMENTS

The authors recognize the support of the National Science Foundation (NSF) under *CBET*-0650843, and the Center for Applied Mathematics (CAM) at University of Notre Dame. A. J. Sommes and J. D. Hauenstein

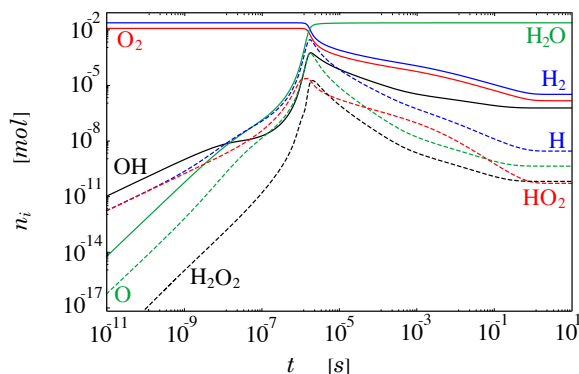


Fig. 3. The time evolution of species for the $H_2 - Air$ reactive system.

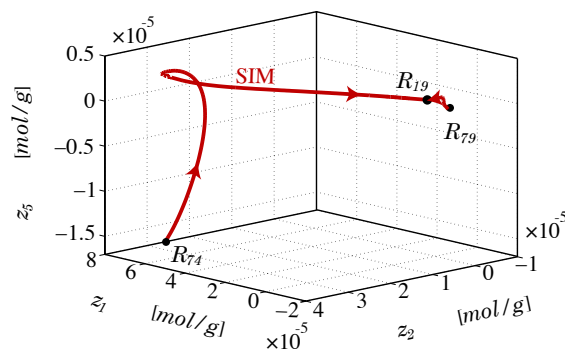


Fig. 4. The 1-D SIM for the detailed $H_2 - Air$ mechanism.

are supported by NSF grants *DMS*-0410047 and *DMS*-0712910. J. A. Diller is supported by NSF grant *DMS*-0653678.

REFERENCES

- [1] S. H. Lam and D. A. Goussis, "Understanding Complex Chemical Kinetics with Computational Singular Perturbation," *Proceedings of the Twenty-second Symposium (International) on Combustion*, Combustion Institute, Pittsburgh, OH, pp. 931–941, 1988.
- [2] M. J. Davis and R. T. Skodje, "Geometric Investigation of Low-Dimensional Manifolds in Systems Approaching Equilibrium," *J. Chem. Phys.*, vol. 111, pp. 859–874, 1999.
- [3] U. Maas and S. B. Pope, "Simplifying Chemical Kinetics: Intrinsic Low-Dimensional Manifolds in Composition Space," *Combust. Flame*, vol. 88, pp. 239–264, 1992.
- [4] S. H. Lam, "Using CSP to Understand Complex Chemical Kinetics," *Combust. Sci. Tech.*, Vol. 89, pp. 375–404, 1993.
- [5] Z. Ren, S. B. Pope, A. Vladimirov, and J. M. Guckenheimer, "The Invariant Constrained Equilibrium Edge Preimage Curve Method for The Dimension Reduction of Chemical Kinetics," *J. Chem. Phys.*, vol. 124, p. 114111, 2006.
- [6] D. Lebedev, "Computing Minimal Entropy Production Trajectories: An Approach to Model Reduction in Chemical Kinetics," *J. Chem. Phys.*, vol. 120, pp. 6890–6897, 2004.
- [7] M. R. Roussel and S. J. Fraser, "On The Geometry of Transient Relaxation," *J. Chem. Phys.*, vol. 94, pp. 7106–7113, 1991.
- [8] A. N. Al-Khateeb, J. M. Powers, S. Paolucci, A. J. Sommes, J. A. Diller, J. D. Hauenstein, and J. D. Mengers, "Constructing Slow Invariant Manifolds for Closed Reactive Systems," *J. Chem. Phys.*, submitted.
- [9] L. Perko, *Differential Equations and Dynamical Systems*. New York, NY: Springer, 2001.
- [10] A. J. Sommes and C. W. Wampler, *The Numerical Solution of Systems of Polynomials Arising in Engineering and Science*. Hackensack, NJ: World Scientific, 2005.
- [11] J. M. Powers and S. Paolucci, "Uniqueness of Chemical Equilibria in Ideal Mixtures of Ideal Gases," *Amer. J. Phys.*, vol. 76, pp. 848–855, 2008.
- [12] R. J. Kee, F. M. Rupley, and J. A. Miller, "Chemkin-II: A Fortran Chemical Kinetics Package for the Analysis of Gas Phase Chemical Kinetics," Sandia National Labs. Livermore, CA: Rept. SAND89-8009B, 1992.
- [13] Bates, D. J., Hauenstein, J. D., Sommes, A. J., and Wampler, C. W., "Bertini: Software for Numerical Algebraic Geometry," Online available: <http://www.nd.edu/~sommese/bertini>.
- [14] D. L. Baulch, et al., "Evaluated Kinetic Data for Combustion Modeling: Supplement II," *J. Phys. Chem. Ref. Data*, vol. 34, pp.757–1326, 2005.
- [15] J. A. Miller, R. E. Mitchell, M. D. Smooke, and R. J. Kee, "Toward a comprehensive chemical kinetic mechanism for the oxidation of Acetylene: Comparison Model Predictions with Results from Flame and Shock Tube Experiments," *Proceedings of the Nineteenth Symposium (International) on Combustion*, Combustion Institute, Pittsburgh, OH, pp. 181–196, 1992.

On the Relation Between Reaction Dynamics and Thermodynamics in Closed Systems

A. N. Al-Khateeb*, J. M. Powers*, S. Paolucci*, A. J. Sommesè†, J. A. Diller†, J. D. Mengers*

*University of Notre Dame, Department of Aerospace and Mechanical Engineering, Notre Dame, Indiana, USA

†University of Notre Dame, Department of Mathematics, Notre Dame, Indiana, USA

Abstract—A reactive system’s slow dynamic behavior is approximated well by its evolution on manifolds of dimension lower than the dimensionality of the full composition space. This work addresses the relation between the isothermal reactive systems’ slow dynamics, described by the actual slow invariant manifolds, and notions from thermodynamics. In addition to mathematical proof, a realistic reactive system is utilized to show that other than identifying the actual equilibrium point, traditional thermodynamic potentials provide no guidance in determining a system’s actual slow invariant manifold. A comparison between several published thermodynamics-based manifolds and the actual slow invariant manifolds is presented.

I. INTRODUCTION

Dimension reduction can significantly reduce the computational cost of modeling detailed kinetics reactive systems. The technique is based on representing the chemistry of a reactive system’s variables in terms of the chemistry of a reduced number of variables. Thus, several methods to describe the multi-scale kinetics that employ a geometrical approach have been developed to reduce the dimensionality of reactive systems.

A number of these methods employ classical thermodynamics to construct the attractive manifolds. Examples include the method of rate-controlled constrained equilibrium (RCCE) [1], the method of invariant manifold (MIM) [2], the minimal entropy production trajectory (MEPT) method [3], the invariant constrained equilibrium edge preimage curve method (ICE-PIC) [4], and other methods which are based on them [5]-[7]. The MEPT approach relies on the principle of entropy production. Utilizing such a principle allows classical thermodynamics quantities to be used away from equilibrium, although the validity of doing this is debatable [8]. The RCCE, MIM and ICE-PIC approaches rely on employing equilibrium thermodynamics potentials away from the equilibrium state. By minimizing the appropriate classical thermodynamics quantities, at some point in the procedure, their low-dimensional manifolds are constructed.

Ref. [9] provides a procedure to construct reactive systems’ actual slow invariant manifolds (SIMs). Such manifolds describe the asymptotic structures of the invariant attracting reactive systems’ trajectories during their relaxation toward equilibrium. Utilizing this procedure to construct reactive systems’ actual one-dimensional (1-D) SIMs makes it possible to examine the relation between thermodynamics and reactive systems’ slow dynamics.

II. ANALYSIS

We consider a closed, spatially homogenous, premixed reactive mixture of calorically imperfect ideal gases described by detailed mass-action kinetics. The mixture is confined to a volume V at temperature T and pressure p . This mixture consists of N species composed of L atomic elements which undergo J reversible reactions.

Here, we confine our attention to isothermal reactive systems. For such a reactive system, the evolution of the species specific moles \mathbf{z} with time t is described by [9]

$$\frac{d\mathbf{z}}{dt} = \dot{\mathbf{w}}(\mathbf{z}), \quad \{\mathbf{z}, \dot{\mathbf{w}}\} \in \mathbb{R}^R, \quad (1)$$

where $\mathbb{R}^R \subset \mathbb{R}^N$ is the reduced composition space, and $\dot{\mathbf{w}}$ is the molar production rate of species in the reduced composition space. The dimensionality of the composition space is reduced to R as a consequence of the conservation of elements, and any additional constraints that can possibly arise. The system’s actual 1-D SIM can be constructed by using the procedure described in [9].

A. Thermodynamic conditions

For a mixture of ideal gases, the Gibbs free energy G is given by the following relation [10],

$$G = \sum_{i=1}^N n_i \bar{\mu}_i, \quad (2)$$

where n_i is the number of moles of species i , and $\bar{\mu}_i$ is the chemical potential of species i . This thermodynamic property is of special interest; the global minimum of G corresponds to the reactive system’s equilibrium state \mathbf{z}^e which satisfies $\dot{\mathbf{w}}(\mathbf{z}^e) = \mathbf{0}$ [10]. This state is unique [11] within the physical region of composition space and is identified by the following relation,

$$\sum_{i=1}^N \nu_{ij} \bar{\mu}_i = 0, \quad j = 1, \dots, J, \quad (3)$$

where ν_{ij} is net stoichiometric matrix.

Similarly, the entropy S of such mixture is given by [10],

$$S = \sum_{i=1}^N n_i \left(\bar{s}_i^o - \bar{\mathfrak{R}} \ln \left(\frac{p n_i}{p^o n} \right) \right), \quad (4)$$

where $\bar{\mathfrak{R}}$ is the universal gas constant, p^o is the reference pressure, \bar{s}_i^o is the partial molar entropy evaluated at p^o ,

and $n = \sum_{i=1}^N n_i$ is the total number of moles. The differential change of this scalar quantity is postulated by the second law of thermodynamics [10], though it is stated differently in non-equilibrium thermodynamics and classical thermodynamics [12]. In non-equilibrium thermodynamics, the differential change of S for such system is given by

$$dS = d_e S + d_i S, \quad (5)$$

where $d_e S$ is the change in S due to the system's exchange of matter and energy with its surroundings, and

$$d_i S = -\frac{1}{T} \sum_{i=1}^N \bar{\mu}_i dn_i, \quad (6)$$

is the change in entropy due to irreversible processes within the system boundary [13]. Thus, an expression for the irreversibility production rate σ , (*i.e.* entropy production rate), can be introduced as [14]

$$\sigma \equiv \frac{d_i S}{dt} = -\frac{1}{T} \sum_{i=1}^N \bar{\mu}_i \frac{dn_i}{dt}. \quad (7)$$

Similar to G , σ is a convex function in the composition space with a global minimum at \mathbf{z}^e .

B. Thermodynamics and SIM

In a 2-D composition space, the scalar fields G and σ can be represented by iso-contours. Near equilibrium these contours approach ellipses. For each of these functions, the major axes of these ellipses are aligned with the eigenvector associated with the largest eigenvalue of that function's local Hessian matrix \mathbf{H}^e . Similarly, the minor axes are aligned with the eigenvector associated with the smallest eigenvalue of \mathbf{H}^e . The deviations from these two functions' equilibrium values are described by,

$$G - G|_{\mathbf{z}=\mathbf{z}^e} = \frac{1}{2} \mathbf{z}^T \cdot \mathbf{H}_G^e \cdot \mathbf{z} + \dots, \quad (8)$$

$$\sigma - \sigma|_{\mathbf{z}=\mathbf{z}^e} = \frac{1}{2} \mathbf{z}^T \cdot \mathbf{H}_\sigma^e \cdot \mathbf{z} + \dots \quad (9)$$

In general, all the system's trajectories within the physically accessible domain \mathbb{S} approach \mathbf{z}^e in infinite time. Near equilibrium, the system's dynamics relax onto the eigenvector associated with the slowest time scale. At \mathbf{z}^e , the eigenvector associated with the least negative eigenvalue of the local Jacobian \mathbf{J}^e defines the direction of the system's slowest mode. At \mathbf{z}^e there is a relation between \mathbf{H}_G^e and \mathbf{H}_σ^e ; one can show that

$$\mathbf{H}_\sigma^e = -\frac{1}{T} \left(\mathbf{H}_G^e \cdot \mathbf{J}^e + (\mathbf{H}_G^e \cdot \mathbf{J}^e)^T \right), \quad (10)$$

where the two terms on the right hand side of (10) are transposes of one another, and their summation is a symmetric matrix.

In the highly unusual case in which \mathbf{H}_G^e is diagonal with identical eigenvalues, the SIM can be identified by consideration of the eigenvectors of \mathbf{H}_σ^e . In general, this is not the case for reactive systems. Thus, \mathbf{H}_G^e operates on \mathbf{J}^e in a non-uniform way, such that the eigenvalues

and the eigenvectors of \mathbf{H}_σ^e are not the same as those of \mathbf{J}^e . Thus, the system's dynamics cannot be deduced by σ or G . We can state that employing equilibrium thermodynamic potentials to obtain a reactive system's dynamic behavior is incorrect. Full details are given by Al-Khateeb, *et al.* [9].

III. MODEL PROBLEM

Here, the Zeldovich mechanism will be employed as a model problem to examine the relation between slow dynamics and thermodynamics. The system's actual 1-D SIM constructed using the procedure described in [9] is shown in Fig. 1.

After calculating G and σ for this system, their iso-contours, along with the system's actual 1-D SIM, are shown in Fig. 2. The top panel of Fig. 2 shows the contours of G and σ far away from the system's physical equilibrium point, R_3 . The bottom panel of Fig. 2 is an expansion in its vicinity, where stretching has been employed to expose the difference between the contours' major/minor axes and the 1-D SIM. Even within the close neighborhood of R_3 , the contours' axes are not aligned with the 1-D SIM! Here equilibrium thermodynamics quantities cannot elucidate the 1-D SIM, which describes the system's preferred path towards equilibrium. Subsequently, the gradients of these thermodynamic scalar functions do not drive the system's dynamics.

Explicitly, the eigenvalues and the associated eigenvectors of \mathbf{H}_σ^e and \mathbf{H}_G^e for the Zel'dovich model are

$$\begin{aligned} \mathbf{H}_\sigma^e : (\boldsymbol{\lambda}, \mathbf{v}) &= (8.17 \times 10^{23}, 1.01 \times 10^{20}), \\ &([1.78 \times 10^{-3}, -1.00]^T, [-1.00, -1.78 \times 10^{-3}]^T), \\ \mathbf{H}_G^e : (\boldsymbol{\lambda}, \mathbf{v}) &= (9.44 \times 10^{19}, 1.06 \times 10^{18}), \\ &([5.97 \times 10^{-4}, -1.00]^T, [-1.00, -5.97 \times 10^{-4}]^T). \end{aligned}$$

However, the direction of the slow mode is assigned by the eigenvector associated with the least negative

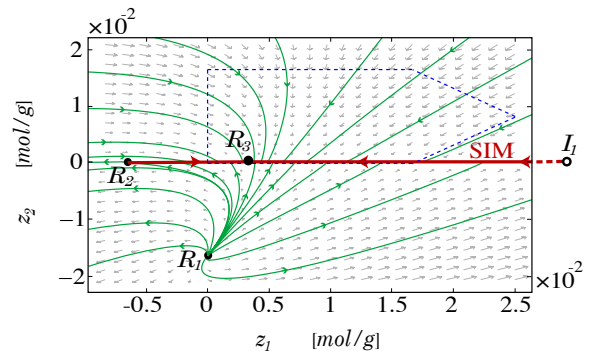


Fig. 1. A region of the finite phase space for the Zel'dovich mechanism. The solid dots represent finite critical points, the open circle represents an infinite critical point, the arrows indicate the flow direction, and the dashed simplex represents \mathbb{S} . The SIM is illustrated as a thick line, the thin lines represent trajectories, and R_3 represents the system's physical equilibrium state.

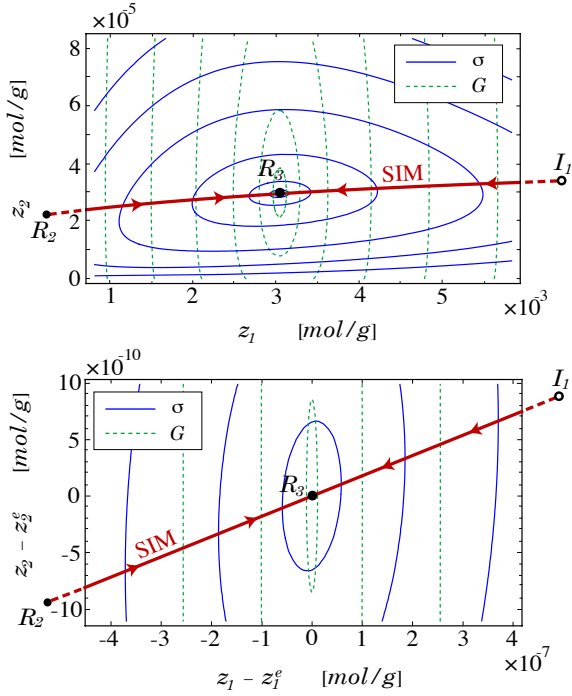


Fig. 2. The 1-D SIM for the Zel'dovich mechanism near the physical equilibrium state, R_3 . The dashed lines and the solid lines represent different levels of the system's irreversibility production rate and Gibbs free energy, respectively. R_2 is a finite critical point, and I_1 is an infinite critical point.

eigenvalue of \mathbf{J}^e , where

$$\mathbf{J}^e : (\lambda, \mathbf{v}) = (-1.73 \times 10^7, -1.91 \times 10^5), \\ ([-1.07 \times 10^{-1}, 9.94 \times 10^{-1}]^T, [1.00, 1.79 \times 10^{-3}]^T).$$

Here, the eigenvalues' and eigenvectors' units are $1/s$ and g/mol , respectively. It is clear that the second eigenvector of \mathbf{J}^e is not aligned with any eigenvector of \mathbf{H}_G^e or \mathbf{H}_σ^e . Indeed, at R_3 the difference with σ is small. But, as shown in the first panel of Fig. 2, this error grows as we move away from R_3 .

IV. THERMODYNAMICS-BASED MANIFOLDS

Here, a comparison between previously published reactive systems' low dimensional manifolds and the actual SIMs for these reactive systems is performed.

A. SIM and MEPT

A simple closed reactive system containing three species given by the following kinetics model, $A + A \rightleftharpoons B \rightleftharpoons C$, is considered. This system is identical to the example employed in [3] to present the MEPT method. To construct the system's actual 1-D SIM, the methodology presented in [9] is employed. In Fig. 3, the system's actual 1-D SIM is shown. We note that the system's 1-D SIM contains only one branch.

The MEPT method is based on minimizing a classical thermodynamic potential, S . Given by the dashed line in the first panel of Fig. 4, the MEPT path shown is identical to the one presented in Fig. 4 of [3]. A closer look at the system's dynamical behavior near the physical

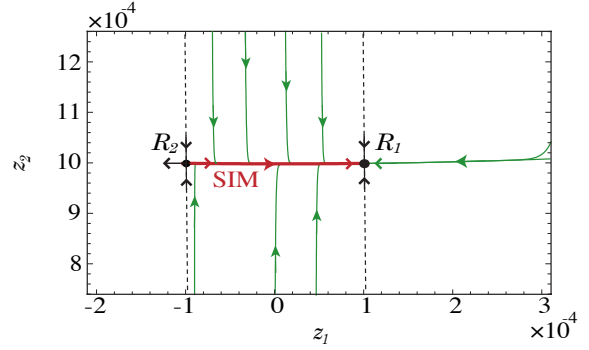


Fig. 3. A small region of the actual finite phase space. The thick line is the SIM, the thin lines represent trajectories, the dashed lines represent the fast invariant manifolds, R_2 is a non-physical finite critical point, and R_1 represents the system's physical equilibrium state.

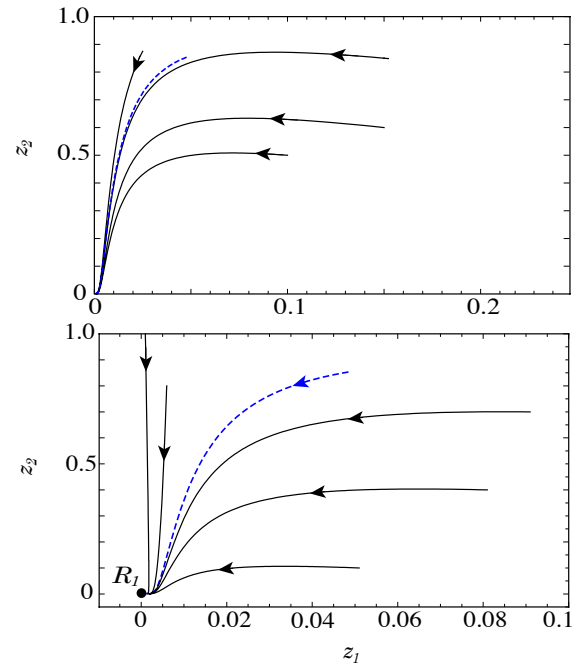


Fig. 4. The dashed line represents the calculated MEPT and the thin lines represent trajectories. The top panel is identical to Fig. (4) in [3], while the bottom panel is a closer look with a different set of trajectories is illustrated. R_1 represent the physical equilibrium state of the system.

equilibrium shows that the MEPT is not an attractive manifold; see the second panel of Fig. 4. Consequently, it does not correspond to the actual SIM of the system.

From Figs. 3-4, we note that none of the trajectories other than the SIM are attractive. Furthermore, due to the fact that all trajectories will approach R_1 , this possibly led to the incorrect conclusion in [3] that the MEPT corresponds to the SIM.

B. SIM and ICE-PIC

Here, the simple hydrogen-oxygen reactive system employed in [4] to illustrate the idea of constructing the ICE-PIC manifold is adopted. To construct the system's actual 1-D SIM, the methodology presented in [9] is used, and the system's 1-D SIM is shown in Fig. 5. The right

branch of the SIM is not presented completely due to scaling effects. Some of the trajectories in Fig. 5 have been generated from inside the physical domain, while others have been initiated from the boundaries of the physical domain. The attractiveness of the SIM is revealed by visually examining the relaxation of several trajectories rapidly onto it.

Generating the ICE manifold is based on minimizing a classical thermodynamics potential. First, the constrained equilibrium manifold (CEM) is developed by minimizing G . The intersection between the CEM and \mathcal{S} defines a closed curve. Then, starting from several points located on this closed curve, trajectories are generated. The collection of all these trajectories defines the ICE manifold. Fig. 6 shows the constructed 1-D SIM and the 2-D ICE manifold. The ICE manifold shown is identical to the manifold illustrated in Fig. 4 of [4].

From Fig. 6, it is clear that there are trajectories within \mathcal{S} which are not attracted to the 2-D ICE manifold. However, all of the system's trajectories are attracted to the actual 1-D SIM. Moreover, the 1-D SIM is not a subset of the 2-D ICE manifold. Consequently, the 2-D ICE manifold cannot fully identify the system's SIM. Although it is difficult to visualize in Fig. 6, the 2-D ICE manifold is not aligned with the system's 1-D SIM. The error in the ICE manifold grows as we move away from R_7 .

V. CONCLUSION

The relationship between thermodynamics and a reactive system's SIM is investigated. It has been illustrated that the 1-D SIM for a realistic reactive system does not coincide with the path identified by minimizing a classical thermodynamic function, such as σ , S , or G , even at the equilibrium state! This point has been confirmed by mathematical proof which shows that classical equilibrium thermodynamic potentials do not provide information about reactive systems' dynamics during their approach towards the physical equilibrium.

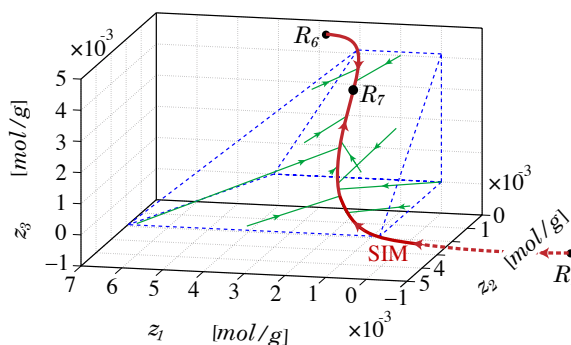


Fig. 5. The SIM for the simple hydrogen-oxygen reactive system as a thick line. R_7 represents the physical equilibrium state, R_1 and R_6 are non-physical finite critical points, the dashed simplex represents \mathcal{S} , and the thin lines illustrate several trajectories.

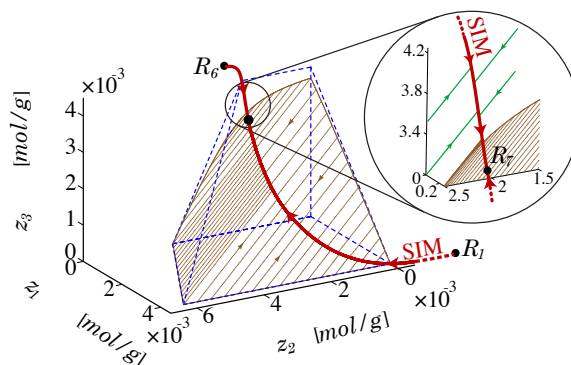


Fig. 6. A comparison between the actual 1-D SIM, illustrated as thick line, and the 2-D ICE manifold, illustrated in brown, for the simple hydrogen-oxygen reactive system. Thin lines illustrate trajectories inside \mathcal{S} .

ACKNOWLEDGMENTS

The authors recognize the support of the National Science Foundation (NSF) under *CBET*-0650843, and the Center for Applied Mathematics (CAM) at the University of Notre Dame. A. J. Sommes is supported by NSF grants *DMS*-0410047 and *DMS*-0712910, and J. A. Diller is supported by NSF grant *DMS*-0653678.

REFERENCES

- [1] J. C. Keck and D. Gillespie, "Rate-Controlled Partial-Equilibrium Method for Treating Reacting Gas-Mixtures," *Combust. Flame*, vol. 17, pp. 237–248, 1971.
- [2] A. N. Gorban and I. V. Karlin, "Method of Invariant Manifold for Chemical Kinetics," *Chem. Eng. Sci.*, vol. 58, pp. 4751–4768, 2003.
- [3] D. Lebedz, "Computing Minimal Entropy Production Trajectories: An Approach to Model Reduction in Chemical Kinetics," *J. Chem. Phys.*, vol. 120, pp. 6890–6897, 2004.
- [4] Z. Ren, S. B. Pope, A. Vladimirov, and J. M. Guckenheimer, "The Invariant Constrained Equilibrium Edge Preimage Curve Method for the Dimension Reduction of Chemical Kinetics," *J. Chem. Phys.*, vol. 124, p. 114111, 2006.
- [5] S. Ugarte, Y. Gao, and H. Metghalchi, "Application of the Maximum Entropy Principle in the Analysis of a Non-Equilibrium Chemically Reacting Mixture," *Int. J. Thermodynamics*, vol. 8, pp. 43–53, 2005.
- [6] Z. Ren, S. B. Pope, A. Vladimirov, J. M. Guckenheimer, and M. John, "Application of the ICE-PIC Method for the Dimension Reduction of Chemical Kinetics Coupled with Transport," *Proceedings of the Thirty-first Symposium (International) on Combustion*, Combustion Institute, Pittsburgh, OH, pp. 473–481, 2007.
- [7] V. Reonhardt, M. Winckler, and D. Lebedz, "Approximation of Slow Attracting Manifolds in Chemical Kinetics by Trajectory-Based Optimization Approaches," *J. Phys. Chem. A*, vol. 112, pp. 1712–1718, 2008.
- [8] I. Müller and W. Weiss, *Entropy and Energy: A Universal Competition*. Berlin, Germany: Springer, 2005.
- [9] A. N. Al-Khateeb, J. M. Powers, S. Paolucci, A. J. Sommes, J. A. Diller, J. D. Hauenstein, and J. D. Mengers, "Constructing Slow Invariant Manifolds for Closed Reactive Systems," *J. Chem. Phys.*, submitted.
- [10] H. B. Callen, *Thermodynamics and an Introduction to Thermostatistics*. New York, NY: Wiley, 1985.
- [11] J. M. Powers and S. Paolucci, "Uniqueness of Chemical Equilibria in Ideal Mixtures of Ideal Gases," *Amer. J. Phys.*, vol. 76, pp. 848–855, 2008.
- [12] W. J. Vincenti and C. H. Kruger, *Introduction to Physical Gas Dynamics*. New York, NY: Wiley, 1965.
- [13] I. Prigogine, *Introduction to Thermodynamics of Irreversible Processes*. New York, NY: Interscience Publishers, 1967.
- [14] S. R. de Groot and P. Mazur, *Non-Equilibrium Thermodynamics*. New York, NY: Dover, 1984.

Invariant Grids and Lattice Boltzmann Method for Combustion

Eliodoro Chiavazzo*, Ilya V. Karlin*[†], Alexander Gorban[‡], Konstantinos Boulouchos*

*Swiss Federal Institute of Technology (ETH)/Department of Mechanical Engineering, Zurich, Switzerland

[†]University of Southampton/Department of Mechanical Engineering, Southampton, UK

[‡]University of Leicester/Department of Mathematics, Leicester, UK

Abstract—The lattice Boltzmann (LB) method is a relatively novel approach to numerical flow simulations, and recent studies have proved that it is highly competitive to traditional methods when simulating compressible and turbulent flows (in terms of accuracy and efficiency). Although this makes LB a good candidate for computing reactive flows, applications in this field are still limited by the stiffness of the governing equations and the large amount of fields to solve. In this sense, the present study intends to provide an effective tool for reactive flow simulations via the LB method.

I. INTRODUCTION

Accurate modeling of reactive flows requires the solution of a large number of conservation equations as dictated by detailed reaction mechanism. In addition to the sometimes prohibitively large number of variables introduced, the numerical solution of the governing equations has to face the stiffness due to the fast time scales of the kinetic terms. These issues make computations of even simple flames time consuming, and have particularly negative impact on the lattice Boltzmann method, whose number of fields (distribution functions or populations) is significantly larger than the number of conventional fields (density, momenta, temperature, species mass fractions) by a factor ranging from tens to hundreds for 2D and 3D simulations. However, the dynamics of complex reactive systems is often characterized by short initial transients when the solution trajectories approach low-dimensional manifolds in the concentration space, known as the *slow invariant manifolds* (SIM). Thus, the construction of SIM enables to establish a simplified description of a complex system by extracting only the slow dynamics and neglecting the fast.

The Method of Invariant Grids (MIG), based on the concept of SIM, has been elaborated for combustion applications with the aim of automating the model reduction procedure, and its realization follows two key steps. First, an initial rough reduced description of the complex chemical mechanism is constructed making use of the notion of *quasi equilibrium manifold* (QEM). Second, the latter initial approximation is iteratively refined until the *invariant grid* is constructed. In fact, according to MIG, the accurate reduced model (invariant grid) is the stable fixed point of one of the following processes: Newton-like iterations for solving the *invariance condition* regarded as an equations, or relaxation due to a *film equation* of dynamics [1], [2]. Lately, the reduced model of the hydrogen

mechanism can be employed in a lattice Boltzmann code for simulating laminar flames throughout a homogeneous mixture.

II. REDUCED DESCRIPTION

In our study, the detailed mechanism of Li et al [3] (9 species, 21 elementary reactions) for hydrogen combustion is considered, and we search for a reduced description with two degrees of freedom. To this end, let us construct the 2D quasi equilibrium manifold for a stoichiometric H_2 -air mixture under fixed pressure $p = 1\text{bar}$ and enthalpy $\bar{h} = 2.8\text{kJ/kg}$, corresponding to the temperature $T_0 = 300\text{K}$ for the stoichiometric unburned mixture $H_2 + 0.5O_2 + 1.88N_2$. A QEM is obtained solving the following minimization problem:

$$\begin{aligned} \min \quad & G \\ \text{s.t.} \quad & \sum_i m_j^i Y_i = \xi^j, \quad j = 1, 2. \end{aligned} \quad (1)$$

Here, G represents the mixture-averaged entropy, and the vector set $\{\mathbf{m}_j = (m_j^1, \dots, m_j^9)\}$ is used to reparameterize the mass fractions Y_i in terms of new variables ξ^j , which are expected to follow a slow dynamics. Many suggestions for defining slow lumped variables in chemical kinetics are known in the literature, and for our purposes here we use the *total number of moles* ξ^1 and *free oxygen* ξ^2 , respectively (see, e.g., [4]). An approximated solution to (1), computed making use of the algorithm introduced in [5], is shown in Fig. 1, and it is called *quasi equilibrium grid* (QEG). The corresponding invariant grid is found by relaxation of the QEG Ω under the following film equation of dynamics [1]

$$\frac{d\Omega}{dt} = \vec{f} - \mathbf{P}\vec{f}, \quad (2)$$

where \vec{f} and \mathbf{P} denote the vector of motion in the phase space and a projector operator onto the manifold tangent space, respectively. Following [1], here we adopt the *thermodynamic projector* which enables to define the fast motions toward the slow manifolds. Finally, the refined grid, approximating the slow invariant manifold, is shown in Fig. 2. More details can be found in the literature [6], [7], [8].

III. LATTICE BOLTZMANN FOR REACTIVE FLOWS

We consider here the simplest lattice Boltzmann formulation suitable for simulations of combustion. To this

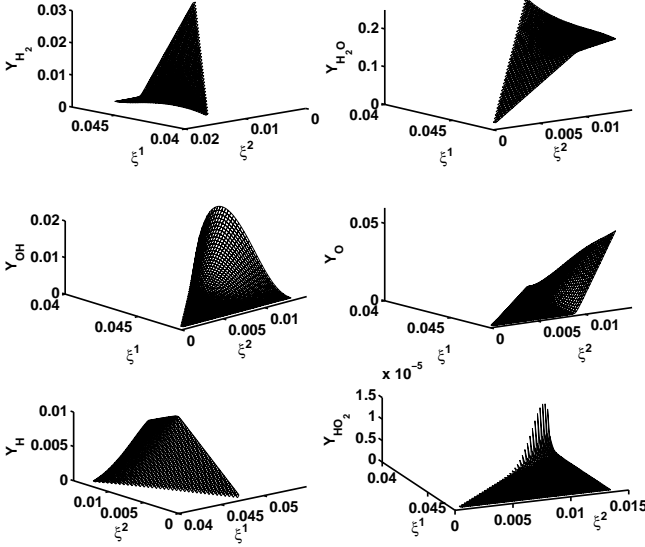


Fig. 1. Quasi equilibrium grid (QEG): Six coordinates function of the parameters ξ^1, ξ^2 .

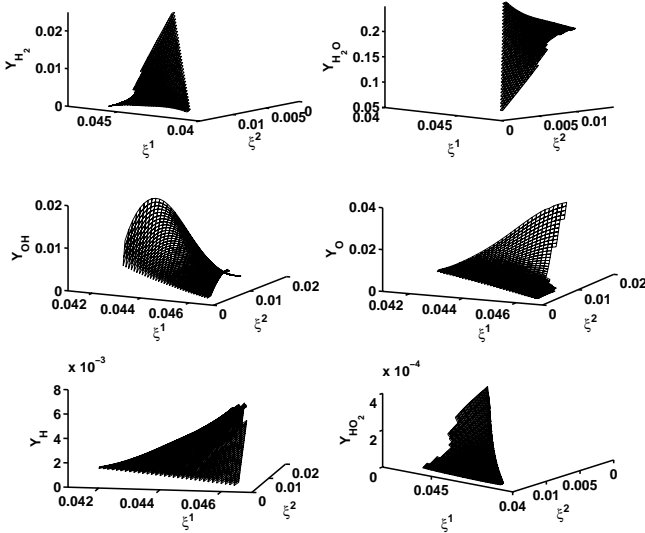


Fig. 2. Invariant grid approximating the slow invariant manifold.

end, following the suggestion of Yamamoto et al [9], reactive flows can be simulated with the lattice Boltzmann method as reported below. Note, however, that more elaborate and complete LB models for mixtures [10], [11] and compressible flows [12] shall be taken into account in the near future, too. According to the standard terminology, LB schemes are denoted as DMQN, meaning that N particles move on a M -dimensional lattice. In Fig. 3, the most popular one-dimensional lattice is shown, where each distribution function is represented by its own peculiar velocity e_α . In the following, we briefly review the LB algorithm with the BGK [13] collision model. A single-component medium is described by a small set of populations, which can be regarded as microscopic properties of the fluid. On the contrary, macroscopic quantities such as density and momentum (energy for thermal cases) are given by different moments of those populations. In terms of pressure distribution functions

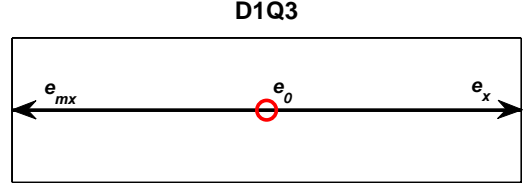


Fig. 3. 1-dimensional 3-velocities lattice: $D1Q3$.

p_α , the LB equation takes the following discrete form at the lattice node \mathbf{x} :

$$p_\alpha(\mathbf{x} + \mathbf{e}_\alpha, t + \delta t) = p_\alpha(\mathbf{x}, t) - \frac{1}{\tau_F} [p_\alpha(\mathbf{x}, t) - p_\alpha^{eq}(p, \mathbf{u})], \quad (3)$$

where the equilibrium populations p_α^{eq} read:

$$p_\alpha^{eq} = w_\alpha p \left[1 + 3(\mathbf{e}_\alpha \mathbf{u}^T) + \frac{9}{2}(\mathbf{e}_\alpha \mathbf{u}^T)^2 - \frac{3}{2} \mathbf{u}^2 \right]. \quad (4)$$

The pressure p and the fluid velocity \mathbf{u} are given by:

$$p = \sum_\alpha p_\alpha, \quad \mathbf{u} = \frac{1}{p_0} \sum_\alpha \mathbf{e}_\alpha p_\alpha, \quad (5)$$

where the reference pressure $p_0 = \rho_0/3$, with ρ_0 denoting the reference density of the LB model. Let δt be the time step, the relaxation parameter τ_F is related to the kinematic viscosity ν by (see, e.g., [14])

$$\nu = \frac{2\tau_F - 1}{6} \delta t. \quad (6)$$

In general, the discrete velocities can be regarded as the nodes of a Gauss-Hermite quadrature applied to the Maxwell-Boltzmann distribution function, and each of them is characterized by a proper weight w_α .

According to [9], the flow field is not affected by the chemical reaction, transport coefficients are constant and Fick's law applies to the diffusion. In this case, the background flow is treated as an one-component medium whose pressure populations evolution obeys (3). Let \bar{h}_0 be a reference enthalpy, the evolution equations for enthalpy and concentration of species i are written as

$$\begin{aligned} \tilde{h}_\alpha(\mathbf{x} + \mathbf{e}_\alpha, t + \delta t) - \tilde{h}_\alpha(\mathbf{x}, t) = \\ - \frac{1}{\tau_h} \left[\tilde{h}_\alpha(\mathbf{x}, t) - \tilde{h}_\alpha^{eq}(\tilde{h}, \mathbf{u}) \right] + w_\alpha Q_h, \end{aligned} \quad (7)$$

$$\begin{aligned} Y_{i\alpha}(\mathbf{x} + \mathbf{e}_\alpha, t + \delta t) - Y_{i\alpha}(\mathbf{x}, t) = \\ - \frac{1}{\tau_{Y_i}} \left[Y_{i\alpha}(\mathbf{x}, t) - Y_{i\alpha}^{eq}(Y_i, \mathbf{u}) \right] + w_\alpha Q_{Y_i}, \end{aligned} \quad (8)$$

where

$$\tilde{h} = \bar{h}/\bar{h}_0 = \sum_\alpha \tilde{h}_\alpha, \quad Y_i = \sum_\alpha Y_{i\alpha}, \quad (9)$$

and the equilibrium populations $\tilde{h}_\alpha^{eq}, Y_{i\alpha}^{eq}$ are expressed as in (4) after replacing p with \tilde{h} and Y_i , respectively. Assume t_0 is a factor for converting physical time into LB time units: $(t)_{LB} = (t)_{phys}/t_0$, the source terms take the explicit form

$$Q_h = \frac{1}{h_0} \left(\sum_{i=1}^9 \frac{\dot{\omega}_i W_i}{\bar{\rho}} h_i \right) t_0 \delta t, \quad Q_{Y_i} = \frac{\dot{\omega}_i W_i}{\bar{\rho}} t_0 \delta t, \quad (10)$$

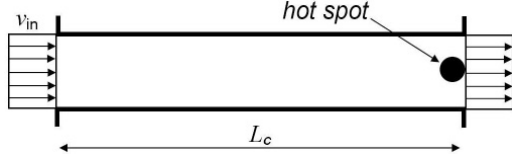


Fig. 4. Schematic representation of the 1D setup.

where $\bar{\rho}$ is the mixture-averaged density, while $\dot{\omega}_i$, W_i , h_i denote the rate of change, molecular weight and enthalpy of species i , respectively. The thermal diffusivity κ and diffusion coefficient D_i of species i are related to the relaxation parameters as follows [14]

$$\kappa = \frac{2\tau_h - 1}{6}\delta t, \quad D_i = \frac{2\tau_{Y_i} - 1}{6}\delta t. \quad (11)$$

IV. EXAMPLE: FREELY PROPAGATING FLAME

In the following, we consider a stoichiometric hydrogen-air mixture entering an adiabatic channel (constant cross section) under room conditions ($T = 300K$, $p = 1bar$) at fixed velocity $v_{in} = 1.2m/s$. A heat source is placed at the outlet in order to ignite the mixture (see Fig. 4). A flame front is formed and propagates upstream since the laminar flame speed is larger than the flow velocity.

For simplicity, we use the assumption of equal diffusivity D for all species and Lewis number $Le = \kappa/D = 1$. In this case, the mixture enthalpy \bar{h} and the element fractions remain constant throughout the domain, and the reduced dynamics takes place along the invariant grid constructed as discussed in the section II. Notice however that, the latter assumption is not restricting and a generalization is obtained by extending the invariant grid with enthalpy and element fractions as additional degrees of freedom. On the other hand, in premixed systems, those quantities are conserved up to small fluctuations and, for such applications, the invariant grid is often sufficient. Finally, in low-Mach combustion, the pressure p can be considered constant for most cases.

Under the latter assumptions, the equations (8) can be written in terms of the slow manifold parameters ξ^1 , ξ^2 as follows:

$$\begin{aligned} & \xi_\alpha^j(\mathbf{x} + \mathbf{e}_\alpha, t + \delta t) - \xi_\alpha^j(\mathbf{x}, t) = \\ & -\frac{1}{\tau_\xi} [\xi_\alpha^j(\mathbf{x}, t) - \xi_\alpha^{jeq}(\xi^j, \mathbf{u})] + w_\alpha Q_{\xi^j}, \end{aligned} \quad (12)$$

where, the equilibrium populations for the reduced variables ξ^j read

$$\xi_\alpha^{jeq} = w_\alpha \xi^j \left[1 + 3(\mathbf{e}_\alpha \mathbf{u}^T) + \frac{9}{2}(\mathbf{e}_\alpha \mathbf{u}^T)^2 - \frac{3}{2}\mathbf{u}^2 \right], \quad (13)$$

and the source terms take the form:

$$Q_{\xi^j} = \sum_{i=1}^9 m_j^i Q_{Y_i}, \quad \xi^j = \sum_{i=1}^9 m_j^i Y_i. \quad (14)$$

The setup of Fig. 4 was simulated by solving both the detailed model (7), (8) and the reduced one (12). In the latter case, the source terms Q_{ξ^j} are tabulated at each

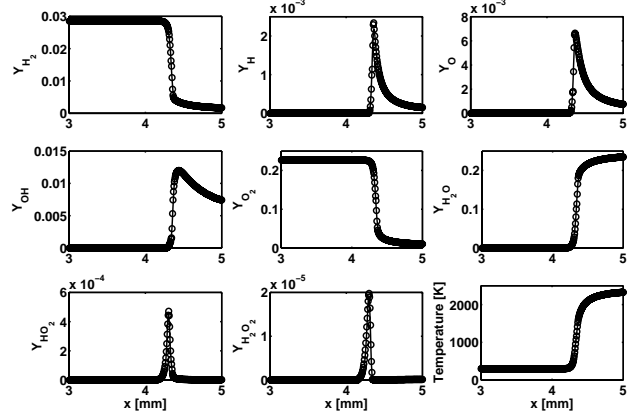


Fig. 5. Fields along the channel at a given time: detailed model (continuous line) and reduced model (circles).

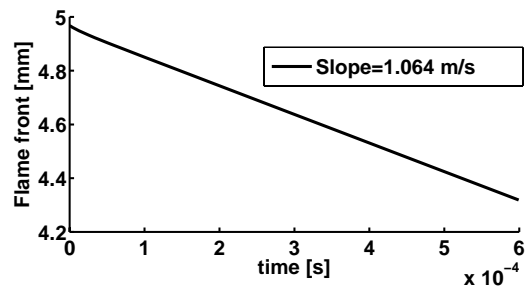


Fig. 6. Flame front position vs time with the inlet velocity $v_{in} = 1.2m/s$.

node of the invariant grid, and accessed through multivariate linear interpolation. When simulating the reduced model, a remarkable saving, in terms of both memory (one-quarter of the density functions are stored at any lattice node) and number of time steps ($\delta t_{reduced} \cong 35\delta t_{detailed}$), can be achieved. Moreover, based on the comparison in Fig. 5, we can argue that the suggested methodology enables to perform detailed simulations with high accuracy. Finally, in Fig. 6 the flame position is shown as function of time. The flame is defined as the point with the highest heat release Q_h at a given time. The linear dependence indicates that the flame moves at constant speed given by: $S_L = \text{slope} + v_{in} \cong 2.26m/s$. The value of the burning velocity S_L is in perfect accordance with the detailed model prediction (up to 2%) and in a good agreement with experimental data (see, e.g. [15]).

V. EXAMPLE: PREMIX COUNTERFLOW FLAMES

Here, we consider the so-called counterflow laminar flame as a two dimensional benchmark of the suggested methodology. A well premixed stoichiometric H_2 -air mixture is uniformly ejected from two parallel stationary flat nozzles, located at $y = \pm L_y$. When properly ignited, the fuel reacts generating two twin flames in this counterflow, while the burned gas exits the domain along the x -direction. As illustrated in the sketch of Fig. 7, under the assumption of symmetrical flow with respect to the stagnation lines $x = 0$ and $y = 0$, the computational

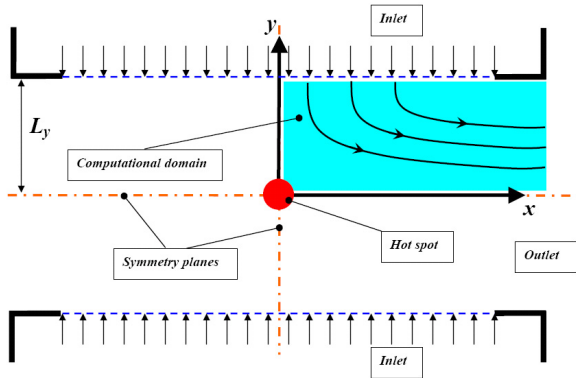


Fig. 7. Schematic representation of the 2D setup.

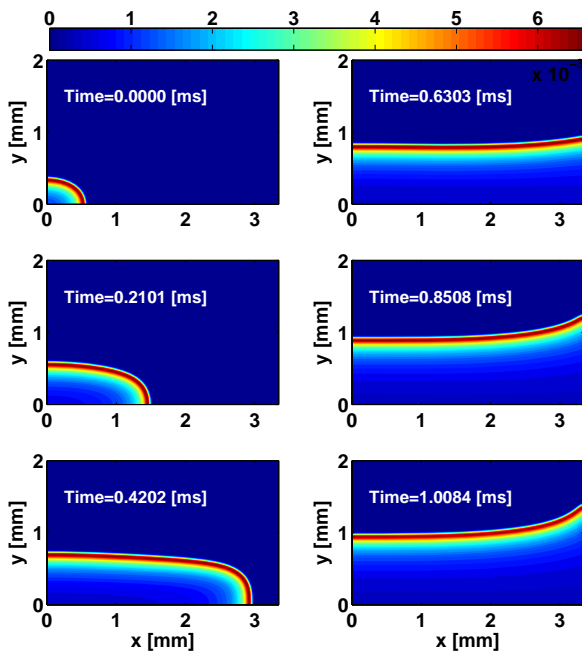


Fig. 8. Detailed model using the $D2Q9$ lattice: O mass fraction evolution

domain can be restricted to the region where $x \geq 0$ and $y \geq 0$, and simulations can be carried out using the standard 2-dimensional lattice $D2Q9$. In both models (detailed and reduced), the mixture, initially under room temperature $T_0 = 300K$, is ignited by placing a hot spot at the origin of the reference system. Very good agreement is demonstrated as reported in Figures 8 and 9, where the time evolution of O radical concentration is shown.

VI. CONCLUSIONS

Here, we suggest a methodology for using accurate reduced chemical kinetics in combination with a lattice Boltzmann solver for simulating reactive flows. It has been shown that the Method of Invariant Grids (MIG) is suitable for providing the reduced description of chemistry, and this approach enables to cope with stiffness when solving the LB species equations. This is particularly desirable in the case of explicit solvers, and it results in a remarkable speedup.

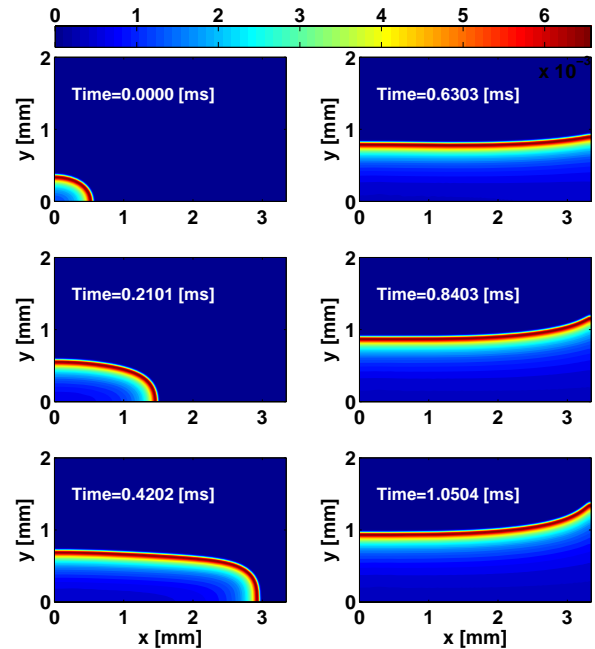


Fig. 9. Reduced model using the $D2Q9$ lattice: O mass fraction evolution

ACKNOWLEDGMENT

This work was accomplished under the financial support of Swiss National Science Foundation (SNF, Project 200021-107885/1) and CCEM-CH.

REFERENCES

- [1] A. Gorban, I. V. Karlin, *Invariant Manifolds for Physical and Chemical Kinetics*. Springer, Berlin, 2005.
- [2] A. N. Gorban, I. V. Karlin, A. Y. Zinovyev, *Physica A*, vol. 333, pp. 106–154, 2004.
- [3] J. Li, Z. Zhao, A. Kazakov, F.L. Dryer, *Int. J. Chem. Kinet.*, vol. 36, pp. 566–575, 2004.
- [4] Q. Tang, S. B. Pope, *Combust. Theory Model.*, vol. 8, pp. 255–279, 2004.
- [5] E. Chiavazzo, I. V. Karlin, *Jour. Comput. Phys.*, vol. 227, pp. 5535–5560, 2008.
- [6] E. Chiavazzo, A.N. Gorban, I.V. Karlin, *Comm. Comput. Phys.*, vol. 2, pp. 964–992, 2007.
- [7] E. Chiavazzo, I.V. Karlin, C.E. Frouzakis, K. Boulouchos, *Proc. Combust. Instit.*, vol. 32, pp. 519–526, 2009.
- [8] E. Chiavazzo, I. V. Karlin, A. N. Gorban, K. Boulouchos, *JSTAT*, (preprint), 2009.
- [9] K. Yamamoto, X. He, G. D. Doolen *Jour. Stat. Phys.*, vol. 107, pp. 367–383, 2002.
- [10] S. Arcidiacono, J. Mantzaras, S. Ansumali, I. V. Karlin, C. E. Frouzakis, *Phys. Rev. E*, vol. 74, 056707, 2006.
- [11] S. Arcidiacono, I. V. Karlin, J. Mantzaras, and C. E. Frouzakis, *Phys. Rev. E*, vol. 76, 046703, 2007.
- [12] N. Prasianakis and I. V. Karlin, *Phys. Rev. E*, vol. 76, 016702, 2007.
- [13] P. L. Bhatnagar, E. P. Gross, M. Krook, *Phys. Rev.*, vol. 94(3), pp. 511–525, 1954.
- [14] S. Chen, G. Doolen, *Annu. Rev. Fluid Mech.*, vol. 30, pp. 329–364, 1998.
- [15] C. K. Law, O. C. Kwon, *Int. Jour. of hydrogen energy*, vol. 29, pp. 867–879, 2004.

Validation of Detailed Chemical Kinetic Models

H. J. Curran

National University of Ireland, Galway, Ireland

Abstract

Stricter emissions legislation combined with the need to reduce greenhouse gas emissions in order to militate against climate change drives fundamental research to produce cleaner more efficient systems. Chemical kinetic mechanisms are used by relevant industries to predict and optimize the operating behaviour of experimental facilities such as internal combustion engines, gas turbines and other combustion devices. More practically, detailed chemical mechanisms are reduced so that they reproduce the relevant target be it ignition delay time, flame speed, etc., and then combined with computational fluid dynamics simulations in order to accurately represent the whole combustion environment.

However, in order to validate and produce accurate detailed chemical kinetic mechanisms in the first instance, a wide range of data is needed, and which is normally generated under well-controlled physical conditions of temperature, pressure, fuel/air ratio and dilution. These data include (i) ignition delay times recorded in shock tubes and in rapid compression machines, (ii) speciation data from flow reactors, jet-stirred reactors and flame experiments and (iii) flame measurements of laminar burning velocity. Typically, these mechanisms for hydrocarbon and oxygenated hydrocarbon systems are generated in a hierarchical way, starting first with the hydrogen/oxygen system, thereafter adding a carbon monoxide/carbon dioxide subset, followed by formaldehyde, methane and other larger C_1 - C_n species.

This work will discuss the development of detailed chemical kinetic mechanisms in the context of hierarchy and range of validation. Some typical problems associated with these mechanisms will be discussed and some ideas on how they may be addressed will be explored. Moreover, the application of detailed kinetic mechanisms to fuel flexibility in gas turbines will be explored in some more detail.

Phase space structure of complex chemical-kinetic mechanisms: Low-dimensional manifolds for homogeneous chemical kinetics and 1-d premixed flames

Michael J. Davis

Chemistry Division
Argonne National Laboratory
Argonne, IL 60439
Email: davis@tcg.anl.gov

Figure 1 shows a typical result for one-dimensional premixed flames. The mass fractions for several species are plotted vs. the distance from the burner.

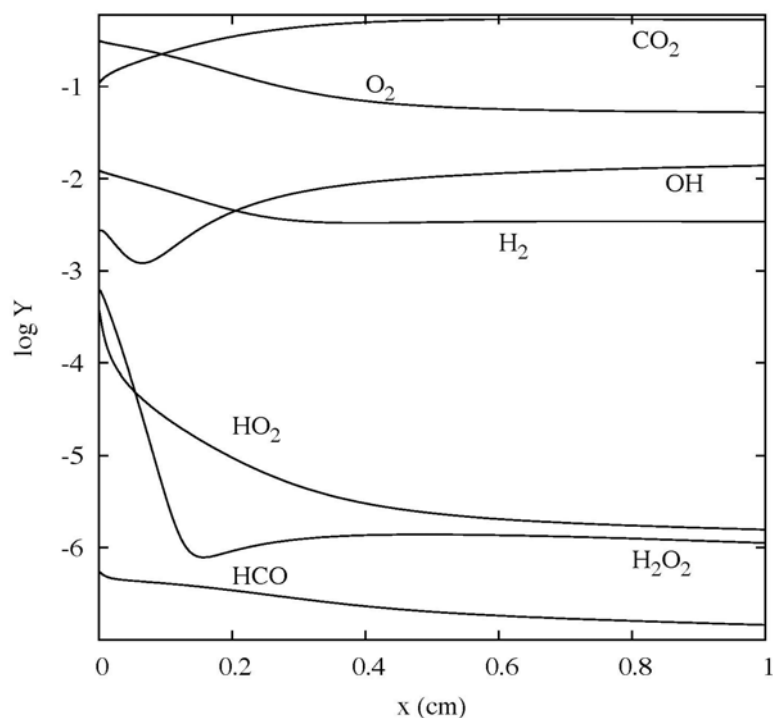
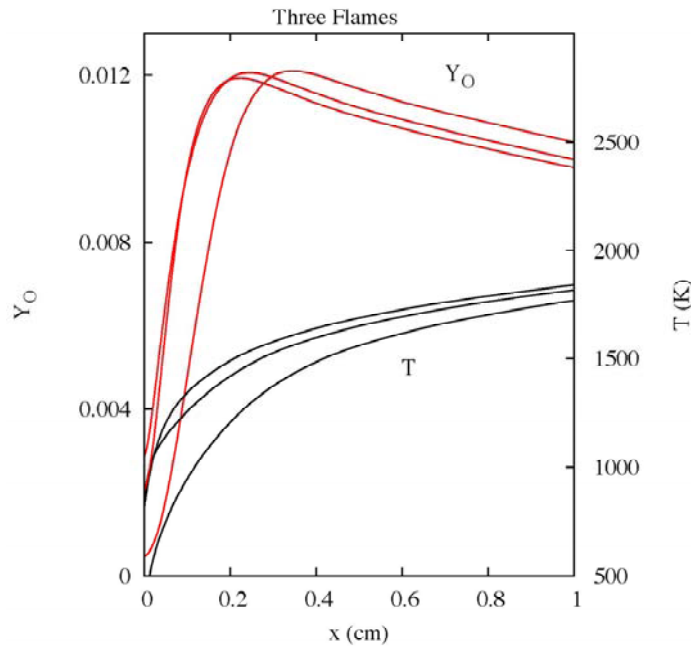


Fig. 1

These results were generated for the formaldehyde/methanol/CO mechanism of Dryer and co-workers. The mixture mole fractions at the burner were: $3/7$ CO, $2/7$ O₂, and $2/7$ H₂, with $T = 300$ K. This result is extended in Fig. 2 to two additional flames, which have different mixtures at the burner and different initial temperatures in Fig. 2. The additional flames have the following mixtures and temperatures: 1) $1/6$ CH₂O, $1/3$ CO,

Fig.
2



1) $1/6 \text{ H}_2$, $1/3 \text{ O}_2$, and $T = 855 \text{ K}$, 2) $0.08 \text{ CH}_3\text{OH}$, 0.42 CO , 0.17 H_2 , 0.33 O_2 , and $T = 809 \text{ K}$.

As Fig. 2 indicates, the behavior of flames can be very similar away from the burner ($x > 0.2 \text{ cm}$ in the figure), even when the mixtures and temperatures are different at the burner. Figure 3 makes this point more strongly, by plotting projections of these

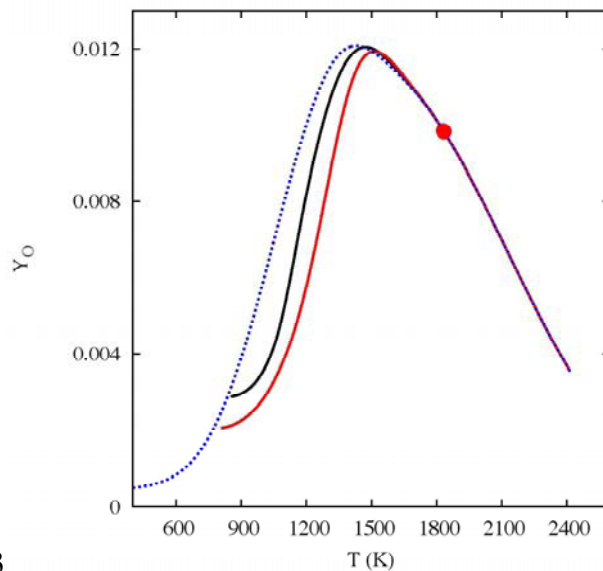


Fig. 3

flames in phase space. This figure makes it clear that the steady flames are approaching a one-dimensional manifold in phase space, although they reach the manifold at different spatial locations (at the dot the spatial locations are 0.98, 1.05, and 1.25 cm).

The purpose of this talk will be to discuss the phenomena observed in the figures in terms of the phase space structure of the system. The talk will also put the behavior in

the broader context of the composite phase space structure of a chemical-kinetic mechanism. Additional topics of the talk will be: 1) how the phase space structure in the flame compares to the phase space structure of the homogeneous chemical kinetics, 2) how the phase space structure changes with stoichiometry, pressure, and enthalpy, and 3) how the phase space structure of this mechanism compares to other hydrocarbon mechanisms. In particular, the latter topic will lead to a comparison of the Princeton methanol mechanism with the C₃ mechanism developed at Galway for the lowest dimensional manifolds.

Time Integration of Reacting Flows with CSP Tabulation

Youssef Marzouk*, Bert Debuschere†, Habib Najm†, Dimitris Goussis‡, Mauro Valorani§, Michael Frenklach¶

*Massachusetts Institute of Technology, Cambridge, MA, USA

†Sandia National Laboratories, Livermore, CA, USA

‡National Technical University of Athens, Athens, Greece

§Università di Roma “La Sapienza”, Rome, Italy

¶University of California at Berkeley and Lawrence Berkeley National Lab., Berkeley, CA, USA

bjdebus@sandia.gov

Abstract— This paper presents recent progress on the use of Computational Singular Perturbation (CSP) techniques for time integration of stiff chemical systems. The CSP integration approach removes fast time scales from the reaction system, thereby enabling integration with explicit time stepping algorithms. For further efficiency improvements, a tabulation strategy was developed to allow reuse of the relevant CSP quantities. This paper outlines the method and demonstrates its use on the simulation of hydrogen – air ignition.

I. INTRODUCTION

The dynamics of chemical systems exhibit a wide range of time scales, with associated stiffness of the governing equations. This stiffness, and the significant complexity of chemical kinetic models, both lead to substantial challenges with the computation of chemical systems. Chemical model simplification and reduction strategies typically target these challenges by reducing the number of reactions and/or species in the model, with associated reduction in model complexity. When done properly, this strategy also reduces the system stiffness. Alternatively, the Computational Singular Perturbation (CSP)-based time integration construction of [1] uses CSP analysis to project out the fast time scales from the detailed chemical source term, thereby rendering the equations non-stiff. The promise of this approach is that explicit time integrators can be used for large-time step integration of the resulting non-stiff source terms, with associated computational speedup as compared to implicit time integration of the non-filtered detailed source term. Further, this can very well eliminate the need for operator-split time integration of reaction-diffusion source terms. Moreover, by tailoring the projection operators to the local chemical state, optimized adaptive strategies can be implemented.

The key challenge with this time integration approach, however, is the large computational cost of solving for the requisite CSP information and the resulting projection matrices. This is where tabulation comes in. By adaptively storing and reusing the CSP information, the significant CSP overhead can be drastically reduced, leading to an efficient overall implementation. We have explored the

utility of tabulation of CSP quantities and their reuse for time integration in earlier works on elementary model problems [2], [3]. Our tabulation strategy is based on the Piecewise Reusable Implementation of Solution Mapping (PRISM) [4] technique, whereby the chemical configuration space is suitably and adaptively subdivided into hypercubes within which low order polynomial response surfaces are used to represent the quantities of interest. In the current work, we extend this approach by using k d-trees [5] to efficiently store the CSP information along manifolds in the chemical configuration space, without requiring *a priori* partitioning of this space.

The paper first outlines the use of CSP analysis for integrating chemically reacting systems, illustrated on the simulation of H₂ – air ignition. Next, the tabulation approach is introduced and employed on this same reacting system. We illustrate the performance of the integrator, and highlight the role of the CSP homogeneous projection operation in the table construction and subsequent time integration of the system.

II. BASICS

Consider the chemical system described by

$$\frac{d\mathbf{y}}{dt} = \mathbf{g}(\mathbf{y}) \quad (1)$$

where $\mathbf{y} \in \mathbb{R}^N$, and $\mathbf{g}(\mathbf{y})$ is the chemical source term. The CSP basis vectors $\{\mathbf{a}_k\}_{k=1}^N$ and covectors $\{\mathbf{b}^k\}_{k=1}^N$, all in \mathbb{R}^N , enable the decoupling of the fast and slow processes, and the identification of low dimensional slow invariant manifolds (SIMs) [6]. Thus, we have

$$\frac{d\mathbf{y}}{dt} = \mathbf{g} = \mathbf{g}_{\text{fast}} + \mathbf{g}_{\text{slow}} \quad (2)$$

$$= \mathbf{a}_1 f^1 + \mathbf{a}_2 f^2 + \dots + \mathbf{a}_N f^N \quad (3)$$

where $f^i = \mathbf{b}^i \cdot \mathbf{g}$, for $i = 1, 2, \dots, N$. After relaxation of fast transients, with M modes exhausted,

$$\mathbf{g}_{\text{fast}} = \sum_{r=1}^M \mathbf{a}_r f^r \approx 0 \quad (4)$$

$$\mathbf{g}_{\text{slow}} = \sum_{s=M+1}^N \mathbf{a}_s f^s = \left(I - \sum_{r=1}^M \mathbf{a}_r \mathbf{b}^r \right) \mathbf{g} = \mathbf{P} \mathbf{g} \quad (5)$$

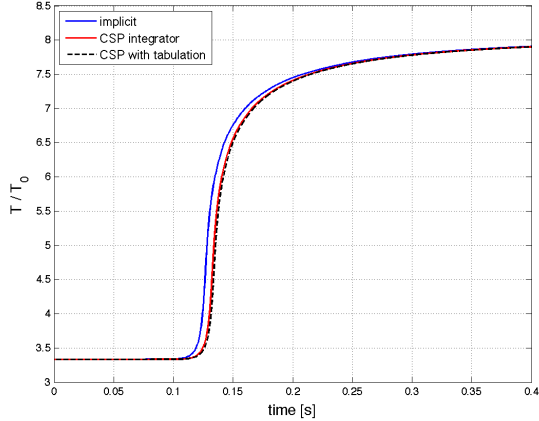


Fig. 1. Evolution of temperature (normalized by $T_0 = 300$ K) in an igniting lean H_2 -air system, using an implicit solver (blue solid line), the CSP solver (red solid line), and the CSP solver with tabulation (black dashed line). All three approaches are in good agreement, except for minor differences in the ignition time delay.

The CSP integrator [1] proceeds in each time step by first integrating the slow dynamics of the system, followed by a homogeneous correction (HC) to correct for the fast time scales:

$$\tilde{\mathbf{y}}(t + \Delta t) = \mathbf{y}(t) + \int_t^{t+\Delta t} \mathbf{P}\mathbf{g} dt' \quad (6)$$

$$\mathbf{y}(t + \Delta t) = \tilde{\mathbf{y}}(t + \Delta t) - \sum_{m,n=1}^M \mathbf{a}_m \tau_n^m |_t \hat{\mathbf{f}}^n \quad (7)$$

$$\hat{\mathbf{f}}^n = \mathbf{b}^n \cdot \mathbf{g}[\tilde{\mathbf{y}}(t + \Delta t)] \quad (8)$$

where τ_n^m is the inverse of λ_n^m , given by

$$\lambda_n^m = \left(\frac{d\mathbf{b}^m}{dt} + \mathbf{b}^m \mathbf{J} \right) \mathbf{a}_n \quad (9)$$

and \mathbf{J} is the Jacobian of \mathbf{g} . Note that the time integration of the slow dynamics can be done using any suitable time integration procedure. Also, the matrix τ_n^m is diagonal with entries the time scales $\{\tau_k\}_{k=1}^N$ when the CSP basis vectors are chosen to be the eigenvectors of \mathbf{J} and the curvature of the SIM is neglected, *i.e.* $d\mathbf{b}^m/dt = 0$.

III. APPLICATION TO H_2 -AIR IGNITION SYSTEM

The CSP integration method outlined in the previous section was applied to the simulation of ignition of a lean homogeneous H_2 -air mixture at a temperature of $T = 1000$ K. The system is modeled using a 9 species reaction mechanism, resulting in a total state space dimension of $N = 10$ (9 species + temperature) [7]. Fig. 1 compares the predicted temperature evolution obtained with a full, implicit integration (using CVODE), and with the CSP integrator (using the explicit RKC integration scheme).

The CSP integrated solution is in good agreement with the full solution, except for a small difference in the ignition time delay. The CSP approximation can be improved by selecting a smaller time step factor α , where α is the integration time step as a fraction of the first non-exhausted time scale τ_{M+1} : $\Delta t = \alpha \cdot \tau_{M+1}$. As shown in

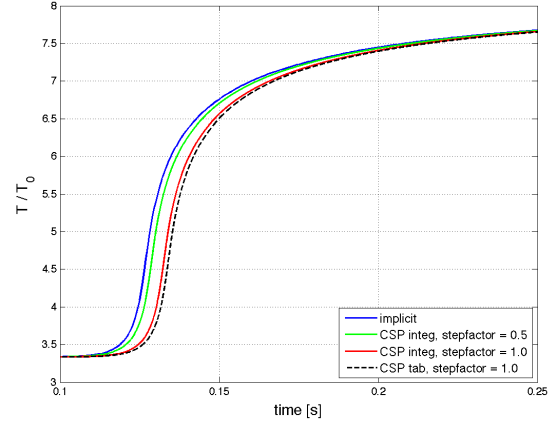


Fig. 2. Close-up of the ignition zone of Fig. 1. The CSP approximation converges to the implicit solution with decreasing time step factor α : $\Delta t = \alpha \cdot \tau_{M+1}$.

Fig. 2, cutting the time step factor to 0.5 greatly improves the accuracy of the predicted ignition time.

As the reaction progresses, the number of exhausted modes M , and the associated CSP radicals change according to the reaction dynamics. Fig. 3 indicates that the system initially has two exhausted modes, followed by a time window during ignition where all modes are active, after which M gradually increases up to three at late time, as more and more modes become inactive.

IV. TABULATION

While the CSP integrator provides an effective way to remove stiffness from the reaction system, the approach is still computationally expensive given the high cost of determining the CSP vectors and covectors \mathbf{a} and \mathbf{b} , as well as the associated time scales. To improve the efficiency of the CSP integrator, a tabulation approach has been developed to enable reuse of the essential CSP quantities: the M fast CSP vectors and covectors, as well as the $M + 1$ fastest time scales, which are sufficient to assemble the slow-manifold projector \mathbf{P} needed for the HC and CSP integration, and to select the time step along the slow manifold.

While other methods have relied on tabulation of integrated source term data over the chemical state space before [4], [8], the combination of CSP with tabulation is particularly powerful as CSP effectively reduces the needed dimension of the tabulation. As the CSP vectors, covectors and time scales can be modeled as functions of the active modes only, it is sufficient to tabulate these quantities in an $N - M$ dimensional table, rather than having to cover the full N -dimensional state space. For example, for the H_2 -air system studied here, tabulation in a 7-dimensional table is sufficient for the section(s) of the 10-dimensional state space where 3 modes are exhausted (see Fig. 3).

Starting from a number of *design points* in state space, successive HCs are applied to identify SIMs in the system. Each SIM is characterized by a unique value of M and the

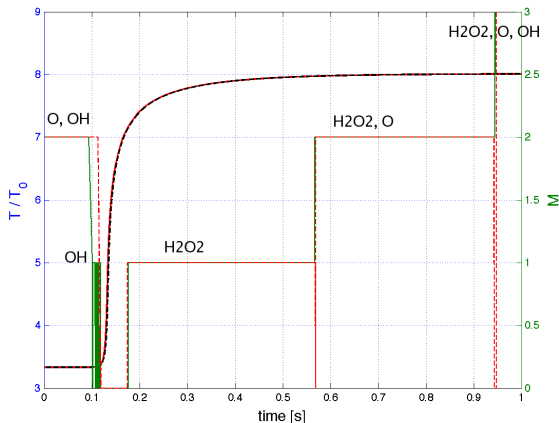


Fig. 3. Evolution of the temperature and the number of exhausted modes, M , as obtained by the CSP integrator (green) and the CSP integrator with tabulation (red). The species labels indicate the CSP radicals corresponding with the exhausted modes.

associated CSP radicals. The extent in \mathbb{R}^N within which each manifold is valid is assumed to be the smallest box, aligned with the Cartesian coordinates (T, Y_1, \dots, Y_k) , that encompasses all design points that are attracted by the manifold.

For each identified SIM, the tabulation of the associated CSP information relies on a nonparametric regression approach, which offers a high degree of flexibility as it does not depend on any pre-determined spatial partitioning. Information is retrieved using efficient nearest-neighbor searches through kd -tree data structures that cover the $N - M$ dimensional slow species space [5], and new data can readily be added to the table as it becomes available. In the current implementation, the CSP information is approximated with the corresponding values at the nearest neighbor point in the table, which amounts to a 0^{th} -order interpolation. Higher order interpolations, relying on interpolation between nearest neighbors or on polynomial response surfaces [2], [4], are the subject of ongoing work.

As indicated in Figs. 1 and 2, the temperature profile in the ignition simulation with the tabulation approximation matches the predictions with the regular CSP integrator very well. While showing overall good agreement, Fig. 3 does reveal small differences in the number of exhausted modes with and without tabulation in a small time span right before ignition, at $t \approx 0.1$ s. However, those differences seem to have no significant effect, as illustrated by the overall good agreement between the CSP predictions with and without tabulation of the temperature profile, as well as the O_2 and H_2O_2 species mass fractions shown in Fig. 4.

In [2], the CSP integrator combined with a tabulation approach was shown to be competitive with direct CVODE integration in terms of CPU cost. The performance of the present tabulation scheme, as a function of the table size, system and manifold dimensionality, degree of stiffness, and desired accuracy is currently under study.

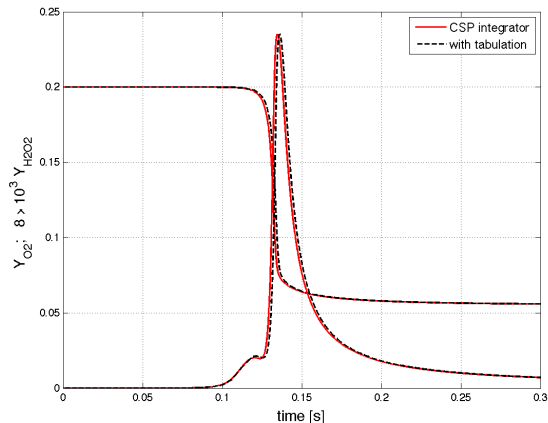


Fig. 4. Mass fractions of O_2 and H_2O_2 using the CSP integrator with (black dashed line) and without tabulation (red solid line). The tabulation approximation is in excellent agreement with the non-tabulated integration.

V. CONCLUSIONS

This paper demonstrated the use of CSP to automatically reduce the stiffness in reaction mechanisms, enabling their integration with efficient explicit time stepping algorithms. To improve the computational efficiency of this approach, a tabulation method has been developed that enables efficient reuse of CSP information. The approach was shown to give good results for the simulation of ignition in a H_2 -air mixture with a 9 species model. Ongoing work focuses on further improvement of the efficiency and accuracy of the tabulation approach.

ACKNOWLEDGMENT

This work was supported by the US Department of Energy (DOE), Office of Basic Energy Sciences (BES), SciDAC Computational Chemistry program. Sandia National Laboratories is a multiprogram laboratory operated by Sandia Corporation, a Lockheed Martin Company, for the United States Department of Energy under contract DE-AC04-94-AL85000. MYF acknowledges the financial support of DOE, BES under contract no. DE-AC03-76SF00098. MV acknowledges the support of the Italian Ministry of University and Research (MIUR).

REFERENCES

- [1] Valorani, M., and Goussis, D.A., *J. Comput. Phys.*, 169:44–79 (2001).
- [2] Lee, J.C., Najm, H.N., Lefantzi, S., Ray, J., Frenklach, M., Valorani, M., and Goussis, D., *Combustion Theory and Modeling*, 11(1):73–102 (2007).
- [3] Lee, J.C., Najm, H.N., Lefantzi, S., Ray, J., and Goussis, D.A., in *Computational Fluid and Solid Mechanics 2005* (K. Bathe, Ed., Elsevier Science, pp. 717–720, (2005).
- [4] Tonse, S.R., Moriarty, N.W., Brown, N.J., and Frenklach, M., *Israel Journal of Chemistry*, 39:97–106 (1999).
- [5] Arya, S., Mount, D. M., Netanyahu, N. S., Silverman, R., and Wu, A. Y., *J. ACM*, 45(6):891–923 (1998).
- [6] Lam, S.H., and Goussis, D.A., *Proc. Comb. Inst.*, 22:931–941 (1988).
- [7] Yetter, R.A., Dryer, F.L., and Rabitz, H., *Combust. Sci. Technol.*, 79:97 (1991).
- [8] Pope, S.B., *Combust. Theory and Modelling*, 1:41–63 (1997).

Reduction and Equivalence of Nonlinear Distributed Symmetric Control Systems

Bill Goodwine* and Baoyang Deng*

*University of Notre Dame/Aerospace and Mechanical Engineering, Notre Dame, IN, USA

Abstract—This paper considers the ‘reduction’ problem for large-scale distributed control systems. In particular, we consider control-theoretic concepts for control systems containing multiple instances of identical controllers or components where the overall system is invariant with respect to interchanging these identical components. The main results are invariance of controllability, motion planning and optimal control properties for an equivalence class of symmetric systems of this type.

I. INTRODUCTION

This paper considers nonlinear control-theoretic properties of large-scale distributed systems, which consist of, perhaps many, interconnected subsystems. Since the size of these systems can make analysis difficult or intractable, the aim of this work is to exploit symmetry properties of such systems to reduce their complexity. Unlike most model reduction problems, the approach here is *exact* in that some control-theoretic properties are equivalent in the reduced order model and large model.

The type of symmetry we consider is when certain subsystems of the overall system can be interchanged with other subsystems without changing the dynamics of the overall system. The general idea is that a distributed system is comprised of sets of multiple, repeated instances of identical hardware, which naturally can be interchanged. We represent such symmetric distributed systems using a graph-theoretic representation, as illustrated in Figure 1. Each node of the graph represents a subsystem of the overall system, and if each of the nodes 2-11 are identical, the system is characterized by an S_{10} symmetry (the symmetric group of order 10), which is a consequence of the fact that each of the subsystems 2-11 can be interchanged without altering the system.

When a subsystem is interchanged, the input/output connections of the subsystem must match the input/output connection of the replaced subsystem. For example, consider a team of mobile robots working together to manipulate an object. Suppose that each robot transmits its horizontal position to one neighboring robot and its vertical position to another. Clearly, if this robot is to be replaced by a similar robot, the system would only work if the correct, *i.e.*, horizontal or vertical, position is transmitted to the correct neighbor since each of the neighbors are expecting and acting on a particular type of information. For the system in Figure 1, for example, node 2 must interact with node 3 in the same manner that node 6 interacts with node 7, otherwise the dynamics of the overall system will be altered if they were interchanged.

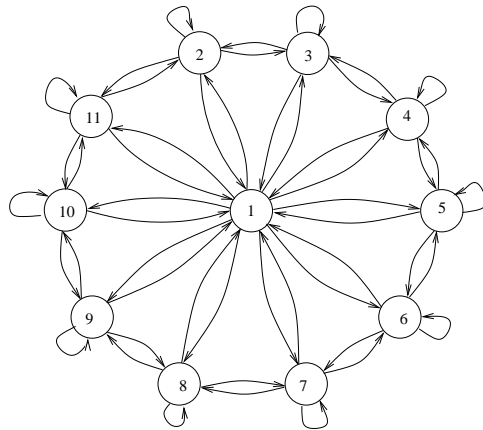


Fig. 1. An eleven node distributed system.

The method presented in this paper constructs a formal means of determining whether subsystems can be interchanged without altering the global system characteristics. Furthermore, this method can be used to then determine if a symmetric subsystem can be added without altering some of the control-theoretic properties of the system. In such a case, computations involving the “small” symmetric systems will provide a means to determine these properties for larger, symmetric systems.

There have been many efforts toward controllability of distributed systems [3], [5], [14], [1] and distributed systems with symmetry [6], [15]. These efforts are limited to *linear* systems; however, this paper considers fully nonlinear systems. There have also been many efforts toward reducing nonlinear mechanical and control systems [8], [9], [7], [10], [11], [2], [20], [21]. A similar approach was considered by Tanaka [19], [18], [17]; again, those results are limited to *linear* controllability, as opposed to the full nonlinear controllability considered in this paper.

II. DRIFTLESS SYMMETRIC NONLINEAR DISTRIBUTED SYSTEMS

A. Nonlinear Distributed Systems

This overview is based upon our previous results in [12]. We will consider smooth analytic driftless systems of the form

$$\begin{aligned} \Sigma: \quad \dot{x} &= g_{1,1}(x)u_{1,1} + g_{1,2}(x)u_{1,2} + \cdots & (1) \\ &+ g_{2,1}(x)u_{2,1} + g_{2,2}(x)u_{2,2} + \cdots \\ &\vdots \end{aligned}$$

$$+ g_{n,1}(x)u_{n,1} + g_{n,2}(x)u_{n,2} + \dots \quad x \in M,$$

where M is a smooth manifold and $g_{i,j}$ are smooth analytic vector fields on M , and $u = \{u_1, \dots, u_n\} \in \mathcal{U}$, where \mathcal{U} is the set of admissible controls. We assume that the set of admissible controls is a subset of \mathbb{R}^n such that,

$$\text{Aff}(\mathcal{U}) = \mathbb{R}^n,$$

where $\text{Aff}(\mathcal{U})$ denotes the affine hull of \mathcal{U} . Since we are considering distributed systems, the system is assumed to be organized into subsystems, corresponding to which are certain vector fields and control inputs. In Equation (1), the first subscript on the g 's and u 's indexes the subsystem to which the vector field and control input corresponds, and the second subscript indexes different vector fields and inputs within that subsystem. To avoid notational clutter, if a vector field only has one subscript, *i.e.*, $g_i(x)$, then it represents the *ordered set* of vector fields associated with node i , *i.e.*, $g_i(x) = \{g_{i,1}, g_{i,2}, \dots\}$. Similarly, u_i would represent the ordered set $u_i = \{u_{i,1}, u_{i,2}, \dots\}$. Any property defined for single-subscripted vector field is understood to apply to each member in that set.

Elaborating further on the distributed nature of the system, we assume that M is partitioned into a set of m regular submanifolds, M_i such that M is the Cartesian product of the M_i , *i.e.* $M = \prod_{i=1}^m M_i$. Each submanifold M_i represents a *subsystem, module, node* or *component* of the distributed system (all these terms will be used interchangeably). For example, in a system of cooperating robots, each M_i would represent the configuration space for one robot in the system and $\{u_{i,1}, u_{i,2}, \dots\}$ would be the control inputs for that robot.

Since, it is often the case that the dynamics of any one module or node is only affected by its own controller and states as well as the control inputs and states of a limited subset of the other nodes (usually its neighbors) and to help aid in providing a clear presentation, we will utilize a graph-theoretic representation of distributed systems. Formally, we define the digraph of a nonlinear control system Σ , written as \mathcal{G}_Σ , to be the pair (\mathbf{V}, \mathbf{E}) consisting of a set of vertices $\mathbf{V} = \{V_1, \dots, V_m\}$ and the set of edges, denoted by \mathbf{E} , which are ordered pairs of elements of \mathbf{V} . Each *vertex* represents one module M_i , *i.e.*, $V_i = M_i$. The *edge directed from V_i to V_j* , $E_{i,j} = \{V_i, V_j\} \in \mathbf{E}$, represents a vector field which maps elements of the vertices V_i and V_j to the tangent space of the end-point vertex V_j *i.e.*,

$$E_{i,j} : V_i \times V_j \rightarrow TV_j.$$

The edge $E_{i,j}$ is the sum of the j th components of the $g_{i,k}(x)$'s from Equation 1 that multiply the control inputs associated with node i . If it is necessary to further distinguish the edges by representing to which vector field within the subsystem it is associated, a third subscript can be added, *i.e.*,

$$E_{i,j,k} : V_i \times V_j \rightarrow TV_j.$$

This edge, $E_{i,j,k}$, still maps between the same spaces, but the third subscript indicates that it is the j th component of

$g_{i,k}$. Again, to avoid unnecessary notational complexities, we will often drop the third subscript (indexing to which control input in node i the vector fields is associated) and use $E_{i,j}$ to represent the *ordered set* of vector fields, $E_{i,j} = \{E_{i,j,1}, E_{i,j,2}, \dots\}$.

Let $\tilde{V}_i = \{V_{i,1}, \dots, V_{i,m}\}$ be an ordered set of vertices which are connected to V_i by edges directed from V_i to the elements of \tilde{V}_i and let $\tilde{E}_i = \{E_{i,\tilde{v}_1}, \dots, E_{i,\tilde{v}_m}\}$ be an ordered set of edges directed from V_i to elements \tilde{V}_i . The manner by which \tilde{V}_i and \tilde{E}_i are ordered is determined by interactions and/or communications between nodes. Note that ordering \tilde{V}_i imposes some topological structure on the system; in particular, for nodes that can be interchanged, the \tilde{V}_i sets must be ordered identically with respect to their neighbors so that their interactions with adjacent nodes are the same before and after they are interchanged to maintain invariance of the overall system dynamics.

B. Symmetric nonlinear distributed systems

Now we will consider what it means for a nonlinear distributed system to be symmetric. This will be represented by the fact that vector fields from various nodes will, in some sense, be equivalent. Since the vector fields directed from different nodes are defined on different spaces, we need a definition of equivalence which is more than just requiring that they be "identical."

Definition 1: Two vector fields, g_1 and g_2 are *equivalent*, denoted $g_1 \sim g_2$, if there exists a diffeomorphism, $\psi : M \mapsto M$, such that

$$\psi_* \circ g_1(W) = g_2(\psi(W))$$

where W is an open set. Equivalently, we can define $E_{i,j} \sim E_{k,l}$ by only considering the j th and l th components of g_i and g_k , respectively.

The definition of vector field equivalence applies to general submanifolds without any assumptions regarding the relationship between the coordinate systems defined on different nodes; however, often each node will be designed with a complimentary coordinate system so that the diffeomorphism, ψ , in definition 1 is a simple permutation of states and the open set, W , is the whole domain of validity of the system equations. Equivalence among vector fields can often be determined by inspection; however, this inspection is typically on an edge-by-edge basis in contrast to the computational approach involving the full control vector field.

Recall that the symmetric group of order $p!$, denoted S_p , is the group of permutations of p objects and that such a permutation of a set $X = \{1, \dots, p\}$ is a one-to-one mapping of X onto itself. Such a permutation ρ is written

$$\rho = \begin{pmatrix} 1 & 2 & \dots & p \\ k_1 & k_2 & \dots & k_p \end{pmatrix}$$

which represents that 1 is mapped to k_1 , 2 is mapped to k_2 , *etc.* Given an equivalence relation among vector fields, we now define a symmetric nonlinear distributed system.

Definition 2: Let a *symmetry orbit*, $\mathbf{O} \subset \mathbf{V}$, be a subset of \mathbf{V} containing p vertices, *i.e.*, $\mathbf{O} = \{V_{k_1}, V_{k_2}, \dots, V_{k_p}\}$, let $\mathbf{F} = \mathbf{V} \setminus \mathbf{O}$ be the subset of V containing $n - p$ fixed vertices, *i.e.*, $\mathbf{F} = \{V_{f_1}, \dots, V_{f_{n-p}}\}$, let \tilde{V}_{k_l} be the ordered set of vertices connected to V_{k_l} , and let $\rho \in S_p$. The system Σ is a *symmetric nonlinear distributed system* if

$$g_{k_i} \sim g_{\rho(k_i)} \quad \forall i \in \{1, \dots, p\} \text{ and } \forall \rho \in S_p.$$

Equivalently, a system is a symmetric nonlinear distributed system if

$$E_{k, \tilde{k}_l} \sim E_{\rho(k_l), \rho(\tilde{k}_l)} \quad \text{and} \quad E_{\tilde{k}_l, k} \sim E_{\rho(\tilde{k}_l), \rho(k_l)},$$

$\forall k \in \{k_1, \dots, k_p\}$, $\forall l \in \{1, \dots, (\tilde{k}_l)_m\}$, and $\forall \rho \in S_p$.

Before we define nonlinear symmetric system equivalence, we need to develop a technique which allows us to compare the relative size of two systems. Let Σ_1 and Σ_2 be symmetric nonlinear distributed systems and let $\mathcal{G}_{\Sigma_1} = \{\mathbf{V}_1, \mathbf{E}_1\}$ and $\mathcal{G}_{\Sigma_2} = \{\mathbf{V}_2, \mathbf{E}_2\}$ denote their corresponding digraphs. We say that $\mathcal{G}_{\Sigma_1} \geq \mathcal{G}_{\Sigma_2}$ if the number of vertices in \mathcal{G}_{Σ_2} is greater than the number of vertices in \mathcal{G}_{Σ_1} . Now nonlinear distributed system equivalence is defined as follows.

Definition 3: Let Σ_1 and Σ_2 be symmetric nonlinear distributed systems and $\mathcal{G}_{\Sigma_1} \geq \mathcal{G}_{\Sigma_2}$. Since each system is a symmetric nonlinear distributed system there exist symmetry orbits $\mathbf{O}_1 \subset \mathbf{V}_1$ and $\mathbf{O}_2 \subset \mathbf{V}_2$ containing p and q ($p \geq q$) vertices, respectively, *i.e.*,

$$\mathbf{O}_1 = \{V_{(k_1)_1}, V_{(k_1)_2}, \dots, V_{(k_1)_p}\}$$

and

$$\mathbf{O}_2 = \{V_{(k_2)_1}, V_{(k_2)_2}, \dots, V_{(k_2)_q}\}.$$

The systems Σ_1 and Σ_2 are *equivalent symmetric nonlinear distributed systems* if

- 1) $E_{k, (\tilde{k}_l)_1} \sim E_{k, (\tilde{k}_l)_2} \quad \forall k \in \{k_1, \dots, k_q\}, \forall l \in \{1, \dots, (\tilde{k}_l)_m\}$
- 2) $\mathbf{F}_1 = \mathbf{V}_1 \setminus \mathbf{O}_1$ and $\mathbf{F}_2 = \mathbf{V}_2 \setminus \mathbf{O}_2$ contain the same number of vertices, *i.e.*, $\mathbf{F}_1 = \mathbf{F}_2 = \{V_1, \dots, V_m\}$, and
- 3) $E_{k, (\tilde{k}_l)_1} \sim E_{k, (\tilde{k}_l)_2} \quad \forall k \in \{1, \dots, m\}, \forall l \in \{1, \dots, (\tilde{k}_l)_m\}$.

Denote the equivalence class of systems defined by this equivalence relation by $\bar{\Sigma}$.

Equivalence between symmetric nonlinear distributed systems requires that every member have an equivalent input/output structure and the same number of fixed nodes. Furthermore, corresponding elements of \tilde{E}_i in each system must be vector field equivalent. Note, not all digraphs have the same number of vertices and edges, so the comparison is only between elements that exist in each digraph. To illustrate the notation used in the definition of system equivalence, consider the following example.

III. RESULTS

This section presents three main classes of results for symmetric distributed systems. The first is related to controllability, the second to a constructive motion

planning algorithm and the third to preliminary results for optimal control of such systems.

A. Nonlinear Controllability

Given an open set $W \subseteq M$, define $R^W(x_0, T)$ to be the set of states x such that there exists $u : [0, T] \rightarrow \mathcal{U}$ that steers the control system from $x(0) = x_0$ to $x(T) = x_f$ and satisfies $x(t) \in W$ for $0 \leq t \leq T$, where \mathcal{U} is the set of admissible controls. Define

$$R^W(x_0, \leq T) = \bigcup_{0 < \tau \leq T} R^W(x_0, \tau). \quad (2)$$

We will refer to $R^W(x_0, \leq T)$ as the set of states reachable up to time T .

Definition 4: A system is *small time locally controllable* ('STLC', or simply 'controllable') if $R^W(x_0, \leq T)$ contains a neighborhood of x_0 for all neighborhoods W of x_0 and $T > 0$.

Let \mathcal{C} denote the smallest subalgebra of $V^\infty(M)$ (the Lie algebra of smooth vector fields on a manifold M whose product is the Lie bracket, $[\cdot, \cdot]$) that contains g_1, \dots, g_m . If $\dim(\mathcal{C}) = \dim M$ at a point x , then the system described by Equation 1 satisfies the *Lie Algebra Rank Condition* ('LARC') at x . The following is well known as 'Chow's Theorem.'

Theorem 5: If the system described by Equation (1) satisfies the LARC at a point x_0 then it is STLC from x_0 .

The following is the main controllability result.

Proposition 6: If any one member, Σ_n , of the equivalence class of symmetric distributed control systems, $\bar{\Sigma}$ is STLC, then all members of the equivalence class, $\Sigma_i \in \bar{\Sigma}$ where $i > n$ of symmetric distributed control systems are STLC.

The proof is a straight-forward construction that makes use of the fact that diffeomorphisms are natural with respect to Lie brackets. A similar theorem for nonlinear systems with drift based on the usual good/bad bracket test due to Sussmann [16] is similarly obtained.

B. Nonholonomic Motion Planning

Symmetries may be exploited in distributed systems for motion planning purposes. Space limitations prevent their inclusion here. An interested reader is referred to [13].

C. Optimal Control

The ultimate goal for considering the optimal control problem are similar reduction results, *i.e.*, solving the optimization problem for a smaller system and using the results for a larger system. Initial results related to the bifurcations of optimal solutions appear in [4]. We adopt a simplified version of the robotic unicycle as a prototypical model. The simple kinematics of this kind of robot are described by

$$\begin{aligned} \dot{x} &= u_1 \\ \dot{y} &= u_2. \end{aligned} \quad (3)$$

The problem is to find the controls $u_{i_1}(t), u_{i_2}(t)$ for each robot i which steer a formation of robots of this

type from the start configuration to its goal configuration, while maintaining a rigid body formation at the beginning and end of the trajectory and minimizing the global performance index

$$J = \int_0^{t_f} \sum_{i=1}^n \left((u_{i1})^2 + (u_{i2})^2 \right) + \sum_{i=1}^{n-1} k (d_i - \bar{d})^2 dt$$

subject to the robotic kinematic constraints in Equation 3, where $n > 2$ is the number of robots, $d_i = ((x_i - x_{i+1})^2 + (y_i - y_{i+1})^2)^{1/2}$ is the Euclidean distance from i th to $(i + 1)$ th robots, \bar{d} is the desired distance between two adjacent robots, and k is a non-negative weighting constant. The cost function minimizes a combination of the control effort (first summation) and the deviation from a desired formation (second summation). Bifurcations in the nature and the form of the solutions are illustrated in Figure 2 for a system of seven robots.

REFERENCES

- [1] Lubomir Bakule, Jose Rodellar, Josep M. Rossell, and Pere Rubio. Preservation of controllability-observability in expanded systems. *IEEE Trans. Auto. Control*, 46(7):1102–1107, July 2001.
- [2] Anthony M. Bloch, P.S. Krishnaprasad, Jerrold E. Marsden, and Richard M. Murray. Nonholonomic mechanical systems with symmetry. *Arch. Rational Mech. Anal.*, 136:21–99, 1996.
- [3] J. P. Corfmat and A. S. Morse. Decentralized control of linear multivariable systems. *Automatica*, 12:479–495, 1976.
- [4] Baoyang Deng, Mihir Sen, and Bill Goodwine. Bifurcations and symmetries of optimal solutions for distributed robotic systems. In *Proceedings of the 2009 American Control Conference*. To appear.
- [5] P. Fessas and M. Mansour. Single-channel controllability of interconnected systems. *IEE Proceedings-D*, 138(3):207–209, 1991.
- [6] M. Hazewinkel and C. Martin. Symmetric linear systems: an application of algebraic systems theory. *Int. J. Control*, 37(6):1371–1384, 1983.
- [7] Jair Koiller. Reduction of some classical non-holonomic systems with symmetry. *Archive for Rational Mechanics and Analysis*, 118(2):113–148, 1992.
- [8] Jerrold E. Marsden, Richard Montgomery, and Tudor S. Ratiu. Reduction, symmetry and phases in mechanics. *Mem. Amer. Math. Soc.*, 436, 1990.
- [9] Jerrold E. Marsden, Richard Montgomery, and Tudor S. Ratiu. Redumction, symmerty and phases in mechanics. *Memoirs of the Americal Mathematical Society*, 88:Nr. 436, 1990.
- [10] Jerrold E. Marsden and J. Scheurle. Lagrangian reduction and the double spherical pendulum. *ZAMP*, 44:17–43, 1993.
- [11] Jerrold E. Marsden and J. Scheurle. The reduced euler-lagrange equations. *Fields Institute Communications*, 1:139–164, 1993.
- [12] M. Brett McMickell and Bill Goodwine. Reduction and nonlinear controllability of symmetric distributed systems. *International Journal of Control*, 76(18):1809–1822, 2003.
- [13] M. Brett McMickell and Bill Goodwine. Motion planning for nonlinear symmetric distributed robotic systems. *International Journal of Robotics Research*, 26(10):1025–1041, October 2007.
- [14] D. D. Siljak. *Decentralized Control of Complex Systems*, volume 184 of *Mathematics in Science and Engineering*. Academic Press, 1991.
- [15] M. K. Sundareshan and R.M. Elbanna. Qualitative analysis and decentralized controller synthesis for a class of large-scale systems with symmetrically interconnected subsystems. *Automatica*, 27(2):383–388, 1991.
- [16] Hector J. Sussmann. A general theorem on local controllability. *Siam J. Control and Optimization*, 25(1):158–194, 1987.
- [17] Reiko Tanaka and Kazuo Murota. Quantitative analysis for controllability of symmetric control systems. *Int. J. Control*, 73(3):254–264, 2000.
- [18] Reiko Tanaka and Seiichi Shin. Fearful symmetry in system structure. In *Third International Symposium on Autonomous Decentralized Systems*, pages 137–146. IEEE, 1997.

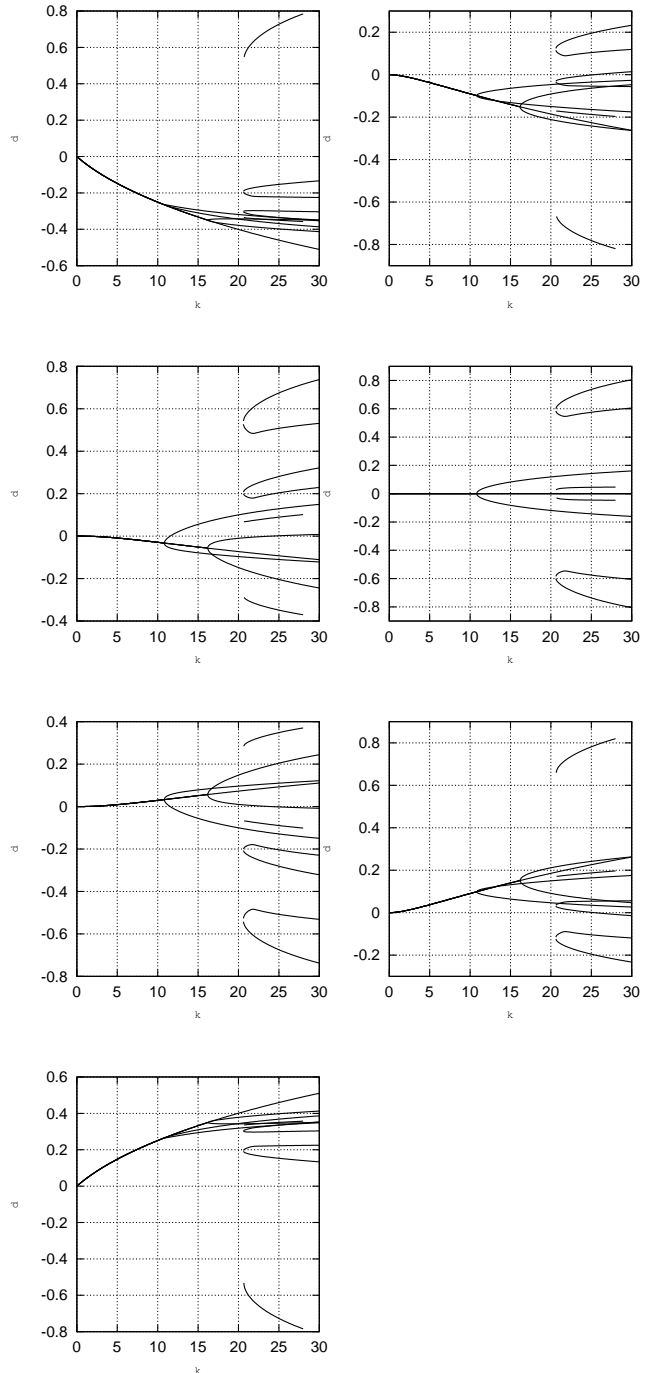


Fig. 2. Bifurcation diagrams for a 7-robotic system, robots 1 through 7, respectively.

- [19] Reiko Tanaka, Seiichi Shin, and Noboru Sebe. Controllability of autonomous decentralized systems. In *Symposium on Emerging Technologies & Factory Automation*, pages 265–272. IEEE, 1994.
- [20] Arjan van der Schaft. Symmetries and conservation laws for hamiltonian systems with inputs and outputs: A generalization of noether's theorem. *Systems & Control Letters*, 1(2):108–118, 1981.
- [21] Arjan van der Schaft. Partial symmetries for nonlinear systems. *Mathematical Systems Theory*, 18(1):79–96, 1985.

Analysis of a Stiff Limit Cycle: Glycolysis in *Saccharomyces cerevisiae*

Panayotis D. Kourdis*, Ralf Steuer†, Dimitris A. Goussis*

* School of Applied Mathematics and Physical Sciences, National Technical University, Athens, Greece

† Manchester Interdisciplinary Biocentre, University of Manchester, Manchester, UK

Abstract—A 22-D glycolysis model is analyzed with CSP, when it exhibits an oscillatory (limit cycle) behavior. Due to the action of a number of fast dissipative timescales and of significant decouplings, it is shown that the limit cycle lies in a 3-D subdomain.

I. INTRODUCTION

The construction of complex mathematical models in biology and genetics demands the development of particular algorithmic tools for the acquisition of the desired physical understanding. As a result, a number of methodologies have recently been developed in order to construct simplified models that are of low dimension but retain all the significant features of the full model. These methodologies have been employed successfully for the analysis of a large number of problems in the field of biochemistry, e.g. [1]-[5].

Simplification of large and complex nonlinear mathematical models is mainly based on the presence of very fast dissipative time scales, which quickly become exhausted, allowing slower scales to characterize the evolution of the physical process. These fast time scales do not affect the progress of the system directly, but they simply constrain its evolution in a low dimensional space. This situation is usually defined as stiffness and the low dimensional space, where the system evolves according to the slow time scales, is defined as a slow manifold.

Here, the CSP algorithm [6], [7] will be employed for the analysis of a model describing the glycolysis cycle of intact yeast cells as a *homogeneous* two-phase (intracellular/extracellular) system [8]; the kinetics of which involves 24 reactions among 22 metabolites, as shown in Table I. Being one of the most significant topics in biochemistry, glycolysis has been the subject of extensive study.

For the 22-dimensional glycolysis model and the oscillatory regime examined here, CSP analysis shows that the long term evolution takes place along a 3-dimensional limit cycle. This feature is the result of (i) the existence of two conservation laws, (ii) the development of ten dissipative fast time scales, which force the trajectory to move on a 10-dimensional slow manifold and (iii) the effective decoupling on this manifold of three dimensions from the remaining seven; the latter being practically decoupled from all other dimensions of the problem as well.

TABLE I
REACTIONS IN THE DETAILED MODEL [8]

1	$\leftrightarrow Glc_x$
2	$Glc_x \leftrightarrow Glc$
3	$Glc + ATP \rightarrow G6P + ADP$
4	$G6P \leftrightarrow F6P$
5	$F6P + ATP \rightarrow FBP + ADP$
6	$FBP \leftrightarrow GAP + DHAP$
7	$DHAP \leftrightarrow GAP$
8	$GAP + NAD^+ \leftrightarrow BPG + NADH$
9	$BPG + ADP \leftrightarrow PEP + ATP$
10	$PEP + ADP \rightarrow Pyr + ATP$
11	$Pyr \rightarrow ACA$
12	$ACA + NADH \rightarrow EtOH + NAD^+$
13	$EtOH \leftrightarrow EtOH_x$
14	$EtOH_x \rightarrow$
15	$DHAP + NADH \rightarrow Glyc + NAD^+$
16	$Glyc \leftrightarrow Glyc_x$
17	$Glyc_x \rightarrow$
18	$ACA \leftrightarrow ACA_x$
19	$ACA_x \rightarrow$
20	$ACA_x + CN_x^- \rightarrow$
21	$\leftrightarrow CN_x^-$
22	$G6P + ATP \rightarrow ADP$
23	$ATP \rightarrow ADP$
24	$ATP + AMP \leftrightarrow 2 ADP$

II. THE LIMIT CYCLE

The governing equations are of the form of the N-dim. system:

$$\frac{dy}{dt} = \mathbf{Q}^{-1} (\mathbf{S}_1 R^1 + \dots + \mathbf{S}_N R^N) = \mathbf{g}(\mathbf{y}) \quad (1)$$

where the elements of the N-dim. column vector \mathbf{y} are the concentrations of the metabolites (mM), t is time (min), the N-dim. column state vector \mathbf{S}_k and the scalar R^k denote the stoichiometric vector and rate, respectively, of the k-th reaction (see [8] for the expressions for the reaction rates). The $N \times N$ matrix \mathbf{Q} is diagonal, its entries equaling either unity for the intracellular metabolites or the ratio of the extracellular volume to the total volume of intracellular cytosol, y_{vol} , for the extracellular ones.

The oscillatory behavior of the glycolysis model is displayed in Fig. 1, where the evolution of the concentration of nicotinamide adenine dinucleotide (NADH) for the period $0 < t < 100$ min is displayed; the behavior of the other metabolites being similar. This oscillatory motion develops as various transient components die-out, is characterized by a frequency $\omega_{ch} = 2\pi/T \approx 10 \text{ min}^{-1}$ and evolves around a limit cycle. As is depicted in Fig. 2, for the interval $450 < t < 500$ min in which all fast

initial transients are exhausted, fully oscillatory motion is established along a limit cycle at sufficiently long times; the structure of the cycle suggesting that it occupies a low-dimensional subspace.

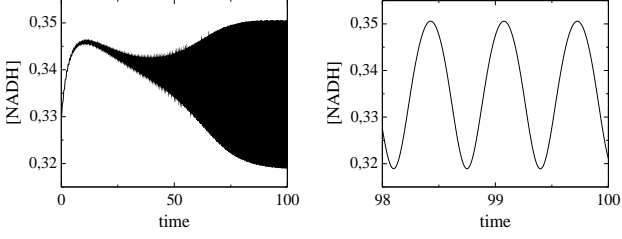


Fig. 1. The evolution of the NADH concentration (mM) with time (min) during the period $0 < t < 100$ min. On the right, magnification when fully oscillatory motion is established.

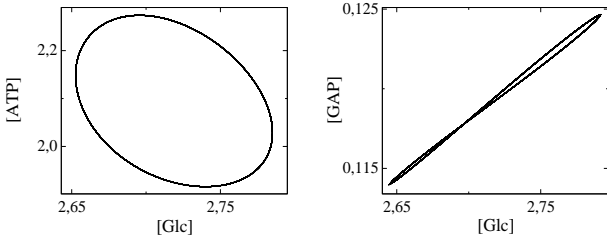


Fig. 2. The trajectory on the $[Glc] - [ATP]$ and the $[Glc] - [GAP]$ planes, during the period $450 < t < 500$ min.

III. CSP RESULTS

Using CSP, various simplified models can be constructed when the solution evolves along the limit cycle, providing different levels of accuracy. Shown in Fig. 3 is the accuracy provided when six or ten fast modes are considered exhausted ($M=6$ or 10). Since $\tau_{11} \approx \omega_{ch}$, $M=10$ provides the maximum simplification possible.

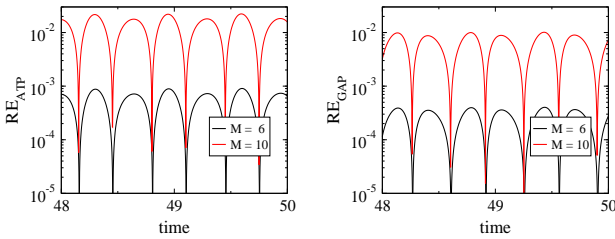


Fig. 3. $M=6, 10$. The relative error of $[ATP]$ and $[GAP]$ when comparing the solutions of the full and simplified models.

The better accuracy provided by the $M=6$ simplified model, relative to the one provided by the $M=10$ one, is due to the fact that a larger time scale gap exists in this case; i.e., τ_6/τ_7 is smaller than τ_{10}/τ_{11} .

Considering the $M=10$ case, CSP data indicate that the ten fast time scales affect the most the ten variables:

$$\mathbf{y}^T = ([BPG], [GAP], [AMP], [PEP], [F6P], [NADH], [DHAP], [ACA], [Glc], [EtOH])^T$$

where $[X]$ denotes the concentration of X in mM , the rates of change of which relate to that of the remaining

twelve variables with the relation:

$$\frac{d\mathbf{y}^r}{dt} = \mathbf{G}_s^r \frac{d\mathbf{y}^s}{dt} \quad (2)$$

where \mathbf{G}_s^r is a $N \times M$ matrix [9] and

$$\mathbf{y}^s = ([ATP], [G6P], [ADP], [FBP], [NAD^+], [Glyc], [Pyr], [Glc_x], [EtOH_x], [Glyc_x], [ACA_x], [CN_x^+])^T$$

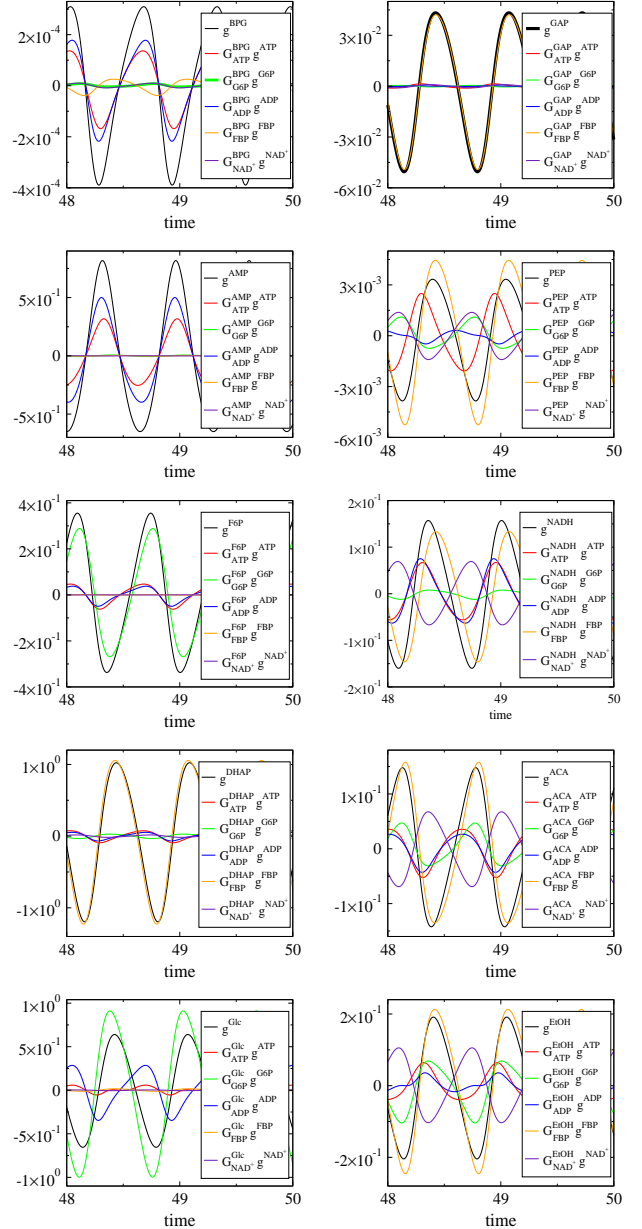


Fig. 4. $M=10$. The evolution in time (min) of the M components in the LHS of Eq. (2) along with the most important additive terms of the corresponding components in the RHS; i.e. g^i ($i=1, M$) and of the largest $C_k^i g^k$ ($k=1, N-M$).

Shown in Fig. 4 are the ten components in the LHS of Eq. (2) along with the most important additive terms of the corresponding components in the RHS. Inspection of the displayed data reveals that the rate of change of the

variables in \mathbf{y}^r depends on the rate of change of only five elements of \mathbf{y}^s , namely:

$$\mathbf{y}^{s1} = ([ATP], [G6P], [ADP], [FBP], [NAD^+])^T$$

being independent on the rate of change of the rest:

$$\mathbf{y}^{s2} = ([Glyc], [Pyr], [Glc_x], [EtOH_x], [Glyc_x], [ACA_x], [CN_x^+])^T$$

Further analysis indicates that the rate of change of \mathbf{y}^{s2} decouples not only from \mathbf{y}^r but from \mathbf{y}^{s1} too. The validity of this statement is demonstrated by the results displayed in Fig. 5, where the solution of the original model is compared with that of a perturbed model; the latter consisting of the original model in which the magnitude of the rate of change of the variables in \mathbf{y}^{s2} is increased by 20% for all times after $t = 25$ min. Both solutions were computed on the basis of initial conditions lying on the limit cycle.

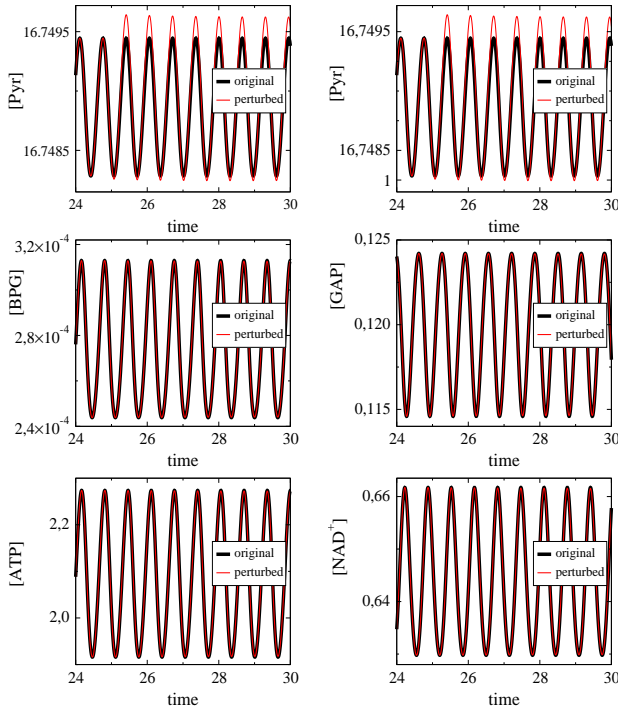


Fig. 5. The effects on the concentration of the metabolites in \mathbf{y}^{s2} ($[Glyc]$, $[Pyr]$), \mathbf{y}^r ($[BPG]$, $[GAP]$) and \mathbf{y}^{s1} ($[ATP]$, $[NAD^+]$) of a 20% perturbation in the magnitude of the rate of change of the seven components in \mathbf{y}^{s2} imposed from $t = 25$.

In other words, in the perturbed model the governing equations for \mathbf{y}^r and \mathbf{y}^{s1} are similar to the ones in the original model, while the governing equation for \mathbf{y}^{s2} is initially, up to $t = 25$ min, similar to that of the original model, say:

$$\frac{\mathbf{y}^{s2}}{dt} = \mathbf{g}^{s2}(\mathbf{y}^r, \mathbf{y}^{s1}, \mathbf{y}^{s2}) = \mathbf{g}^{s2}(\mathbf{y}) \quad (3)$$

being replaced for all subsequent times, $t \geq 25$ min, by the equation:

$$\frac{\mathbf{y}^{s2}}{dt} = 1.20 \mathbf{g}^{s2}(\mathbf{y}^r, \mathbf{y}^{s1}, \mathbf{y}^{s2}) = 1.20 \mathbf{g}^{s2}(\mathbf{y}) \quad (4)$$

The results displayed in Fig. 5 show that the perturbation imposed from $t = 25$ is immediately felt by the components in \mathbf{y}^{s2} , such as $[Glyc]$ and $[Pyr]$. Regarding the components in \mathbf{y}^r , such as $[BPG]$ and $[GAP]$, Fig. 5 verifies that the imposed perturbation has no effect on them. Moreover, Fig. 5 indicates that the imposed perturbation has no effect in the components of \mathbf{y}^{s1} , such as $[ATP]$ and $[NAD^+]$.

These results indicate that a 5-dimensional simplified model can be constructed for the accurate simulation of the glycolysis process along the limit cycle. This size can be further reduced by taking into account the two conservation laws:

$$[NAD^+] + [NADH] = \text{const.}$$

$$[ATP] + [ADP] + [AMP] = \text{const.}$$

that involve variables in \mathbf{y}^r and \mathbf{y}^{s1} , so that a 3-dimensional simplified model can be constructed, involving the rate of change of $[ATP]$, $[G6P]$ and $[ADP]$ only.

IV. CONCLUSIONS

A demonstration on the usefulness of the $N \times M$ matrix \mathbf{G}_s^r was presented, in identifying the couplings operating along the limit cycle. This matrix, measuring the sensitivity of the variables in \mathbf{y}^r with respect to those in \mathbf{y}^s [9], identifies the couplings enforced by the fast time scales as the solution relaxes and then moves on the slow manifold.

REFERENCES

- [1] Z.P. Gerdtzen, P. Daoutidis, W.S. Hu, "Non-linear reduction for kinetic models of metabolic reaction networks", *Metabolic Engr.*, vol 6, pp. 140-154, 2004.
- [2] J. Zobeley, D. Lebiedz, J. Kammerer, A. Ishmurzin, U. Kummer, "A new time-dependent complexity reduction method for biochemical systems", *Trans. Comput. Systems Biology I*, Springer Verlag, Berlin Germany, 2005, pp. 90-110.
- [3] D.A. Goussis, H.N. Najm, "Model Reduction and Physical Understanding of Slowly Oscillating Processes: the Circadian Cycle", *SIAM Multiscale Model. Simul.*, vol. 5, pp. 1297-1332, 2006.
- [4] A. Lovrics, A. Csikasz-Nagy, I.G. Zsely, J. Zador, T. Turanyi, B. Novak, "Time scale and dimension analysis of a budding yeast cell cycle model", *BMC Bioinformatics*, vol. 7, art.no. 494, 2006.
- [5] S.R. Taylor, F.J. Doyle III, L.R. Petzold, "Oscillator Model Reduction Preserving the Phase Response: Application to the Circadian Clock", *Biophysical J.*, vol. 95, pp. 1658-1673, 2008.
- [6] S.H. Lam, D.A. Goussis, "Understanding complex chemical kinetics with computational singular perturbation", *Proc. of the Comb. Inst.*, vol. 22, pp. 931-941, 1988.
- [7] S.H. Lam, D.A. Goussis, "Conventional asymptotics and computational singular perturbation for simplified kinetics modeling", in *Reduced Kinetic Mechanisms and Asymptotic Approximations for Methane-Air Flames*, Springer Lecture Notes 384, M. O. Smooke, ed., Springer, Berlin, pp. 227-242, 1991.
- [8] F. Hynne, S. Dano and P.G. Sorensen, "Full-scale model in *Saccharomyces cerevisiae*", *Biophysical Chemistry*, vol. 94, pp. 121-163, 2001.
- [9] D.A. Goussis, M. Valorani, "An efficient iterative algorithm for the approximation of the fast and slow dynamics of stiff systems", *J. Comput. Phys.*, vol. 214, 2006, pp 316-346.

Adaptive dimensionality reduction of stochastic differential equations for protein dynamics

Jesús A. Izaguirre*, Christopher R. Sweet*

*University of Notre Dame, Notre Dame, IN, USA

Abstract—The dynamics of proteins can be described as the superposition of motions at a continuum of time scales. In the special case of a protein immersed in an implicit solvent, a stochastic differential equation (SDE) can model the dynamics of the solute protein. Traditional model reduction techniques fail because *a priori* characterization of the slow variables in these SDEs is nearly impossible. We present an approach that instead, does a local dimensionality reduction of the SDE in a neighborhood of phase space, which is adaptively performed when the reduced model is no longer valid. The local slow variables, which we call approximate normal modes (ANM), are found using the diagonalization of a coarse-grained Hessian (CGH) from the potential energy function. We call this procedure coarse-grained normal mode analysis, or CNMA. Diagonalization of the CGH can be achieved in $O(N \log N)$ time and $O(N)$ memory rather than $O(N^3)$ time and $O(N^2)$ memory of ordinary diagonalization. CNMA is able to capture the low frequency motions of the protein. An SDE on the ANM is found by using a *saddle-point approximation* of the mean fast-frequency force experienced by the slow variables, and an implicit solvent model that considers the protein as a Brownian particle. This mean force can be computed at a cost no greater than a fine-grained force evaluation. Discretization of the resulting SDE achieves very long time steps compared to the discretization of the fine-grained SDE. A metric is used to monitor the validity of the ANM as slow variables and prompt re-diagonalization of the CGH or adaptation of the time step used. I will present numerical results on small peptide and protein system that show that this coarse-graining scheme allows up to three orders of magnitude speedup due to increase in the SDE discretization time step, and that the scheme is able to preserve kinetics when compared to the fine-grained SDE.

I. INTRODUCTION

Proteins are polymers of mostly naturally occurring aminoacids. Proteins are molecular machines, and as any machine, they must move in order to function. Understanding protein motion or dynamics is critical to solving problems as diverse as protein folding, functional conformational changes, and to computationally predict the effectiveness of drugs that target proteins. Simulating protein dynamics remains very challenging. The most straightforward approach, molecular simulation of Newton’s equations of motion using standard atomistic models, quickly runs into a significant sampling problem for all but the most elementary of systems. While small proteins fold or have biologically relevant conformational changes on the microseconds to second timescale, detailed atomistic simulations are currently limited to the nanosecond regime, with a few “heroic” simulations breaking the microsecond timescale.

The fundamental challenge to overcome is the presence of multiple time scales: typical bond vibrations are on the order of femtoseconds (10^{-15} sec) while proteins fold on a time-scale of microsecond to millisecond. This is a 10^{12} difference in time scales! We tackle the problem of developing timescale-coarse-grained models of proteins to understand their thermodynamics (e.g. statistical properties) and kinetics (e.g. rates). Among other multiscale problems, coarse graining dynamical protein models in a rigorous and computationally tractable way is particularly challenging. Two specific difficulties can be identified.

The *identification of the slowest variables* in the system (e.g. associated with the slowest time scales and transition rates) is to a large extent an unresolved problem. Even when people agree on a specific definition, the actual computation can be intractable. This is the case for example if one attempts to calculate the committor function, the probability at a given point that the protein folds rather than unfolds, by brute force. This is typically done by starting many trajectories from a given point and directly computing how many fold the protein. Additionally, computing dynamics of the slow variables is non-trivial because they are intricately coupled to the fast variables. In other words, there is in general *no timescale separation*. In protein modeling, there is a dense spectrum of frequencies due to the highly coupled nature of the force field. Unfortunately, most multiscale methods start by assuming that it is in fact possible to extract variables whose time scale is significantly slower than the rest. Some of the unresolved variables will have time scale (faster but) comparable to time scales of some of the resolved variables. No sharp cutoff can be found. Therefore special techniques need to be developed to go beyond the time scale separation approximation.

II. COARSE-GRAINED NORMAL MODE LANGEVIN DYNAMICS (CNML)

Rather than attempting to identify slow variables that are valid globally, our approach is based on adaptively identifying slow variables valid locally. Once these slow variables have been identified, we derive a SDE where the effect of fast variables is described through average and fluctuating forces. We discretize this SDE, which allows much longer time steps than the original fine-grained equations of motion. Whenever these slow variables are no longer valid, defined by a metric explained below, we identify a new set of slow variables, or alternatively adapt the time step for the solution of the SDE. Earlier,

we presented an approach using similar slow variables and SDE, but that attempted no adaptive dimensionality reduction in [7]. Our current approach is more robust and scalable.

Choice of slow variables. Our slow variables are approximate low-frequency normal modes (ANM) derived from a coarse-grained Hessian (CGH). Normal modes are the eigenvectors of the Hessian matrix of the potential energy U at an equilibrium or minimum point x_0 with proper mass normalization. More formally assume a system of N atoms with $3N$ Cartesian positions and diagonal mass matrix \mathbf{M} . To perform the normal mode analysis (NMA) for these systems we can formally expand the potential energy about an equilibrium point, which we assume to be a local minimum. The Hessian \mathbf{H} is a factor in the first non-constant, non-zero term of this expansion and a harmonic approximation to the original system can be found by truncating the expansion at this point. To rewrite the harmonic approximation as a set of decoupled oscillators it is insufficient to diagonalize the Hessian as the resulting oscillators would be coupled through the projected mass matrix. Instead we mass re-weight the system using and then diagonalize the resulting mass re-weighted Hessian, $\mathbf{M}^{-\frac{1}{2}}\mathbf{H}\mathbf{M}^{-\frac{1}{2}}\mathbf{Q} = \mathbf{Q}\mathbf{\Lambda}$, where $\mathbf{\Lambda}$ is the diagonal matrix of ordered eigenvalues and \mathbf{Q} the matrix of column eigenvectors $\mathbf{e}_1, \dots, \mathbf{e}_{3N}$. The frequency of a mode is equal to $\sqrt{|\lambda|}$ where λ is the eigenvalue. If we choose a cut-off frequency $\sqrt{\lambda_i}$ to partition the normal modes such that $\mathbf{Q} = [\mathbf{Q}, \bar{\mathbf{Q}}]$, $\mathbf{Q} = [\mathbf{e}_1, \dots, \mathbf{e}_i]$ and $\bar{\mathbf{Q}} = [\mathbf{e}_{i+1}, \dots, \mathbf{e}_{3N}]$ are rectangular matrices whose columns span a slow subspace C and fast subspace C^\perp respectively. In the following discussion we will assume the dimensions of \mathbf{Q} to be $3N \times m$. In the linear case the time-step is bounded by the asymptotic stability of the method [2] at a frequency equal to the $\sqrt{|\lambda_i|}$, rather than the highest frequency in the system. Our results show this is a good heuristic to choose the time-step.

Dynamics of the slow variables. Once the slow variables have been identified, equations for the rate of change of these variables need to be formulated. Let us denote by q a set of resolved variables with momenta p . We assume that the number of coordinates q is very small compared to $3N$ where N is the number of atoms in the system. Typically N can be as large as hundreds of thousands while the number of resolved variables is 10 to 100. We wish to find a way to calculate dp/dt in terms of q and p only. The following exact equation for dp/dt can be derived:

$$\frac{dq(t)}{dt} = p,$$

$$\frac{p(t)}{t} = \underbrace{-\nabla_q A}_{\text{drift}} - \underbrace{\int_0^t C_r(s) \cdot p(t-s) ds}_{\text{friction}} + \underbrace{r(t)}_{\text{noise}}, \quad (1)$$

$$C_r(s) = \langle r(\tau+s) r(\tau)^T \rangle, \quad \forall \tau \quad (2)$$

(fluctuation dissipation theorem)

These equations are in reduced units and we neglected the dependence of the memory kernel C_r on q and p . The brackets $\langle \rangle$ define the thermodynamic average in the canonical ensemble. Equation (1) can be derived using the Mori-Zwanzig projection [8]. The potential $A(q)$ is the Potential of Mean Force (PMF, or Helmholtz free energy) for variable q . The integral in (1) represents a friction. In this model the friction includes memory so this equation is often called the Generalized Langevin Equation (GLE). The last term $r(t)$ is a fluctuating force with zero mean: $\langle r(t)|q_0, p_0 \rangle = 0$. This is a conditional average over Cartesian coordinates x and momenta p_x keeping $q = q_0$ and $p = p_0$ fixed.

This equation can be rigorously derived from statistical mechanics and is therefore an attractive starting point to build coarse grained models. However, it is also, in principle, very expensive to calculate. The most common approximation is to assume a separation of time scales; then $C_r(s)$ is simply equal to the auto-correlation of $dp(t)/dt$ which can be readily computed. As was pointed out earlier this assumption does not hold in general. We next discuss how our choice of slow variables and saddle point approximation of the drift term make this approximation feasible and results in a computationally tractable coarse-grained dynamical model.

Choosing low frequency modes as resolved variables was motivated by the physical insight that low frequency modes contain the physically relevant motions close to the minimum [3], [4]. For small numbers of modes we observe that the coupling between C and C^\perp is small, though not zero. The drift term of (1) can be simplified using a *saddle-point approximation*. The mean force is approximated by the instantaneous projection of the force onto the slow subspace, subject to the constraint that the conformation is a minimum in the fast subspace. This is the most probable value of the mean force when the spaces are decoupled. At that point the friction term can be approximated as the autocorrelation of the slow force, and the noise can be evaluated as white noise. Thus, we numerically enforce a quasi-adiabatic decoupling between C and C^\perp .

The simplification of the drift term proceeds as follows. The choice of frequency partition separates the positions around the equilibrium point x_0 into \hat{x} in C and \bar{x} in C^\perp such that $x = \hat{x} + \bar{x} + x_0$. These are defined as

$$\hat{x} = \mathbf{P}_x(x - x_0), \quad \bar{x} = \mathbf{P}_x^\perp(x - x_0),$$

where the projection matrices take the positions from Cartesian to mode coordinates and back to Cartesian space, and are given by

$$\mathbf{P}_x = \mathbf{M}^{-1/2} \mathbf{Q} \mathbf{Q}^T \mathbf{M}^{1/2},$$

$$\mathbf{P}_x^\perp = \mathbf{M}^{-1/2} (\mathbf{I} - \mathbf{Q} \mathbf{Q}^T) \mathbf{M}^{1/2}.$$

The mean force for the drift term for a particular value of can be written as

$$\text{Average } f(\hat{x}) = -\frac{1}{Z} \int \exp(-\beta U(x)) \delta(\mathbf{P}_x(x - x_0) - \hat{x}) \mathbf{P}_f \nabla U(x) dx. \quad (3)$$

We have introduced the usual canonical ensemble partition function and the force projection matrix:

$$\mathbf{P}_f = \mathbf{M}^{1/2} \mathbf{Q} \mathbf{Q}^T \mathbf{M}^{-1/2}.$$

The average $f(\hat{x})$ is dominated by the slow force term, $-\mathbf{P}_f \nabla U(x)$, corresponding to the smallest $U(x)$ due to the Boltzmann weight. This $U(x_{\min})$ is the minimum potential energy that satisfies the constraint $\mathbf{P}_x(x_{\min} - x_0) = \hat{x}$. We can rewrite it as $U(x_{\min}) = U(x_0 + \hat{x} + \bar{x}_{\min})$. Since $x_0 + \hat{x}$ is fixed, this is equivalent to minimizing the projection of the positions onto the fast subspace. Hence $\bar{x}_{\min} = \operatorname{argmin} U(x_0 + \hat{x} + \bar{x}_{\min})$ with x_0, \hat{x} fixed. This implies that the mean force can be approximated by the instantaneous slow force:

$$\text{Average } f(\hat{x}) \approx -\mathbf{P}_f \nabla U(x_{\min}). \quad (4)$$

A second important approximation is that the protein is modeled using implicit solvent (ISM). ISMs have been shown to be sufficiently accurate for a number of applications, including protein folding studies, and they are attractive because they greatly reduce the cost of simulating a protein. Thus, to model the coarse-grained dynamics of an implicitly solvated protein, (1) is simplified into a Langevin equation:

$$\begin{aligned} dx &= v dt, \quad M dv = f dt - \Gamma M v dt \\ &+ (2k_B T \Gamma)^{1/2} \mathbf{M}^{1/2} d\mathbf{W}(t), \end{aligned} \quad (5)$$

where $\mathbf{f} = -\mathbf{P}_f \nabla U(x_{\min})$ is derived in (4), t is time, $\mathbf{W}(t)$ is a collection of Wiener processes, k_B is the Boltzmann constant, T is the system temperature, \mathbf{v} are the velocities and Γ is the diagonalizable damping matrix. The system diffusion tensor \mathbf{D} gives rise to $\Gamma = k_B T \mathbf{D}^{-1} \mathbf{M}^{-1}$. \mathbf{D} is chosen to model the dynamics of an implicit solvent and the coarse-graining of the dynamics.

Discretization of the dynamics. We discretize (5) using the Langevin Impulse (LI) integrator [6]. We call this discretization the Normal Mode Langevin (NML) propagator. Schematically, half a step of NML performs the following steps:

Half slow kick: advance velocities using half a long timestep $\Delta t/2$ using the projection of internal and random force unto slow subspace C .

Slow Fluctuation: advance positions using the projection of internal and random force unto slow subspace C .

Fast Fluctuation: minimize positions on fast subspace C^\perp using steepest descent.

Coarse grained diagonalization. To adaptively find the slow variables we need a cheap procedure to extract them. We introduce a *coarse-grained normal mode analysis that is scalable* (CNMA). CNMA uses a dimensionality reduction strategy that allows computation of low frequency modes in $O(N \log N)$ time, and with $O(N)$ memory, rather than $O(N^3)$ time and $O(N^2)$ memory of brute-force diagonalization. The coarse-graining strategy to computing the frequency partitioning is based on three ideas. The first is to find a reduced set of normalized vectors \mathbf{E} that spans the low frequency space of interest, C . The second is to recursively extract a minimal set of

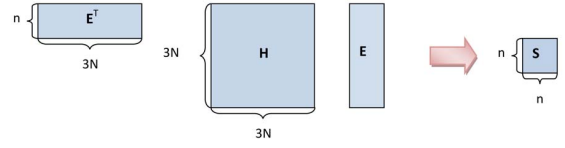


Fig. 1. Illustration of the dimensionality reduction strategy for the diagonalization. If the vectors in \mathbf{E} span the low frequency space of interest in \mathbf{H} , then the diagonalization of \mathbf{S} can produce a low frequency basis set.

vectors \mathbf{Q} from \mathbf{E} and the coarse grained Hessian \mathbf{H} . The third is form \mathbf{H} in linear cost, $O(N)$.

Assume that we have found \mathbf{E} . Figure 1 illustrates the dimensionality reduction strategy. \mathbf{H} is the Hessian at a given simulation step. The dimensions of \mathbf{E} are $3N \times n$, where $n \ll N$. The quadratic product $\mathbf{E}^T \mathbf{H} \mathbf{E}$ produces a matrix \mathbf{S} of reduced dimensions $n \times n$. Below we show that from the diagonalization of \mathbf{S} we can obtain \mathbf{E} . In particular, we (cheaply) diagonalize the symmetric matrix \mathbf{S} to find orthonormal matrix $\tilde{\mathbf{Q}}$ s.t.

$$\mathbf{S} \tilde{\mathbf{Q}} = \tilde{\mathbf{Q}} \Omega,$$

for diagonal matrix Ω . We can then write

$$\mathbf{Q}^T \mathbf{H} \mathbf{Q} = \Omega,$$

for $\mathbf{Q} = \mathbf{E} \tilde{\mathbf{Q}}$. Our subspace of dynamical interest, C , is then defined as the span of the first m columns of \mathbf{Q} . Recall that m is the number of reduced collective motions, typically in the range of 1 - 100.

We can evaluate how well the span of \mathbf{E} represents C using the following result (we skip the proof for space limitation): Let the i^{th} ordered diagonal of Ω be $\sigma_i = \Omega_{ii}$. Then the highest frequency mode in C , f_{\max} , satisfies

$$f_{\max} \leq \sqrt{|\sigma_m|}.$$

Then the Rayleigh quotient σ_m can be used to establish the maximum time step that can be taken in subspace C for stability. It follows that if λ_m is close to the m^{th} ordered eigenvalue of \mathbf{H} , then the first m vectors of \mathbf{Q} are a good representation of the low frequency space of interest.

We form \mathbf{E} , by starting from a ‘local’ block Hessian in which each block $\tilde{\mathbf{H}}_{ij}$ (composed of 1 or more residues) is zero if $i \neq j$. The remaining blocks on the diagonal are assumed to be independent of all other blocks. This block Hessian is then diagonalized, which is equivalent to performing independent diagonalization for each block. Let us determine each block Hessian eigenvectors and eigenvalues, \mathbf{Q}_i and \mathbf{D}_i , as follows:

$$\tilde{\mathbf{H}}_{ii} \mathbf{Q}_i = \mathbf{Q}_i \mathbf{D}_i.$$

Our hypothesis is that interactions among residues responsible for the low frequency space of interest will be included, either by projection or directly, in the first

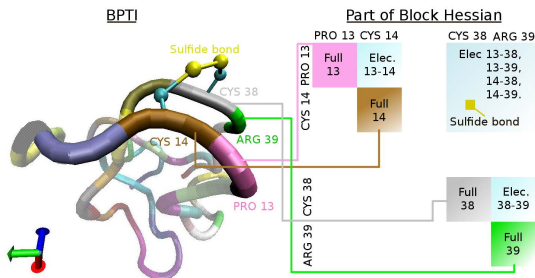


Fig. 2. Segment of a BPTI molecule and its associated block Hessian entries. Here, for illustration, a block is defined by one residue. Each residue corresponds to a Hessian block containing all of the forces within the residue, denoted ‘Full’. Adjacent residues have a corresponding electrostatic block denoted ‘Elec.’, e.g. Elec. 13-14. Physically local residues within the cutoff distance have a corresponding electrostatic block, e.g. Elec. 13-38. Bonds connecting non-adjacent residues, such as the disulfide bond shown, correspond to small 3×3 blocks in the Hessian.

few eigenvectors of Q_i , and need to be included in \mathbf{E} . The source of these vectors is as follows:

- 1) External low frequency motions due to nonbonded interactions can be projected onto the first 6 eigenvectors of Q_i , corresponding to conserved d.o.f. per block. In other words, external forces manifest themselves in rotations or translations of each residue-block.
- 2) External low frequency motions due to bonded interactions can be projected onto the dihedral space, and will consist of up to 4 vectors of Q_i , due to the peptide bond dihedrals of up to 2 connecting blocks.
- 3) Internal low frequency motions, for instance due to side-chain dihedral motions, will also be in the dihedral space and thus will be in Q_i .

We expect that the eigenvectors identified above will correspond to the first k ordered eigenvalues. The number k will vary between blocks and will be determined by selecting a cutoff frequency from the block eigenvalues. Figure 2 illustrates the block structure of \mathbf{H} for protein BPTI with cutoff for the electrostatics. This is very similar to a protein contact map. Contiguous residues give a tri-diagonal block structure. Non-contiguous residues that are nearby form off-diagonal blocks due to nonbonded forces. Special structural features like disulfide bonds create 3×3 small blocks. The block structure of \mathbf{E} follows from its composition from eigenvectors of the block Hessians \tilde{H}_{ii} . Thus, the cost of the matrix-matrix multiplication will be $O(N)$.

The multilevel application of this dimensionality reduction leads to a scheme with $O(N \log N)$ cost. We first diagonalize each residue. The cost for this stage is $O(N)$ as the average number of residue atoms is fixed and the number of residues is proportional to N . We then need to consider the diagonalization cost of the ‘block projected’ matrices. If we took a large system and recursively assigned block size ‘factor’ b , each linear block dimension

is b times the previous, then we get a diagonalizations with $b^{a+1} = N$, so total cost is $O(N \log N)$. This leaves the projection of the actual Hessian, but we can assign $b \propto \sqrt[3]{N \log N}$ to yield the correct scaling.

III. NUMERICAL RESULTS

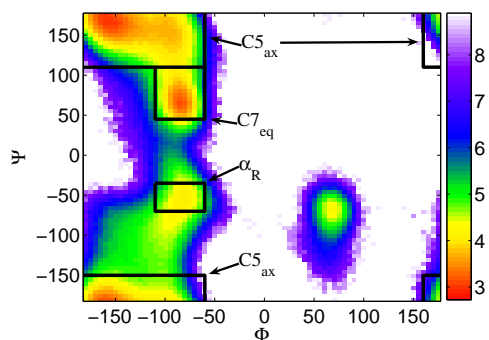
Adaptive NML recovers long time dynamics. We applied NML to study the isomerization kinetics of blocked alanine dipeptide (ACE ALA NME). With a small molecule like alanine dipeptide it is possible to sample for a sufficient length of time to measure the rates of transition between two states: in this case we measure the isomerization rate between the $C7$ equatorial and α_R conformations. The rate from states A and B , denoted k_{AB} , can be calculated using the approximation proposed by Best and Hummer [1] from the probability of transition, P_{TP} , and the average transition time $\langle t_{TP} \rangle$:

$$2c_A k_{AB} = P_{TP} / \langle t_{TP} \rangle,$$

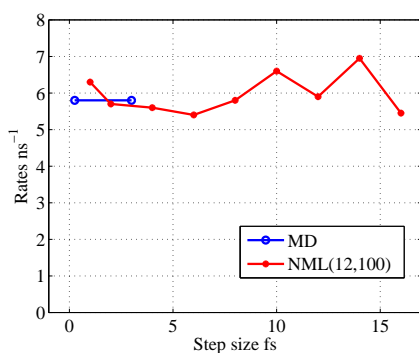
where c_A is the equilibrium mole fraction of conformation A. Figure 3(a) shows the free energy as a Ramachandran plot for Alanine Dipeptide using the sigmoidal screened Coulomb potential of [5]. Conformation A is $C7$ equatorial and $C5$ axial combined, and conformation B is α_R . Figure 3(b) shows that NML is capable of correctly computing the rate with only 12 modes with a re-diagonalization frequency of 100 fs as the time step increases up to 16 fs. As a reference, the rate computed for the fine-grained SDE using molecular dynamics (MD) with time steps up to 3 fs are shown. MD cannot go beyond this time step due to the fast frequencies present in the system. Let $\text{NML}(m, \text{freq})$ be NML where m is the number of slow modes propagated, and freq refers to the re-diagonalization frequency in femtoseconds. Figure 3(c) shows the isomerization rate for AD running $\text{NML}(m, 0)$ (no re-diagonalization), $\text{NML}(m, 100)$ and $\text{NML}(m, 1000)$. It can be observed that whereas the rate quickly goes down for $\text{NML}(m, 0)$, the rate is correctly computed for $\text{NML}(m, 100)$ for even 7 modes (only 1 real mode excluding the 6 conserved modes). $\text{NML}(m, 1000)$ is somewhere in between the two results.

Coarse-grained normal mode analysis is scalable. Five models were used for the comparison of the ‘brute force’ diagonalization and the coarse grained CNMA method: PIN1 WW domain (PDB 1I6C), BPTI (PDB 4PTI), Calmodulin (PDB 1CLL), Tyrosine kinase (PDB 1QCF), and F1-ATPase (PDB 2HLD). The results can be seen in Figures 4(a) and 4(b), which match the scaling analysis of $O(N \log N)$ time and $O(N)$ memory.

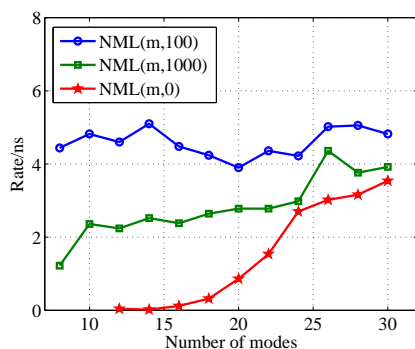
NML with re-diagonalization using CNMA can greatly accelerate dynamics calculations. We are currently applying NML with re-diagonalization using CNMA to study the folding of the WW domain and other proteins. Figure 5 illustrates analytical predictions of the accelerations in sampling the dynamics that we expect when using our approach on progressively larger protein systems. Thousand fold acceleration should be possible for systems with a few thousand atoms.



(a) Free Energy.



(b) Rate vs. time step



(c) Rate vs. number of modes

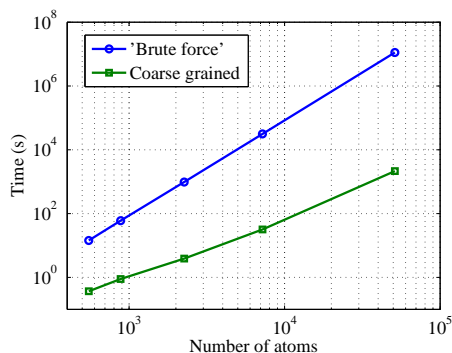
Fig. 3. (a) Ramachandran plot for the free energy (in kcal mol^{-1}) of alanine dipeptide using a sigmoidal screened Coulomb potential. (b) Isomerization rate of alanine dipeptide as a function of the time step using 12 modes and re-diagonalization every 100 fs. (c) Rate as a function of varying re-diagonalization frequencies and number of modes.

ACKNOWLEDGMENT

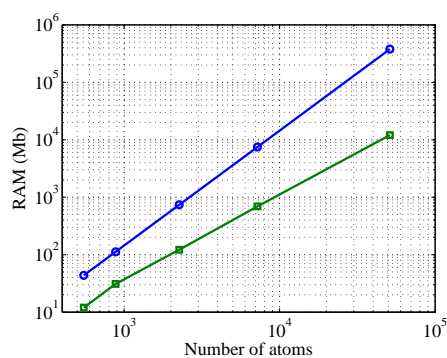
JAI acknowledges partial funding from NSF grants DBI-0450067 and CCF-0622940. This work is part of a collaboration with Vijay S. Pande, Paula Petrone, and Eric Darve from Stanford University.

REFERENCES

- [1] R. B. Best and G. Hummer. Chemical Theory and Computation Special Feature: Reaction coordinates and rates from transition paths. *PNAS*, 102(19):6732–6737, 2005.
- [2] B. Leimkuhler and S. Reich. *Simulating Hamiltonian Dynamics*. Cambridge University Press, 2004.
- [3] C. S. M. Levitt and P. Stern. Protein normal-mode dynamics: trypsin inhibitor, crambin, ribonuclease and lysozyme. *J. Mol. Biol.*, 181:423–447, 1985.



(a) Diagonalization time.



(b) Diagonalization RAM.

Fig. 4. (a) Comparison of the scaling with time for 'brute force' and coarse grained CNMA methods. (b) Comparison of the scaling with RAM usage for 'brute force' and coarse grained CNMA methods.

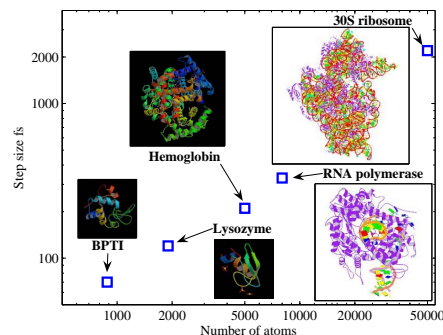


Fig. 5. Prediction of time steps possible using 100 modes and re-diagonalization using CNMA in NML.

- [4] P. Petrone and V. S. Pande. Can Conformational Change Be Described by Only a Few Normal Modes? *Biophys. J.*, 90(5):1583–1593, 2006.
- [5] M.-Y. Shen and K. F. Freed. A simple method for faster nonbonded force evaluations. *J. Comp. Chem.*, 26(7):691–698, 2005.
- [6] R. D. Skeel and J. A. Izaguirre. An impulse integrator for Langevin dynamics. *Mol. Phys.*, 100(24):3885–3891, 2002.
- [7] C. R. Sweet, P. Petrone, V. S. Pande, and J. A. Izaguirre. Normal mode partitioning of Langevin dynamics for biomolecules. *J. Chem. Phys.*, 128(11):1–14, 2008.
- [8] R. Zwanzig. *Nonequilibrium Statistical Mechanics*. Oxford, 2001.

An efficient multi-time scale (MTS) method for combustion modeling with reduced and detailed kinetic mechanisms

Xiaolong Gou, Wenting Sun, Zheng Chen, and Yiguang Ju
Department of Mechanical and Aerospace Engineering, Princeton University

A dynamic multi time scale (MTS) method and a dynamic hybrid multi time scale (HMTS) model are developed to achieve efficient and time accurate reduced kinetic modeling of syngas combustion with detailed kinetic mechanisms. The methods are applied to ignition of hydrogen, methane, and n-decane/air mixtures and compared, respectively, with standard Euler and implicit ODE solvers by using detailed and reduced chemical kinetic mechanisms. The results showed that both methods can accurately reproduce the species time history and ignition delay times. In addition, compared to the explicit Euler method, MTS is not only computationally efficient but also robust at larger time steps. Compared to the implicit ODE solver, MTS is about one-order more computationally efficient. In addition, unlike the implicit ODE solver, whose computation time is proportional to the square of the species number, the computation time required for MTS is only proportional linearly to the species number. As such, MTS has advantages particularly for large equation systems such as large chemical kinetic mechanisms. To further accommodate the specification of a limiting time scale of the equation system and to improve the computation efficiency and robustness at large time scales, HMTS is developed by integrating MTS with a fully implicit algorithm. Therefore, the present HMTS is a generalized scheme which includes the Euler scheme, MTS, and implicit scheme, and compatible to both incompressible and compressible flow solvers. The results showed HMTS is rigorous and efficient. The computational efficiency of the MTS method can be further increased by integrating it with a dynamically reduced mechanism generated by using path a flux analysis (PFA) method. This scheme can be used for direct numerical simulations and large eddy simulation with detailed chemical mechanisms to improve the computation efficiency, accuracy, and robustness.

Contact email: yju@princeton.edu

"Analysis of Reduction Methods for ODEs"

Authors: Hans Kaper, Tasso Kaper, Antonios Zagaris

Abstract:

We present an analysis of methods to reduce the dimension of systems of nonlinear ordinary differential equations involving two (or more) time scales: a fast time scale, where the dynamics take the orbits close to an invariant low-dimensional manifold, and a slow time scale, where the dynamics evolve in the neighborhood of the invariant (slow) manifold. Reduction methods offer a systematic way to identify the slow manifold and reduce the original equation to an autonomous equation on the slow manifold.

Diffusion maps for model reduction: exploiting data mining to accelerate simulation

Benjamin Sunday*, Amit Singer*, Ioannis G. Kevrekidis*[†]

*Program in Applied and Computational Mathematics, Princeton University, Princeton, NJ, USA

[†]Department of Chemical Engineering, Princeton University, Princeton, NJ, USA

Abstract—In many complex/multiscale systems, the long-term dynamics are reducible: they lie on a low-dimensional manifold parameterized by appropriate coarse variables (observables). Knowing these observables *a priori*, through experience or intuition, can be crucial in accelerating the computational extraction of information from detailed, “fine scale” simulators. Indeed, when such variables parameterizing the slow dynamics are known, the so-called equation-free approach [1] [2], provides a systematic way of designing computational “wrappers” that enable fine scale simulators to perform accelerated simulation as well as a wide range of additional tasks (coarse-grained stability and bifurcation computations, parametric continuation, coarse controller design etc.).

When such coarse observables are not known, data-mining tools can be used to extract them from simulation databases. Linking data-mining tools (and, in particular, the diffusion map approach of Coifman and coworkers [3]) and the design of equation-free computational experiments provides an integrated framework for coarse-grained computations of complex/multiscale systems. We will illustrate these two components as well as their combination through a number of computational examples. In particular, we will focus on the exchange of information between fine-scale and coarse-scale descriptions. We will explore coarse projective integration alternating between diffusion map and physical settings, and discuss the construction of physical initial conditions consistent with new, “out of sample” diffusion map coordinate values [4].

REFERENCES

- [1] I. G. Kevrekidis, C. Gear, J. Hyman, P. Kevrekidis, O. Runborg, and C. Theodoropoulos, “Equation-free, Coarse-grained multiscale computation: enabling microscopic simulators to perform system-level analysis,” *Commun. Math. Sci.*, vol. 1, pp. 715–762, June 2003.
- [2] I. G. Kevrekidis, C. Gear, and G. Hummer, “Equation-Free: The Computer-Aided Analysis of Complex Multiscale Systems,” *AIChE Journal*, vol. 50, pp. 1346–1355, June 2004.
- [3] B. Nadler, M. Maggioni, R. R. Coifman, A. B. Lee, S. W. Zucker, S. Lafon, F. Warner, “Geometric diffusions as a tool for harmonic analysis and structure definition of data: Diffusion maps,” *PNAS*, vol. 21, pp. 7432–7437, May 2005.
- [4] R. R. Coifman, S. Lafon, “Geometric harmonics: A novel tool for multiscale out-of-sample extension of empirical functions,” *Appl. Comput. Harmon. Anal.*, vol. 21, pp. 31–52, July 2005.

Two Stage Ignition of n -heptane: Identifying the Chemistry Setting the Explosive Time Scales

Dimitris J. Diamantis ^{*}, Dimitris C. Kyritsis [†], Dimitris A. Goussis ^{* ‡}

^{*}Foundation for Research and Technology Hellas, Inst. of Chem. Engr. and High Temp. Chem. Proc., Patras, Greece

[†]University of Illinois at Urbana-Champaign, Dept. of Mechanical Science and Engineering, Urbana, USA

[‡]National Technical University, School of Applied Math. and Phys. Sciences, Dept. of Mechanics, Athens, Greece

Abstract—The explosive time scales developing during a two stage ignition of n -heptane are examined. The elementary reactions contributing the most for their development are identified.

I. INTRODUCTION

In reacting systems, a wide spectrum of time scales arise, rendering the mathematical model stiff. Usually, the fastest time scales are of *dissipative* character, forcing the solution to evolve on a low dimensional manifold. However, some of the intermediate time scales are of *explosive* character and relate directly to ignition. From the early works on reacting systems based on time scale analysis, it was well understood that interesting information, such as ignition delays and chain-branching mechanisms, can readily be derived by analyzing these explosive modes [1].

Recent work has revealed that these explosive time scales need not be present in a flame configuration, where diffusion is the main mechanism for initiating the reaction process in the fresh mixture [2]. In contrast, in homogeneous systems the absence of transport makes the development of such kind of time scales a necessity for ignition.

The algorithmic methodology of Computational Singular Perturbation (CSP) method [1], [3] was employed for the identification of the chemical kinetics components responsible for the amplitudes of the explosive modes developing during a two-stage ignition of n -heptane and dimethyl ether [4], [5].

Here, the chemical kinetics components responsible for the developing explosive time scales during a two-stage ignition of n -heptane will be examined. The concept of *Time Scale Importance Index* will be employed, being a component of the CSP methodology, which has been successfully employed for the analysis of the time scales relating to the NO_x chemistry [6] and to the circadian cycle in the cell [7].

II. GOVERNING EQUATIONS AND METHODOLOGY

We consider homogeneous adiabatic ignition at constant volume of a stoichiometric n -heptane/air mixture at initial pressure of 13.5 bar and temperature of 850K, as in Ref. [4]. We employ a kinetic model consisting of $N = 561$ species and $K = 2539$ reactions [8], the forward and backward directions of which are considered

separately. The governing equations for the species mass fraction and temperature are:

$$\frac{d\mathbf{y}}{dt} = \frac{1}{\rho} \mathbf{W} (\mathbf{S}_1 R^1 + \dots + \mathbf{S}_{2K} R^{2K}) \quad (1)$$

$$\frac{dT}{dt} = \frac{1}{\rho c_v} \left(-\dot{H}_c + RT \sum_{i=0}^N \dot{\omega}_i \right) \quad (2)$$

where \mathbf{y} is the N -dim. vector of the species mass fraction, ρ is the mixture density, \mathbf{W} is a $N \times N$ matrix with the species molecular weights in the diagonal, \mathbf{S}_k and R^k are the N -dim. stoichiometric vector and rate of the k -th reaction, T is temperature, c_v is the heat capacity, \dot{H}_c is the heat release rate, R is the universal gas constant and $\dot{\omega}_i$ is the molar production rate of the i -th species.

These equations can be cast in the form of an $(N+1)$ -dim. system:

$$\frac{d\mathbf{z}}{dt} = \mathbf{g}(\mathbf{z}) = \hat{\mathbf{S}}_1 R^1 + \dots + \hat{\mathbf{S}}_{2K} R^{2K} \quad (3)$$

where \mathbf{z} is composed of \mathbf{y} and T and each additive term on the RHS corresponds to the forward or backward direction of the K reactions.

To leading order, the CSP vectors \mathbf{a}_i and covectors \mathbf{b}^i ($i = 1, N$), which define the directions in the phase space along which the i -th time scale act, can be approximated by the right and left, respectively, eigenvectors of the Jacobian \mathbf{J} of \mathbf{g} . In this case, the following expression for the developing time scales in the problem can be obtained:

$$\tau_i = |\lambda_i|^{-1} \quad (4)$$

where λ_i ($i = 1, N$) are the eigenvalues of \mathbf{J} :

$$\lambda_i = \mathbf{b}^i \mathbf{J} \mathbf{a}_i \quad (5)$$

Given the decomposition of the RHS in Eq. (3), the i -th eigenvalue can be expressed as:

$$\lambda_i = \mathbf{b}^i \mathbf{Q}^1 \mathbf{a}_i + \dots + \mathbf{b}^i \mathbf{Q}^{2K} \mathbf{a}_i \quad (6)$$

where

$$\mathbf{Q}^k = \mathit{grad} \left(\hat{\mathbf{S}}_k R^k \right) \quad (7)$$

so that the contribution to the value of λ_i of the two directions of each of the K reactions can be computed.

In order to assess the contribution of each chemical reaction to the value of the i -th time scale τ_i , through

the related term in Eq. (6), the following *Time Scale Importance Index* is introduced:

$$J_k^i = \frac{\mathbf{b}^i \mathbf{Q}^k \mathbf{a}_i}{|\mathbf{b}^i \mathbf{Q}^1 \mathbf{a}_i| + \dots + |\mathbf{b}^i \mathbf{Q}^{2K} \mathbf{a}_i|} \quad (8)$$

where $\sum_{k=1}^{2K} |J_k^i| = 1$ [6]. J_k^i measures the contribution of the k -th reaction to the i -th time scale.

Explosive time scales relate to positive eigenvalues (or positive real parts, in case of a complex conjugate pair). Therefore, non-negligible positive values of J_k^i identify reactions having a significant influence in establishing the explosive character of the i -th mode and in making the corresponding time scale τ_i faster. However, the fact that λ_i is positive, does not preclude the possibility that some of the $2K$ additive terms in the RHS of Eq. (6) are non-negligible and negative. In this case, the related reactions exhibit a significant influence to counter the explosive character of the i -th mode and make τ_i slower.

III. DYNAMICS OF TWO STAGE IGNITION

Shown in Figs. 1 and 2 are the evolution of temperature, fuel and representative final products; the two stages clearly depicted.

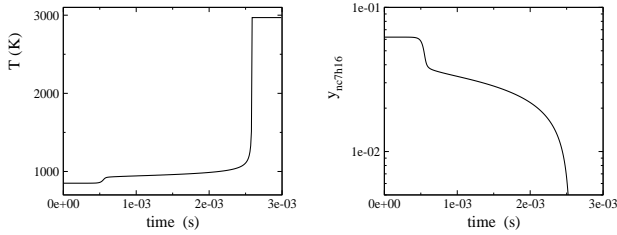


Fig. 1. The evolution of Temperature and mass fraction of n-heptane with time.

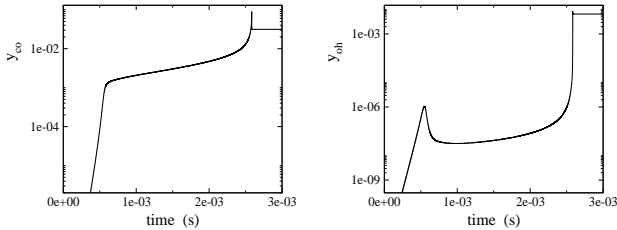


Fig. 2. The evolution of the mass fraction of co and oh with time.

The developing real positive eigenvalues (or real positive parts of complex eigenvalues), which according to Eq. (4) produce the explosive time scales, are displayed in Fig. 3.

It is shown that before the two temperature jumps there exist two explosive time scales, one fast and one slow; converging to each other at the start of each jump. As Fig. 4 clearly shows, in both cases the convergence of the two time scales follows their merging, as they become quickly slower on their way to loose their explosive character.

Next, Importance Indices for the explosive time scales before the two jumps will be presented, in order to clarify the operating explosive mechanisms in each temperature jump.

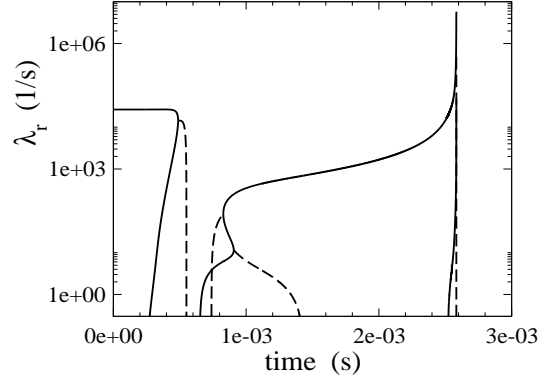


Fig. 3. The evolution of real positive eigenvalues (solid line) and real positive parts of complex eigenvalue pairs (broken line).

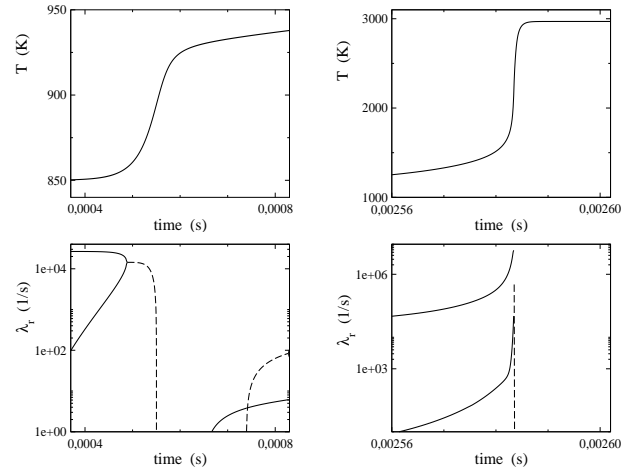


Fig. 4. Top: Magnification of the two temperature jumps. Bottom: the corresponding evolution of the real positive eigenvalues (solid line) and real positive parts of complex eigenvalue pairs (broken line).

IV. CHEMISTRY RELATED TO THE EXPLOSIVE TIMESCALES

Figure 5 shows the Importance Indices for the fast and the slow timescales at two instances, right before the first stage of ignition. In this period, the top row of Fig. 5 shows that the fast time scale is mainly set by isomerization reactions of RO_2 to $QOOH$ (R denotes $C_n H_{2n+1}$ and Q denotes $C_n H_{2n}$ groups) as well as of peroxyalkylhydroperoxides ($QOOH - O_2$) to ketohydroperoxides and OH , in agreement with Ref. [4]. This latter step is particularly significant both because it initiates the preparation of the OH pool, which will be very significant for the dynamics at later times, see Fig. 2, but also because the decomposition of ketohydroperoxides can lead to low-temperature chain-branching [8]. As shown in the bottom row of Fig. 5, the time scale of the slow chemistry in this period is mainly carried first ($t = 0.3704 \times 10^{-3} s$) by termination reactions, such as $ho_2 + ho_2 \rightarrow h_2o_2 + o_2$ or by reactions generating OH such as $c714ooh2 - 4o_2 \rightarrow c714ooh2 - 4 + o_2$ followed by the decomposition $c714ooh2 - 4 \rightarrow c7h14o_2 - 4 + oh$. Later on ($t = 0.4664 \times 10^{-3} s$) the contribution of $c714ooh2 - 4o_2 \rightarrow c714ooh2 - 4 + o_2$ and of $c714ooh3 -$

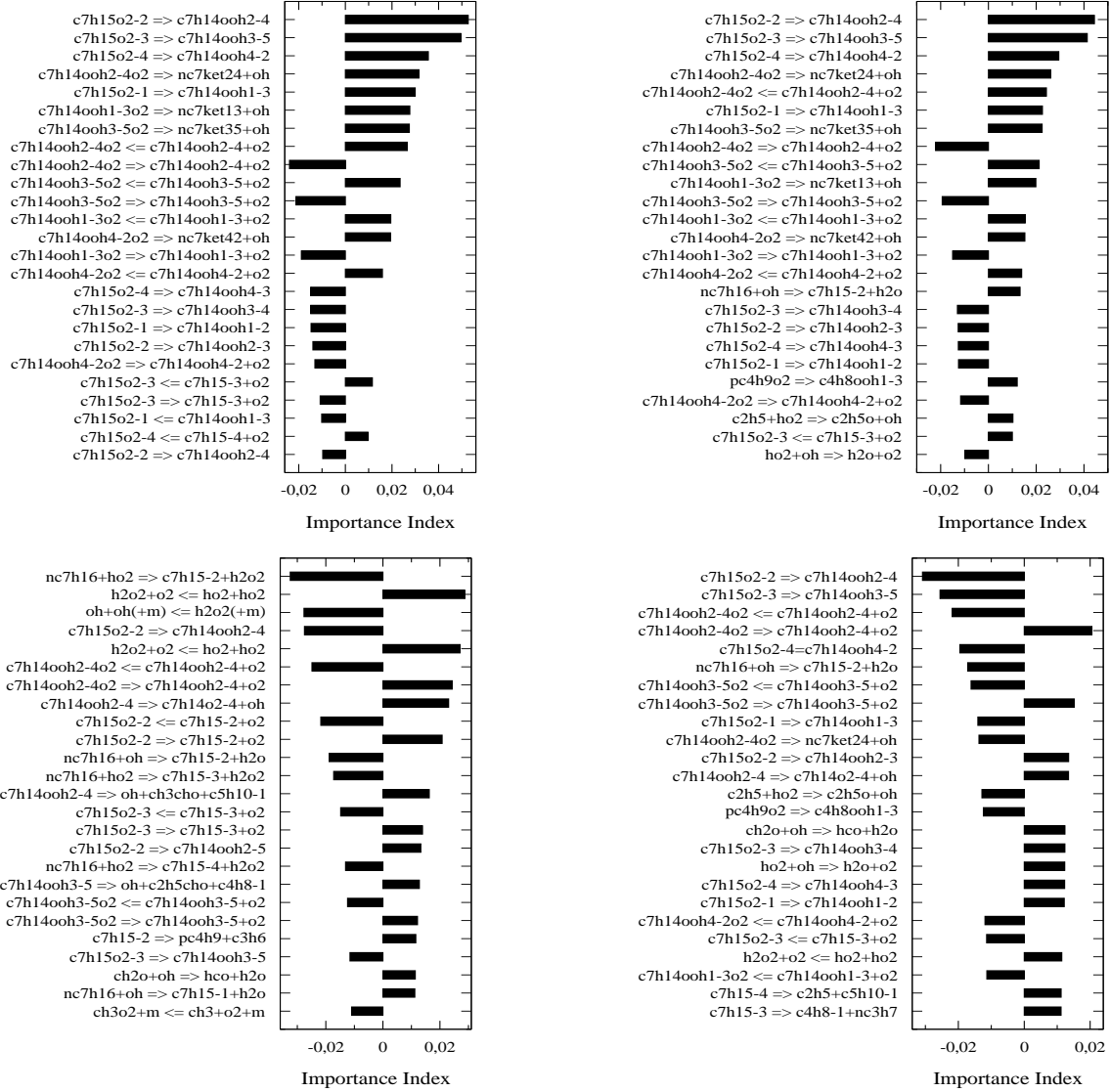


Fig. 5. Importance Indices right before the first jump. Top row: the fast time scale. Bottom row: the slow time scale. Left column: $t = 0.3704 \times 10^{-3} \text{ s}$ ($\lambda_{fast} = 0.2657 \times 10^5 \text{ s}^{-1}$, $\lambda_{slow} = 0.9938 \times 10^2 \text{ s}^{-1}$). Right column: $t = 0.4664 \times 10^{-3} \text{ s}$ ($\lambda_{fast} = 0.2421 \times 10^5 \text{ s}^{-1}$, $\lambda_{slow} = 0.3937 \times 10^4 \text{ s}^{-1}$).

$5 \rightarrow c7h14ooh3 - 5 + o2$ to the slow timescale of the explosive mode is still important, but the importance of $HO2$ termination is diminished and can also occur through the alternate route $ho2 + oh \rightarrow h2o + o2$. It is worth noting that, as the two eigenvalues converge short before the first stage of ignition, the isomerization and oxygen addition reactions that promote strongly the fast-time-scale chemistry have an equally strong inhibiting effect on the slow chemistry.

Similarly, Fig. 6 shows the Importance Indices for the fast and the slow timescales at two instances right before the second stage of ignition. In this period, fast chemistry is carried out by chain-branching producing OH radicals (e.g. $h + o2 \rightarrow o + oh$ and $h2o2 + m \rightarrow oh + oh + m$) assisted first ($t = 0.2570 \times 10^{-2} \text{ s}$) by low-C-number chemistry (mainly C2 and C1) and then ($t = 0.2584 \times 10^{-2} \text{ s}$) by the strongly exothermic oxidation of CO . Similarly to what happens in the first stage, as the fast and

the slow eigenvalue approach to each other the reaction having the strongest positive contribution to the fast time scale (e.g. $h + o2 \rightarrow oh + o$) inhibits the slow time scale equally strong. Similarly, the reaction $o + oh \rightarrow h + o2$ seems to have a converse but equivalent effect, i.e. it inhibits the fast scale but promotes the slow one. Notably, the strongly exothermic $co + oh \rightarrow co2 + h$ promotes both fast and slow chemistry.

V. CONCLUSIONS

For initial conditions that are of relevance to practical devices, the stoichiometric n-heptane mixture presents a two-stage ignition behavior. Both ignition stages occur at instances where two positive, real eigenvalues (corresponding to a fast and to a slow time scale) converge and yield one complex eigenvalue with a positive - but rapidly decreasing - real part. In both stages of ignition, the reaction groups contributing the most to the converging fast and slow time scales contain a significant number of

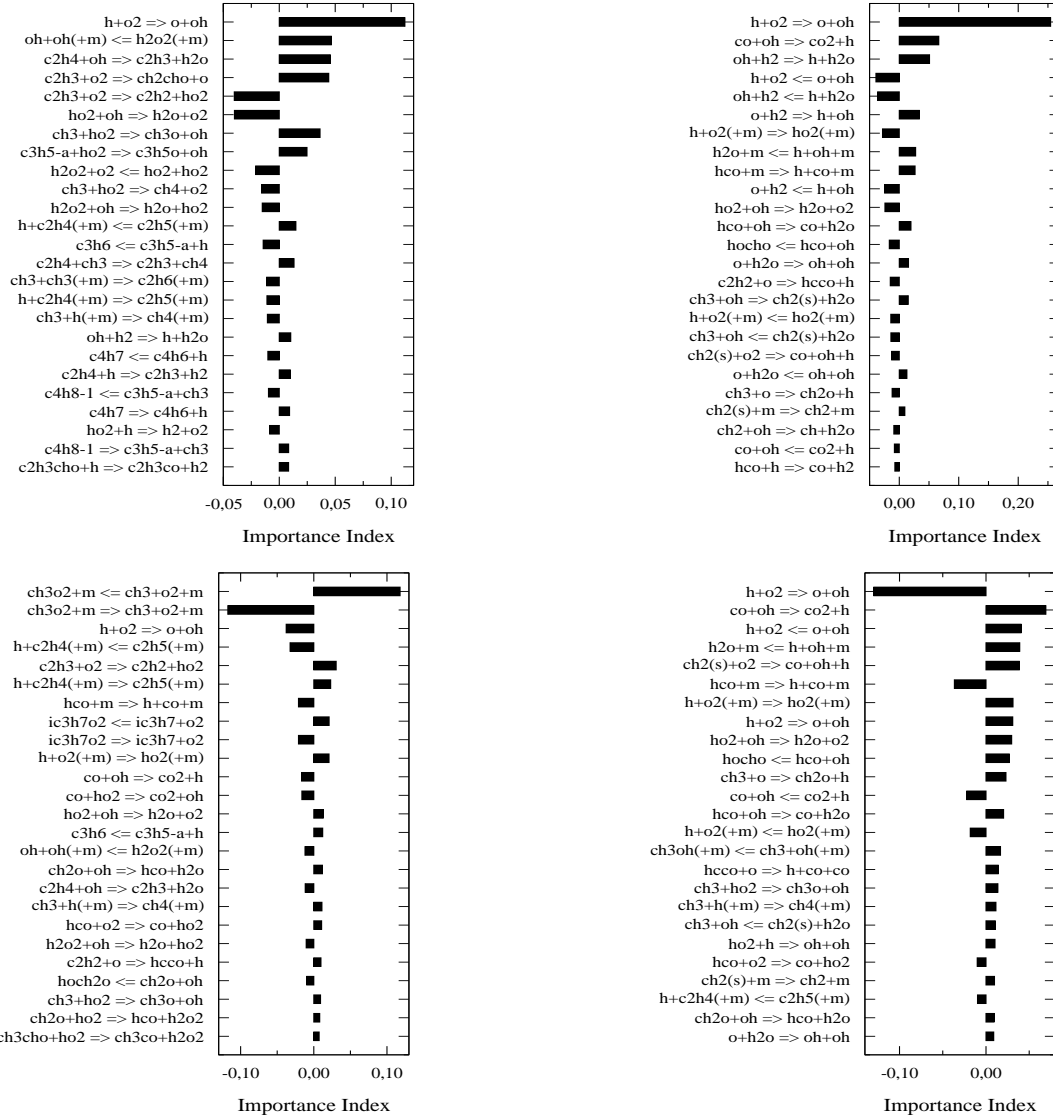


Fig. 6. Importance Indices right before the second jump. Top row: the fast time scale. Bottom row: the slow time scale. Left column: $t = 0.2570 \times 10^{-2} s$ ($\lambda_{fast} = 0.8253 \times 10^5 s^{-1}$, $\lambda_{slow} = 0.3003 \times 10^2 s^{-1}$). Right column: $t = 0.2584 \times 10^{-2} s$ ($\lambda_{fast} = 0.5778 \times 10^7 s^{-1}$, $\lambda_{slow} = 0.4705 \times 10^5 s^{-1}$).

reactions that have opposite effects to the fast and the slow chemistry, most usually favoring the fast and inhibiting the slow time scale.

ACKNOWLEDGMENTS

DJD and DAG gratefully acknowledge the support from the E.U. project TIMECOP-AE. DCK would like to acknowledge support from the U.S. N.S.F. through grant CTS 04-48968CAR

REFERENCES

- [1] S. H. Lam, D. A. Goussis, "Conventional asymptotics and computational singular perturbation for simplified kinetics modelling", in *Reduced Kinetic Mechanisms and Asymptotic Approximations for Methane-Air Flames*, M.O. Smooke (Editor), pp. 227242, Springer Lecture Notes 384, Berlin, 1991.
- [2] J.C. Lee, H.N. Najm, S. Lefantzi, J. Ray, M. Frenklach, M. Valorani, D.A. Goussis, "On chain branching and its role in homogeneous ignition and premixed flame propagation", in *Computational Fluid and Solid Mechanics 2005*, K.J. Bathe (Editor), pp. 717-720, Elsevier, Amsterdam, 2005.
- [3] S. H. Lam, D. A. Goussis, "Understanding complex chemical kinetics with computational singular perturbation", *Proc. Combust. Inst.*, vol. 22, pp. 931-941, The Combustion Institute, Pittsburgh, 1988.
- [4] A. Kazakov, M. Chaos, Z. Zhao, F.L. Dryer, "Dimethyl ether autoignition in a rapid compression machine: Experiments and chemical kinetic modeling", *J. Phys. Chem. A*, vol 110, pp. 7003-7009, 2006.
- [5] G. Mittal, M. Chaos, C.J. Sung, F.L. Dryer, "Computational Singular Perturbation Analysis of Two-Stage Ignition of Large Hydrocarbons", *Fuel Proc. Techn.*, vol 89, pp. 1244-1254, 2008.
- [6] D. A. Goussis, G. Skevis, "Nitrogen chemistry controlling steps in methane-air premixed flames", in *Computational Fluid and Solid Mechanics*, K. J. Bathe (Editor), pp. 650653, Elsevier, Amsterdam, 2005.
- [7] D.A. Goussis, H.N. Najm, "Model Reduction and Physical Understanding of Slowly Oscillating Processes: the Circadian Cycle", *SIAM Multiscale Model. Simul.*, vol. 5, pp. 1297-1332, 2006.
- [8] H.J. Curran, P. Gaffuri, W.J.Pitz, C.K. Westbrook, "A Comprehensive Modeling Study of n-Heptane Oxidation", *Combust. Flame*, vol. 114, pp. 149-177, 1998.

Finite-Time Lyapunov Analysis and Optimal Control

Erkut Aykutluğ*, Kenneth D. Mease*

*University of California, Mechanical and Aerospace Engineering, Irvine, CA, USA

Abstract—Hyper-sensitive optimal control problems present difficulty for general purpose solvers. A numerical implementation of an approach analogous to the method of matched asymptotic expansions requires determining initial and final conditions on appropriate invariant manifolds to sufficient accuracy. Finite-time Lyapunov exponents and vectors are employed for this purpose. The approach is explained and illustrated in the context of a simple transparent example.

I. INTRODUCTION

Numerical methods for solving optimal control problems (OCPs) can be divided into two main categories, direct and indirect. Indirect methods involve solving the associated Hamiltonian boundary value problem (HBVP) for an extremal solution that satisfies the first-order necessary conditions. A survey of direct and indirect methods, noting their advantages and disadvantages, is given in [5].

An OCP is called hyper-sensitive if the final time is large relative to some of the contraction and expansion rates of the associated Hamiltonian system [13], [14]. The solution to a hyper-sensitive problem can be qualitatively described in three segments as “take-off”, “cruise” and “landing” analogous to optimal flight of an aircraft between distant locations. The “cruise” segment is primarily determined by the cost function and the state dynamics, whereas the “take-off” and “landing” segments are determined by the boundary conditions and the goal of connecting these to the “cruise” segment. As the final time increases so does the duration of the cruise segment which shadows a slow reduced-order manifold. When the final time is large, the sensitivity of the final state to the unknown initial conditions makes the HBVP ill-conditioned. The ill-conditioning can be removed by approximating the solution with a composite one: a concatenation of boundary-layer solutions (take-off/landing segments) with a solution segment on the slow manifold (cruise segment). The completely hyper-sensitive case is a degenerate case for which the ‘cruise segment’ is near-equilibrium motion, and rather than a slow manifold, there is an equilibrium point. The more general case in which the cruise segment shadows a trajectory on the slow manifold is called partially hyper-sensitive.

Solution approximation for completely hyper-sensitive optimal control problems, based on the geometric structure of the associated Hamiltonian dynamics, has been addressed in [2], [13]. The solution to the HBVP is such that the solution in the initial boundary layer is approximated by a trajectory on the stable manifold of

the equilibrium point, the solution in the final boundary layer is approximated by a trajectory on the unstable manifold of the equilibrium, and the boundary layer solutions are approximately matched at the equilibrium point. The focus of the present paper is on determining the unknown boundary conditions such that the solution end points lie on the appropriate invariant manifolds to sufficient accuracy.

Rather than use information related to the equilibrium point which would not be available in the partially hyper-sensitive case, our approach uses a dichotomic basis for the phase space tangent bundle to define conditions satisfied by points on the stable and unstable manifolds of an equilibrium point. Dichotomy transformations have been used to solve boundary-value problems for ordinary differential equations [3], and to solve fixed end-point optimal control problems [2], [17]. Chow used dichotomy transformations to solve nonlinear HBVPs with linear boundary-layer dynamics [7]. For nonlinear HBVPs, a dichotomic basis has been approximated using eigenvalues and eigenvectors [13] and finite-time Lyapunov exponents and vectors [16]. The latter information can provide greater accuracy and is more generally applicable [11], [12]. Finite-time Lyapunov exponents, and in some cases vectors, have also been used to analyze fluids [8], [9], [15] and atmospheric circulation [6].

II. FINITE-TIME LYAPUNOV ANALYSIS

In previous work [11] and [12] finite-time Lyapunov analysis (FTLA) was applied to autonomous nonlinear dynamical systems to define and diagnose two-timescale behavior and compute points on a slow manifold, if one exists. The approach is to decompose the tangent bundle into subbundles on the basis of the characteristic exponential rates for the associated linear flow, and then to translate the tangent bundle structure into manifold structure in the base space. In FTLA, the characteristic exponential rates and associated directions are given, respectively, by finite-time Lyapunov exponents (FTLEs) and finite-time Lyapunov vectors (FTLVs). This approach has been guided by the asymptotic theory of partially hyperbolic invariant sets [4]. The finite-time tangent bundle decomposition can be viewed as an approximation of the asymptotic Oseledec’s decomposition [4]. It has been established in [12] that under certain conditions the finite-time decomposition approaches the (suitably defined) asymptotic decomposition exponentially fast, the

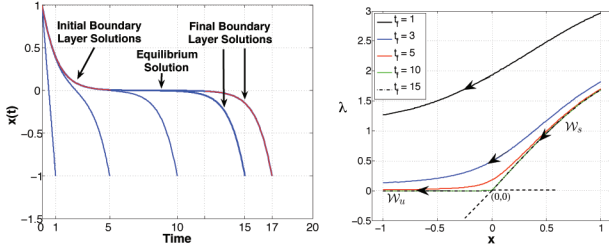


Fig. 1. Optimal solutions from GESOP[©] for different final times, $t_f = 1, 5, 10, 15$ and 17 , where $x(0) = 1$ and $x(t_f) = -1$ in the time domain (left) and in the phase space (right).

rate being given by the size of the gaps in the spectrum of the FTLEs.

III. SOLUTION APPROXIMATION STRATEGY FOR A COMPLETELY HYPER-SENSITIVE PROBLEM

We use a simple transparent example to present the approximate solution strategy, and later to address some implementation issues, for a completely hyper-sensitive optimal control problem. Consider Lam’s optimal control problem [10]: determine the control u^* and corresponding state trajectory x^* that minimize the cost

$$J = \frac{1}{2} \int_0^{t_f} u^2 dt \quad (1)$$

subject to the dynamic constraint

$$\dot{x} = \sin x + u \quad (2)$$

for a given final time t_f and boundary conditions $x(0) = 1$ and $x(t_f) = -1$. The first-order necessary conditions lead to the following Hamiltonian boundary value problem (HBVP)

$$\begin{aligned} \dot{x} &= \sin x - \lambda \\ \dot{\lambda} &= -\lambda \cos x \\ x(0) &= 1, \quad x(t_f) = -1 \end{aligned} \quad (3)$$

for extremal solutions. Defining the Hamiltonian $H = (1/2)u^2 + \lambda(\sin x + u)$ and the phase $p = (x, \lambda)^T$, we can write the state/costate dynamics in (3) in the form $\dot{p} = h(p)$, where $h = (\partial H / \partial \lambda, -\partial H / \partial x)^T$, to show that we are dealing with a Hamiltonian system.

We have solved the OCP using the optimization program GESOP[©] [1] for different final times; see Fig. 1. GESOP has several options, of these we used the direct multiple shooting method. The optimal trajectory and control are determined. Using the necessary condition, $u^* = -\lambda$, the solutions can be plotted in the (x, λ) phase plane. We see that as the final time gets larger the solution trajectories shadow more and more closely branches of the stable, \mathcal{W}^s , and unstable, \mathcal{W}^u , invariant manifolds of the equilibrium point, p_{eq} , at $(0, 0)$, and the solution spends more and more time near the equilibrium point. As t_f gets beyond 17, obtaining a numerical solution with GESOP[©] gets more and more difficult. In contrast, as t_f increases, the following approximate solution becomes more and more accurate and no harder to obtain.

For sufficiently large final times, the optimal strategy can be viewed in phase space as getting on $\mathcal{W}^s(p_{eq})$

where $x(0) = 1$ and steering along it to the equilibrium point and then steering along $\mathcal{W}^u(p_{eq})$ to reach the point on it where $x(t_f) = -1$. Consistent with this viewpoint, the solution to a completely hyper-sensitive OCP, $p^*(t)$, can be approximated by the composite function

$$\hat{p}(t) = \begin{cases} \hat{p}_s(t) & 0 \leq t \leq t_{ibl} \\ p_{eq} & t_{ibl} < t \leq t_{fbl} \\ \hat{p}_u(t) & t_{fbl} \leq t \leq t_f \end{cases} \quad (4)$$

where $\hat{p}_s(t)$ is the approximate initial boundary-layer solution for $t \in [0, t_{ibl}]$ with the initial condition on the stable manifold, i.e., $\hat{p}_s(0) = (x_0, \lambda_0) \in \mathcal{W}^s(p_{eq})$; p_{eq} is the equilibrium solution which approximates the slow “cruise” segment; and $\hat{p}_u(t)$ is the approximate final boundary-layer solution for $t \in [t_{fbl}, t_f]$ with the final condition on the unstable manifold, i.e., $\hat{p}_u(t_f) = (x_{t_f}, \lambda_{t_f}) \in \mathcal{W}^u(p_{eq})$. The solutions in the boundary-layers can be constructed by integrating, in forward and backward time respectively, the Hamiltonian dynamics from initial and final phase points on the corresponding invariant manifolds that satisfy the boundary conditions. The composite approximate solution is obtained by concatenating the boundary-layer solutions with the equilibrium solution. The times, t_{ibl} and t_{fbl} , defining the initial and final boundary-layer durations are selected such that \hat{p}_s and \hat{p}_u reach the equilibrium point up to a specified accuracy in forward and backward time respectively.

The primary challenge in developing this approach is to determine the unknown boundary conditions such that the initial and final phase points are sufficiently close to $\mathcal{W}^s(p_{eq})$ and $\mathcal{W}^u(p_{eq})$ respectively. The choice to base our approach on finite-time Lyapunov exponents and vectors (FTLE/Vs), rather than use other methods particularly suited to the structure near the equilibrium point, is driven by the goal of extending the approach to the partially hyper-sensitive case.

IV. DIAGNOSING HYPER-SENSITIVITY

If numerical solution of an OCP using a software package such as GESOP[©] proves difficult and reducing the final time alleviates the difficulty, hyper-sensitivity should be investigated. By observing how the solution evolves as t_f is varied, the relevant phase space region can be identified. Computing the FTLE spectrum at selected phase points in this region can quantify the exponential rates. If the spectrum uniformly separates into fast stable, slow, and fast unstable subsets, and the ‘fast’ rates are indeed fast relative to the time interval of interest, then hyper-sensitivity is confirmed. To describe the general case, let n be the dimension of the state dynamics; then it follows that $2n$ is the dimension of the associated Hamiltonian system. The spectrum also reveals the equal dimensions, n^{fs} and n^{fu} , of the fast stable and fast unstable behavior, respectively. If $n^{fs} + n^{fu} = 2n$, then the OCP is completely hyper-sensitive for sufficiently large t_f . If $n^{fs} + n^{fu} < 2n$, then the OCP is partially hyper-sensitive for sufficiently large t_f .

An important issue is how to select T , the averaging time. Lyapunov exponents are averages of the pointwise exponential rates, i.e., the averages of the appropriate kinematic eigenvalues (KEs) [3], over a segment of a trajectory of the Hamiltonian system. Points of the trajectory segment can be indexed by elapsed time. As long as the trajectory evolves in a phase space region where the KEs are uniform, larger averaging time T allows further progress in convergence of both the FTLEs and the FTLVs and better information. However once the trajectory enters a region of different KEs this ceases to be true. In Lam's problem, there is a qualitative difference between the local FTLEs and the asymptotic Lyapunov exponents. The two asymptotic Lyapunov exponents are zero at all points except points on the heteroclinic orbits connecting the equilibria. On the other hand, the FTLEs can indicate the hyperbolic nature of the dynamics in a neighborhood of a stable or unstable manifold associated with an equilibrium point. This is also the observation that led to the maximum FTLE method that has been used to identifying Lagrangian coherent structures in fluids [8], [9], [15].

A systematic approach to selecting the averaging time T such that the FTLEs indicate the local nature of the flow to sufficient accuracy, for a flow with non-uniform kinematic eigenvalues is as follows. Fig. 2 shows trajectories that shadow the invariant manifolds of the equilibria. The KE for the vector field $h(p)$, given by

$$\rho_h(t) = \frac{1}{2} h^T(p) ((Dh(p))^T + Dh(p)) h(p) \quad (5)$$

was computed along these trajectories. The red circles mark points where the ρ_h is zero; it is positive on one side of such a point and negative on the other. The positive sign indicates that neighboring points on the trajectory are separating with time, and negative sign indicates that they are getting closer to each other. Thus the red circles mark the boundaries separating regions of uniform (in sign) ρ_h . The time T should be selected to average as long as possible over a uniform region. Fig. 3 shows for a grid of $\lambda(0)$ values, the trajectories that evolve in forward time from the corresponding initial phase points. The zero-crossing for ρ_h are indicated, as are the times T over which the FTLE/Vs can be computed to determine the stable subspace. Although some of the trajectories begin in a different uniform region, most of the time stated is spent in the uniform region where the attraction to the equilibrium point is sensed. Fig. 4 shows that with proper selection of T , the maximum FTLE contours identify the stable and unstable manifolds of $(0, 0)$.

V. APPROXIMATE SOLUTION CONSTRUCTION

To implement the solution approximation strategy, we need to compute $\lambda(0)$ such that the point $p(0) = (x(0), \lambda(0))^T$ is on the stable manifold \mathcal{W}^s . The FTLE approach is to determine the point $p(0)$ such that $h(p(0)) \in E^s(p(0))$, where $E^s(p(0))$ is the stable subspace approximation by the span of appropriate Lyapunov

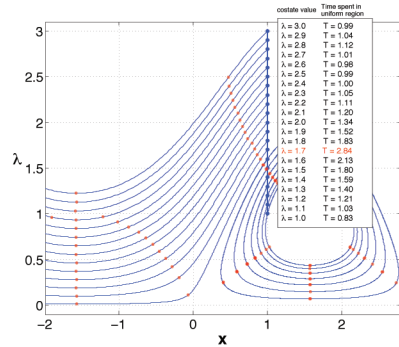


Fig. 3. Trajectories starting at $p(0) = (1, \lambda(0))$ for a grid of $\lambda(0)$ values. On each trajectory the zero ρ_h points are noted. The maximum averaging time is noted for each value of $\lambda(0)$.

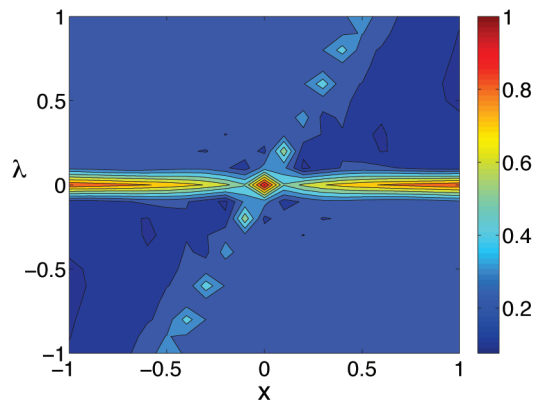


Fig. 4. Level contours of the FTLE field for the Hamiltonian system in (3) on a grid of points $\mathcal{M} = \{(x, \lambda) \in \mathbb{R}^2 \mid x \in [-1, 1], \lambda \in [-1, 1]\}$.

vectors. To accomplish this, we determine $\lambda(0)$ such that $\langle h(p(0)), w \rangle = 0$ for all $w \in E^s(p(0))^\perp$.

Fig. 2 shows the 'lines of ambiguity' at $x = -\pi/2$ and $x = \pi/2$. At these values of x , the orthogonality condition is satisfied for all values of λ and cannot be used to identify the particular value of λ that would place p on the appropriate invariant manifold. For all other values of x in this range, there are isolated solutions to the orthogonality condition corresponding to the desired manifolds.

An analogous procedure is followed to place the final phase point on the unstable manifold.

Applying this approach, the solution approximation to Lam's optimal control shown in Fig. 5 was obtained.

VI. PARTIALLY HYPER-SENSITIVE OPTIMAL CONTROL PROBLEMS

The consideration of completely hyper-sensitive OCPs in this paper is just a stepping stone to the consideration of partially hyper-sensitive OCPs. Partially hypersensitive optimal control problems are associated with HBVPs that have fast and slow behavior. Ill-conditioning is only associated with certain directions. An accurate approximation to the solution of a partially hyper-sensitive problem can be constructed from three components: a short duration initial boundary-layer segment, a long duration slow segment, and a short duration terminal

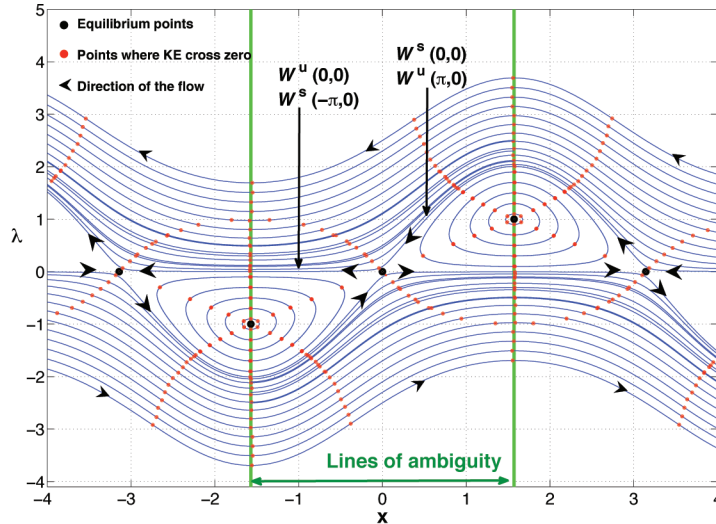


Fig. 2. Hamiltonian phase space of the system given in (3) showing stable and unstable manifolds of the equilibria, trajectories shadowing these manifolds, regions of uniformity (boundaries denoted by green circles), and lines of ambiguity.

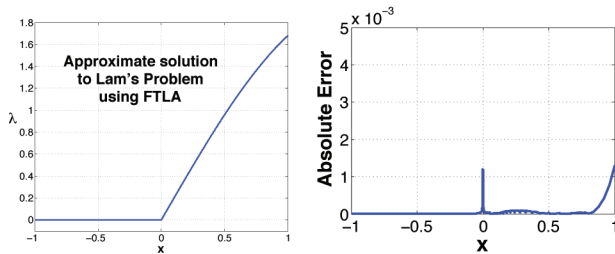


Fig. 5. **Left:** Approximation to Lam's problem using FTLA. The approximation to the stable invariant manifold is constructed with re-initializations for every $T=0.1$. **Right:** The absolute error between the optimal solution from GESOP and the approximate solution constructed by FTLA vs x .

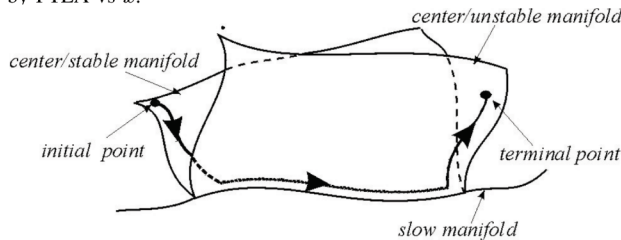


Fig. 6. Geometry of solution to partially hyper-sensitive optimal control problem in Hamiltonian phase space. Slow manifold should be 2D.

boundary-layer segment; loosely analogous to the method of matched asymptotic expansions. In this manner, the hyper-sensitivity can be avoided. Constructing segments requires locating points on invariant manifolds. Rather than stable and unstable manifolds of an equilibrium, in the partially hyper-sensitive case the manifolds of interest are center-stable and center-unstable. Fig. 6 illustrates the manifold structure, showing the initial and final boundary-layers and the intermediate segment that shadows a slow invariant manifold. Because we are dealing with a Hamiltonian system the phase space would be 4-dimensional and the slow manifold would be 2-dimensional, though the figure does not accurately depict the dimension of the slow manifold.

REFERENCES

- [1] www.gesop.de.
- [2] B.O. Anderson and P.V. Kokotovic, *Optimal control problems over large time intervals*, Automatica **23** (1987), no. 3, 355 – 363.
- [3] U.M. Ascher, R.M. Mattheij, and R.D. Russell, *Numerical solution of boundary value problems for ordinary differential equations*, SIAM press, Philadelphia, 1995.
- [4] L. Barreira and Y.B. Pesin, *Lyapunov exponents and smooth ergodic theory*, American Mathematical Society, Providence, USA, 2002.
- [5] J.T. Betts, *Survey of numerical methods for trajectory optimization*, Journal of Guidance, Control, and Dynamics **21** (1998), no. 2, 193 – 207.
- [6] R. Buizza and T.N. Palmer, *The singular-vector structure of the atmospheric global circulation*, J. Atmos. Sci. **52** (1995), no. 9, 1434 – 1459.
- [7] J.H. Chow, *A class of singularly perturbed nonlinear, fixed end-point control problems*, J. Opt. Theory Appl. **29** (1979), 231 – 251.
- [8] R. Doerner, B. Hubinger, W. Martienssen, S. Grossmann, and S. Thomae, *Stable manifolds and predictability of dynamical systems*, Chaos, Solitons and Fractals **10** (1999), no. 11, 1759 – 1782.
- [9] G. Haller, *Distinguished material surfaces and coherent structures in three-dimensional fluid flows*, Physica D **149** (2001), 248 – 277.
- [10] S.-H. Lam, *Personal communication*.
- [11] K.D. Mease, S. Bharadwaj, and S. Iravanchy, *Timescale analysis for nonlinear dynamical systems*, J. Guidance Control and Dynamic **26** (2003), no. 1, 318 – 330.
- [12] K.D. Mease, U. Topcu, and E. Aykutluğ, *Characterizing two-timescale nonlinear dynamics using finite-time Lyapunov exponents and vectors*, arXiv:0807.0239 [math.DS] (2008).
- [13] A.V. Rao and K.D. Mease, *Dichotomic basis approach to solving hyper-sensitive optimal control problems*, Automatica **35** (1999), 3633–3642.
- [14] ———, *Eigenvector approximate dichotomy basis method for solving hyper-sensitive optimal control problems*, Optimal Control: Applications and Methods **21** (2000), 1–19.
- [15] S. C. Shadden, F. Lekien, and J. E. Marsden, *Definition and properties of Lagrangian coherent structures from finite-time Lyapunov exponents in two-dimensional aperiodic flows*, Physica D **212** (2005), 271 – 304.
- [16] U. Topcu and K.D. Mease, *Using Lyapunov vectors and dichotomy to solve hyper-sensitive optimal control problems*, Proceedings of the 45th IEEE Conference on Decision and Control, 2006.
- [17] R.R. Wilde and P.V. Kokotovic, *A dichotomy in linear control theory*, IEEE Transactions on Automatic control **17** (1972), 382 – 383.

Analysis of Methane-Air Edge Flame Structure using CSP

Habib N. Najm* Mauro Valorani[†], Dimitris A. Goussis[‡],

* Sandia National Laboratories, Livermore, CA, USA

[†] Sapienza, University of Rome, Rome, Italy

[‡] National Technical University, Athens, Greece

Abstract— We study the structure of a methane-air edge flame stabilized against an incoming mixing layer. The flame is computed using detailed chemical kinetics, and the analysis is based on computational singular perturbation theory. We focus on examination of the low-dimensional structure of the flame, analyzing the number of exhausted modes, along with the distribution of fast and active timescales. Results are used to enhance understanding of the flame, and the role of different chemical and transport processes in its observed structure.

I. INTRODUCTION

Edge flames can be encountered in many reacting flow configurations in which partial premixing of fuel and oxidizer occurs [1]–[7]. The idealized edge flame is composed of three distinct branches: a lean premixed branch, a rich premixed branch and a diffusion flame branch; hence it is also known as a triple or tribrachial flame. The two premixed branches form curved fronts behind which a diffusion flame develops and stabilizes. Symmetric, tribrachial, edge flame structure, as well as bibrachial and monobrachial edge flames have been observed, depending on the incoming mixture composition as well as the flow/mixing layer structure.

There is a large number of experimental, analytical and numerical studies of triple and edge flames [2], [8]–[13]. The reviews by Buckmaster [6] and Chung [7] provide a broad overview of the history and recent developments in the study of edge flames. Methane-air triple flames in particular have been the focus of numerous studies [4], [5], [14], [15].

Based on the literature, it is evident that detailed C_2 kinetics are necessary in modeling these flames. Takahashi *et al.* [16] studied methane-air edge flame structure using skeletal 17-species kinetics. The detailed chemical structure of a methane-air edge flame was also studied by Takahashi and Katta [17] using C_2 and C_1 chemistry mechanisms. Inclusion of C_2 kinetics was found to lead to an increase in the flame lift-off height. Use of a global single-step reaction mechanism was found to lead to significant differences in edge flame stability and structure, including a dominant rich premixed branch, in disagreement with the detailed chemistry predictions [18].

Walsh *et al.* [19] used a 26-species C_2 mechanism for computations of lifted methane-air diffusion flames. They generally found good agreement with experimental measurements, except at diluted fuel conditions. Ali and

Daou [20] presented an analytical study of the effect of reversibility of chemical reactions on triple flames. Cho and Takita [21] presented computational studies of edge flames using detailed kinetics for both methane-air and propane-air mixtures. Briones *et al.* [22] conducted a numerical investigation of methane-air edge flames using detailed kinetics, with a focus on liftoff, stabilization, and blowout. Guo *et al.* [23] presented a numerical study of methane-air edge flames using a subset of GRIMech3.0 [24] excluding Nitrogen chemistry. Najm *et al.* [25] studied the NO structure in a methane-air edge flame using GRIMech3.0 [24], analyzing the four significant NO_x pathways.

In the present work we consider the methane-air edge flame of [25], and focus on the analysis of the flame structure using Computational Singular Perturbation (CSP) theory [26], [27]. CSP analysis enables identification of fast and slow reaction processes in chemical models, and the decoupling of fast-exhausted/dormant modes from the slow modes that drive the time evolution of the chemical system. The method relies on the identification of a suitable set of basis vectors that enable the decoupling of fast and slow processes. A leading-order approximation of these vectors is provided by the eigenvectors of the Jacobian of the chemical source term. There is an extensive literature on CSP and its utilization for analysis and reduction of chemically reacting flows [26]–[41].

We set up the methane-air edge flame stabilized against a prescribed uniform-velocity mixing layer using detailed chemistry (GRIMech3.0 [24]) and mixture-averaged transport [42]. CSP analysis of the computed flame structure highlights the spatial variation of the fast and driving time scales and the number of exhausted modes over the edge flame, revealing significant internal structure, and identifying important associated chemical/transport processes. In the following, we outline the setup of the problem, then present the analysis of the edge flame using CSP. We finish with conclusions summarizing the main findings of the work.

II. PROBLEM SETUP

We consider a methane-air edge flame in two-dimensions (2D) stabilized against an incoming mixing layer flowfield with a uniform inflow velocity profile. The computational model uses the low Mach number approximation, and employs GRIMech3.0 [24] kinetics

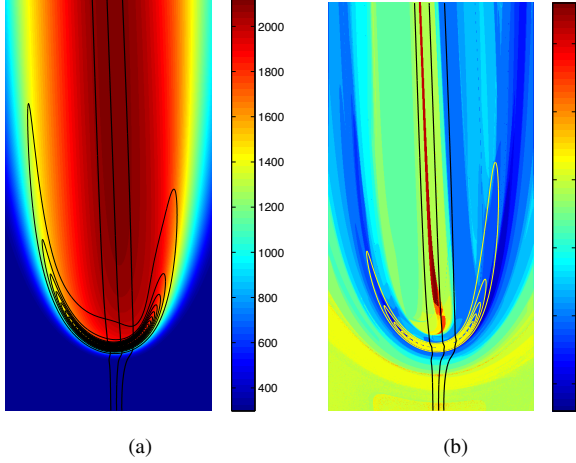


Fig. 1. The two-dimensional spatial distribution of temperature, shown with superposed heat release rate and ξ -contours (a) and the dimension of the fast subspace M (b), shown with superposed w_{CH_4} and ξ -contours. The ξ -contours are drawn at $(0.9, 1.0, 1.1)\xi_{\text{st}}$. This is a 512×1024 subset of the domain, with $x \in [0.4, 1.2]$ cm, $y \in [0, 1.6]$ cm.

and mixture-averaged transport [42]. The rectangular domain size is $1.6 \times 3.2 \text{ cm}^2$. The inflow is specified with a uniform velocity of 60 cm/sec and an analytically prescribed mixture-fraction profile, going from pure air on one side of the domain to pure CH_4 on the other [25]. The mixture fraction ξ is defined as in Bilger [43]. Note that ξ is zero in the air stream, and unity in the fuel stream. The stoichiometric value of the mixture fraction is $\xi = \xi_{\text{st}} = 0.055$ for the given fuel/air streams.

The global structure of the edge flame is illustrated in Figure 1(a). The inflow at the bottom edge of the domain is at 300 K, with the fuel stream on the right and the air stream on the left. The mixture fraction contours are drawn at $(0.9, 1.0, 1.1)\xi_{\text{st}}$. The flame temperature field is shown, exhibiting a fast rise from the cold reactants temperature to that of the hot combustion products across a narrow region where the primary edge flame reaction zone exists. The contours of the consumption rate of the fuel, w_{CH_4} , are superposed to highlight the curved premixed front structure, with clear rich and lean premixed branches. The region behind the premixed flame edge, extending along the central ξ_{st} line upwards through the domain, has a diffusion-flame structure, approximating the ideal one-dimensional non-premixed flame structure with downstream distance.

III. CSP ANALYSIS OF THE EDGE FLAME STRUCTURE

We recall that, with an N -dimensional ODE system, $dy/dt = g$, CSP employs a set of basis vectors/co-vectors, $\mathbf{a}_i/\mathbf{b}_i$, $i = 1, \dots, N$, to decompose the source term into a sum of (ideally) decoupled modes $\{\mathcal{M}_k\}_{k=1}^N$, given by $g = \sum_{r=1}^M \mathbf{a}_r f^r + \sum_{s=M+1}^N \mathbf{a}_s f^s$, where f^k is the amplitude of \mathcal{M}_k . The modes are ordered from fastest to slowest, with associated time scales $\tau_1 < \dots < \tau_N$. The first M (fast) modes, having sufficiently small amplitude according to chosen thresholds, are either “frozen”, having no chemical activity, or “exhausted”, involving

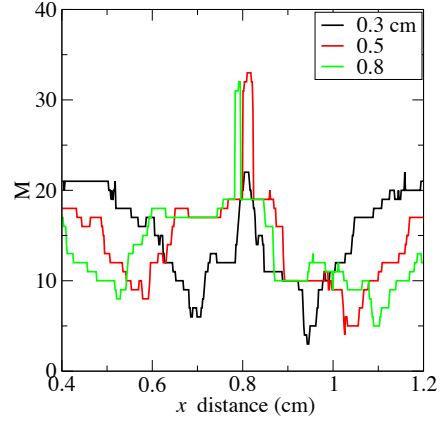


Fig. 2. M cut along different y levels

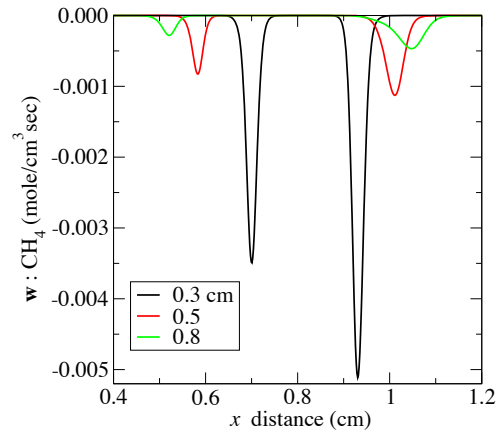


Fig. 3. w_{CH_4} cut along different y levels

cancellations of opposed processes. The remaining $N - M$ modes are slow, constrained to evolve along a slow manifold defined by the fast processes. In a PDE context, we identify the CSP basis vectors based on the chemical source term alone, however, the determination of M is based on the projection of the full right-hand-side on this basis. Finally, for any given mode k , the CSP Participation Index (PI) of any process i , \mathcal{P}_k^i , is a normalized measure of the importance of that process in this mode, where a process is defined as any of the forward/backward reactions in the system, or a convection/diffusion transport term for a given species.

With this cursory definition of terminology, we now examine the structure of the edge flame using CSP analysis. Figure 1(b) shows the spatial distribution of M , the dimension of the fast subspace, with superposed w_{CH_4} and ξ -contours. The detailed structure of the M field is complex, but some key features may be readily observed in this 2D plot. The primary reaction zone region, where w_{CH_4} is largest, exhibits generally the lowest M values, where only 3-8 modes are exhausted. Note however, the misalignment between the w_{CH_4} contours and the region with lowest M values in the downstream end of the rich edge flame branch. The central, diffusion flame region has the highest number of exhausted modes, with $M > 30$. At

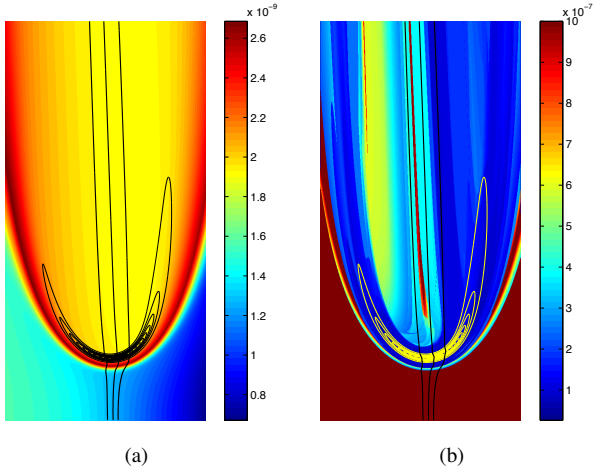


Fig. 4. The spatial distribution of the fastest chemical timescale τ_1 (a), and the driving chemical time scale τ_{M+1} (b), in the edge flame, shown with superposed w_{CH_4} and mixture fraction contours. The ξ -contours and domain size are as those in Fig. 1. Note that the color map for the τ_{M+1} plot has been truncated at $1 \mu\text{s}$ for clarity.

the base of the edge flame, this high- M region coincides with the $\xi = \xi_{\text{st}} = 0.055$ line, shifting towards leaner mixtures mid-way up the domain. This is the region which is closest to equilibrium as the reaction products from the lean/rich sides of the edge flame come together.

Further, horizontal cuts of the domain at three y -locations of (0.3, 0.5, 0.8) cm, showing the spatial profiles of M and the chemical production rate of the fuel, w_{CH_4} , at different elevations in the edge flame, are shown in Figures 2, and 3 respectively. The high M -plateau in the cold gas is evident in the 0.3 cm profile, with $M \sim 22$ for $x \sim 0.4, 1.2$ cm, and $w_{\text{CH}_4} \sim 0$. As we approach regions of significant CH_4 consumption, with $x \sim 0.7, 0.93$ cm, we find largely monotonic decrease in M towards a minimum that roughly coincides with the peak consumption rate of the fuel. Going further, towards the domain centerline, M is found to increase again, with an eventual peak value at $x \sim 0.8$ cm. This picture is roughly similar at the other two y -elevations. The central peak is observed to shift towards the left, reflecting the shift observed in the 2D image in Fig. 1(b). Similarly, the locations of the minima in M are observed to shift away from the centerline, reflecting the increased width of the edge flame in Fig. 1(b). Further, these minima are broader reflecting the increased thickness of the reaction zone at these rich/lean locations. The minimum value of M also increases, indicating that less/more modes are active/exhausted in the premixed front nearer stoichiometric conditions. Finally, note that the deviation between the location of the M -minimum and peak fuel consumption in the rich region at higher y -elevations, as observed in Fig. 1(b).

Figure 4(a) shows the spatial distribution of the fastest chemical timescale τ_1 in the edge flame. The cold fuel-rich region exhibits the fastest τ_1 , ~ 0.7 ns, while the curved preheat zone ahead of the primary edge flame reaction zone exhibits the slowest τ_1 , ~ 2.7 ns. In this zone, important low temperature flame processes are active.

Specifically, this zone coincides with the regions of low temperature peak production rates of HO_2 and CH_3O , and associated processes. Thus, for example, the conversion of NO to NO_2 is peaked in this region, dominated by the forward rate of the reaction R_{186} : $\text{HO}_2 + \text{NO} = \text{NO}_2 + \text{OH}$. Here and in the following, we use the reaction numbers to identify the specific reaction in GRImech3.0 [24]. Moreover, we adopt the following convention, denoting the net, forward, and backward reaction i by R_i , F_i , and B_i respectively.

Along the domain inlet, and spanning the x -length of the domain, we find that the processes with the largest PI in mode 1, \mathcal{P}_1^i , are largely the convection and diffusion of O_2 . Occasionally, *i.e.* at some x -locations, the diffusive fluxes of CH_4 dominate, but the far majority of points exhibit the stated dominance of O_2 transport fluxes in mode 1. Note that, in this region there is barely any chemical activity, in fact many modes are frozen, such that the only significant activity is the transport of reactants. Thus, the observed dominance of these transport processes in the PI of mode 1 (PI_1), indicating that only transport is significant along \mathbf{a}_1 , is not surprising.

Looking at cuts at three elevations through the edge flame (0.3, 0.5, 0.8 cm), the PI results for mode 1 at all y -locations are as follows. The results are essentially similar on either side of the flame, in the fuel or air streams, as at the lower location near the domain inlet, with dominance of O_2 transport processes. As we enter the preheat zone on either side of the thin premixed flame zones, various transport processes gain dominance in narrow spatial regions, namely diffusion and convection of Temperature, H_2 , and H_2O , along with the diffusion and convection of CO on the air-side only. Going further into the preheat zone, a range of reactive processes exhibit narrow regions of dominance. These are: F_{97} : $\text{OH} + \text{CH}_3 \Rightarrow \text{CH}_2(\text{S}) + \text{H}_2\text{O}$, F_{125} : $\text{CH} + \text{O}_2 \Rightarrow \text{O} + \text{HCO}$, F_{130} : $\text{CH} + \text{CH}_4 \Rightarrow \text{H} + \text{C}_2\text{H}_4$, F_{142} : $\text{CH}_2(\text{S}) + \text{N}_2 \Rightarrow \text{CH}_2 + \text{N}_2$, B_{126} : $\text{CH} + \text{H}_2 \Leftarrow \text{H} + \text{CH}_2$, and, in the air-side preheat zone only, F_{144} : $\text{CH}_2(\text{S}) + \text{O}_2 \Rightarrow \text{H} + \text{OH} + \text{CO}$. These reactions are part of the cascade of fast fuel-breakdown reactions. As for the region *inside* the edge flame, including on either side the two primary flames, the reaction R_{204} : $\text{NNH} = \text{N}_2 + \text{H}$, has the dominant participation index in mode 1 at all y -locations.

Moreover, recall that examining the CSP pointer for exhausted modes, allows the identification of the associated CSP radical species for that mode. In other words, this is the species whose fast consumption processes have high PIs, and therefore are key participants in the associated equilibrium and corresponding time scale of this mode. In the present case, and considering all y -locations, we find the following regarding mode 1. In the cold flow region outside the edge flame, the species pointed to by mode 1 is CH . Further, this mode is found to be either frozen or exhausted in different parts of this region. While the transport of O_2 or CH_4 dominates the PI, this is, as indicated above, because there is hardly any chemical activity. However, recall that the time scales τ_k result from the analysis of the *chemical* source term. Further,

the fact that this mode points to CH suggests that CH consumption reactions are relevant here in establishing τ_1 . In fact, looking at the most dominant PIs for *chemical* processes we find that reactions F_{125} : $\text{CH}+\text{O}_2 \Rightarrow \text{O}+\text{HCO}$ (on the air side) and F_{130} : $\text{CH}+\text{CH}_4 \Rightarrow \text{H}+\text{C}_2\text{H}_4$ (on the fuel side), both CH consumption reactions, are generally among the highest amplitude PIs among the reactive processes in this region. Further, it is likely that the difference in τ_1 between the cold fuel and air streams, evident in Fig. 4(a), is a direct result of the dominance of one or the other of these reactions in each zone. In the preheat zones, where low-temperature chemistry is active, and mode 1 is exhausted, the associated CSP pointer points to $\text{CH}_2(\text{S})$. This is consistent with the observed dominance of several reactions involving $\text{CH}_2(\text{S})$ in this region in PI_1 , as observed above. On the other hand, inside the edge flame, NNH is the corresponding species pointed to by mode 1, again exhausted, which is again consistent with the above dominance of R_{204} in PI_1 in this region.

Consider next the spatial structure of the driving chemical time scale τ_{M+1} , shown in Figure 4(b). Recall that \mathfrak{M}_{M+1} is the fastest of the slow modes, such that the system evolves locally with time scale τ_{M+1} . We note first that the cold fuel/air regions, where largely only slow transport processes are active, exhibit a large $\tau_{M+1} \geq 1 \mu\text{sec}$. Further, as we approach the primary flame, in the preheat region, a narrow region of alternating fast/slow activity is evident, before the broad region of fast chemical activity in the edge flame is reached. In this internal region, fastest chemical activity is evident in the primary premixed flame zone, with slower τ_{M+1} evident in the central region around ξ_{st} where chemical equilibrium is approached.

Let us examine the PIs for \mathfrak{M}_{M+1} along horizontal cuts. As for \mathfrak{M}_1 , the lack of chemical activity in the cold flow regions outside the edge flame highlights the action of transport fluxes. Here again, we find the transport of O_2 to dominate the PI. Among reactive processes, the reactions with the largest PIs (albeit small relative to transport) in this region are found to be F_{11} : $\text{O}+\text{CH}_4 \Rightarrow \text{OH}+\text{CH}_3$, F_{179} : $\text{N}+\text{O}_2 \Rightarrow \text{NO}+\text{O}$, F_{216} : $\text{HNO}+\text{O}_2 \Rightarrow \text{HO}_2+\text{NO}$, F_{291} : $\text{CH}_2+\text{O}_2 \Rightarrow \text{O}+\text{CH}_2\text{O}$, and B_{207} : $\text{NNH}+\text{O} \Rightarrow \text{OH}+\text{N}_2$. As we approach the flame edge, reaction fluxes become significant, dominating the role of transport in PI_{M+1} . In the preheat zone, reactions such as F_{119} : $\text{HO}_2+\text{CH}_3 \Rightarrow \text{OH}+\text{CH}_3\text{O}$, and F_{98} : $\text{OH}+\text{CH}_4 \Rightarrow \text{CH}_3+\text{H}_2\text{O}$, as well as F_{170} : $\text{CH}_3\text{O}+\text{O}_2 \Rightarrow \text{HO}_2+\text{CH}_2\text{O}$ are found to be dominant. This is a reflection of the dominant role of these reactions in the fuel breakdown chemistry on the reactants side of the premixed flame.

Finally, we note that the detailed structure inside the flame is quite complex. Consider in particular the region with minimum M , in the vicinity of the primary premixed flame reaction zone, shown in Figs. 1(b) and 2. In this region, and focusing on a cut at $y = 0.3 \text{ cm}$ for illustration, we find that reactions with dominant PI_{M+1} in the lean branch include F_{97} : $\text{OH}+\text{CH}_3 \Rightarrow \text{CH}_2(\text{S})+\text{H}_2\text{O}$,

F_{68} : $\text{H}+\text{CH}_3\text{OH} \Rightarrow \text{CH}_2\text{OH}+\text{H}_2$, F_{169} : $\text{CH}_2\text{OH}+\text{O}_2 \Rightarrow \text{HO}_2+\text{CH}_2\text{O}$, and F_{126} : $\text{CH}+\text{H}_2 \Rightarrow \text{H}+\text{CH}_2$. On the other hand, in the rich branch, the following reactions dominate this mode, F_{122} : $\text{C}+\text{O}_2 \Rightarrow \text{O}+\text{CO}$, F_{58} : $\text{H}+\text{CH}_2\text{O} \Rightarrow \text{HCO}+\text{H}_2$, F_{168} : $\text{HCO}+\text{O}_2 \Rightarrow \text{HO}_2+\text{CO}$, along with B_{126} . A detailed study of the internal structure of the premixed flame primary reaction zone is greatly informed by these specific findings, identifying the reactive processes controlling the chemical evolution of the system in each internal flame layer. Similar information is equally useful in other internal regions of the edge flame.

IV. CONCLUSIONS

We have studied the structure of a methane-air edge flame using CSP analysis. Results identified the structure of the flame at different spatial locations, illustrating the spatial distribution of the dimensionality of the fast subspace and the structure of the fastest and active modes. We identified the dominant processes defining these modes, and highlighted their spatial distribution. Of particular note, relevant to the fastest chemical mode (whose structure is clearly consequential to requisite time integration strategies), is the observation of the dominance of R_{204} : $\text{NNH} = \text{N}_2+\text{H}$ everywhere inside the edge flame, with NNH being the associated CSP radical. On the other hand, a number of CH and $\text{CH}_2(\text{S})$ reactions dominate the fastest mode in the premixed flame preheat zones around the outer rim of the edge flame, with $\text{CH}_2(\text{S})$ being the associated CSP radical.

ACKNOWLEDGMENTS

This work was supported by the US Department of Energy (DOE), Office of Basic Energy Sciences (BES) Division of Chemical Sciences, Geosciences, and Biosciences. Sandia National Laboratories is a multiprogram laboratory operated by Sandia Corporation, a Lockheed Martin Company, for the United States Department of Energy under contract DE-AC04-94-AL85000. M. Valorani acknowledges the support of the Italian Ministry of University and Research (MIUR).

REFERENCES

- [1] P. K̄ioni, B. Rogg, K. Bray, A. Liñán, Flame spread in laminar mixing layers: the triple flame, *Combustion and Flame* 95 (1993) 276–290.
- [2] G. Reutsch, L. Vervisch, A. Liñán, Effects of heat release on triple flames, *Phys. Fluids* 7 (6) (1995) 1447–1454.
- [3] D. Veynante, L. Vervisch, T. Poinso, A. Liñán, G. Ruetsch, Triple flame structure and diffusion flame stabilization, in: *Center for Turbulence Research, Proceedings of the Summer Program*, Stanford University, Stanford Univ., Stanford, CA, 1994, pp. 55–73.
- [4] J. Ray, H. Najm, R. Milne, K. Devine, S. Kempka, Triple Flame Structure and Dynamics at the Stabilization Point of an Unsteady Lifted Jet Diffusion Flame, *Proc. Comb. Inst.* 28 (2000) 219–226.
- [5] C. Mueller, R. Schefer, Coupling of diffusion flame structure to an unsteadyvortical flowfield, in: *Twenty-Seventh Symposium (International) on Combustion*, Vol. 27, The Combustion Institute, 1998, pp. 1105–1112.
- [6] J. Buckmaster, Edge-flames, *Progress in Energy and Combustion Science* 28 (2002) 435–475.
- [7] S. Chung, Stabilization, propagation and instability of tribrachial triple flames, *Proceedings of the Combustion Institute* 31 (2007) 877–892.

- [8] L. Muñiz, M. Mungal, Instantaneous Flame-Stabilization Velocities in Lifted-Jet Diffusion Flames, *Combustion and Flame* 111 (1997) 16–31.
- [9] B. Lee, S. Chung, Stabilization of Lifted Tribranched Flames in a Laminar Nonpremixed Jet, *Combust. Flame* 109 (1997) 167.
- [10] S. Ghosal, L. Vervisch, Stability Diagram for Lift-Off and Blowout of a Round Jet Laminar Diffusion Flame, *Combust. Flame* 123 (2001) 646.
- [11] J. Daou, A. Liñán, The role of unequal diffusivities in ignition and extinction fronts in strained mixing layers, *Combust. Theory Modelling* 2 (1998) 449–477.
- [12] T. Echehki, J. Chen, Structure and Propagation of Methanol-Air Triple Flames, *Combustion and Flame* 114 (1998) 231–245.
- [13] H. Im, J. Chen, Effects of Flow Strain on Triple Flame Propagation, *Combust. Flame* 126 (2001) 1384.
- [14] P. Kioni, N. Bray, D. Greenhalgh, B. Rogg, *Combust. Flame* 116 (1999) 192.
- [15] T. Plessing, P. Terhoeven, N. Peters, M. Mansour, An Experimental and Numerical Study of a Laminar Triple Flame, *Combust. Flame* 115 (1998) 335.
- [16] F. Takahashi, W. Schmoll, V. Katta, Attachment mechanisms of diffusion flames, *Proc. Comb. Inst.* 27 (1998) 675–686.
- [17] F. Takahashi, V. Katta, Chemical kinetic structure of the reaction kernel of methane jet diffusion flames, *Combustion Sci. and Tech.* 155 (2000) 243–279.
- [18] F. Takahashi, V. Katta, A reaction kernel hypothesis for the stability limit of methane jet diffusion flames, *Proc. Comb. Inst.* 28 (2000) 2071–2078.
- [19] K. Walsh, J. Fielding, M. Smooke, M. Long, A. Liñán, A comparison of computational and experimental lift-off heights of coflow laminar diffusion flames, *Proc. Comb. Inst.* 30 (2005) 357–365.
- [20] S. Ali, J. Daou, Effect of the reversibility of the chemical reaction on triple flames, *Proc. Comb. Inst.* 31 (2007) 919–927.
- [21] S. Cho, K. Takita, Numerical study of premixed twin edge flames in a counterflow field, *Combustion and Flame* 144 (2006) 370–385.
- [22] A. Briones, S. Aggarwal, V. Katta, A numerical investigation of flame liftoff, stabilization, and blowout, *Physics of Fluids* 18 (2006) 043603:1–13.
- [23] H. Guo, F. Liu, G. Smallwood, A numerical study of laminar methane/air triple flames in two-dimensional mixing layers, *Int. J. Thermal Sci.* 45 (2006) 586–594.
- [24] G. Smith, D. Golden, M. Frenklach, N. Moriarty, B. Eiteneer, M. Goldenberg, C. Bowman, R. Hanson, S. Song, W. G. Jr., V. Lissianski, Q. Zhiwei, GRI mechanism for methane/air, version 3.0, 7/30/99, www.me.berkeley.edu/gri_mech.
- [25] H. Najm, D. Ponganis, J. Prager, Analysis of NO Structure in a Methane-Air Edge Flame, *Proc. Comb. Inst.* 32 (1) (2008) 1117–1124.
- [26] S. Lam, D. Goussis, Understanding complex chemical kinetics with computational singular perturbation, *Proc. Comb. Inst.* 22 (1988) 931–941.
- [27] D. Goussis, S. Lam, A study of homogeneous methanol oxidation kinetic using csp, *Proc. Comb. Inst.* 24 (1992) 113–120.
- [28] S. Lam, Singular perturbation for stiff equations using numerical methods, in: C. Casci (Ed.), *Recent Advances in the Aerospace Sciences*, Plenum Press, New York, 1985, p. 3.
- [29] S. Lam, D. Goussis, *Basic Theory and Demonstration of Computational Singular Perturbation for Stiff Equations, Modelling and Simulation of Systems*, Baltzer Scientific Publishing Co., P. Breedveld et al. Eds., 1989.
- [30] S. Lam, D. Goussis, Conventional Asymptotics and Computational Singular Perturbation for Simplified Kinetics Modelling, in: M. Smooke (Ed.), *Reduced Kinetic Mechanisms and Asymptotic Approximations for Methane-Air Flames*, no. 384 in Springer Lecture Notes, Springer Verlag, 1991, Ch. 10, pp. 227–242.
- [31] S. Lam, Using CSP to Understand Complex Chemical Kinetics, *Combustion Science and Technology* 89 (1993) 375–404.
- [32] S. Lam, D. Goussis, The CSP Method for Simplifying Kinetics, *International Journal of Chemical Kinetics* 26 (1994) 461–486.
- [33] D. Goussis, On the Construction and Use of Reduced Chemical Kinetics Mechanisms Produced on the Basis of Given Algebraic Relations, *J. Comput. Physics* 128 (1996) 261–273.
- [34] M. Valorani, D. Goussis, Explicit Time-Scale Splitting Algorithm For Stiff Problems: Auto-Ignition Of Gaseous-Mixtures Behind A Steady Shock, *J. Comput. Phys.* 169 (2001) 44–79.
- [35] M. Valorani, H. Najm, D. Goussis, CSP Analysis of a Transient Flame-Vortex Interaction: Time Scales and Manifolds, *Combustion and Flame* 134 (1-2) (2003) 35–53.
- [36] D. Goussis, M. Valorani, F. Creta, H. Najm, Reactive and Reactive/Diffusive Time Scales in Stiff Reaction-Diffusion Systems, *Progress in Computational Fluid Mechanics* 5 (6) (2005) 316–326.
- [37] M. Valorani, D. Goussis, F. Creta, H. Najm, Higher Order Corrections in the Approximation of Low Dimensional Manifolds and the Construction of Simplified Problems with the CSP Method, *J. Comput. Phys.* 209 (2005) 754–786.
- [38] M. Valorani, F. Creta, D. Goussis, J. Lee, H. Najm, Chemical Kinetics Simplification via CSP, *Combustion and Flame* 146 (2006) 29–51.
- [39] M. Valorani, F. Creta, F. Donato, H. Najm, D. Goussis, Skeletal Mechanism Generation and Analysis for *n*-heptane with CSP, *Proc. Comb. Inst.* 31 (2007) 483–490.
- [40] D. Goussis, M. Valorani, An Efficient Iterative Algorithm for the Approximation of the Fast and Slow Dynamics of Stiff Systems, *J. Comp. Phys.* 214 (2006) 316–346.
- [41] D. Goussis, H. Najm, Model Reduction and Physical Understanding of Slowly Oscillating Processes: The Circadian Cycle, *Multiscale Modeling and Simulation* 5 (4) (2006) 1297–1332.
- [42] H. Najm, O. Knio, Modeling Low Mach Number Reacting Flow with Detailed Chemistry and Transport, *J. Sci. Comp.* 25 (1) (2005) 263–287.
- [43] R. Bilger, S. Starner, R. Kee, On reduced mechanisms for methane-air combustion in non-premixed flames, *Comb. and Flame* 80 (1990) 135–149.

Range-Constrained Simultaneous Reaction and Species Elimination in Kinetic Mechanisms

Geoffrey M. Oxberry*, Alexander Mitsos†, Paul I. Barton*, William H. Green*

*Massachusetts Institute of Technology/Department of Chemical Engineering, Cambridge, MA, USA

†Massachusetts Institute of Technology/Department of Mechanical Engineering, Cambridge, MA, USA

Abstract—Although many techniques exist to generate a reduced model from a large, detailed chemical model, few model reduction techniques generate reduced models that can reproduce the solution of the detailed model to within known error bounds. Furthermore, error bounds imposed on the reduced model at a finite set of reaction conditions cannot be propagated through a numerical method to yield error bounds on the numerical solution of the reduced model relative to the solution of the detailed model. In order to reproduce the numerical solution of the detailed model to within a known error tolerance using a reduced model, the reduced model must be generated with known error bounds that are satisfied over a range of reaction conditions.

To generate a reduced model satisfying error bounds over a range of reaction conditions, we propose the method of range-constrained simultaneous reaction and species elimination. This method uses the solution of an integer linear program restriction of an integer linear semi-infinite program to determine a reduced model from a given detailed model, error tolerances on the time derivatives of state variables and range of reaction conditions. The reduced model obtained from the solution of the integer linear program can then be used within a numerical method to approximate faithfully the solution of the detailed model from which it was generated. Error bounds on the reduced model could then be propagated through the numerical method in order to obtain error bounds on the solution of the detailed model, yielding a more computationally efficient means of obtaining a numerical solution for currently intractable reacting flow problems to within known numerical error.

I. INTRODUCTION

The purpose of a kinetic model reduction technique is to generate an approximate, simplified chemical model from a more detailed chemical model in order to reduce the computational effort needed to simulate reacting flows. Many different methods exist to accomplish this task (such as [6], [14] and [7]), based on very different principles.

When carrying out model reduction, there are two competing objectives: reducing CPU effort and minimizing approximation error due to model reduction. Since the purpose of model reduction is to enable the simulation of computationally demanding reacting flow problems by generating less resource-intensive reduced models, we would like our model reduction technique to yield a reduced model that decreases as much as possible the CPU time required to simulate a reacting flow. Simultaneously, we would like to minimize the difference (or error) between the solution of our reduced model and the solution of the detailed model. Since CPU time limits the set of reacting flow problems that can be solved

currently, our primary objective is to achieve maximum reduction of CPU effort subject to constraints that ensure that the error between the numerical solution of the detailed model and the solution of the reduced model is bounded to within acceptable limits over certain reaction conditions (temperatures and species mass fractions). In order to limit this error when using the reduced model in a numerical integration routine, it is necessary to bound the difference between the chemical source term of the detailed model and the chemical source term of the reduced model for each species. Although many methods have some form of error control (usually in the form of an adjustable parameter), few methods attempt to determine error bounds on the chemical source term of the reduced model with respect to the detailed model. Without these error bounds, it is extremely difficult to estimate the error in the solution obtained by applying a model reduction technique when solving a detailed model numerically.

It is also worth noting that bounding locally the error due to model reduction does not suffice [11]. Oluwole *et al.* have demonstrated that error bounds satisfied by a reduced model at points in state space do not necessarily hold within their convex hull. For this reason, a reduced model with error bounds satisfied at a finite collection of points in state space may not satisfy its stated error tolerances after one time step of numerical integration. Consequently, it is absolutely critical that reduced models be generated with error bounds on the time derivatives of state variables, and that these error bounds are satisfied over ranges in state space.

Optimization is a natural mathematical framework for model reduction because elements of model reduction problems can be adapted to an optimization formulation. Typically, the mode of model reduction can be cast in terms of decision variables of the optimization problem. The mode of model reduction can be thought of as the rules or allowable transformations that can take place in generating a reduced model from a detailed model. Reaction elimination [3] is one example of such rules. Error bounds can be formulated as constraints, and CPU effort can be formulated as an objective. Since simulation CPU time cannot be expressed directly as a continuous function of the decision variables, the number of reactions, species, or state variables is typically used as a proxy, because the CPU time needed to solve a reacting flow problem scales empirically as $O(N_R N_S^2)$, where N_R is the number of reactions and N_S is the number of

species [13]. Adapting a model reduction technique to an optimization framework ensures that a given detailed model is maximally (or close to maximally) reduced, subject to the error constraints and model reduction rules supplied by the model reduction technique.

In this work, we propose using an optimization framework to generate reduced models by simultaneous reaction and species elimination, such that the resulting models satisfy given error constraints over ranges in state space. This approach, called range-constrained simultaneous reaction and species elimination, is a natural extension of existing work on both reaction elimination [3], [10] and simultaneous reaction and species elimination [8]. In order to provide the necessary background for the development of range-constrained simultaneous reaction and species elimination, we first review the previous point-constrained reaction and species elimination by Mitsos *et al.* [8].

II. EXISTING POINT-CONSTRAINED SIMULTANEOUS REACTION AND SPECIES ELIMINATION FORMULATION

Bhattacharjee [1] proposed an integer nonlinear programming (INLP) formulation for simultaneous reaction and species elimination. Although this formulation was novel, it was also computationally demanding, since algorithms that solve INLPs are time-consuming. Mitsos *et al.* [8] discovered an equivalent integer linear program (ILP) reformulation of the original INLP that can be solved much more quickly. The resulting point-constrained reaction and species elimination ILP is presented below as in [8], restricting the formulation to the case where $\alpha_j = 1$ for all j and $\beta_i = 0$ for all i :

$$\min_{\mathbf{z}, \mathbf{w}} \sum_{j=1}^{N_S} w_j, \quad (1a)$$

$$\text{s.t.} \left| \frac{\sum_{j=1}^{N_S} h_j(T_l) M_j \sum_{i=1}^{N_R} \nu_{ji} z_i r_i(\mathbf{x}_l, T_l)}{\rho_l (C_P)_l} - \Gamma_0^{ref}(\mathbf{x}_l, T_l) \right| \leq (atol)_0 + (rtol)_0 |\Gamma_0^{ref}(\mathbf{x}_l, T_l)|, \quad l = 1, \dots, N_t, \quad (1b)$$

$$\left| \frac{M_j \sum_{i=1}^{N_R} \nu_{ji} z_i r_i(\mathbf{x}_l, T_l)}{\rho_l} - \Gamma_j^{ref}(\mathbf{x}_l, T_l) \right| \leq (atol)_j + (rtol)_j |\Gamma_j^{ref}(\mathbf{x}_l, T_l)|, \quad j = 1, \dots, N_S; l = 1, \dots, N_t, \quad (1c)$$

$$(N_R)_j w_j \geq \sum_{\{i: \nu_{ji} \neq 0\}} z_i, \quad j = 1, \dots, N_S, \quad (1d)$$

$$z_i \in \{0, 1\}, \quad i = 1, \dots, N_R, \quad (1e)$$

$$w_j \in \{0, 1\}, \quad j = 1, \dots, N_S. \quad (1f)$$

The formulation in (1) requires some explanation. In (1), three subscripts are used. The subscript i indexes the N_R reactions present in the detailed mechanism, and is used in conjunction with reaction-based quantities, such as the rate of reaction. The subscript j indexes the N_S species present in the detailed mechanism, and is used in conjunction with species-based quantities, such as the species mass fractions. The subscript l indexes N_t user-supplied points in state space to be used as a reference data set for model reduction. This reference data set defines the conditions in state space over which the reduced model will be “valid,” in that it satisfies error

tolerances on the time derivatives of the state variables relative to the detailed model. In our case, state space is defined as the mass fractions of each species present in the detailed model and temperature; we assume that our detailed model describes the chemical source term in an adiabatic-isobaric batch reactor.

Reaction elimination is encoded by the binary decision variables z_i , and species elimination is encoded by the binary decision variables w_j . If $z_i = 1$, reaction i is included in the reduced model generated by this technique. If $z_i = 0$, reaction i is excluded from the reduced model generated by this technique. Similarly, if $w_j = 1$, species j is included in the reduced model generated by this technique. If $w_j = 0$, species j is excluded from the reduced model generated by this technique. Consequently, an optimal solution to (1) yields a reduced mechanism derived from the detailed mechanism supplied as input to point-constrained simultaneous reaction and species elimination. Given this interpretation of the binary decision variables, the objective function (1a) equals the number of species included in the reduced model.

Assuming that our detailed model describes the chemical source term in an adiabatic-isobaric batch reactor, the error constraints in (1b) and (1c) limit the difference between the time derivatives of the state variables in the detailed model and the time derivatives of the corresponding state variables in the reduced model. In these equations, h_j is the specific enthalpy of species j , M_j is the molar mass of species j , ν_{ji} is the stoichiometric coefficient of species j in reaction i (using the standard sign convention that $\nu_{ji} > 0$ if species j is produced in reaction i , and $\nu_{ji} < 0$ if species j is consumed in reaction i), r_i is the molar rate of reaction i , \mathbf{x}_l is the vector of species mass fractions in the batch reactor at reference point l , T_l is the temperature in the batch reactor at reference point l , ρ_l is the density of the gas in the batch reactor at reference point l , $(C_P)_l$ is the specific heat capacity of the mixture in the batch reactor at reference point l , Γ_0^{ref} is the chemical source term for the temperature evaluated at a reference point specified as an argument, and Γ_j^{ref} is the chemical source term for species j evaluated at a reference point specified as an argument. The absolute error tolerance for the time derivative of species j is defined as $(atol)_j$, and the absolute error tolerance for the time derivative of temperature is defined as $(atol)_0$; these tolerances are set by the user. Corresponding relative tolerances are defined as $(rtol)_j$ for species j and $(rtol)_0$ for temperature.

Mitsos *et al.* [8] recognized that in order to avoid the production or destruction of mass via the reactions of the reduced mechanism, a species may only be eliminated from the detailed mechanism if all of the reactions in which it participates (in the detailed mechanism) are also eliminated. The mass conservation constraint (1d) encodes this condition, where $(N_R)_j$ is the number of reactions of the detailed mechanism in which species j participates. In the case of unimolecular, bimolecular, and explicit termolecular reactions, participation of a chemical species

is unambiguous. However, some reaction mechanisms contain third body reactions, in which a molecule called a third body acts upon the reactants to give them enough kinetic energy for reaction to occur. If a third body reaction is treated as a bimolecular reaction, in that the third body species are not considered to participate in that reaction, then the estimates of the time derivatives of the state variables in (1d) may be inaccurate. For most practical purposes, these inaccuracies are insignificant and can be ignored. If the inaccuracies due to neglecting the participation of third body species are significant, Mitsos *et al.* [8] propose alternate treatments for third body species.

Point-constrained species elimination has been applied to mechanisms as large as the LLNL n-heptane mechanism [4] successfully. Due to the $O(N_R N_S^2)$ scaling of reacting flow solvers, simultaneous elimination of reactions and species reduces the computational effort of reacting flow solvers to a greater extent than elimination of reactions only. However, since the chemical source term is, in general, a non-convex function of the state variables over the convex hull of the reference points supplied to (1), the error in the reduced model is also a non-convex function over the convex hull of the reference points. Consequently, if a reduced model is generated satisfying error bounds at the reference points, it is not necessarily true that the reduced model also satisfies the same error bounds at any point in state space within the convex hull of the reference points. For this reason, if error-controlled reduced models are desired over regions in state space (for example, in a reacting flow solver using an adaptive chemistry algorithm [12]), either a valid range must be determined from a point-constrained reduced model by using the range-finding algorithm of Oluwole *et al.* [11], or the constraints in the point-constrained model reduction formulation (1) must be revised to limit errors over ranges in state space.

III. PROPOSED RANGE-CONSTRAINED SPECIES ELIMINATION FORMULATION

By analogy to the previous work on reaction elimination by Bhattacharjee *et al.* [1], [3] and Oluwole *et al.* [10], we propose the following range-constrained simultaneous reaction and species elimination formulation as an extension of a combination of the work of [8] and [10]:

$$\min_{\mathbf{z}, \mathbf{w}} \sum_{j=1}^{N_S} w_j, \quad (2a)$$

$$\text{s.t.} \left| \frac{\sum_{j=1}^{N_S} h_j(T) M_j \sum_{i=1}^{N_R} \nu_{ji} z_i r_i(\mathbf{x}, T)}{\rho(\mathbf{x}, T) C_P(\mathbf{x}, T)} - \Gamma_0^{ref}(\mathbf{x}, T) \right| \leq (atol)_0 + (rtol)_0 |\Gamma_0^{ref}(\mathbf{x}, T)|, \quad \forall(\mathbf{x}, T) \in \Phi, \quad (2b)$$

$$\left| \frac{M_j \sum_{i=1}^{N_R} \nu_{ji} z_i r_i(\mathbf{x}, T)}{\rho(\mathbf{x}, T)} - \Gamma_j^{ref}(\mathbf{x}, T) \right| \leq (atol)_j + (rtol)_j |\Gamma_j^{ref}(\mathbf{x}, T)|, \quad j = 1, \dots, N_S; \forall(\mathbf{x}, T) \in \Phi, \quad (2c)$$

$$(N_R)_j w_j \geq \sum_{\{i: \nu_{ji} \neq 0\}} z_i, \quad j = 1, \dots, N_S, \quad (2d)$$

$$z_i \in \{0, 1\}, \quad i = 1, \dots, N_R, \quad (2e)$$

$$w_j \in \{0, 1\}, \quad j = 1, \dots, N_S, \quad (2f)$$

where Φ is the Cartesian product of intervals $\Phi = [\mathbf{x}^L, \mathbf{x}^U] \times [T^L, T^U]$ in mass fraction-temperature space. Note that the set Φ in (2) replaces the finite set of reference points in (1). Even though (2) is linear in the decision variables, it contains infinitely many constraints, indexed by the set Φ , and is classified as a semi-infinite program (SIP) [10].

Solving SIPs to global optimality is computationally demanding, and current algorithms cannot determine an optimal solution for large problem instances, corresponding to large kinetic mechanisms. Bhattacharjee *et al.* [2] developed an algorithm using interval extensions [9] that determines guaranteed feasible points for an SIP by formulating a restriction of the SIP. The optimal objective function value of the resulting program is an upper bound on the solution of the exact formulation of the original SIP. In the case of the SIP in (2), this restriction will be an ILP.

Oluwole *et al.* [10] used ideas from the SIP restriction algorithm of Bhattacharjee *et al.* within a range-constrained reaction elimination formulation to overestimate the difference between the detailed model source terms and the reduced model source terms with constraints similar to (2b) and (2c) and determine reduced models guaranteed to satisfy the error constraints for reaction elimination. Our proposed formulation extends the work of Oluwole *et al.* by adding the binary variables w_j and the mass conservation constraint in (2d); it extends the work of Mitsos *et al.* by replacing the finite set of reference points with an interval in state space and modifying the appropriate constraints accordingly. In applying the approach of Oluwole *et al.* to (2), DAEPACK [15] is used to generate Taylor model interval extensions that overestimate the error between the detailed model source terms and reduced model source terms. These overestimates are used to formulate the ILP restriction of (2), which is then solved to global optimality using CPLEX [5]. Since an optimal solution of the ILP restriction of (2) corresponds to a feasible point of the range-constrained SIP formulation (2), the objective function value at this point is an upper bound on the optimal objective function value for the SIP. Cast in terms of the problem at hand, our proposed algorithm will determine a reduced model with fewer species that is guaranteed to satisfy error bounds on the source term in the reduced model over a specified range of conditions of interest, but it will not necessarily determine the reduced model with the fewest species satisfying those error bounds over the range of interest.

IV. CONCLUSIONS AND FUTURE WORK

A method for automatically generating error-controlled range-validated reduced kinetic mechanisms by simultaneous reaction and species elimination is presented. The method follows either by extending the point-constrained simultaneous species and reaction elimination formulation to a range-constrained formulation, or by extending

the range-constrained reaction elimination formulation to include simultaneous reaction and species elimination. The resulting range-constrained simultaneous reaction and species elimination formulation is a semi-infinite program solved approximately by constructing an ILP restriction using interval extensions and solving that ILP to global optimality. The solution obtained by this algorithm is a feasible point for the original SIP, but it is not necessarily the best possible.

Given the recent proliferation of model reduction methods in the literature, it would be interesting to attempt to cast some of the existing model reduction methods into the form of optimization problems for the sake of comparison. Model reduction methods could then be compared using comparable error constraints in order to determine the extent to which they reduce the computational requirements of reacting flow solvers. This endeavor would also be useful in that it could facilitate the combination of different model reduction methods in order to further reduce the computational requirements of reacting flow solvers.

Finally, it would be interesting to examine how error-controlled model reduction methods interact with different numerical methods, as well as different problem formulations. Currently, little theory exists [10] to bound the errors in the numerical solution of a reduced model, as compared to the numerical solution of its corresponding detailed model. A theory explaining how error-controlled model reduction methods interact with different numerical methods for solving reacting flow problems could then be applied to range-constrained, error-controlled model reduction techniques to solve reduced models to within known error bounds, greatly enhancing the utility of model reduction techniques by clearly quantifying the error incurred by model reduction.

ACKNOWLEDGMENTS

We would like to thank Joseph K. Scott and Dr. Ajay Selot for helpful discussions. GMO gratefully acknowledges support under a DOE CSGF fellowship provided under grant DE-FG02-97ER25308. Financial support from the U.S. Department of Energys Office of Basic Sciences, Division of Chemical Sciences, Geosciences and Biosciences through Grant DE-FG02-98ER14914 is gratefully acknowledged.

REFERENCES

- [1] B. Bhattacharjee. *Kinetic Model Reduction using Integer and Semi-infinite Programming*. PhD thesis, MIT, December 2003.
- [2] B. Bhattacharjee, W. H. Green, and P. I. Barton. Interval methods for semi-infinite programs. *Computational Optimization and Applications*, 30:63–93, 2005.
- [3] B. Bhattacharjee, D. A. Schwer, P. I. Barton, and W. H. Green. Optimally-reduced kinetic models: reaction elimination in large-scale kinetic mechanisms. *Combustion and Flame*, 135:191–208, 2003.
- [4] H. J. Curran, P. Gaffuri, W. J. Pitz, and C. K. Westbrook. A comprehensive modeling study of n-heptane oxidation. *Combustion and Flame*, 114:149–177, 1998.
- [5] ILOG. *ILOG CPLEX 11.0 User's Manual*.
- [6] S. H. Lam. Using CSP to understand complex chemical kinetics. *Combustion Science and Technology*, 89(5):375–404, 1993.

- [7] T. Lu and C. K. Law. Systematic approach to obtain analytic solutions of quasi steady state species in reduced mechanisms. *Journal of Physical Chemistry A*, 110:13202–13208, 2006.
- [8] A. Mitsos, G. M. Oxberry, P. I. Barton, and W. H. Green. Optimal automatic reaction and species elimination in kinetic mechanisms. *Combustion and Flame*, 155(1-2):118–132, 2008.
- [9] R. E. Moore. *Methods and Applications of Interval Analysis*. Society for Industrial and Applied Mathematics, Philadelphia, 1987.
- [10] O. O. Oluwole, P. I. Barton, and W. H. Green. Obtaining accurate solutions using reduced chemical kinetic models: a new model reduction method for models rigorously validated over ranges. *Combustion Theory and Modelling*, 11(1):127–146, 2007.
- [11] O. O. Oluwole, B. Bhattacharjee, J. E. Tolsma, P. I. Barton, and W. H. Green. Rigorous valid ranges for optimally reduced kinetic models. *Combustion and Flame*, 146:348–365, 2006.
- [12] D. A. Schwer, P. Lu, and W. H. Green. An adaptive chemistry approach to modeling complex kinetics in reacting flows. *Combustion and Flame*, 133:451–465, 2003.
- [13] D. A. Schwer, J. E. Tolsma, W. H. Green, and P. I. Barton. On upgrading the numerics in combustion chemistry codes. *Combustion and Flame*, 128:270–291, 2002.
- [14] S. Singh, J. M. Powers, and S. Paolucci. On slow manifolds of chemical reactive systems. *Journal of Chemical Physics*, 117(4):1482–1496, 2002.
- [15] J. Tolsma and P. I. Barton. DAEPACK: An open modeling environment for legacy models. *Industrial and Engineering Chemistry Research*, 36(6):1826–1839, 2000.

Affine Lumping Formalism for Comparison of Model Reduction Techniques

Geoffrey M. Oxberry*, William H. Green*, Paul I. Barton*

*Massachusetts Institute of Technology/Department of Chemical Engineering, Cambridge, MA, USA

Abstract—Numerous methods exist for generating smaller, reduced chemical models from large, detailed chemical models. These methods arise from a variety of different theoretical backgrounds, yet few comparisons have been made between different model reduction methods. In order to assess the relative quality of these different model reduction techniques, these methods must be compared with each other using a common framework. As one element of such a framework, we propose a formalism called affine lumping. This formalism defines two affine mappings. The first affine mapping is used to lump the state variables from a detailed model to a reduced model with reduced state variables. The second affine mapping is used to un lump the reduced state variables and lift the reduced model back into the original state space. Conditions are stated under which the application of these two affine mappings in succession yields a solution of the original model. Finally, the techniques of species lumping by Li *et al.*, computational singular perturbation and reaction invariants are all cast as special cases of affine lumping, to illustrate the potential usefulness of the affine lumping formulation. Given that three different model reduction techniques can be recast using the affine lumping formalism, it is possible that other model reduction techniques may also be special cases of affine lumping. The affine lumping formalism could then be used as a common standard against which different model reduction techniques can be compared in order to assess their relative quality.

I. INTRODUCTION

Many practical problems involve combustion under inhomogeneous, transient conditions, and therefore require the use of numerical methods that solve large systems of coupled, nonlinear partial differential equations of the kind typically found in reacting flow solvers. These practical problems typically require large, detailed chemical models in order to simulate faithfully the physics involved. However, reacting flow simulations of large chemical models have prohibitively large computational costs. Consequently, smaller reduced models are used in place of large chemical models in order to obtain approximate numerical solutions to the large chemical models at decreased computational cost.

Many methods are available for generating reduced models from detailed chemical models (see [2], [5], [3] and [4] for examples). However, these different methods originate from different theoretical backgrounds, including methods based on singular perturbation, methods based on a graph-theoretic interpretation of chemistry, and others. Given this variation in the theoretical development of model reduction methods, it is difficult to compare two given model reduction techniques. Previous work

has made progress in this area by showing that the intrinsic low-dimensional manifold (ILDM) technique is a special case of computational singular perturbation (CSP) [2], facilitating the comparison of the two techniques in subsequent work. To make further progress in comparing model reduction techniques, we propose a formalism called “affine lumping.”

In this work, we provide a definition of affine lumping. Affine lumping defines two affine mappings. The first affine mapping transforms a detailed model to a reduced-dimension representation called the reduced model; this process is called lumping. The second affine mapping lifts the reduced state variables into the space of the original state variables, recovering a representation of the reduced model in the original state variables that approximates the detailed model; this process is called un lumping. It can be shown that applying these two affine mappings in sequence is equivalent to projecting the original model onto an affine subspace. This projection is the reduced model, lifted into the space of the original state variables. It can be shown that under certain conditions, lifting the solution of the reduced model into the space of the original state variables yields a solution of the detailed model. In other words, under certain conditions, the solution of the detailed model lies in an affine subspace so that the solution of the reduced model can be used to construct the exact solution of the detailed model, and the reduced model can be described with fewer differential equations and state variables than the detailed model.

After presenting a definition of affine lumping, we present examples of existing model reduction techniques that are special cases of affine lumping. We show that the species lumping technique of Li *et al.* [3], CSP and the technique of reaction invariants reviewed by Waller and Mäkilä [6] are all special cases of affine lumping by translating the nomenclature and mathematics used in each of these techniques to the nomenclature and mathematics of affine lumping. These results suggest that other methods could also be expressed using the affine lumping formalism, and indicate that apparently different techniques could have similar properties despite different theoretical backgrounds. These similarities could then be used in future work to assess the relative merits of each model reduction technique that fits the formalism.

II. DEFINITION AND PROPERTIES OF AFFINE LUMPING

In order to define affine lumping, we first motivate the definition by exploring the concept of lumping in

the specific case of chemical reaction in an adiabatic-isobaric batch reactor. Since the chemical source term in this model is used within reacting flow solvers that use operator splitting, it is the primary model under consideration; we postpone discussion of any other models to future work, since they will be extensions of this case. After briefly discussing the model and informally discussing ideas behind affine lumping, a definition of affine lumping is provided. Finally, we state without proof the main result of affine lumping: the solution of the reduced model obtained from affine lumping can be used to reconstruct the solution of the detailed model with no approximation error, provided that the affine lumping and reduced model have certain properties.

Consider the following model for a well-mixed, isolated chemically reacting system (that is, an adiabatic-isobaric batch reactor):

$$\dot{\mathbf{y}}(t) = \mathbf{\Gamma}(\mathbf{y}(t)), \quad (1)$$

where $\mathbf{y}(t) \in \mathbb{R}^{N_S}$ represents the original state variables (such as species compositions, temperatures, and pressures), and the source function $\mathbf{\Gamma} : \mathbb{R}^{N_S} \rightarrow \mathbb{R}^{N_S}$ describes changes in the state variables due to chemistry.

Consider the ‘‘affine lumping’’:

$$\phi(t) = \mathbf{A}(\mathbf{y}(t) - \mathbf{y}_0), \quad (2)$$

where $N_S \geq N_L$, $\phi(t) \in \mathbb{R}^{N_L}$ is a set of reduced state variables, $\mathbf{A} \in \mathbb{R}^{N_L \times N_S}$ is the assembly (or lumping) matrix, and $\mathbf{y}_0 \in \mathbb{R}^{N_S}$ is a point in the (original) state variable space corresponding to the origin of the new reduced-dimension space corresponding to the reduced state variables. We treat the matrix \mathbf{A} as a function of the original state variables, and therefore, as a function of the solution $\mathbf{y}(t)$, but assume that the functional form of $\mathbf{A}(\mathbf{z})$ is piecewise constant over \mathbb{R}^{N_S} (here, \mathbf{z} is a dummy variable). Therefore, instead of using the notation $\mathbf{A}(\mathbf{z})$, we will use the notation \mathbf{A} under the assumption that we have restricted the use of \mathbf{A} to a subset of \mathbb{R}^{N_S} over which its elements have constant values; this subset must be specified when defining a specific instance of lumping.

Having given an informal description of affine lumping, additional properties are needed to make a description of the lumping process more concrete. Suppose that we can find a generalized inverse \mathbf{D} corresponding to \mathbf{A} (for the properties of generalized inverses, see [1]). The matrix $\mathbf{D} \in \mathbb{R}^{N_S \times N_L}$ will be called the disassembly (or unlumping) matrix, since its purpose will be to recover approximately the original state variables from their reduced state variable counterparts. Like \mathbf{A} , we treat the matrix \mathbf{D} as a piecewise constant function over state space. Therefore, instead of using the notation $\mathbf{D}(\mathbf{z})$, we will use the notation \mathbf{D} under the assumption that we have restricted the use of \mathbf{D} to a subset of \mathbb{R}^{N_S} over which its elements have constant values; this subset must be specified when defining a specific instance of lumping, and it must be equal to the subset used in defining \mathbf{A} .

For any $\mathbf{y}^* \in \mathbb{R}^{N_S}$, the values of the reduced state variables resulting from lumping once the values of the original state variables should be equivalent to the values of the reduced state variables resulting from lumping the values of the state variables, unlumping the resulting values of the reduced state variables, and then lumping again the values of the state variables obtained from unlumping. Put another way, after lumping once, repeated unlumping and lumping should yield the same values for the lumped variables. Mathematically, this implies that for any $\mathbf{y}^* \in \mathbb{R}^{N_S}$, $\mathbf{A}\mathbf{D}\mathbf{A}\mathbf{y}^* = \mathbf{A}\mathbf{y}^*$, and thus

$$\mathbf{A}\mathbf{D}\mathbf{A} = \mathbf{A}. \quad (3)$$

Equation (3) is Penrose’s First Equation, indicating that \mathbf{D} is a $\{1\}$ -inverse of \mathbf{A} .

Also, assume that \mathbf{A} has full rank; if it does not, we could describe the subspace $\mathcal{R}(\mathbf{A})$ with a smaller basis and obtain an equivalent lumped representation using a smaller assembly matrix and fewer variables. Since the goal of this work is to reduce as much as possible the number of state variables used to represent a chemically reacting system, a full rank assumption is not restrictive.

Since \mathbf{A} has full rank, by Lemma 1.2 of [1], it follows that

$$\mathbf{A}\mathbf{D} = \mathbf{I}_{N_L}, \quad (4)$$

where \mathbf{I}_{N_L} is an $N_L \times N_L$ identity matrix. From this equation,

$$\mathbf{D}\mathbf{A}\mathbf{D} = \mathbf{D} \quad (5)$$

also holds. Equation (5) is Penrose’s Second Equation, indicating that \mathbf{D} and \mathbf{A} are $\{1, 2\}$ -inverses of each other.

These arguments motivate the following definition of an affine lumping:

Definition 2.1 (Affine Lumping): An **affine lumping** is a 3-tuple $(\mathbf{A}, \mathbf{D}, \mathbf{y}_0)$, where

- 1) \mathbf{A} is a full rank $N_L \times N_S$ matrix called the *assembly matrix*, with $N_L \leq N_S$,
- 2) \mathbf{D} is a $\{1, 2\}$ -inverse of \mathbf{A} called the *disassembly matrix*,
- 3) $\mathbf{y}_0 \in \mathbb{R}^{N_S}$ is the *origin* of the lumping.

Having defined affine lumping, we next explore the properties of the definition. Suppose we have an affine lumping $(\mathbf{A}, \mathbf{D}, \mathbf{y}_0)$ associated with (1), and suppose that $\mathbf{y}(t)$ is a solution to (1). From (2), the chain rule, and (1), it follows that

$$\dot{\phi}(t) = \mathbf{A}\dot{\mathbf{y}}(t) = \mathbf{A}\mathbf{\Gamma}(\mathbf{y}(t)). \quad (6)$$

Therefore, given a solution $\mathbf{y}^*(t)$ of (1) with $\mathbf{y}^*(0) = \mathbf{y}_0^*$, it is possible to prescribe initial conditions ϕ_0 and solve (6). Actually carrying out this process, however, would defeat the purpose of lumping, since the idea of species lumping is to cast the original state space into a reduced-dimensional state space for the purposes of reducing the computational effort needed to solve the ODE system in the reduced space; solving the original

ODE would yield all of the desired results. Consequently, it is necessary to determine a closure relation that allows us to express (6) as an autonomous ODE system.

The closure relation for constructing the solution of the original model from a suitably defined reduced model can be found under certain conditions using our main result, stated here without proof:

Theorem 2.1: Given an affine lumping $(\mathbf{A}, \mathbf{D}, \mathbf{y}_0)$, let

- 1) $Z = \{\mathbf{z} \in \mathbb{R}^{N_S} : \mathbf{z} = \mathbf{D}\mathbf{w} + \mathbf{y}_0, \mathbf{w} \in \mathbb{R}^{N_L}\}$,
- 2) $\phi(t) \in \mathbb{R}^{N_L}$ be a solution of the reduced model

$$\dot{\phi}(t) = \mathbf{A}\Gamma(\mathbf{D}\phi(t) + \mathbf{y}_0) \quad (7)$$

with $\phi(0) = \mathbf{0}$,

- 3) $\mathbf{x}(t) \equiv \mathbf{D}\phi(t) + \mathbf{y}_0$.

Suppose that $\Gamma(\mathbf{z}) \in \mathcal{R}(\mathbf{D})$, $\forall \mathbf{z}$ in Z . It follows that $\mathbf{x}(t)$ is a solution of (1) with $\mathbf{x}(0) = \mathbf{y}_0$ and that $\phi(t) = \mathbf{A}(\mathbf{x}(t) - \mathbf{y}_0)$.

If the conditions of Theorem 2.1 hold, then lifting the reduced model into the space of the original state variables yields the equation

$$\dot{\mathbf{x}}(t) = \mathbf{D}\mathbf{A}\Gamma(\mathbf{x}(t)). \quad (8)$$

Aside from the change of variables from \mathbf{y} to \mathbf{x} (chosen to distinguish between the solution of the detailed model and the lifted solution of the reduced model), note that the right hand side of the lifted reduced model (8) is the same as the right-hand side of the original model (1) premultiplied by the matrix $\mathbf{D}\mathbf{A}$. From Corollary 2.7 of [1], the matrix $\mathbf{D}\mathbf{A}$ is a projector onto $\mathcal{R}(\mathbf{D})$ along $\mathcal{N}(\mathbf{A})$, yielding the interpretation that the solution of the reduced model, lifted into the space of the original state variables, is the solution to the original model projected onto the affine subspace $\mathcal{R}(\mathbf{D}) + \mathbf{y}_0$ along $\mathcal{N}(\mathbf{A})$.

It is worth noting that a simple choice for \mathbf{D} that satisfies Theorem 2.1 is a maximal set of linearly independent columns of the stoichiometry matrix \mathbf{N} . However, in order to reduce models more aggressively, the assumptions of Theorem 2.1 will have to be relaxed so that the right-hand side of the reduced model, lifted into the space of the original state variables differs from the right-hand side of the reduced model to within a known error bound. A method for error-controlled affine lumping will be the focus of future work.

III. SPECIAL CASES OF AFFINE LUMPING

Having defined the affine lumping formalism and established conditions under which a reduced model can be used to determine exactly the solution of the detailed model, we now give some examples of model reduction techniques that are special cases of affine lumping. We discuss three techniques: the technique of species lumping by Li *et al.* [3], the technique of CSP by Lam [2] and the technique of reaction invariants reviewed by Waller and Mäkilä [6].

Li *et al.* [3] define their species lumping scheme using the matrices \mathbf{M} and $\bar{\mathbf{M}}$ that take the roles of the matrices \mathbf{A} and \mathbf{D} , respectively, in an affine lumping. Cast in terms

of the notation for affine lumping by setting $\mathbf{A} = \mathbf{M}$, $\mathbf{D} = \bar{\mathbf{M}}$, and $\phi = \hat{\mathbf{y}}$, the species lumping scheme in [3] is defined as

$$\phi(t) = \mathbf{A}\mathbf{y}(t), \quad (9)$$

and the matrices \mathbf{A} and \mathbf{D} are related by $\mathbf{A}\mathbf{D} = \mathbf{I}_{N_L}$. Li *et al.* do not place any restrictions on \mathbf{A} and \mathbf{D} other than to state that $\bar{\mathbf{M}}$ is one of the generalized inverses of \mathbf{M} . If we restrict \mathbf{M} and $\bar{\mathbf{M}}$ to be $\{1, 2\}$ -inverses of each other, we have an affine lumping $(\mathbf{A}, \mathbf{D}, \mathbf{y}_0)$ where $\mathbf{A} = \mathbf{M}$, $\mathbf{D} = \bar{\mathbf{M}}$ and $\mathbf{y}_0 = \mathbf{0}$. We postpone a more detailed comparison of affine lumping with the species lumping of Li *et al.* to future work.

Computational singular perturbation defines affine lumping-like objects through the CSP basis vectors. Let \mathbf{A}^{CSP} be the CSP basis matrix whose columns are the CSP basis vectors, and let \mathbf{B}^{CSP} be the CSP reciprocal basis matrix whose rows are the CSP reciprocal vectors, such that

$$\mathbf{B}^{CSP} = (\mathbf{A}^{CSP})^{-1}. \quad (10)$$

We assume here that the matrix \mathbf{A}^{CSP} is a constant, rather than treating it as time-varying, as in the general case of CSP.

To discuss CSP in the context of affine lumping, some additional notation is necessary. Using the notation of Ben Israel and Greville [1], denote by

$$Q_{k,n} = \{(i_1, i_2, \dots, i_k) : 1 \leq i_1 < i_2 < \dots < i_k \leq n\} \quad (11)$$

the set of increasing sequences of k elements from the set $\{1, \dots, n\}$ for given integers $0 < k \leq n$. Also, for a given matrix $\mathbf{M} \in \mathbb{R}^{m \times n}$, and index sets $I \in Q_{p,m}$ and $J \in Q_{q,n}$, let the $p \times n$ submatrix \mathbf{M}_{I*} be the matrix whose elements are m_{ij} for $i \in I$ and $j \in \{1, \dots, n\}$ and let the $m \times q$ submatrix \mathbf{M}_{*J} be the matrix whose elements are m_{ij} for $i \in \{1, \dots, m\}$ and $j \in J$.

Returning to CSP, let N_L be the number of active, slow CSP modes, and let $S \in Q_{N_L, N_S}$ be the set of indices of CSP basis vectors corresponding to the slow CSP modes. The matrices \mathbf{B}_{S*}^{CSP} and \mathbf{A}_{*S}^{CSP} take the roles of \mathbf{A} and \mathbf{D} in affine lumping and have the property that

$$\mathbf{B}_{S*}^{CSP} \mathbf{A}_{*S}^{CSP} = \mathbf{I}_{N_L}, \quad (12)$$

implying that \mathbf{A}_{*S}^{CSP} is a $\{1\}$ -inverse of \mathbf{B}_{S*}^{CSP} by rearranging (12) to yield Penrose's First Equation. Since \mathbf{A}_{*S}^{CSP} and \mathbf{B}_{S*}^{CSP} are both full rank matrices, they are $\{1, 2\}$ -inverses of each other, by Corollary 2.1 of [1]. If the approximate equations of state in [2] are treated as equalities, then CSP replaces the original model (1) with the approximate, reduced model

$$\dot{\mathbf{y}}(t) = \mathbf{A}_{*S}^{CSP} \mathbf{B}_{S*}^{CSP} \Gamma(\mathbf{y}(t)), \quad (13)$$

which resembles the reduced model lifted into the space of the original state variables, shown in (8). This result suggests that CSP fits the affine lumping formalism

without defining a lumping operation explicitly. In order to complete the definition of affine lumping from the CSP basis matrices, an appropriate origin of the lumping must be defined; in this case, set \mathbf{y}_0 equal to the current point in state space at which these particular CSP basis matrices are used to approximate the original model. Again, we postpone a more detailed comparison for future work.

The reaction invariants methods use a basis transformation to change the state variables from the state variables of the original model in (1) to state variables that can be classified as one of two types: reaction variants and reaction invariants. Reaction invariants are state variables that are constant with time, and reaction variants are state variables that change over time. Using the notation of Waller and Mäkilä [6], suppose that $\mathbf{v}(t) \in \mathbb{R}^{N_L}$ are new state variables representing the reaction invariants, and $\mathbf{w}(t) \in \mathbb{R}^{N_S - N_L}$ are new state variables representing the reaction variants. Suppose also that there exist matrices $\mathbf{P}^{RI} \in \mathbb{R}^{N_S \times (N_S - N_L)}$, $\mathbf{T}^{RI} \in \mathbb{R}^{N_S \times N_L}$, $\mathbf{D}^{RI} \in \mathbb{R}^{(N_S - N_L) \times N_S}$ and $\mathbf{L}^{RI} \in \mathbb{R}^{N_L \times N_S}$ such that the matrix $[\mathbf{P}^{RI} \ \mathbf{T}^{RI}]$ is nonsingular, and the equations

$$\mathbf{y}(t) = \begin{bmatrix} \mathbf{P}^{RI} & \mathbf{T}^{RI} \end{bmatrix} \begin{bmatrix} \mathbf{w}(t) \\ \mathbf{v}(t) \end{bmatrix}, \quad (14a)$$

$$\begin{bmatrix} \mathbf{D}^{RI} \\ \mathbf{L}^{RI} \end{bmatrix} = \begin{bmatrix} \mathbf{P}^{RI} & \mathbf{T}^{RI} \end{bmatrix}^{-1}, \quad (14b)$$

both hold. From (14b), it follows that $\mathbf{L}^{RI}\mathbf{T}^{RI} = \mathbf{I}_{N_L}$, and by Penrose's First Equation, \mathbf{T}^{RI} is a $\{1\}$ -inverse of \mathbf{L}^{RI} . Since the columns of the matrix $[\mathbf{P}^{RI} \ \mathbf{T}^{RI}]$ are linearly independent, \mathbf{L}^{RI} and \mathbf{T}^{RI} are both full rank matrices. Consequently, by Corollary 2.1 of [1], \mathbf{L}^{RI} and \mathbf{T}^{RI} are $\{1, 2\}$ -inverses, suggesting that \mathbf{L}^{RI} and \mathbf{T}^{RI} take the roles of the assembly matrix \mathbf{A} and disassembly matrix \mathbf{D} in an affine lumping scheme.

In addition, $\mathbf{w}(t)$ does not vary with time, so for given initial conditions of the detailed model (1), $\mathbf{w}(t)$ is fixed. Setting $\mathbf{A} = \mathbf{L}^{RI}$ and $\mathbf{y}_0 = \mathbf{P}^{RI}\mathbf{w}(0)$, we can use (2) to define an affine lumping from the matrices of the reaction invariants technique, and $(\mathbf{L}^{RI}, \mathbf{T}^{RI}, \mathbf{P}^{RI}\mathbf{w}(0))$ is an affine lumping. A more detailed comparison of affine lumping and reaction invariants will follow in future work.

IV. CONCLUSIONS AND FUTURE WORK

A formalism called affine lumping has been defined to facilitate the comparison of different model reduction techniques that attempt to reduce the number of state variables used to describe a chemically reacting system. In addition to defining affine lumping, conditions have been stated under which an affine lumping can be used to reconstruct exactly the solution of a detailed model from a reduced model. The model reduction techniques of species lumping by Li *et al.* [3], computational singular perturbation by Lam [2] and reaction invariants [6] have been shown to be affine lumpings, under certain assumptions.

To further develop this work, more detailed comparisons of the theory of affine lumping with the theory of

existing model reduction techniques should be conducted to get a better idea of the breadth of techniques that can be expressed using the ideas of projection and generalized inverses as a theoretical basis. In parallel, a technique to determine an error-controlled affine lumping could be developed. The idea behind error-controlled affine lumping would be to replace the condition under which the solution of a detailed model can be reconstructed from a reduced model exactly with conditions under which the solution of a detailed model can be reconstructed from a reduced model approximately with known error bounds. These error bounds could then be used in conjunction with additional information to determine the affine lumping that yields the reduced model with the fewest reduced state variables, subject to error bounds. Such a technique could then be compared with existing techniques for model reduction with (or without) error control in order to better assess the strengths and weaknesses of various model reduction methods.

ACKNOWLEDGMENTS

GMO would like to thank Joseph K. Scott, Dr. Ajay Selot and Mehmet Yunt for helpful discussions. He would also like to gratefully acknowledge support under a DOE CSGF fellowship provided under grant DE-FG02-97ER25308. Finally, he would like to thank Drs. Bert Debusschere and Habib N. Najm for their hospitality and for discussions about computational singular perturbation during a practicum at Sandia National Laboratory in Livermore, CA over Summer 2008. Financial support from the U.S. Department of Energy's Office of Basic Sciences, Division of Chemical Sciences, Geosciences and Biosciences through Grant DE-FG02-98ER14914 is gratefully acknowledged.

REFERENCES

- [1] A. Ben-Israel and T. N. E. Greville. *Generalized Inverses: Theory and applications*. Springer-Verlag, New York, 2nd edition, 2003.
- [2] S. H. Lam. Using CSP to understand complex chemical kinetics. *Combustion Science and Technology*, 89(5):375–404, 1993.
- [3] G. Li and H. Rabitz. A general analysis of exact lumping in chemical kinetics. *Chemical Engineering Science*, 44(6):1413–1430, 1989.
- [4] T. Lu and C. K. Law. Systematic approach to obtain analytic solutions of quasi steady state species in reduced mechanisms. *Journal of Physical Chemistry A*, 110:13202–13208, 2006.
- [5] S. Singh, J. M. Powers, and S. Paolucci. On slow manifolds of chemical reactive systems. *Journal of Chemical Physics*, 117(4):1482–1496, 2002.
- [6] K. V. Waller and P. M. Mäkilä. Chemical reaction invariants and variants and their use in reactor modeling, simulation, and control. *Industrial and Engineering Chemistry Process Design and Development*, 20:1–13, 1981.

Adaptive Model Reduction and the G-Scheme

S. Paolucci* and M. Valorani†

*University of Notre Dame, Notre Dame, IN, USA

†University of Rome “La Sapienza”, Rome, Italy

Abstract—The numerical solution of mathematical models for reaction systems in general, and reacting flows in particular, is a challenging task because of the simultaneous contribution of a wide range of time scales to the system dynamics. However, the dynamics can develop very slow and very fast time scales separated by a range of active time scales. We propose a numerical technique consisting of an algorithmic framework, named the *G-Scheme*, to achieve multi-scale adaptive model reduction along-with the integration of the differential equations (DEs). We assume that the dynamics is decomposed into active, slow, fast, and when applicable, invariant subspaces. Adjusting the active DEs dynamically during the time integration is the most significant feature of the *G-Scheme*, since the numerical integration is accomplished by solving a number of DEs typically much smaller than the dimension of the original problem. To demonstrate the effectiveness of the *G-Scheme*, we present results from an illustrative problem.

I. INTRODUCTION

Solutions of reaction systems in general are computationally very expensive because of the presence of a very large range of scales. However, to within an arbitrary but fixed accuracy, there are in general vary fast and very slow time scales whose contributions to the active dynamics is small. Recently, we proposed a new methodology [1] that exploits this dynamic behavior to design a numerical framework able to achieve adaptive reduction of the dynamical system based on accuracy requirements. As a result, the original problem not only becomes substantially smaller, but more importantly non-stiff. The frozen (slow) and near-equilibrium (fast) modes play crucial roles in defining the active (dynamic) subspace, and thus it is mandatory to account for their contributions. In this work, we provide an overview of the *G-Scheme* and present results of an illustrative low dimensional system to demonstrate the effectiveness of the method.

II. BASIC CONCEPTS

The present work deals with model reduction concepts that are used to develop a time accurate computational tool that is able to exploit, adaptively, opportunities for reduction from both fast/active and slow/active spectral gaps. [1] The class of multi-scale problems which can be efficiently addressed with the new framework is that of stiff problems characterized by fast time scales of dissipative nature. Operationally, the new framework is designed to deal with the same class of problems as those handled efficiently by BDF methods.

The proposed numerical technique consists of an algorithmic framework, that for convenience will be referred to as the *G-Scheme*, to achieve model reduction along-with the numerical integration of a set of differential

equations (DEs). The method is directly applicable to initial-value ordinary differential equations (ODEs), and by using the method of lines to partial differential equations (PDEs) as well. We describe the *G-Scheme* as a “framework”, since the scheme consists of a modular procedure, where several of its components can be replaced or improved, while the overall framework remains unchanged, and can be used in different ways to achieve different goals.

The rationale used in constructing the *G-Scheme* is as follows [1]. The construction of reduced models for a dynamical system whose asymptotic behavior might involve fixed equilibrium points, or nontrivial limit sets, such as limit cycles or chaotic attractors, is strictly related to the occurrence of a gap in the spectrum of its characteristic time scales (time-scale separation). A temporal gap separates fast modes relaxing towards a SIM from the slow modes that drive the system, whereas for systems possessing nontrivial invariant limit sets, the temporal dichotomy is between stable and unstable modes. In both cases, the most relevant asymptotic behavior of the system is confined to an invariant set which is attracting: the SIM or the limit attractor.

The characterization of the local structure of these invariant subspaces can be of great importance in the development of methods aimed at achieving a low-dimensional description of dynamical systems. The basic idea is that the invariant subspaces, ordered in a decreasing way with respect to their characteristic time scales, provide the most convenient and natural basis for describing the unstable/slow and stable/fast components of the dynamics. Consequently, model reduction can be achieved by filtering out the dynamically irrelevant degrees of freedom associated with the most stable (fast) components characterized by the most negative characteristic time scales.

Ideally, one would like to decompose the tangent space \mathcal{T}_x at any point $\mathbf{x} \in C \subset \mathbb{R}^N$ in N invariant subspaces, so that the dynamics within each invariant subspace is fully decoupled from all other invariant subspaces, and is associated with a single characteristic time scale. This goal is not easy to achieve. However, decomposing the tangent space in subspaces, not necessarily invariant, characterized by time scales of comparable magnitude is at the core of the *G-Scheme* [1]. We assume that the tangent space \mathcal{T}_x can be decomposed as the sum of four subspaces,

$$\mathcal{T}_x = \mathbb{E} \oplus \mathbb{H} \oplus \mathbb{A} \oplus \mathbb{T},$$

where the active subspace \mathbb{A} contains all the current

intermediate dynamic time scales, all scales faster and slower than the active ones are confined in the fast and slow subspaces \mathbb{T} and \mathbb{H} , respectively, and, \mathbb{E} is the linear subspace spanned by directions associated with invariants, if any exist.

At each state point \mathbf{x} corresponding to time t , the *G-Scheme* introduces a curvilinear frame of reference, defined by a set of orthonormal basis vectors with corresponding coordinates, attached to the decomposition of the tangent space in the four subspaces. At any time instant of the system evolution, the curvilinear coordinates are suitable (linear) combinations of the perturbations $\Delta\mathbf{x}$ of the original state vector \mathbf{x} about \mathbf{x} itself, which are assumed to be valid only within a time scale suitably defined. Thus, they can be thought of as “lumped” variables dynamically adjusting to the system’s evolution.

The evolution of the curvilinear coordinates associated with the subspace \mathbb{A} is described by $N_A = \dim(\mathbb{A}) \leq N$ ODEs, whereas the variation of the curvilinear coordinates associated with the subspaces \mathbb{T} and \mathbb{H} are accounted for by applying $N_T = \dim(\mathbb{T}) \geq 0$ and $N_H = \dim(\mathbb{H}) \geq 0$ algebraic corrections derived from asymptotics of the original ODEs. Note that if we have $N_E = \dim(\mathbb{E}) \geq 0$ invariants, they can be formally eliminated so that the dynamics is restricted to move in the subspace $\mathbb{H} \oplus \mathbb{A} \oplus \mathbb{T}$ that satisfies the invariants exactly. Adjusting the active ODEs dynamically during time integration is the most significant feature of the *G-Scheme*, because the numerical integration of the state vector $\mathbf{x} \in \mathbb{R}^N$ is obtained by solving a number of ODEs typically much smaller than N . The active ODEs evolve in \mathbb{A} , which is freed from fast scales, and thus they are non-stiff. They can be solved by resorting to any explicit time integration scheme (*e.g.*, ERK). When compared to a standard BDF implicit scheme for stiff problems, the *G-Scheme* offers the advantage of requiring the solution of $N_A \ll N$ explicit instead of N implicit ODEs, at the expense of identifying the time scales and computing the set of orthonormal basis vectors that define the curvilinear frame of reference.

A. Basis Vectors and Time Scales

Clearly, the success of the *G-Scheme* relies on the ability to identify a decomposition of \mathcal{T}_x which ensures minimal (ideally no) coupling among slow, fast, and active subspaces. The problem of finding a frame of reference yielding the maximal degree of fast/slow decoupling can be approached by resorting to the CSP refinements procedure [2]. In this work, we identify the set of basis vectors \mathbf{a}_i , defining the mapping of the change of frame of reference, with the right eigenvectors of the Jacobian matrix J of the vector field related to the problem of interest, with the dual vectors \mathbf{a}^j coinciding with the left eigenvectors of J . This yields a leading order approximation of the CSP vectors [3]. As estimate of the characteristic time scales, we consider the reciprocal of the eigenvalues, λ_i , of J . The ordering of the basis vectors is critical for proper decomposition. Here, we order the modes according to

the magnitude of the complex eigenvalues, that is

$$0 = |\lambda_1| = \dots = |\lambda_E| < |\lambda_{E+1}| < \dots < |\lambda_{H-1}| \ll |\lambda_H| < \dots < |\lambda_T| \ll |\lambda_{T+1}| < \dots < |\lambda_N|,$$

where

$$\begin{aligned} 0 = |\lambda_1| = \dots = |\lambda_E| & \quad \text{identify the time scales in } \mathbb{E}, \\ |\lambda_{E+1}| < \dots < |\lambda_{H-1}| & \quad \text{identify the time scales in } \mathbb{H}, \\ |\lambda_H| < \dots < |\lambda_T| & \quad \text{identify the time scales in } \mathbb{A}, \\ |\lambda_{T+1}| < \dots < |\lambda_N| & \quad \text{identify the time scales in } \mathbb{T}, \end{aligned}$$

with $N_E = E$, $N_H = H - E - 1$, $N_A = T - H + 1$, and $N_T = N - T$. Note that, because of this ordering, (possibly complex) eigenvalues with both negative and positive real parts can be found in \mathbb{H} and \mathbb{A} , whereas we expect the eigenvalues in \mathbb{T} to have dominant negative real parts. This is the distinguishing feature of the class of problems for which the *G-Scheme* is expected to perform efficiently. The ratios $\epsilon_T \equiv |\lambda_T/\lambda_{T+1}| < 1$ and $\epsilon_H \equiv |\lambda_{H-1}/\lambda_H| < 1$ are measures of the spectral gaps between active and fast subspaces, and slow and active subspaces, respectively. Since the *G-Scheme* approximates the contribution of the very slow and very fast time scales with asymptotic corrections, it is expected that its accuracy and efficiency will be higher for larger spectral gaps, that is for smaller values of ϵ_T and/or ϵ_H . The controlling (driving) time scale of the dynamics is given by the fastest of the (active) time scales present in \mathbb{A} , and will be of the order of $\tau_T = 1/|\lambda_T|$.

III. THE *G-Scheme*

Consider the Cauchy problem defined by a set of autonomous ODEs:

$$\frac{d\mathbf{x}(t)}{dt} = \mathbf{f}(\mathbf{x}(t)),$$

with $\mathbf{x} \in \mathbb{R}^N$, and $\mathbf{f} : E \subset \mathbb{R}^N \rightarrow \mathbb{R}^N$. We wish to find the numerical solution for $t \in (t_0, t_f]$ with given initial condition $\mathbf{x}(t_0) = \mathbf{x}_0$.

The state vector $\mathbf{x}(t)$ at time $t = t_n + \tau$, with $\tau \in \Omega \equiv (0, \Delta t] \subset \mathbb{R}$, where $\Delta t = (t_{n+1} - t_n)$, can always be expressed as the sum of the state vector $\mathbf{x}(t_n)$, for $n = 0, 1, 2, \dots$, and a perturbation vector $\Delta\mathbf{x}(\tau)$. We note that t_n is some fixed arbitrary time. The component-wise representation of the perturbation vector $\Delta\mathbf{x}(\tau)$ can be expressed in terms of curvilinear coordinates $\Delta\mathbf{x} = \Delta\xi^i \mathbf{a}_i = \Delta\xi_j \mathbf{a}^j$ related to the sets of orthonormal covariant and contravariant basis vectors \mathbf{a}_i and \mathbf{a}^j , respectively, here taken to correspond to the eigenbases of

$$J(\mathbf{x}(t)) \equiv \left[\frac{\partial \mathbf{f}}{\partial \mathbf{x}} \right]_{\mathbf{x}(t)}.$$

We take a curvilinear frame of reference that varies with time. If the system is autonomous, then the frame of reference depends only on the state of the system.

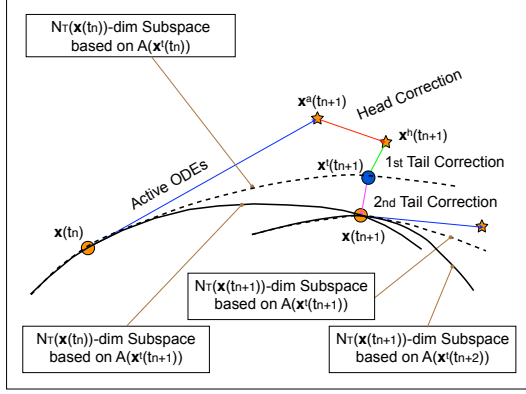


Fig. 1. The *G-Scheme* step-by-step starting from a given state $\mathbf{x}(t_n)$ on a subspace of dimension evaluated at t_n : orange stars denote intermediate new states before the application of head or tail corrections, the blue circle denotes the new state after head and tail corrections onto the subspace evaluated at t_n and where the basis vectors are subsequently updated to t_{n+1} , orange circle denotes the new state $\mathbf{x}(t_{n+1})$ and the location where the subspace dimension possibly changes. Note that in reality the orange circles are not exactly on the SIM; we're actually calculating the ASIM. We do not show both the SIM and ASIM so as not to make the figure unduly complex.

Subsequently, we can write

$$\begin{aligned} \mathbf{x}(t) &= \mathbf{x}_n + \Delta \mathbf{x}, \\ &= \mathbf{x}_n + A_e \Delta \xi^e + A_h \Delta \xi^h + A_a \Delta \xi^a + A_t \Delta \xi^t, \\ &= \mathbf{x}_n + \Delta \mathbf{x}^e + \Delta \mathbf{x}^h + \Delta \mathbf{x}^a + \Delta \mathbf{x}^t, \end{aligned}$$

where

$$B(\tau) \equiv \begin{bmatrix} \mathbf{a}^1(\tau) \\ \dots \\ \mathbf{a}^j(\tau) \\ \dots \\ \mathbf{a}^N(\tau) \end{bmatrix}, \quad \Delta \xi(\tau) \equiv \begin{bmatrix} \Delta \xi^1(\tau) \\ \dots \\ \Delta \xi^j(\tau) \\ \dots \\ \Delta \xi^N(\tau) \end{bmatrix},$$

where

$$A(\tau) B(\tau) = B(\tau) A(\tau) = I,$$

I being the identity matrix, Note that by construction, the contribution $\Delta \mathbf{x}^e$ of the invariant subspace is identically zero.

A. The Framework Step-by-Step

The *G-Scheme* is fully described in [1]. Here the algorithmic steps of the framework are summarized with reference to Fig. 1. We use indices $i = 1, \dots, N$, $a = H, \dots, T$, $h = E + 1, \dots, H - 1$, and $t = T + 1, \dots, N$.

We initialize the calculation by prescribing that $T(\mathbf{x}(t_0)) = N$, and compute $J(\mathbf{x}(t_0))$, $\lambda_i(t_0) = \lambda_i(\mathbf{x}(t_0))$, $A(t_0) = A(\mathbf{x}(t_0))$ and $B(t_0) = B(\mathbf{x}(t_0))$. Next, for each time interval t_n ($\tau = 0$), and for the state vector $\mathbf{x}(t_n)$, with $n = 0, 1, 2, \dots$, we proceed as follows:

1) Define the time step as:

$$\Delta t = \gamma / |\lambda_T(\mathbf{x}(t_n))|, \quad \gamma \leq 1; \quad (1)$$

2) Update time:

$$t_{n+1} = t_n + \Delta t; \quad (2)$$

3) Find $H(\mathbf{x}(t_n))$ since, as discussed in [1], it depends on Δt ;

4) Solve the set of non-stiff ODE's for $\tau \in \Omega = (0, \Delta t]$:

$$\begin{aligned} \frac{d\Delta \xi^a}{d\tau} &= B^a(t_n) \mathbf{f}(\mathbf{x}(t_n)) + A_a(t_n) \Delta \xi^a(\tau), \\ \Delta \xi^a(0) &= \mathbf{0}^a; \quad (3) \end{aligned}$$

5) Update the state vector:

$$\mathbf{x}^a(t_{n+1}) = \mathbf{x}(t_n) + A_a(t_n) \Delta \xi^a(\Delta t); \quad (4)$$

6) Apply the head correction:

$$\mathbf{x}^h(t_{n+1}) = \mathbf{x}^a(t_{n+1}) + A_h(t_n) \Delta \xi_{\text{FF}}^h(\Delta t); \quad (5)$$

where the head correction is estimated as:

$$\begin{aligned} \Delta \xi_{\text{FF}}^h(\Delta t) &= \Delta t B^h(t_n) \cdot \\ &\quad \left[I + \frac{1}{2} \Lambda_h^h(\mathbf{x}(t_n), t_n) \Delta t \right] \mathbf{f}(\mathbf{x}(t_n)) \quad (6) \end{aligned}$$

7) Apply the tail correction to project the solution onto the subspace obtained using the basis vectors found at t_n :

$$\mathbf{x}^t(t_{n+1}) = \mathbf{x}^h(t_{n+1}) + A_t(t_n) \Delta \xi_{\text{SIM}(t_n)}^t(\Delta t), \quad (7)$$

where the tail correction is estimated as:

$$\begin{aligned} \Delta \xi_{\text{SIM}(t_n)}^t(\Delta t) &= \\ &= - (B^t(t_n) J(\mathbf{x}(t_n)) A_t(t_n))^{-1} \cdot \\ &= B^t(t_n) \mathbf{f}(\mathbf{x}^h(t_n)); \quad (8) \end{aligned}$$

8) Update $J(\mathbf{x}^t(t_{n+1}))$, $\lambda_i(t_{n+1}) = \lambda_i(\mathbf{x}^t(t_{n+1}))$, and the set of new basis vectors $A(t_{n+1}) = A(\mathbf{x}^t(t_{n+1}))$ and $B(t_{n+1}) = B(\mathbf{x}^t(t_{n+1}))$;

9) Apply a bases rotation correction if necessary (*i.e.*, if the fast subspace changes) to find the state $\mathbf{x}(t_{n+1})$ by projecting $\mathbf{x}^t(t_{n+1})$ located on the manifold evaluated at t_n onto the manifold evaluated at t_{n+1} :

$$\mathbf{x}(t_{n+1}) = \mathbf{x}^t(t_{n+1}) + A(t_{n+1}) \Delta \xi_{\text{SIM}(t_{n+1})}(\Delta t); \quad (9)$$

where the basis rotation correction is estimated as:

$$\begin{aligned} \Delta \xi_{\text{SIM}(t_{n+1})}(\Delta t) &= \\ &= - (B^t(t_{n+1}) J(\mathbf{x}^t(t_{n+1})) A_t(t_{n+1}))^{-1} \cdot \\ &= B^t(t_{n+1}) \mathbf{f}(\mathbf{x}^t(t_{n+1})); \quad (10) \end{aligned}$$

10) Find $T(\mathbf{x}(t_{n+1}))$ as discussed in [1];

11) Update the counter: $n = n + 1$;

12) If $[t_{n+1} < t_f]$ go back to step (1).

The choice of the safety factor γ has an impact on the local error of the solution, given that $\Delta t = \gamma O(\tau_T^p)$ where p is the formal order of accuracy of the quadrature scheme adopted to integrate (3).

IV. RESULTS USING A PLANAR ODE MODEL

The reference solutions presented in this section are obtained with the module *NDSolve* in Mathematica[©] 6.0, the *Automatic* method of integration (by default an LSODA approach is used, switching between a non-stiff Adams method and a stiff Gear BDF method), a precision (or *rtol*) of 10^{-10} , and accuracy (or *atol*) of 10^{-14} . The calculations carried out with the *G-Scheme* use the explicit Runge-Kutta four-stage scheme (ERK4) to integrate the active dynamics, and, unless otherwise stated, we use *rtol* = 10^{-4} and *atol* = 10^{-13} in the threshold vector ϵ defined in [1]. We note that the present meanings of *rtol* and *atol* as used by *NDSolve* and the *G-Scheme* are somewhat different.

As a test featuring stiff explosive/dissipative nonlinear behavior, we use the Semenov model, which represents the dynamics of the first-order exothermal batch reaction $A \rightarrow B$ in a well-stirred jacketed reactor:

$$\frac{dy}{dt} = \varepsilon^{-1} f(y, z) \quad \text{and} \quad \frac{dz}{dt} = g(y, z),$$

where

$$f(y, z) = g(y, z) - \delta y \quad ; \quad g(y, z) = z \exp(y/(1 + \beta y)),$$

with parameter values $\beta = 0.21$, $\delta = 1.0$, and $\varepsilon = 10^{-3}$, and initial condition $\{y(0), z(0)\} = \{5, 2\}$. The bifurcation properties of this model have been studied in [4]. This model problem is aimed at illustrating the operating characteristics of the *G-Scheme*.

For this set of parameters the solution proceeds from the initial condition to a fixed point (equilibrium), but with a fairly complex dynamics as can be seen from the phase trajectory or from the time evolution of y shown in Fig. 2. The relative error and the size of the time step are shown as functions of time in Fig. 3. The total number of time steps necessary to obtain the solution using the *G-Scheme* is 63. In Figs. 4 we show the number of active modes N_A , and the values of the head (H) and tail (T) indices as functions of time. It is clear from the figure that most of the time it is only necessary to integrate one ODE; integration of both ODEs is only necessary the first time step, and near the sharp corners shown in Fig. 2. We also see from Fig. 4 that from right after the initial condition until after the first turn $H = T = 2$. This indicates that the dynamics is effectively one-dimensional and is controlled by the fast time-scale (explosive stage). Afterwards, with the exception of the period spent in negotiating the second turn, the dynamics is again effectively one-dimensional, but this time it is controlled by the slow time scale (dissipative stage) since $H = T = 1$.

To illustrate the internal mechanics of the *G-Scheme*, Fig. 5 shows the contributions of the slow (head) and fast (tail) corrections to the phase trajectory. Note that in this two-dimensional Semenov model, as long as we have one active mode, then at any time only a head or tail correction to active dynamics can be applied. We see from the figure that in the first turn only head corrections are necessary. However, from the figure we see that small

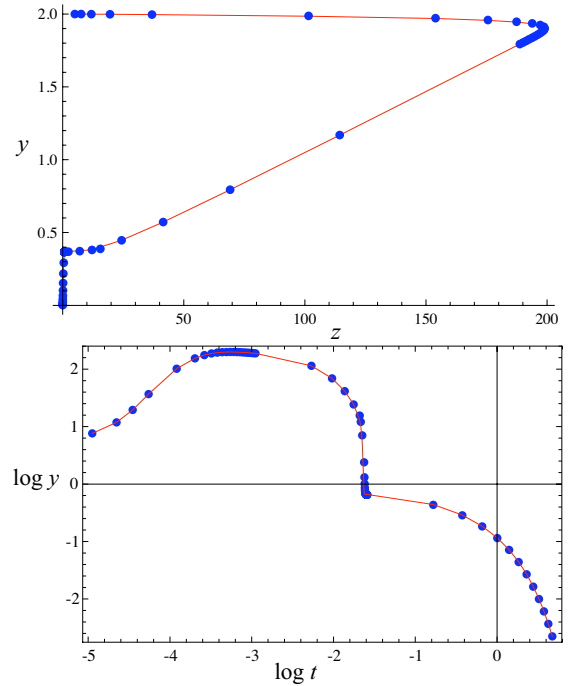


Fig. 2. Reference (line) and computed (points) trajectory in the (y, z) -plane and evolution of y .

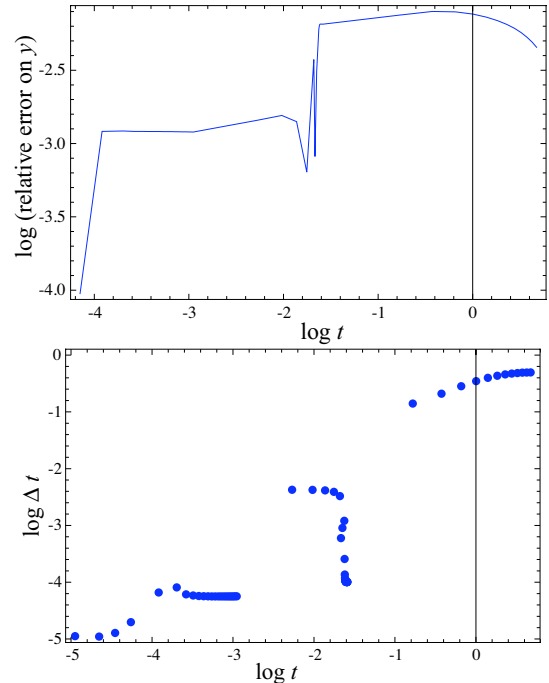


Fig. 3. Relative error on y and time step Δt as functions of time.

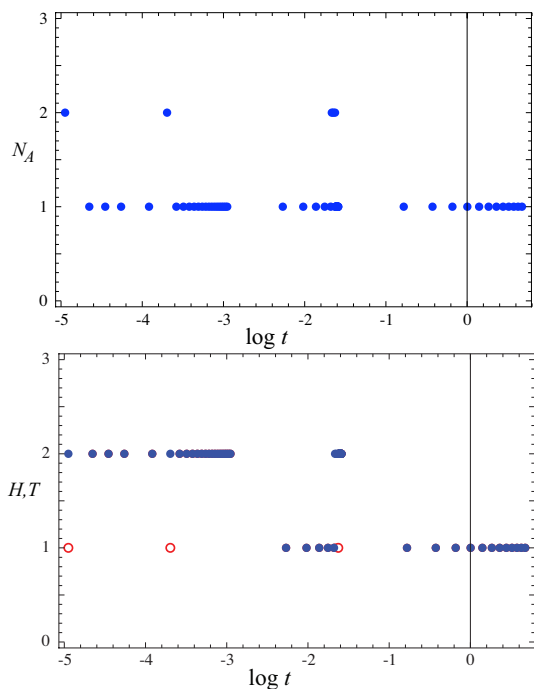


Fig. 4. Number of active modes N_A , and head H (hollow red circles) and tail T (solid blue circles) indices as functions of time.

head corrections are applied before the second turn, while tail corrections are necessary after the turn. In the figure, the blue arrows identify the state vector change due to the active time scales, the red/green arrows are parallel to the slow/fast direction and identify the state vector change due to the application of the head/tail correction, whereas the black arrows refer to the reference solution evaluated at the same time instants as the *G-Scheme* solution. The distance between the points of the red and black arrows or the green and black arrows is the error associated with the particular values of γ and $rtol$ used in this calculation.

V. CONCLUSION

We conclude by stressing that the main goal of this work is the presentation of the *G-Scheme* framework and the verification of its ability in achieving an adaptive model reduction. Regarding this aspect, the validation carried out by considering a range of test cases involving both linear and nonlinear behavior, both ODEs and PDEs, containing both simple and non trivial asymptotic dynamics, has successfully demonstrated the potential of the *G-Scheme* [1]. We already have successfully tested the *G-Scheme* in problems related to the kinetics of large hydrocarbons. In addition to addressing issues related to computational efficiency and error analysis, much work is still needed to translate this framework into a useful computational tool. We plan to make the package available to users and voluntary developers under the open-source paradigm in the near-future.

ACKNOWLEDGMENTS

MV acknowledges the support of the Italian Ministry of University and Research (MIUR) and the US Department

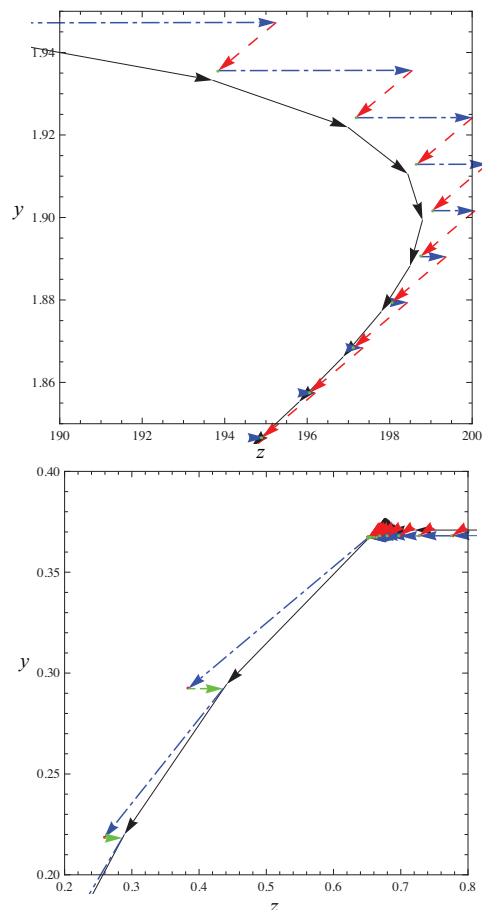


Fig. 5. Corrections to the state vector in the (y, z) -plane: reference (black line), active scales (short-long-dash blue line), head correction (long-dash red line), tail correction (short-dash green line).

of Energy, Office of Basic Energy Sciences, SciDAC Computational Chemistry Program. SP acknowledges the support of the University of Notre Dame and NSF (CBET-0650843) while working on the *G-Scheme* during his stay at the University of Rome.

REFERENCES

- [1] M.Valorani, S.Paolucci, The G-Scheme: A framework for multi-scale adaptive model reduction, In print, J.Comp.Phys. (2009).
- [2] S.H.Lam, D.A.Goussis, The CSP method for simplifying kinetics, International Journal of Chemical Kinetics 26 (1994) 461–486.
- [3] M.Valorani, D.A.Goussis, F.Creta, H.N.Najm, Higher order corrections in the approximation of low dimensional manifolds and the construction of simplified problems with the CSP method, J. Comput. Phys. 209 (2005) 754–786.
- [4] F.Creta, A.Adrover, S.Cerbelli, M.Valorani, M.Giona, Slow manifold structure in explosive kinetics. 1. bifurcations of points-at-infinity in prototypical models, J. Phys. Chem. A 110(50) (2006) 13447–13462.

Application of the *G-Scheme* to Reactive Systems

M. Valorani* and S. Paolucci†

* Sapienza, University of Rome, Rome, Italy

† University of Notre Dame Notre Dame, IN, USA

Abstract—The theory relevant to the *G-Scheme* framework is presented in a companion paper. Here, we will present results relevant to hydrocarbon kinetics, to a CSTR model involving CO/H₂ mixtures, and reactive systems described by PDEs to demonstrate the effectiveness of the method. We also present results obtained by combining a Wavelet Adaptive Multilevel Representation (WAMR) technique to define the spatial discretization of the model with the time integration carried out with the *G-Scheme*. This approach allows to obtain time accurate solutions of prescribed accuracy with a much lower number of space-time degrees of freedom.

I. INTRODUCTION

The next frontier in numerical simulation involves multi-physics, multi-scale, multi-disciplinary problems. Disciplines eager of computing power range from genetics, earth climate, biology, energy and combustion, micro/nano science and technology, among the most prominent. This demand cannot be simply accommodated by progress achieved in computer power alone, but requires breakthroughs in physical-mathematical modeling and numerical/algorithmic developments. Indeed, solutions of reaction systems in general are computationally very expensive because of the presence of a very large range of scales. However, to within an arbitrary but fixed accuracy, there are in general very fast and very slow time scales whose contributions to the active dynamics is negligible. Recently, we presented a new methodology [1] that exploits this circumstance to design a numerical framework able to achieve adaptive reduction of the dynamical system based on accuracy requirements. As a result, the original problem not only becomes substantially smaller, but more importantly non-stiff. The frozen (slow) and near-equilibrium (fast) modes play crucial roles in defining the active (dynamic) subspace, and thus it is mandatory to account for their contributions. To demonstrate the effectiveness of the method, we will present results relevant to three different reactive systems, namely a Continuously Stirred Tank Reactor (CSTR) with a CO/H₂ mixture, the auto-ignition of hydrocarbon/air mixtures in homogeneous systems, and a reaction/diffusion system featuring limit cycle behavior. The reaction/diffusion system is solved by combining a Wavelet Adaptive Multilevel Representation (WAMR) technique [2][3][4] to define the spatial discretization of the model with the time integration carried out with the *G-Scheme*.

II. BASIC CONCEPTS

The numerical technique proposed in [1], referred to as the *G-Scheme*, embodies both the model reduction and the subsequent numerical integration of the reduced set of Ordinary Differential Equations (ODEs). The *G-Scheme* exploits the circumstance that systems arising from large kinetic mechanisms contain a very large range of scales with the fastest scales having a dissipative nature. This property ensures that the actual dimension of the system becomes much smaller than the original size after a short initial transient period. This lower dimensional subspace, named Slow Invariant Manifold (SIM), is present if there exists a spectral gap of characteristic time scales that separates slow and fast components of the dissipative kinetic systems. In this case, the most relevant asymptotic behavior of the system is confined in the SIM or the limit attractor (for a system having nontrivial asymptotic kinetics), which is invariant and exponentially attracting. Consequently, model reduction can be achieved by filtering out the dynamically irrelevant degrees of freedom (irrelevancy is based on an accuracy requirement) associated with the fastest components characterized by the most negative characteristic time scales.

Ideally, one would like to decompose the tangent space \mathcal{T}_x at any point $\mathbf{x} \in C \subset \mathbb{R}^N$ in N invariant subspaces, so that the dynamics within each invariant subspace is fully decoupled from all other invariant subspaces, and is associated with a single characteristic time scale. This goal is not easy to achieve. However, decomposing the tangent space in subspaces, not necessarily invariant, characterized by time scales of comparable magnitude is at the core of the *G-Scheme*. We assume that the tangent space \mathcal{T}_x can be decomposed as the sum of four subspaces,

$$\mathcal{T}_x = \mathbb{E} \oplus \mathbb{H} \oplus \mathbb{A} \oplus \mathbb{T},$$

where the active subspace \mathbb{A} contains all the current intermediate dynamic time scales, all scales faster and slower than the active ones are confined in the fast and slow subspaces \mathbb{T} and \mathbb{H} , respectively, and, \mathbb{E} is the linear subspace spanned by directions associated with invariants, if any exist.

At each point \mathbf{x} of the Chemical Composition Space (CCS), the *G-Scheme* introduces a curvilinear frame of reference, defined by a set of ortho-normal basis vectors, with corresponding curvilinear coordinates, which is tied to the decomposition of the tangent space in the four

subspaces. The evolution of the curvilinear coordinates associated with the subspace \mathbb{A} is described by $N_A = \dim(\mathbb{A}) \leq N$ ODEs, whereas the variation of the curvilinear coordinates associated with the subspaces \mathbb{T} and \mathbb{H} are accounted for by applying $N_T = \dim(\mathbb{T}) \geq 0$ and $N_H = \dim(\mathbb{H}) \geq 0$ algebraic corrections derived from asymptotics of the original ODEs. Note that if we have $N_E = \dim(\mathbb{E}) \geq 0$ invariants, they can be formally eliminated so that the dynamics is restricted to move in the subspace $\mathbb{H} \oplus \mathbb{A} \oplus \mathbb{T}$ that satisfies the invariants exactly. Adjusting the active ODEs dynamically during time integration is the most significant feature of the *G-Scheme*, because the numerical integration of the state vector $\mathbf{x} \in \mathbb{R}^N$ is obtained by solving a number of ODEs typically much smaller than N . The active ODEs evolve in \mathbb{A} , which is freed from fast scales, and thus they are non-stiff. They can be solved by resorting to any explicit time integration scheme (e.g., ERK). When compared to a standard BDF implicit scheme for stiff problems, the *G-Scheme* offers the advantage of requiring the solution of N_A explicit instead of N implicit ODEs, at the expense of identifying the time scales and computing the set of orthonormal basis vectors that define the curvilinear frame of reference.

A. Basis Vectors and Time Scales

Clearly, the success of the *G-Scheme* relies on the ability to identify a decomposition of \mathcal{T}_x which ensures minimal (ideally no) coupling among slow, fast, and active time scales. The problem of finding a frame of reference yielding the maximal degree of fast/slow decoupling can be approached by resorting to the CSP refinements procedure [5]. In this work, we identify the set of basis vectors \mathbf{a}_i , defining the mapping of the change of frame of reference, with the right eigenvectors of the Jacobian matrix J of the vector field related to the kinetic problem of interest, with the dual vectors \mathbf{a}^j coinciding with the left eigenvectors of J . This yields a leading order approximation of the CSP vectors [6]. As estimate of the characteristic time scales, we consider the magnitude of the reciprocal of the eigenvalues, λ_i of J . The ordering of the basis vectors is critical for proper decomposition. Here, we order the modes according to the magnitude of the complex eigenvalues, that is

$$0 = |\lambda_1| = \dots = |\lambda_E| < |\lambda_{E+1}| \leq \dots \leq |\lambda_{H-1}| \ll \ll |\lambda_H| \leq \dots \leq |\lambda_T| \ll |\lambda_{T+1}| \leq \dots \leq |\lambda_N|,$$

where

$$\begin{aligned} 0 = |\lambda_1| = \dots = |\lambda_E| & \text{ identify the time scales in } \mathbb{E}, \\ |\lambda_{E+1}| \leq \dots \leq |\lambda_{H-1}| & \text{ identify the time scales in } \mathbb{H}, \\ |\lambda_H| \leq \dots \leq |\lambda_T| & \text{ identify the time scales in } \mathbb{A}, \\ |\lambda_{T+1}| \leq \dots \leq |\lambda_N| & \text{ identify the time scales in } \mathbb{T}. \end{aligned}$$

with $N_E = E$, $N_H = H - E - 1$, $N_A = T - H + 1$, and $N_T = N - T$. Note that, because of this ordering, (possibly complex) eigenvalues with both negative and positive real parts can be found in \mathbb{H} and \mathbb{A} , whereas we expect the eigenvalues in \mathbb{T} to have negative real

parts, since this is the distinguishing feature of the class of problems for which the *G-Scheme* is expected to perform efficiently. The ratios $\epsilon_T \equiv |\lambda_T/\lambda_{T+1}| < 1$ and $\epsilon_H \equiv |\lambda_{H-1}/\lambda_H| < 1$ are measures of the spectral gaps between active and fast subspaces, and slow and active subspaces, respectively. Since the *G-Scheme* approximates the contribution of the very slow and very fast time scales with asymptotic corrections, it is expected that its accuracy and efficiency will be higher for larger spectral gaps, that is for smaller values of ϵ_T and/or ϵ_H . The controlling (driving) time scale of the dynamics is given by the fastest of the (active) time scales present in \mathbb{A} , and will be of the order of $\tau_T = 1/|\lambda_T|$.

For the problems discussed below, the reference solutions are obtained with *DVODE* [7] set with a precision (or *rtol*) of 10^{-8} , and accuracy (or *atol*) of 10^{-14} . The calculations carried out with the *G-Scheme* use the explicit four-stage Runge-Kutta scheme (ERK4) to integrate the active dynamics, and, except where noted otherwise, *rtol* = 10^{-4} and *atol* = 10^{-14} are user-defined parameters defining the relative and absolute values, respectively, of the total variation of the state variable over the time interval. They are used to form a threshold vector $\varepsilon^j(\Delta t)$ defined as

$$\varepsilon^j(\Delta t) \equiv \text{rtol}^j |x^j(t_{n+1})| + \text{atol}^j,$$

which is used to identify the integer indices H and T that enter in the definition of the dimensions of the subspaces \mathbb{A} , \mathbb{H} , and \mathbb{T} .

III. CSTR MODEL

As a test model featuring complicated nonlinear behavior we consider the isobaric CSTR system at very low pressure involving CO/H₂ kinetics proposed by Brad *et al.* [8]. The kinetic mechanism involves 11 species and 33 reactions. The set of ODEs involves 11 rate equations and the energy conservation equation for the molar concentrations and temperature representing the state of the CSTR. The equations, the constants, as well as all other constitutive relations are the same as in [8]. The CSTR is an open system which possesses three invariants, one for each atomic species, with characteristic time scales equal to the residence time $t_R = 1$.

The dynamics of this system features different types of asymptotic behavior (fixed point, limit cycle, and chaotic attractor). Here we report results of the *G-Scheme* under the conditions involving limit cycle behavior, corresponding to the initial condition $\{p^0, T^0\} = \{14 \text{ torr}, 680 \text{ K}\}$. The temperature evolutions along the periodic orbit is shown in Fig. 1. Although we do not present additional details on the solution, over each cycle one can note a very fast ignition phase, where both T and HO₂ peak, followed by a relaxation phase, during which HO₂ is consumed, and lastly a new re-generation phase, during which HO₂ is produced, with the latter two phases occurring at nearly isothermal conditions. The relative error in T is below 1% (not shown), the maximum value being attained during the explosive stage, whereas the

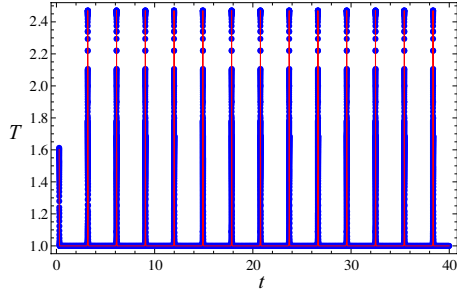


Fig. 1. Evolutions of T from *NDSolve* (line) and *G-Scheme* (points).

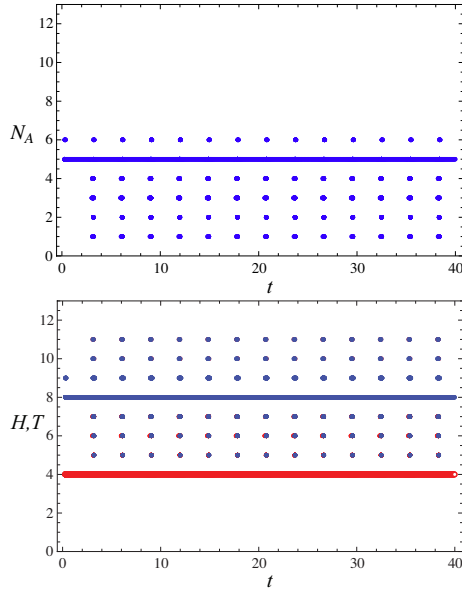


Fig. 2. Evolutions of number of active modes N_A (top), and H (red points) and T (blue points) indices (bottom).

error drops by several orders of magnitude during the relaxation and re-generation phases. The periodicity of the solution in Figs. 1 and of the number of active modes, N_A , shown in Fig. 2 demonstrates that the *G-Scheme* is able to provide repeatable sequences of the tangent space decomposition. The embedding dimension of the asymptotic dynamics of the CSTR model along the limit cycle, estimated as the $\max(N_A)$ over a period is 6, whereas the average number of active equations weighed with respect to time, is approximately 5. Figure 3 (top) shows the time evolution of the integration time step, from which it is apparent that small time steps ($\approx 10^{-5}$) are required for accuracy reasons in the ignition regime, and that large time steps ($\approx 10^{-1.5}$) can be taken during the relaxation and re-generation phases. Figures 2 (bottom) and 3 (bottom) show that during the explosive regime both the T and H indices increase in such a way that their difference decreases. Thus, although the driving time scale τ_T becomes small during the explosion stages because of the larger value of T , the degree of reduction increases, (N_A attains the value of unity). Instead, in-between two successive explosions, H and T attain constant values (4 and 8, respectively), so that N_A remains uniformly equal to 5. The analysis of the evolution of the time

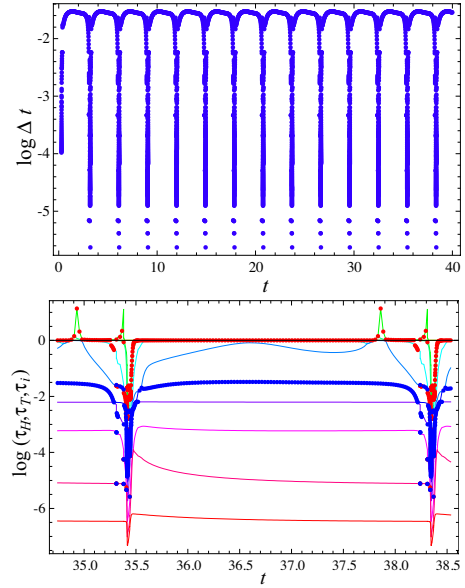


Fig. 3. Evolutions of integration time step (top), and the τ_H time-scale (red points), the τ_T time-scale (blue points), and all other time-scales (lines) (bottom).

rate of change of J demonstrates that the system has a nearly linear behavior (also confirmed in Fig. 3 (bottom) by the small changes in the time scales), whereas the nonlinearities are confined within the explosions.

IV. HYDROCARBON KINETICS

The *G-Scheme*'s performance is compared to that of the *DVODE* package, with reference to the auto-ignition process of stoichiometric mixtures of Methane/Air, Propane/Air, and n-Heptane/Air. The kinetic mechanisms considered are those of GRI 3.0 [9] (53 species; 325 reactions), Petersen *et al.* [10] (119 species; 665 reactions), and Curran *et al.* [11] (560 species; 2538 reactions), respectively. The initial temperature T_0 is 750 K and $p_0 = 1$ atm for all cases; they are chosen so as to yield a long ignition time which makes the auto-ignition very stiff¹. The ratio of the reaction time τ_{rea} to the ignition time τ_{ign} for the tests considered is reported in Table I. Indeed, the *G-Scheme* is designed so as to be cost effective when the problem is stiff. The typical accuracy level produced by the *G-Scheme* can be appreciated by examining Fig. 4. The figure displays a trajectory of the constant volume, adiabatic, auto-ignition of a stoichiometric Propane/Air mixture, in a two-dimensional cross-section of the 119-dimensional CCS, and an enlargement of the temperature evolution near the ignition time. The figure indicates that the state values (points) found by the *G-Scheme* follow the reference trajectory quite accurately, and that a small time shift error (≈ 0.01) develops in the prediction of the ignition time. The ratio of the average number of degrees of freedom, $\langle N_A \rangle$ (average number of active ODEs per iteration step), integrated by the *G-Scheme* to

¹Here we assume a measure of stiffness to be given by the ratio between the driving time scale during the ignition and the ignition time itself.

TABLE I

 $T_0 = 750 \text{ K}, p_0 = 1 \text{ ATM}, \text{ ALL CASES.}$

Mech	$\tau_{ign} [\text{s}]$	$\tau_{rea} [\text{s}]$	τ_{rea}/τ_{ign}	N	$\langle N_A \rangle$	$\langle N_A \rangle/N$
Methane	366.5	0.2	5.46×10^{-4}	53	3.78	0.07
Propane	16.38	0.05	3.05×10^{-3}	119	3.83	0.03
n-Heptane	2.93×10^{-1}	3.50×10^{-3}	1.19×10^{-2}	560	41.11	0.07

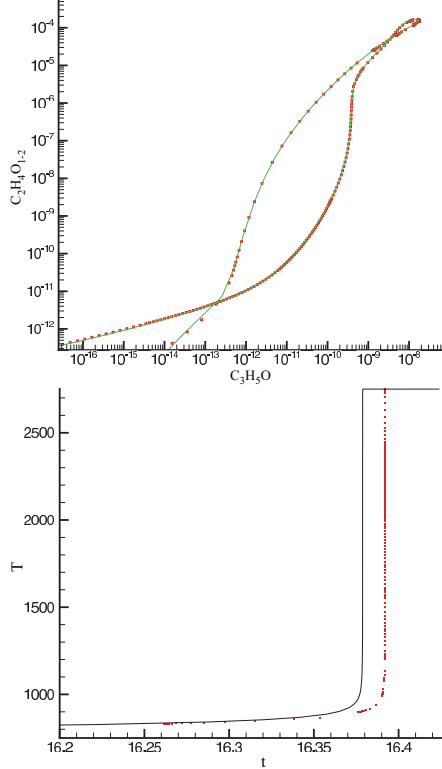


Fig. 4. Trajectory in CCS (left) and T evolution obtained for Propane/Air (right) with *DVODE* (solid line) and *G-Scheme* (red symbols).

the problem dimension, N (number of ODEs per iteration step), given in Table I, is a measure of the degree of (adaptive) reduction realized by the *G-Scheme*. Note that the degree of reduction is highly problem-dependent: for the cases studied, it is always below 10%. Figure 5 shows the time evolution of the active (N_A), slow (N_H), and fast (N_T) subspace dimensions. Note that N_A is initially equal to $N = 119$ (no reduction) and quickly drops below 5; later, it stays between 20 and 30 during the long nearly isothermal induction stage. It is noteworthy to observe that even during the explosion stage, when the temperature experiences the largest growth, N_A remains small because in this period most of the modes slower than the driving ones are essentially frozen, so H stays very close to T , and thus a small number of active modes are obtained. Finally, N_A attains a unit value while the kinetics approaches the equilibrium state at the slowest pace ($\tau_T = \tau_{E+1}$). Figure 6 shows the time evolution of the time scales corresponding to modes $H - 1$, H , T , $T + 1$, and N . The regions between τ_{H-1} and τ_H , and τ_T and τ_{T+1} represent the slow/fast gaps, respectively. During the induction stage and the equilibrium stage,

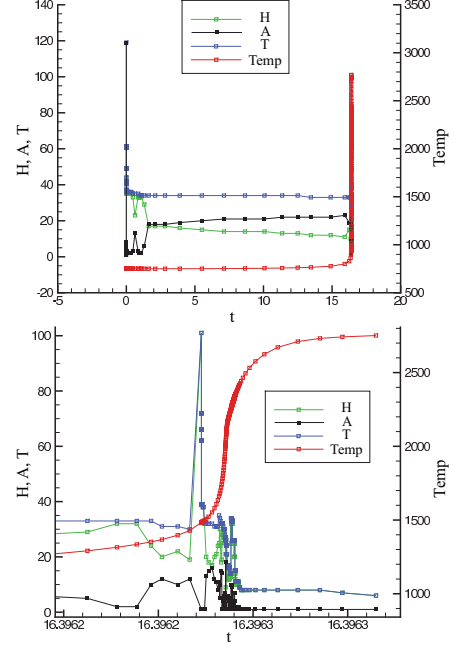


Fig. 5. Active N_A (black), slow N_H (green), and fast N_T (blue) subspace dimensions; induction stage (left); explosion stage (right).

the fast gap ϵ_T is well developed and clearly identifiable, whereas the slow gap ϵ_H is always rather narrow and mostly identified by the enforced error control. Note that during the explosion stage, the driving time scale attains its lowest value although the value of T keeps decreasing. This happens because the large growth in temperature induces a corresponding growth of the eigenvalues at all scales. Thus all active scales become smaller, albeit still confined in the range $H - T \approx 10-40$. The region between τ_{T+1} and τ_N represents the fast subspace. The ratio τ_H/τ_T is a measure of the stiffness of the reduced problem, which can be compared with the stiffness ratio of the original problem τ_{E+1}/τ_N , from which one can conclude that the reduced problem is significantly less stiff than the original. Finally, the time evolution of the integration time steps found by the *G-Scheme* and *DVODE* are shown in Fig. 7. Note that both histories follow a similar pattern with smaller steps during the initial transient and the explosion stage, and larger steps during the induction period and the approach to equilibrium.

V. REACTION-DIFFUSION MODEL

As a typical reaction-diffusion model exhibiting a rich dynamic structure, we consider the model proposed by Elezgaray and Arneodo [12] (EA model). The EA model

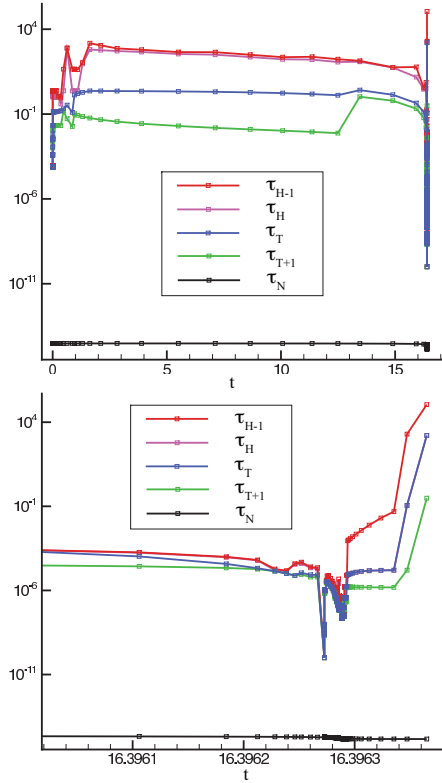


Fig. 6. Time scales and gaps: induction stage (top), explosion stage (bottom); τ_H (slowest active scale); τ_T (fastest active or driving scale); fastest scale τ_N (black). Note that $\epsilon_H = \tau_{H-1}/\tau_H$ and $\epsilon_T = \tau_T/\tau_{T+1}$ measure the slow/fast gaps, respectively.

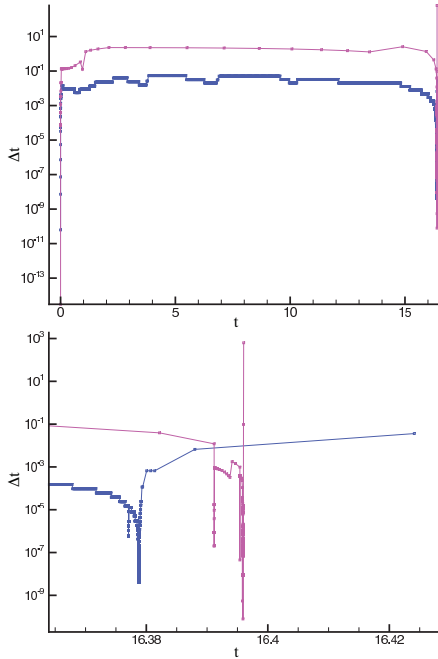


Fig. 7. Integration time step evolutions obtained with DVODE (blue) and *G-Scheme* (purple).

is a system of two coupled nonlinear PDEs:

$$\begin{aligned} \frac{\partial u}{\partial t} &= D \frac{\partial^2 u}{\partial x^2} + \epsilon^{-1} (v - (u^2 + u^3)), \\ \frac{\partial v}{\partial t} &= D \frac{\partial^2 v}{\partial x^2} - u + \alpha, \end{aligned}$$

in $(u(x, t), v(x, t))$, $(x, t) \in ([0, 1], [0, \infty))$, representing the concentrations of two chemical species with an isothermal explosive kinetics displaying intermittent bursting for some values of the parameters. Here D , α , and ϵ are positive parameters. The system is solved with initial conditions $u(x, 0) = v(x, 0) = 0$ for $x \in [0, 1]$, and boundary conditions $u(0, t) = u(1, t) = -2$ and $v(0, t) = v(1, t) = -4$ for $t > 0$. For small and large values of diffusion D , the system stabilizes onto ignited and extinguished steady states, respectively. Intermediate values of D correspond to operating conditions that allow competition between the tendency to ignition due to the nonlinear kinetics, and the extinguishing behavior at the boundaries. This induces complex oscillations and intermittent bursting in the center of the spatial domain. In this case, no invariants are present, hence $E = 0$. The calculations refer to $D = 0.032$, $\alpha = 0.01$, and $\epsilon = 0.01$ so as to obtain a limit cycle behavior.

A Wavelet Adaptive Multilevel Representation (WAMR) technique [2][3][4] is used to provide the spatial discretization of the model. We analyzed this same model problem in [1], where a uniform mesh discretization was used. The time integration is obtained by both the *G-Scheme* and DVODE, and the two solutions are compared. To demonstrate the accuracy of the *G-Scheme*, we plot in Fig. 8 the evolutions of u at the mid-point $x = 0.5$ and the corresponding phase trajectory's approach to the limit cycle as computed by DVODE and the *G-Scheme* with two different relative tolerances ($rtol = 10^{-3}$ and 10^{-4}). The convergence of the *G-Scheme* solutions to the reference orbit is apparent, whereas a small time shift develops after 20 time units. In Fig. 9, we report the time evolution of the number of wavelet collocation points, N , and of the active modes N_A found by the *G-Scheme* when using the two tolerances. The number of collocation points at one time instant defines the minimum number of spatial degrees of freedom required to achieve the prescribed spatial accuracy. Similarly the number of active modes N_A defines the minimum number of temporal degrees of freedom required to achieve the prescribed temporal accuracy. The number of collocation points N during one cycle undergoes a slow growth up to about 260, followed by a rapid decrease down to about 120. In contrast, the number of active modes N_A remains rather constant during the slow growth of N , and develops two peaks a little earlier than the drop in N . The largest N_A is approximately 150, and the smallest is 10. The integration time step, Δt , used by the *G-Scheme*, oscillates between 10^{-4} and 10^{-1} as can be seen from Fig. 9.

In the present calculations, the coarsest spatial scale consists of 16 uniformly spaced collocation points, and

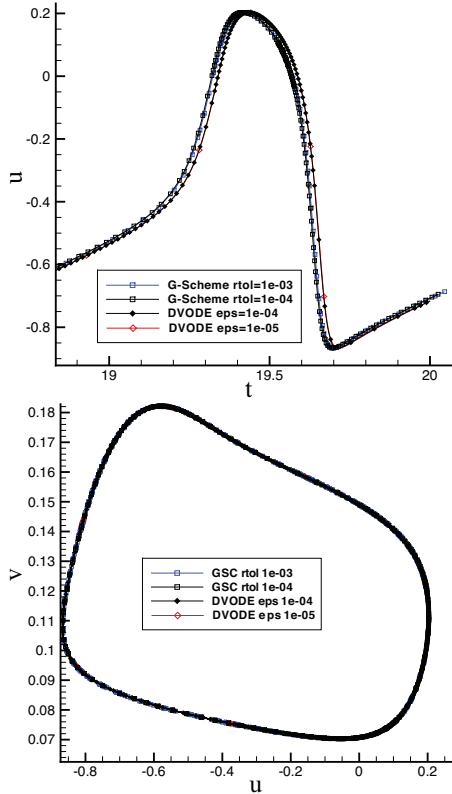


Fig. 8. Time evolution of u at $x = 0.5$ (left), and trajectories in the $(u-v)$ -plane, as computed by DVODE and G -Scheme with two different relative tolerances ($rtol = 10^{-3}$ and 10^{-4}).

the spatial resolution is adaptively increased up to a resolution equivalent to a uniform mesh of $16 \times 2^{10} = 16,384$ collocation points. With $rtol = 10^{-4}$, the number of integration steps required to reach 20 time units is 3,390, which is equivalent to a total number of space-time degrees of freedom (dof) of 111,083,520. It should be noted that in this problem we have two unknowns, u and v , for each spatial point. Instead, the dof required by the adaptive spatial discretization is 914,492, which implies a saving factor of 121.5. The actual number of equations solved by the G -Scheme with is 262,977, which involves a reduction by a factor of 3.5 with respect to using DVODE and of 422.4 with respect to using a uniform mesh of equivalent spatial accuracy. With $rtol = 10^{-3}$, the equivalent reduction factor is approximately 540. Thus, combining the adaptive wavelet technique with the G -Scheme allows to obtain a time accurate solution of prescribed accuracy with a much smaller number of space-time degrees of freedom.

VI. ACKNOWLEDGEMENTS

MV acknowledges the support of the Italian Ministry of University and Research (MIUR) and the US Department of Energy, Office of Basic Energy Sciences, SciDAC Computational Chemistry Program. SP acknowledges the support of the University of Notre Dame and NSF (CBET-0650843) while working on the G -Scheme during his

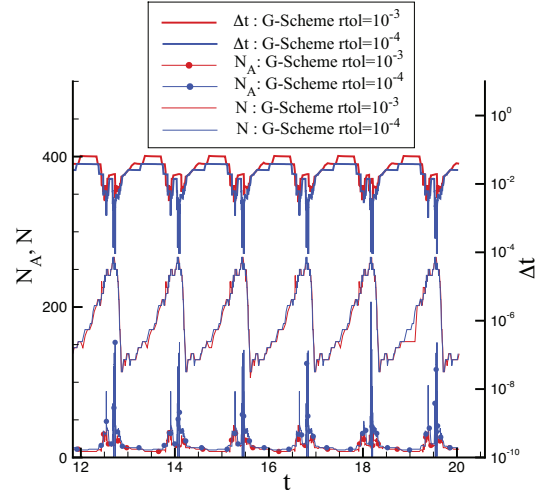


Fig. 9. Time evolution of the number of wavelet collocation points, N , and of the active modes, N_A , for two different relative tolerances ($rtol = 10^{-3}$ and 10^{-4}); Δt is the integration time step used by the G -Scheme.

stay at the University of Rome. We acknowledge the technical support of T. Grenga in the development of the FORTRAN porting of the G -Scheme, and of Z. Zicoski for the WAMR/ G -Scheme merging and calculations.

REFERENCES

- [1] M.Valorani, S.Paolucci, The G -Scheme: A framework for multi-scale adaptive model reduction, In print, J.Comp.Phys. (2009).
- [2] S.Singh, Y.Rastigejev, S.Paolucci, J.M.Powers, Viscous detonation in H_2-O_2-Ar using intrinsic low-dimensional manifolds and wavelet adaptive multilevel representation, Combust. Theory Modelling 5 (2001) 163–184.
- [3] Y.A.Rastigejev, S.Paolucci, Wavelet adaptive multiresolution representation: Applications to viscous multiscale flow simulations, Int. J. Wavelets Multiresolution and Information Processing 4 (2) (2006) 333–343.
- [4] Y.A.Rastigejev, S.Paolucci, Wavelet-based adaptive multiresolution computation of viscous reactive flows, Int. J. Num. Methods in Fluids 52 (7) (2006) 749–784.
- [5] S.H.Lam, D.A.Goussis, The CSP method for simplifying kinetics, International Journal of Chemical Kinetics 26 (1994) 461–486.
- [6] M.Valorani, D.A.Goussis, F.Creta, H.N.Najm, Higher order corrections in the approximation of low dimensional manifolds and the construction of simplified problems with the CSP method, J. Comput. Phys. 209 (2005) 754–786.
- [7] P.N.Brown, G.D.Byrne, A.C.Hindmarsh, VODE, A variable-coefficient ODE solver, SIAM Journal on Scientific and Statistical Computing 10 (5) (1989) 1038–1051.
- [8] R.B.Brad, A.S.Tomlin, M.Fairweather, J.F.Griffiths, The application of chemical reduction methods to a combustion system exhibiting complex dynamics, Proceedings of the Combustion Institute 31 (2007) 455–463.
- [9] G.P.Smith, D.M.Golden, M.Frenklach, N.W.Moriarty, B.Eiteneer, M.Goldenberg, C.T.Bowman, R.K.Hanson, S.Song, W. J. V.V.Lissianski, Q.Zhiwei, GRI mechanism for Methane/Air, Version 3.0. URL www.me.berkeley.edu/gri_mech/.
- [10] E.L.Petersen, D.M.Kalitan, S.Simmons, G.Bourque, H.J.Curran, J.M.Simmie, Methane/Propane oxidation at high pressures: Experimental and detailed chemical kinetic modeling, Proc. Combust. Inst 31 (2007) 447–454.
- [11] H.J.Curran, P.Gaffuri, W.J.Pitz, C.K.Westbrook, n -Heptane, detailed mechanism, Version 2 (2002). URL www-cms.llnl.gov/combustion/combustion2.html
- [12] J.Elezgaray, A.Arneodo, Crisis-induced intermittent bursting in reaction-diffusion chemical systems, Phys. Rev. Lett. 68 (1992) 714–717.

Sensitivity indices based on the *G-Scheme*

Mauro Valorani*, S. Paolucci†, Habib N. Najm‡

* Sapienza, University of Rome, Rome, Italy

† University of Notre Dame Notre Dame, IN, USA

‡ Sandia National Laboratories, Livermore, CA, USA

Abstract—A new set of importance indices based on the *G-Scheme* framework are presented. They provide information on the relative importance of selected processes in determining the slow, active, and fast dynamics of individual species/variables. These new indices are scaled measures of the (projected) contribution of each process over the currently driving time scale. This fact allows the introduction of *G-Scheme* sensitivity indices as well as of new importance indices.

I. INTRODUCTION

Lam carried out a CSP-based sensitivity analysis in [1] showing that “the most interesting sensitivity questions [in the analysis of a kinetic system] can be answered by interrogating the CSP data,” *i.e.*, participation and importance indices, and pointers to CSP radicals. In addition, he derived an estimate of the response of the kinetic system *in the slow time epoch* as induced by perturbations of the original vector field evaluated along the unperturbed trajectory.

Later, the CSP data were extensively and successfully used in the development of methods to generate simplified kinetic mechanisms, where the opportunity emerged to attribute the adjective “slow” to the original importance index, and at the same time, to introduce a new “fast” importance index [2]. These extended definitions of the indices were instrumental to assess both the relative importance of a specific process (reaction) in the slow dynamics of a major (non-CSP radical) species/variable through the corresponding slow importance index, and in the construction of a slow invariant manifold defining an equation of state for a CSP radical through the corresponding fast importance index.

Recently, we introduced a numerical technique consisting of an algorithmic framework [3], named the *G-Scheme*, to achieve multi-scale adaptive model reduction along-with the integration of the reduced differential equations (DEs). The dynamics is decomposed into active, slow, fast, and when applicable, invariant subspaces. The *G-Scheme* introduces a locally curvilinear frame of reference, defined by a set of orthonormal basis vectors with corresponding coordinates, attached to this decomposition. The evolution of the curvilinear coordinates associated with the active subspace is described by non-stiff DEs, whereas those associated with the slow and fast subspaces are accounted for by applying algebraic corrections derived from asymptotics of the original system. Adjusting the number of active DEs dynamically during the time integration is the most significant feature of the *G-Scheme*, since the numerical integration is accomplished

by solving a number of DEs typically much smaller than the dimension of the original problem, with corresponding saving in computational work.

Considering that the formulation of the set of ODEs integrated in the *G-Scheme* is obtained by performing a local perturbation of the system dynamics, in the present work we derive a new set of *local* indices, which provide estimates of the error affecting a specific species/variable associated with the removal/modification of a reaction/process contributing to the vector field. Moreover, we introduce sensitivity indices to assess the relative importance of a process to the slow, active, and fast dynamics according to the decomposition of the tangent space defined by the *G-Scheme*. Global information can be deduced by considering the infinity-norm or the time-weighted averages of these indices along selected trajectories.

II. THEORY

In the *G-Scheme* framework, a local change of frame of reference, defined by a set of orthonormal basis vectors $\{\mathbf{a}_i\}_{i=1}^N$ and their duals $\{\mathbf{b}^i\}_{i=1}^N$, is used to decompose the tangent space \mathcal{T}_x at $\mathbf{x}(t)$ as the direct sum of four basic subspaces¹ $\mathcal{T}_x = \mathbb{E} \oplus \mathbb{H} \oplus \mathbb{A} \oplus \mathbb{T}$. Under this mapping, the time evolution of the state vector $\mathbf{x} \in \mathbb{R}^N$ can be obtained as:

$$\begin{aligned} \mathbf{x}(t) &= \mathbf{x}_n + \Delta\mathbf{x}, \\ &= \mathbf{x}_n + \Delta\mathbf{x}^e + \Delta\mathbf{x}^h + \Delta\mathbf{x}^a + \Delta\mathbf{x}^t, \end{aligned} \quad (1)$$

where $\mathbf{x}_n = \mathbf{x}(t_n)$ is the state vector at time t_n , and $e = 1, E, h = E+1, H-1, a = H, T$, and $t = T+1, N$. The contributions of the four subspaces to the perturbation vector $\Delta\mathbf{x}$ over the currently active time scale² τ_T , is estimated, after local linearization, as:

$$\Delta\mathbf{x}^h \approx \tau_T A_h B^h \left(I + \frac{1}{2} \Lambda_h^h \tau_T \right) \mathbf{f}(\mathbf{x}_n), \quad (2)$$

$$\Delta\mathbf{x}^a \approx A_a B^a \left(\frac{e^{\Lambda_a^a \tau_T} - I}{\Lambda_a^a} \right) \mathbf{f}(\mathbf{x}_n), \quad (3)$$

$$\Delta\mathbf{x}^t \approx -A_t (B^t J A_t)^{-1} B^t \mathbf{f}(\mathbf{x}_n + \Delta\mathbf{x}^h + \Delta\mathbf{x}^a) \quad (4)$$

for the contribution of the slow, \mathbb{H} , active, \mathbb{A} , and fast, \mathbb{T} , subspaces respectively, where the matrices $A_{h,a,t}$ are formed by the column vectors $\mathbf{a}_{h,a,t}$, respectively, the matrices $B^{h,a,t}$ are formed by the row vectors $\mathbf{b}^{h,a,t}$, J is the Jacobian matrix of the vector field \mathbf{f} , and, to leading

¹The active subspace \mathbb{A} contains all intermediate, currently active (dynamic) time scales. All scales slower/faster than the active ones are confined to the subspaces \mathbb{H}/\mathbb{T} , and, if the system possesses invariants, \mathbb{E} is the subspace spanned by the directions associated with them.

² τ_T is the fastest of the time scales in the active subspace \mathbb{A} .

order, $\Lambda_i^i \approx B^i J A_i$. By construction, the contribution $\Delta \mathbf{x}^e$ of the invariant subspace is identically zero.

Eq. (4) provides an estimate of the asymptotic contribution of the fast scales, whose accuracy increases with the magnitude of the gap between the fastest of the active scales, τ_T , and the slowest of the fast scales, τ_{T+1} . In the *G-Scheme*, the contribution of the active scales is obtained by solving a set of nonlinear ODEs with an explicit solver (ERK4).

Now, let us consider the case of a vector field having the structure

$$\mathbf{f}(\mathbf{x}) = \sum_{k=1}^{\mathfrak{R}} \mathbf{f}_k(\mathbf{x}) = \sum_{k=1}^{\mathfrak{R}} \mathbf{S}_k r^k(\mathbf{x}) \quad (5)$$

where \mathbf{S}_k and $r^k(\mathbf{x})$ are the stoichiometric vector and the (forward/reverse) rate associated with the k -th reaction, $\mathfrak{R} = 2N_r$, and N_r is the number of reversible reactions.

It is worth recalling the definitions of the slow/fast CSP importance indices:

$$\begin{aligned} I_{s,k}^i &= \frac{C_{s,k}^i r^k}{\sum_{k'=1}^{\mathfrak{R}} |C_{s,k'}^i r^{k'}|}, & C_{s,k}^i &= \sum_s a_s^i (\mathbf{b}^s \cdot \mathbf{S}_k), \\ I_{r,k}^i &= \frac{C_{r,k}^i r^k}{\sum_{k'=1}^{\mathfrak{R}} |C_{r,k'}^i r^{k'}|}, & C_{r,k}^i &= \sum_r a_r^i (\mathbf{b}^r \cdot \mathbf{S}_k). \end{aligned} \quad (6)$$

where $s=1,T$, and $r=T+1,N$. These indices measure the (non-dimensional) relative importance of the *instantaneous* contribution of the k -th reaction to the slow/fast dynamics of the i -th species in the projected vector field $P_{s,r} \mathbf{f}(\mathbf{x}(t))$, with the projector matrices defined as $P_{s,r} = A_{s,r} B^{s,r}$.

Given the linearity of Eqs. (2-4) and (5), the contribution of the k -th reaction reads (no sum on k):

$$\begin{aligned} \Delta \mathbf{x}_k^h &\approx \tau_T A_h B^h \left(I + \frac{1}{2} \Lambda_h^h \tau_T \right) \mathbf{S}_k r^k(\mathbf{x}_n), \\ \Delta \mathbf{x}_k^a &\approx A_a B^a \left(\frac{e^{\tau_T \Lambda_a^a} - I}{\Lambda_a^a} \right) \mathbf{S}_k r^k(\mathbf{x}_n), \\ \Delta \mathbf{x}_k^t &\approx -A_t (B^t J A_t)^{-1} B^t \mathbf{S}_k r^k(\mathbf{x}_n). \end{aligned} \quad (7)$$

where all coefficients are evaluated at \mathbf{x}_n . The terms $\Delta \mathbf{x}_k^t$ in (7) are evaluated at \mathbf{x}_n since these terms are computed during the post-processing of numerical solutions generated by the G-Scheme, whereas $\Delta \mathbf{x}^t$ in (4) is evaluated at $\mathbf{x}_n + \Delta \mathbf{x}^h + \Delta \mathbf{x}^a$ since it is used to generate the solution during the numerical integration. The state vector \mathbf{x}_n lies by construction on a (N-T)-dimensional SIM, whereas in general $\mathbf{x}_n + \Delta \mathbf{x}^h + \Delta \mathbf{x}^a$ does not. As a consequence the sum of the non-zero terms $\Delta \mathbf{x}_k^t$ over all reactions at \mathbf{x}_n is approximately zero whereas $\Delta \mathbf{x}^t$ in (4) is usually different from zero³.

The terms $\Delta \mathbf{x}_k^{h,a,t}$ in (7) are approximations of the *integral over the driving time scale*, τ_T , of the projection

³The specific role of $\Delta \mathbf{x}^t$ in (4) consists in forcing the state vector to lie on a (N-T)-dimensional SIM.

of the k -th reaction over the slow (h), active (a), and fast (t) subspaces, that is:

$$\Delta \mathbf{x}_k^{h,a,t} \approx \int_{t_n}^{t_n + \tau_T} P_{h,a,t} \mathbf{f}_k(\mathbf{x}(t)) dt, \quad (8)$$

with the projector matrices now defined as $P_{h,a,t} = A_{h,a,t} B^{h,a,t}$.

The variation Δx_k^i of the i -th species/variable due to the action of the k -th reaction over the three subspaces can be estimated as:

$$\Delta x_k^i = \Delta x_k^{i,h} + \Delta x_k^{i,a} + \Delta x_k^{i,t}. \quad (9)$$

Summing over all reactions, $\sum_{k=1}^{\mathfrak{R}} \Delta x_k^i$, yields a good approximation of the actual state vector change over the time scale τ_T as computed by the *G-Scheme* integration. Thus, we can introduce an error index as:

$$\varepsilon^i := \left| \frac{\sum_{k=1}^{\mathfrak{R}} \Delta x_k^i}{x^i(t_n + \tau_T) - x^i(t_n)} - 1 \right|. \quad (10)$$

which measures the accuracy of the linearizations used to obtain Eqs. (7).

In the same spirit of the CSP indices, we can now introduce the following normalized indices (no sum on k):

$$G_{(h,a,t),k}^i = \frac{\Delta x_k^{i;h,a,t}}{\sum_{k'=1}^{\mathfrak{R}} |\Delta x_{k'}^{i;h,a,t}|}. \quad (11)$$

The indices $G_{(h,a,t),k}^i$ provide a non-dimensional measure of the *integrated contribution over the driving time scale*, τ_T , of the k -th reaction to the slow (h), active (a), and fast (t) dynamics of the i -th species/variable. By construction, $\sum_k G_{(h,a,t),k}^i = 1$. The main difference between this set of indices and the CSP-based importance indices (6) is the fact that the former are scaled measures of the (projected) contribution of each process to the change in the state vector over the currently driving scale, whereas the latter are scaled measures of the (projected) contribution of each process to the vector field at one time instant. This circumstance suggests using the estimates (7) to construct sensitivity indices as illustrated in the next section.

A. Sensitivity Indices

Let us now consider the case of applying a perturbation $\delta \mathbf{f}_k$ at time t_n to the original vector field \mathbf{f} having the structure

$$\mathbf{f} - \delta \mathbf{f}_k = \sum_{k'=1}^{\mathfrak{R}} \mathbf{S}_{k'} r^{k'} - \mathbf{S}_k \delta r^k. \quad (12)$$

That is, we perturb only the k -th reaction at time t_n . We now want to estimate the local response of the system, *i.e.* its local sensitivity, to such perturbation.

To leading order, the perturbation on the k -th reaction rate will be felt through Eqs. (7) only as a variation

$\delta\Delta\mathbf{x}_k^{h,a,t}$ of the corresponding $\Delta\mathbf{x}_k^{h,a,t}$ as follows (no sum on k):

$$\begin{aligned}\delta\Delta\mathbf{x}_k^h &\approx \tau_T A_h B^h \left(I + \frac{1}{2} \Lambda_h^h \tau_T \right) \mathbf{S}_k \delta r^k, \\ \delta\Delta\mathbf{x}_k^a &\approx A_a B^a \left(\frac{e^{\tau_T \Lambda_a^a} - I}{\Lambda_a^a} \right) \mathbf{S}_k \delta r^k, \\ \delta\Delta\mathbf{x}_k^t &\approx -A_t (B^t J A_t)^{-1} B^t \mathbf{S}_k \delta r^k,\end{aligned}\quad (13)$$

where, again, all coefficients are evaluated at \mathbf{x}_n .

Lam [1] provides an estimate of the response of the kinetic system *in the slow time epoch* τ^T as induced by perturbations $\delta\mathbf{f}_k$ of the original vector field \mathbf{f} as follows (Eq. (54) of [1]):

$$\delta\eta^m \approx O\left(\sum_{m'=1}^M \tau_{m'}^m \delta f_k^{m'}\right), \quad m = T+1, \dots, N, \quad (14)$$

with

$$\delta\eta^m := \mathbf{b}^m \cdot \delta\mathbf{x}, \quad \text{and} \quad \delta f_k^m := \mathbf{b}^m \cdot \delta\mathbf{f}_k, \quad (15)$$

where $\delta\eta^m$ is the perturbation of the m -th fast curvilinear coordinate η^m induced by $\delta\mathbf{f}_k$, and \mathbf{b}^m is the m -th dual (fast) CSP vector. Inspection of Eq. (14) reveals that when the projection of the perturbation $\delta\mathbf{f}_k$ is orthogonal or nearly orthogonal to the m -th CSP vectors \mathbf{a}_m then $\delta\eta^m \approx 0$, *i.e.*, the system's dynamics are unaltered by this specific perturbation. As far as the order of magnitude of the remaining (active and slow) mode amplitude perturbations, Lam states that they can be similarly estimated (or computed), and leaves to the reader the exercise of deriving the explicit expressions.

The third expression in Eq. (13) is equivalent to Eq. (14), once the estimate $\delta\eta^m$ is mapped back to the perturbation vector⁴ $\delta\Delta\mathbf{x}$ by inverting the definition (15): $\delta\Delta\mathbf{x} = \mathbf{a}_m \delta\eta^m$, and considering that in our case $\tau_{m'}^m = (B^t J A_t)^{-1}$, for $m, m' = T+1, \dots, N$. The first two expressions in Eq. (13) are the explicit contributions of the perturbations due to the active and slow modes⁵.

If the perturbation of the k -th rate has the form $\delta r^k = \alpha^k r^k$ in Eq. (13); *e.g.*, if $\alpha^k = 1$, the k -th rate is zeroed out in Eq. (12).

The variation $\delta\Delta x_k^i$ of the i -th species/variable due to the action of the k -th perturbed rate over the three subspaces is estimated as:

$$\delta\Delta x_k^i = \delta\Delta x_k^{i,h} + \delta\Delta x_k^{i,a} + \delta\Delta x_k^{i,t}. \quad (16)$$

Thus, we introduce the error index

$$\epsilon_k^{i;h,a,t}(t) := \frac{|\delta\Delta x_k^{i,h,a,t}(t)|}{|x^i(t + \tau_T) - x^i(t)|} \quad (17)$$

which measures the contribution at time t of the k -th reaction to the perturbation of the i -th species/variable over the driving time scale and for the slow (h), active (a), fast (t) subspaces, respectively, and

$$\epsilon_k^i(t) := \epsilon_k^{i;h}(t) + \epsilon_k^{i;a}(t) + \epsilon_k^{i;t}(t) \quad (18)$$

⁴From Eq. (1), $\delta\mathbf{x} = \delta\Delta\mathbf{x}$.

⁵The ‘‘slow’’ (head) modes in the *G-Scheme* are equivalent to the ‘‘dormant’’ modes in Lam [1].

for the contribution over all subspaces.

Introducing the parameters $\Psi_k^{h,a,t}$ as

$$\Psi_k^{h,a,t} = \max_{i=1,N} \left\{ \frac{1}{T} \int_{t=0}^T \epsilon_k^{i;h,a,t}(t) dt \right\}, \quad (19)$$

allows us to rank the reactions from the most (largest $\Psi_k^{h,a,t}$) to the least (smallest $\Psi_k^{h,a,t}$) significant to the overall trajectory, and for the slow (h), active (a), fast (t) subspaces, respectively, whereas

$$\Psi_k = \max_{i=1,N} \left\{ \frac{1}{T} \int_{t=0}^T \epsilon_k^i(t) dt \right\} \quad (20)$$

for the contribution over all subspaces.

Using the estimates Eqs. (13) allows the evaluation of the logarithmic derivatives (local sensitivities) for each subspace as

$$\sigma_k^{h,a,t} := \frac{d \ln(\Delta\mathbf{x}^{h,a,t})}{d \ln(r^k)} = \frac{r^k}{\Delta\mathbf{x}^{h,a,t}} \frac{\delta\Delta\mathbf{x}_k^{h,a,t}}{\delta r^k}, \quad (21)$$

and the overall (due to all time scales) local sensitivities:

$$\sigma_k := \frac{d \ln(\Delta\mathbf{x})}{d \ln(r^k)} = \frac{r^k}{\Delta\mathbf{x}} \frac{\delta\Delta\mathbf{x}_k}{\delta r^k}, \quad (22)$$

where both $\Delta\mathbf{x}^{h,a,t}$ and $\Delta\mathbf{x}$ are given by the *G-Scheme* reference solution.

B. Projected vs. Unprojected Estimates

An estimate $\Delta\tilde{\mathbf{x}}_k$ of the changes in the state vector on the basis of the k -th unprojected contribution \mathbf{f}_k of the vector field over the time scale τ is given by:

$$\begin{aligned}\Delta\tilde{\mathbf{x}}_k &\approx \int_{t_n}^{t_n+\tau} \mathbf{f}_k(\mathbf{x}(t)) dt \approx \int_{t_n}^{t_n+\tau} (\mathbf{f}_k(\mathbf{x}_n) + J_{\mathbf{x}_n} \Delta\tilde{\mathbf{x}}_k) dt \\ &\approx \left(\frac{e^{J_{\mathbf{x}_n} \tau} - I}{J_{\mathbf{x}_n}} \right) \mathbf{f}_k(\mathbf{x}_n) \approx \tau \left(I + \frac{\tau}{2} J_{\mathbf{x}_n} \right) \mathbf{f}_k(\mathbf{x}_n).\end{aligned}\quad (23)$$

It is instructive to compare $\Delta\tilde{\mathbf{x}}_k$ with the estimate $\Delta\mathbf{x}_k$ found after projection of the term \mathbf{f}_k , Eqs. (7) and (2)-(4), as approximations of the actual value.

The estimate (23) is accurate only for time intervals τ of the order of the smallest scale τ_{min} contained in $J_{\mathbf{x}_n}$. Clearly, when $\tau_{min} \ll \tau_T$, Eq. (23) becomes inaccurate on the scale $\tau \approx \tau_T$, whereas Eqs. (2)-(4) become more accurate as the gap between τ_{min} and τ_T increases. Thus, for non-stiff problems Eq. (23) can be used safely, whereas Eqs. (2)-(4) ought to be used in stiff problems.

This conclusion might suggest that a set of (unprojected) indices defined on the basis of the (net) reaction rates as:

$$\omega_k^i = \frac{S_k^i(r_f^k - r_r^k)}{\sum_{k=1}^{\mathfrak{R}} |S_k^i(r_f^k - r_r^k)|}, \quad (24)$$

as in the DRG method [4], can be used safely for non-stiff problems, whereas the (projected) indices defined in (6) or (11) ought to be used in stiff problems.

III. AN EXAMPLE

To provide a simple illustration of the differences between the approximations of Eq. (2-4) and (23), we resort to two 3-dimensional linear models, constructed so as to have the real, negative eigenvalues $\text{diag}(\Lambda) = \{-\epsilon_T^{-1}, -1, -\epsilon_H\}$, where $\epsilon_T, \epsilon_H < 1$ represent the gaps between the active/fast, and active/slow subspaces. By construction, the driving time scale is $\tau_T = 1$. We next consider a diagonal system, Model I, defined by choosing a 3×3 identity matrix as the right eigenvector matrix A , and a fully coupled system, Model II, defined by choosing A as

$$A = \begin{pmatrix} -1.5 & 0.1 & -0.3 \\ 3. & 4. & 1. \\ -1. & -0.3 & 0.6 \end{pmatrix} \quad (25)$$

with the dual basis matrix $B = A^{-1}$. The linear model is given by

$$\begin{bmatrix} \delta y \\ \delta w \\ \delta z \end{bmatrix}' = A \begin{pmatrix} -\epsilon_T^{-1} & 0 & 0 \\ 0 & -1 & 0 \\ 0 & 0 & -\epsilon_H \end{pmatrix} B \begin{bmatrix} \delta y - \delta y_{ss} \\ \delta w - \delta w_{ss} \\ \delta z - \delta z_{ss} \end{bmatrix}, \quad (26)$$

with initial conditions $\delta y(0) = \delta y_0$, $\delta w(0) = \delta w_0$, $\delta z(0) = \delta z_0$, and $\delta y_{ss}, \delta w_{ss}, \delta z_{ss}$ the fixed point values approached at large times. For Model I, we set $\delta y_0 = \delta w_0 = \delta z_0 = 1$, and $\delta y_{ss} = 0.1, \delta w_{ss} = 0.2, \delta z_{ss} = 0.3$. For Model II, we set $\delta y_0 = \sum_{j=1}^3 A_j^1 \eta_0^j, \delta w_0 = \sum_{j=1}^3 A_j^2 \eta_0^j, \delta z_0 = \sum_{j=1}^3 A_j^3 \eta_0^j$, with $\eta_0 = (1, 1, 1)$ and $\delta y_{ss} = 0, \delta w_{ss} = 0, \delta z_{ss} = 0$.

These linear models mimic the (dissipative) dynamics of the state vector perturbations due to a perturbation of the vector field at any time t of the original trajectory $\mathbf{x}(t)$. Thus, we should verify whether both Eqs. (2-4) and Eq. (23) are able to approximate the value attained by the state vector, starting from the given initial conditions, after a time interval of the order of the active time scale ($O(1)$). To this end, we report in Figs. 1-4, the comparison of the perturbations δy , δw , and δz , computed by Eqs. (2-4) and (23). Note that each symbol corresponds to the state vector obtained using a different integration time step. The accuracy can be assessed by comparing the symbols with the solid lines, which trace the exact solutions. Although many dots are drawn on the figures, the only interesting comparisons refer to the time steps of order of 1, since we expect to evaluate Eqs. (2-4) and (23) for $\tau = \tau_T (= 1)$.

Figs. 1-2 relate to Model I whose dynamics is fully decoupled and each unknown decays with a single time scale: δy with the fast scale $\tau = \epsilon_T$, δw with the active scale $\tau = 1$, and δz with the slow scale $\tau = \epsilon_H^{-1}$. Fig. 1 shows that already for a relatively narrow gap ($\epsilon_T = \epsilon_H = 0.2$), Eqs. (2-4) at $\tau = 1$ provide an accurate approximation of the exact solution, whereas the time step of order 1 is too large for the first order approximation used in Eq. (23). This translates into an error which is the largest for the fastest time scales (δy) and progressively decreases for the slower time scales (δw and δz). In this latter case, increasing the accuracy requires the increase

of the order of the polynomial in Eq. (23), or reducing the time step to the order of ϵ_T . The comparison becomes even more favorable for Eqs. (13) for gaps wider than 0.2.

In contrast, narrowing the gaps by taking $\epsilon_T = \epsilon_H = 0.9$, Fig. 2 shows that the accuracy of Eqs. (2-4) is far from satisfactory for δy because at time $\tau = 1$ the (not so) fast process has not reached its asymptotic value. Indeed, when the gap narrows too much, the problem is neither stiff nor multi-scale, and therefore applying the asymptotic corrections (2-4), instead of using the regular perturbations (23) causes large errors.

Figs. 3-4 relate to Model II whose dynamics is fully-coupled and all unknowns decay with all time scales. In the stiff case, Fig. 3, the error incurred at $\tau = 1$ on the fast scale by Eq. (23) affects all the unknowns, whereas, at $\tau = 1$, Eqs. (2-4) provide accurate estimates for all three solution components.

Finally, Fig. 4 shows that in the non-stiff case, using Eq. (2-4), instead of the regular perturbation Eq. (23), causes large errors.

IV. CONCLUSIONS

We have presented estimates of the contribution of each process to the change in the state vector over the driving time scale, projected over the slow, \mathbb{H} , active, \mathbb{A} , and fast, \mathbb{T} subspaces, respectively, in the context of the *G-Scheme*. We used these estimates to define associated importance indices. The main difference between the new set of importance indices based on the *G-Scheme* framework and the CSP-based importance/participation indices is the fact that the former are scaled measures of the (projected) contribution of each process to the change in the state vector over the currently driving scale, whereas the latter are scaled measures of the (projected) contribution of each process to the vector field at one time instant. We used this construction to formulate local sensitivity coefficients. We compared the utility of this approach for estimation of the change in the state vector with an alternate approach that does not make use of projections onto a slow manifold. We illustrated the need for using the present projected approach in the case of a stiff problem, where fast processes are quickly exhausted. On the other hand, the unprojected approach is more appropriate when there is no time scale separation.

ACKNOWLEDGMENTS

This work was supported by the Italian Ministry of University and Research (MIUR) and the US Department of Energy, Office of Basic Energy Sciences, SciDAC Computational Chemistry Program. Sandia National Laboratories is a multiprogram laboratory operated by Sandia Corporation, a Lockheed Martin Company, for the United States Department of Energy under contract DE-AC04-94-AL85000. SP acknowledges the support from NSF (Award #0650843). We acknowledge the technical support of Ing. T. Grenga in the development of the work reported herein.

REFERENCES

- [1] S.H.Lam, Reduced Chemistry Modeling and Sensitivity Analysis, in: Lecture Notes for Aerothermochemistry for Hypersonic Technology, 1994-1995 Lecture Series Programme, Von Karman Institute for Fluid Dynamics, 1995, p. 3.
- [2] M.Valorani, F.Creta, D.A.Goussis, H.N.Najm, J.C.Lee, An automatic procedure for the simplification of chemical kinetics mechanisms based on CSP, Comb. and Flame 146 (Issues 1-2) (2006) 29-51.
- [3] M.Valorani, S.Paolucci, The G-Scheme: A framework for multi-scale adaptive model reduction, In print on J.Comp.Phys. (2009).
- [4] T.Lu, C.K.Law, A directed relation graph method for mechanism reduction, Proc. Comb. Inst. 30 (2005) 1333-1341.

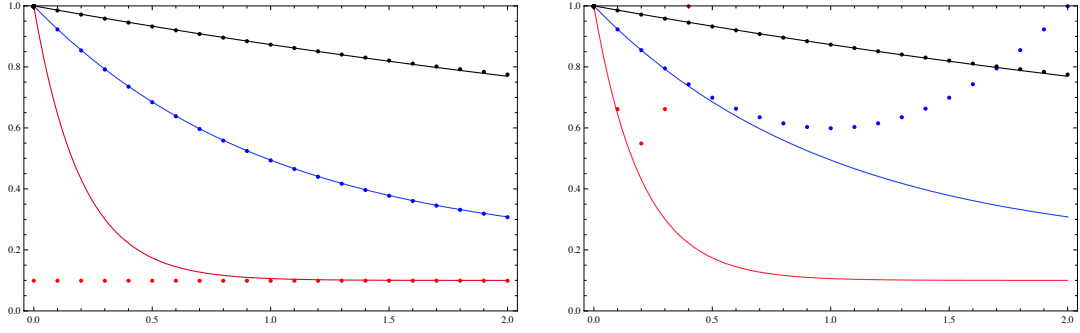


Fig. 1. Model I: $\epsilon_T = \epsilon_H = 0.2$ (stiff) and δy (red), δw (blue), δz (black). Lines are exact and symbols are computed from Eqs. (2)-(4) (left) and Eq. (23) (right).

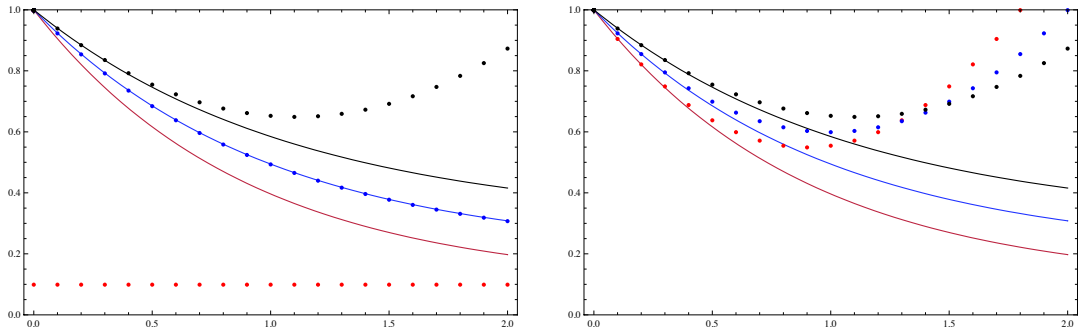


Fig. 2. Model I: $\epsilon_T = \epsilon_H = 0.9$ (non-stiff) and δy (red), δw (blue), δz (black). Lines are exact and symbols are computed from Eqs. (2)-(4) (left) and Eq. (23) (right).

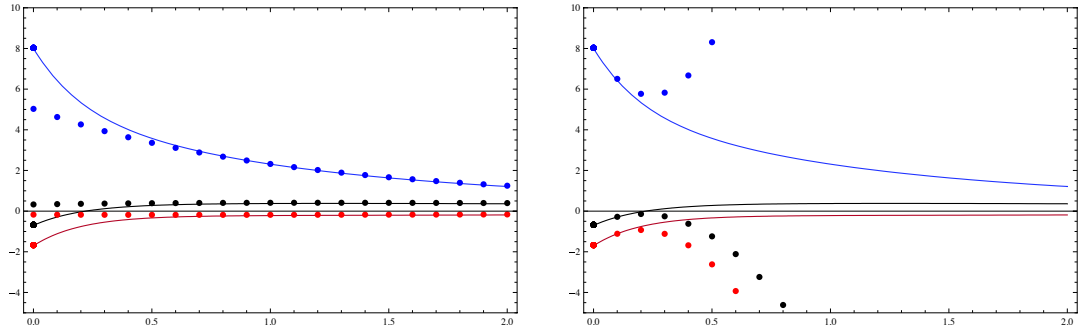


Fig. 3. Model II: $\epsilon_T = \epsilon_H = 0.2$ (stiff) and δy (red), δw (blue), δz (black). Lines are exact and symbols are computed from Eqs. (2)-(4) (left) and Eq. (23) (right).

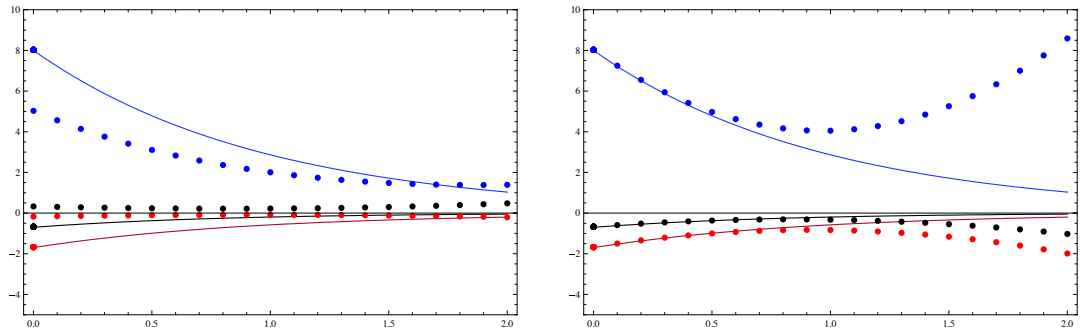


Fig. 4. Model II: $\epsilon_T = \epsilon_H = 0.9$ (non-stiff) and δy (red), δw (blue), δz (black). Lines are exact and symbols are computed from Eqs. (2)-(4) (left) and Eq. (23) (right).

Sensitivity Analysis, Model Reduction, and Circadian Oscillators

Linda Petzold
Department of Mechanical Engineering
Department of Computer Science
University of California Santa Barbara

Sensitivity analysis is a powerful tool that enables model development, parameter estimation, design optimization and experimental design in a wide range of areas of science and engineering. In this lecture we examine the forward and adjoint methods for sensitivity analysis applied to differential-algebraic equation systems and show how they can be extended to address some interesting problems in the study of the generation of circadian rhythms. Then we show how sensitivity analysis can be used in the development of reduced order models for biochemical systems that preserve important qualitative properties such as the phase response behavior of a circadian oscillation.

Dimension Reduction and Tabulation of Combustion Chemistry using ICE-PIC and ISAT

Stephen B. Pope*, Zhuyin Ren†, Varun Hiremath*

*Cornell University, Mechanical & Aerospace Engineering, Ithaca, NY 14853, USA

†ANSYS, Inc., 10 Cavendish Court, Lebanon, NH 03766, USA

Abstract—Progress is reported in the integration of two methodologies to enable the efficient application of realistic combustion chemistry in computational fluid dynamics. These methodologies are ICE-PIC (invariant constrained-equilibrium edge manifold using the pre-image curve method) for dimension reduction, and ISAT (*in situ* adaptive tabulation) for tabulation of the reduced system. New results are reported on the tangent vectors of the constrained-equilibrium and ICE manifolds, which are important quantities in ICE-PIC/ISAT. The test case of a partially-stirred reactor with methane combustion is used to demonstrate the accuracy and efficiency of the combined approach.

I. INTRODUCTION

Dimension reduction is essential to the use of detailed chemical kinetics in computations of combustion and many other reactive flows. Modern chemical mechanisms for hydrocarbon fuel may contain of order 1,000 species [1], and it is clearly impracticable to use this detailed information directly in multi-dimensional computational fluid dynamics (CFD) calculations. A combination of three approaches that enables the use of detailed chemical information consists of: (1) reduction to a skeletal mechanism [2], [3], [4] involving of order 100 species; (2) dimension reduction (DR) to reduce the number of degrees of freedom to of order ten; and (3) tabulation to significantly reduce the cost of expensive evaluations, e.g., the integration of ordinary differential equations (ODEs). In this work we consider the integration of two successful techniques, namely, the invariant constrained-equilibrium edge pre-image curve (ICE-PIC) method for dimension reduction [5], [6], [7], and *in situ* adaptive tabulation (ISAT) [8], [9].

In the next section we briefly review the ICE-PIC method as implemented in conjunction with ISAT. Then we derive expressions for the tangent vectors of the constrained-equilibrium manifold (CEM) and the ICE manifold, which are needed by ISAT. Finally, at the Workshop results will be given for the test case of a partially-stirred reactor, showing the accuracy of the dimension reduction and the efficiency gains achieved by ISAT.

II. THE ICE-PIC METHOD

We give here a succinct overview of the ICE-PIC method, as it is implemented in conjunction with ISAT. More details can be found in [5], [6], [7].

We consider a gas-phase mixture of n_s chemical species composed of n_e elements. The thermochemical state of the mixture (at a given position and time) is completely characterized by the pressure p , the species enthalpy h , and the n_s -vector \mathbf{z} of the specific moles of the species. To simplify the exposition, we take p and h to be given constants, and so the state is given by \mathbf{z} .

Due to chemical reactions, the composition evolves by

$$\frac{d\mathbf{z}}{dt} = \mathbf{S}(\mathbf{z}), \quad (1)$$

where \mathbf{S} is the n_s -vector of chemical production rates. The “reaction mapping” $\mathbf{R}(\mathbf{z}, t)$ is defined to be the solution to (1) after time t from the initial condition \mathbf{z} . And the mapping gradient $\mathbf{A}(\mathbf{z}, t)$ is the $n_s \times n_s$ matrix with components

$$A_{ij} = \partial R_i / \partial z_j. \quad (2)$$

In practice \mathbf{R} and \mathbf{A} are obtained together using the ODE solver DASAC [10].

In the ICE-PIC method, the species are decomposed as $\mathbf{z} = \{\mathbf{z}^r, \mathbf{z}^u\}$, where \mathbf{z}^r is an n_{rs} vector of “represented” species, and \mathbf{z}^u is an n_{us} -vector of “unrepresented” species (with $n_{rs} + n_{us} = n_s$ and $n_{rs} < n_s - n_e$). At the present stage of development of the methodology, the represented species are specified: ultimately, the methodology should identify the optimal specification. The “reduced representation” of the species used in ICE-PIC is $\mathbf{r} \equiv \{\mathbf{z}^r, \mathbf{z}^{u,e}\}$, where $\mathbf{z}^{u,e}$ is an n_e -vector giving the specific moles of the elements in the unrepresented species. Thus \mathbf{r} is a vector of length $n_r = n_{rs} + n_e$, and the dimensions of the system is reduced from n_s to $n_r < n_s$. This dimension reduction process can be written

$$\mathbf{r} = \mathbf{B}^T \mathbf{z}, \quad (3)$$

where \mathbf{B} is a known constant $n_s \times n_r$ matrix.

The fundamental issue in dimension reduction of combustion chemistry is “species reconstruction” that is, given \mathbf{r} , define an appropriate full composition \mathbf{z} . We denote by $\mathbf{z}^{ICE}(\mathbf{r})$ the species reconstruction given by the ICE-PIC method. We also consider $\mathbf{z}^{CE}(\mathbf{r})$ which is the constrained-equilibrium (maximum-entropy) composition, as used in the rate-controlled constrained equilibrium method (RCCE, [11], [12], [13]). This is readily computed using the constrained-equilibrium code CEQ [14].

In the n_r -dimensional reduced space, the “realizable region” is the convex polytope in which each component of \mathbf{r} is non-negative. Its boundary consists of at most n_r facets on which one component of \mathbf{r} is zero. The “constrained equilibrium edge” is defined as $\mathbf{z}^{CE}(\mathbf{r})$ for all \mathbf{r} on the boundary. The ICE manifold is defined as $\mathbf{R}(\mathbf{z}^{CE}(\mathbf{r}), t)$ for all \mathbf{r} on the boundary and all $t \geq 0$. Thus the ICE manifold is the trajectory-generated manifold originating from all the constrained equilibrium compositions on the boundary. Some important properties of the ICE manifold are:

- 1) existence: for all realizable \mathbf{r} there exists a manifold point $\mathbf{z}^{ICE}(\mathbf{r})$
- 2) invariance: the ICE manifold is invariant with respect to (1)
- 3) continuity: the ICE manifold is continuous
- 4) smoothness: the ICE manifold is piecewise smooth, and is the union of smooth manifolds generated by the facets
- 5) uniqueness: for a reasonable specification of the represented species, the manifold is not “folded”, so that for given \mathbf{r} there is a unique manifold point $\mathbf{z}^{ICE}(\mathbf{r})$.

Provided that the manifold is not folded, given a realizable value of \mathbf{r} , there is a unique “generating boundary point” \mathbf{r}^g , and time τ such that

$$\mathbf{z}^{ICE}(\mathbf{r}) = \mathbf{R}(\mathbf{z}^{CE}(\mathbf{r}^g), \tau). \quad (4)$$

The pre-image curve method is used to identify \mathbf{r}^g (given \mathbf{r}). Of course, consistency conditions are

$$\mathbf{B}^T \mathbf{z}^{ICE}(\mathbf{r}) = \mathbf{B}^T \mathbf{z}^{CE}(\mathbf{r}) = \mathbf{r}. \quad (5)$$

At the Workshop, the presentation will focus on an exposition of the ICE-PIC/ISAT methodology and on its performance for the test case described in Sec.V. In the next two sections, we present some new theoretical results which provide quite simple means of determining the tangent vectors of the constrained-equilibrium and ICE manifolds.

III. THE CEM TANGENT VECTORS

An important quantity in the ICE-PIC method is the $n_s \times n_r$ matrix \mathbf{T}^{CE} whose columns span the tangent space of the CE manifold, and which relates infinitesimal changes in \mathbf{z}^{CE} to those in \mathbf{r} by

$$d\mathbf{z}^{CE} = \mathbf{T}^{CE} d\mathbf{r}. \quad (6)$$

We have obtained a new, simple expression for \mathbf{T}^{CE} . It is presented here for the case of fixed pressure and temperature, from which the corresponding result for fixed p and h is readily obtained.

For the case considered, the constrained equilibrium composition is given by [14]

$$\mathbf{z}^{CE} = \bar{N} \exp(-\tilde{\mathbf{g}} + \mathbf{B}\boldsymbol{\lambda}), \quad (7)$$

where $\bar{N} = \sum_{i=1}^{n_s} z_i^{CE}$ are the specific moles of all species; $\tilde{\mathbf{g}}$ are normalized Gibbs functions; and $\boldsymbol{\lambda}$ are constraint potentials (or Lagrange multipliers).

Considering infinitesimals, we obtain from (7)

$$d\mathbf{z}^{CE} = \mathbf{z}^{CE} d \ln(\bar{N}) + \mathbf{ZB}d\boldsymbol{\lambda}, \quad (8)$$

where \mathbf{Z} is the diagonal matrix formed from \mathbf{z}^{CE} . Summing (8) over all the species leads to the constraint

$$0 = \mathbf{z}^T \mathbf{B}d\boldsymbol{\lambda} = \mathbf{r}^T d\boldsymbol{\lambda}. \quad (9)$$

Equation (8) can be re-expressed as

$$d\mathbf{z}^{CE} = \mathbf{M}d\hat{\boldsymbol{\lambda}}, \quad (10)$$

with

$$d\hat{\boldsymbol{\lambda}} \equiv d\boldsymbol{\lambda} + \frac{\mathbf{r}d\bar{N}}{|\mathbf{r}|^2 \bar{N}}, \quad (11)$$

and

$$\mathbf{M} \equiv \mathbf{z}\mathbf{r}^T + \mathbf{ZB} \left(\mathbf{I} - \frac{\mathbf{r}\mathbf{r}^T}{|\mathbf{r}|^2} \right). \quad (12)$$

We observe from (10) that the columns of \mathbf{M} span the tangent space. Let \mathbf{W} denote any $n_s \times n_r$ matrix with $\text{span}(\mathbf{W}) = \text{span}(\mathbf{M}) = \text{span}(\mathbf{T}^{CE})$. Then there exists a non-singular $n_r \times n_r$ matrix \mathbf{D} such that $\mathbf{T}^{CE} = \mathbf{W}\mathbf{D}$. From (5) we obtain

$$\mathbf{B}^T d\mathbf{z}^{CE} = d\mathbf{r} = \mathbf{B}^T \mathbf{T}^{CE} d\mathbf{r} = \mathbf{B}^T \mathbf{W}\mathbf{D}d\mathbf{r}, \quad (13)$$

and hence

$$\mathbf{B}^T \mathbf{T}^{CE} = \mathbf{I}, \quad (14)$$

$$\mathbf{D} = (\mathbf{B}^T \mathbf{W})^{-1}, \quad (15)$$

and finally

$$\mathbf{T}^{CE} = \mathbf{W}(\mathbf{B}^T \mathbf{W})^{-1}. \quad (16)$$

In practice \mathbf{W} is best taken as an orthonormal basis for $\text{span}(\mathbf{T}^{CE})$, obtained from the SVD or QR decomposition of \mathbf{M} .

It is interesting to observe that \mathbf{T}^{CE} is solely determined by \mathbf{z}^{CE} and \mathbf{B} , and does not otherwise depend on any thermodynamic information (such as p , T or $\tilde{\mathbf{g}}$).

IV. THE ICE MANIFOLD TANGENT VECTORS

Also important in combining ISAT with ICE-PIC is the matrix of ICE manifold tangent vectors \mathbf{T}^{ICE} defined such that

$$d\mathbf{z}^{ICE} = \mathbf{T}^{ICE} d\mathbf{r}. \quad (17)$$

We are considering now the relevant case of constant pressure and enthalpy, so that (6) and (17) are at fixed p and h . (This implies a re-definition of \mathbf{T}^{CE} .)

From (4), considering infinitesimal changes $d\mathbf{r}^g$ and $d\tau$, we have correspondingly

$$d\mathbf{z}^{CE} = \mathbf{T}^{CE} d\mathbf{r}^g, \quad (18)$$

and

$$d\mathbf{z}^{ICE} = \mathbf{A}(\mathbf{z}^g, \tau) \mathbf{T}^{CE}(\mathbf{r}^g) d\mathbf{r}^g + \mathbf{S}(\mathbf{z}^{ICE}) d\tau. \quad (19)$$

Let k denote the index of the component of \mathbf{r}^g which is zero on the boundary facet, i.e. $r_k^g = 0$. Since we require $\mathbf{r}^g + d\mathbf{r}^g$ to be on the boundary, it follows that dr_k^g is zero. This consideration and (19) show that the tangent space of the ICE manifold is spanned by $\mathbf{S}(\mathbf{z}^{ICE})$ and

the $n_r - 1$ vectors obtained from \mathbf{AT}^{CE} , with the k -th column omitted. Then, by the same argument that leads to (16), we have

$$\mathbf{T}^{ICE} = \hat{\mathbf{W}}(\mathbf{B}^T \hat{\mathbf{W}})^{-1}, \quad (20)$$

where $\hat{\mathbf{W}}$ is an $n_s \times n_r$ matrix (obtained from \mathbf{S} and \mathbf{AT}^{CE}) which spans the ICE manifold tangent space.

V. RESULTS

At the Workshop, results will be presented for the test case of a partially-stirred reactor (PaSR) with methane combustion [9]. The results quantify the dimension reduction errors in the ICE-PIC and RCCE as functions of the number of represented variable, n_r . Also, the efficiency of the ISAT implementation is characterized in terms of table size and retrieve time.

VI. CONCLUSIONS

The combination of ICE-PIC and ISAT offers accurate dimension reduction and efficient tabulation. Advances have been made both in the theory (e.g., in the accurate and efficient evaluation of the tangent vectors) and in the computational implementation.

ACKNOWLEDGMENT

This work is supported by Department of Energy under Grant DE-FG02-90ER and the National Science Foundation under Grant CBET-0426787.

REFERENCES

- [1] C.K. Law, Proc. Combust. Inst. 31 (2007) 1-29.
- [2] T. Lu, C.K. Law, Proc. Combust. Inst. 30 (2005) 1333-1341.
- [3] P. Pepiot, H. Pitsch, Combust. Flame 154 (2008) 61-81.
- [4] T. Nagy, T. Turányi, Combust. Flame 156 (2009) 417-428.
- [5] Z. Ren, S.B. Pope, A. Vladimirovsky, J.M. Guckenheimer, J. Chem. Phys. 124 (2006) 114111.
- [6] Z. Ren, S.B. Pope, A. Vladimirovsky, J.M. Guckenheimer, Proc. Combust. Inst. 31 (2007) 473-481.
- [7] Z. Ren, S.B. Pope, J. Phys. Chem. A 111(34) (2007) 8464-8474.
- [8] S.B. Pope, Combust. Theory Modelling 1 (1997) 41-63.
- [9] L. Lu, S.B. Pope, J. Comput. Phys. 228 (2009) 361-386.
- [10] M. Caracotsios, W.E. Stewart, Comput. Chem. Eng. 9(4) (1985) 359-365.
- [11] J.C. Keck, D. Gillespie, Combust. Flame 17 (1971) 237-241.
- [12] J.C. Keck, Prog. Energy Combust. Sci. 16 (1990) 125-154.
- [13] Q. Tang, S.B. Pope, Proc. Combust. Inst. 29 (2002) 1411-1417.
- [14] S.B. Pope, Combust. Flame 139 (2004) 222-226.

Limitation and averaging for deterministic and stochastic biochemical reaction networks

Ovidiu Radulescu ^{*}, Alexander N. Gorban [†]

^{*}University of Rennes 1/Mathematics, Rennes, France

[†]University of Leicester/Mathematics, Leicester, UK

Abstract— We discuss model reduction of multiscale networks of biochemical reactions used in systems biology as models for cell physiology and pathology. For linear kinetic models, which appear as "pseudo-monomolecular" subsystems of the nonlinear reaction networks, we obtain a general reduction algorithm based on cycle averaging and surgery. The same algorithm, when applied to stochastic networks, allows to reduce simulation time by many orders of magnitude.

I. INTRODUCTION

Systems biology uses networks of biochemical reactions as paradigms for normal and pathologic cell functioning. In such models, the cell has several compartments (nucleus, cytosol, organelles, etc.) but each compartment is considered to be well stirred. Transport between compartments is possible. The models are usually medium size (tens to hundreds of reactions and species). Therefore, their simulation by ODE solvers is not really a problem even for stiff systems. However, biological models present specific difficulties. Thus, the reaction mechanism is most of the time hypothetical and finding parameter values is difficult. For such systems, we would like to have simple rules allowing us to understand why a model functions the way it does and which consequences have on dynamics the various modifications of the mechanism. Furthermore, one would like to know which aspects (for instance parameter values) of the model are essential and which are not. All these questions could be answered by computing reduced mechanisms. Another specificity of molecular systems in biology is their stochasticity. The law of large numbers does not apply in biology as it does in physics, where fluctuations existing at microscopic scale are wiped-out in the thermodynamic limit (except for critical and turbulent systems). Biological systems behave similarly to critical or turbulent physical systems: they have many fluctuating scales. Molecular species in small number are responsible for stochastic phenomena such as intermittence or bursting, occurring in protein production, random action potential firing, calcium signalling, etc.. In systems biology, stochastic modelling by Markov jump dynamics (Gillespie SSA algorithm [1]) represents a very time consuming industry. There are two solutions to this problem. The first one is similar to the one employed by stiff deterministic solvers: avoiding adaptatively, but blindly the individual simulation of reactions that repeat very frequently. The second solution, that we propose here is to pre-condition the system by

simplifying it to a less stiff model.

In this paper we present such a pre-conditioning algorithm that works equally well for deterministic and for stochastic models. This algorithm is based on nontrivial generalizations of limitation (whose "naive" versions are well-known for chains and acyclic networks) to hierarchies of cycles and on averaging.

II. ALGORITHMS

A. Linear submechanisms

There are two types of linear submechanisms: monomolecular networks and first order networks. The structure of monomolecular reaction networks can be completely defined by a simple digraph, in which vertices correspond to chemical species A_i , edges correspond to reactions $A_i \rightarrow A_j$ with rate constants $k_{ji} > 0$. For each vertex, A_i , a positive real variable c_i (concentration) is defined.

The deterministic kinetic equation is

$$\frac{dc_i}{dt} = \sum_j k_{ij}c_j - \left(\sum_j k_{ji}\right)c_i, \quad (1)$$

First order reaction networks include monomolecular networks as a particular case, and are characterized by a single substrate and by reaction rates that are proportional to the concentration of the substrate. First order reaction networks can contain reactions that are not monomolecular, such as $A \rightarrow A + B$, or $A \rightarrow B + C$. We shall restrict ourselves to pseudo-conservative first order reactions, ie reactions that do not change the total number of molecules in a given submechanism ($A \rightarrow A + B$ reactions are allowed, provided that B is external to the submechanism; similarly $A \rightarrow B + C$ reactions are allowed, provided that either B or C is external to the submechanism). With such constraints, the total number of molecules in the sub-mechanism is conserved and the kinetic equations are the same as (1). Degradation reactions can be studied in this framework by considering a special component (sink), that collects degraded molecules. Further release of the constraints is possible. For instance, the system can be opened by allowing constant (or slowly variable) production terms in Eq.(1). These terms will change the steady state, but will not influence the relaxation times of the system.

The algorithms described in the paper can be applied to linear sub-mechanisms of a non-linear network, given

fixed (or slowly changing) values of external inputs (boundaries). For instance, even in systems of binary reactions, one can define pseudo-monomolecular reactions when one of the substrates of the binary reaction is not changing (or changing slowly). This condition can be fulfilled if the substrate is in excess, for instance.

B. Dominant pathways by cycle surgery in deterministic networks

The idea of dominant subsystems in asymptotic analysis of dynamical systems is due to Newton and developed by Kruskal [6]. Complex regulatory networks in metabolism and signalling activate only a limited number of pathways in order to fulfill a given physiologic task. The set of active pathways can change for unusual stresses (such as exposure to a toxin) or in pathologic situations. The concept of dominant pathways could serve to explain such dynamic transitions. In [3] we have based the construction of dominant subsystems on a generalized limitation approach. This approach selects dominant pathways and produces simplified reaction mechanisms.

We consider total separation of the constants namely either $k_I \ll k'_I$ or $k'_I \ll k_I$ for all $I = ij, I' = i'j'$. In this case the dominant subsystem can be worked-out by cycle surgery [3]. The algorithm, justified by estimates for the eigenvalues and eigenvectors (inspired, but not fully covered by Gershgorin theorem) of the kinetic matrix [3], consists of three stages:

I. Constructing the auxiliary reaction network.

For each A_i , let us define κ_i as the maximal kinetic constant for reactions $A_i \rightarrow A_j$: $\kappa_i = \max_j \{k_{ji}\}$. For correspondent j we use the notation $\phi(i)$: $\phi(i) = \arg \max_j \{k_{ji}\}$.

An auxiliary reaction network \mathcal{W} is the set of reactions $A_i \rightarrow A_{\phi(i)}$ with kinetic constants κ_i . The correspondent kinetic equation is

$$\dot{c}_i = -\kappa_i c_i + \sum_{\phi(j)=i} \kappa_j c_j, \quad (2)$$

II Glueing cycles

In general, the auxiliary network \mathcal{V} has several cycles C_1, C_2, \dots with periods $\tau_1, \tau_2, \dots > 1$.

These cycles will be “glued” into points and all nodes in the cycle C_i , will be replaced by a single vertex A^i .

Reactions $A \rightarrow B$ exiting from cycles ($A \in C_i, B \in C_j, j \neq i$ or $B \in C_i$) are changed into $A^i \rightarrow B$ with the rate constant renormalization: let the cycle C^i be the following sequence of reactions $A_1 \rightarrow A_2 \rightarrow \dots \rightarrow A_{\tau_i} \rightarrow A_1$, and the reaction rate constant for $A_i \rightarrow A_{i+1}$ is k_i (k_{τ_i} for $A_{\tau_i} \rightarrow A_1$). For the limiting reaction of the cycle C_i we use notation $k_{\text{lim } i}$. If $A = A_j$ and k is the rate reaction for $A \rightarrow B$, then the new reaction $A^i \rightarrow B$ has the rate constant $k k_{\text{lim } i} / k_j$. This rate is obtained using quasi-stationary distribution for the cycle.

The new auxiliary network \mathcal{V}^1 is computed for the network of glued cycles. Then we decompose it into cycles, glue them, iterate until a acyclic network is obtained \mathcal{V}^n .

III Restoration of cycles

The dynamics of species inside glued cycles is lost after the previous step. A full multi-scale approximation (including relaxation inside cycles) can be obtained by cycle restoration. This is done starting from the acyclic auxiliary network \mathcal{V}^n back to \mathcal{V}^1 through the hierarchy of cycles. Each cycle is restored according to the following procedure:

For each glued cycle node A_i^m , node of \mathcal{V}^m ,

- Recall its nodes $A_{i1}^{m-1} \rightarrow A_{i2}^{m-1} \rightarrow \dots \rightarrow A_{i\tau_i}^{m-1} \rightarrow A_{i1}^{m-1}$; they form a cycle of length τ_i .
- Let us assume that the limiting step in A_i^m is $A_{i\tau_i}^{m-1} \rightarrow A_{i1}^{m-1}$
- Remove A_i^m from \mathcal{V}^m
- Add τ_i vertices $A_{i1}^{m-1}, A_{i2}^{m-1}, \dots, A_{i\tau_i}^{m-1}$ to \mathcal{V}^m
- Add to \mathcal{V}^m reactions $A_{i1}^{m-1} \rightarrow A_{i2}^{m-1} \rightarrow \dots \rightarrow A_{i\tau_i}^{m-1}$ (that are the cycle reactions without the limiting step) with correspondent constants from \mathcal{V}^{m-1}
- If there exists an outgoing reaction $A_i^m \rightarrow B$ in \mathcal{V}^m then we substitute it by the reaction $A_{i\tau_i}^{m-1} \rightarrow B$ with the same constant, i.e. outgoing reactions $A_i^m \rightarrow \dots$ are reattached to the heads of the limiting steps
- If there exists an incoming reaction in the form $B \rightarrow A_i^m$, find its prototype in \mathcal{V}^{m-1} and restore it in \mathcal{V}^m
- If in the initial \mathcal{V}^m there existed a “between-cycles” reaction $A_i^m \rightarrow A_j^m$ then we find the prototype in \mathcal{V}^{m-1} , $A \rightarrow B$, and substitute the reaction by $A_{i\tau_i}^{m-1} \rightarrow B$ with the same constant, as for $A_i^m \rightarrow A_j^m$ (again, the beginning of the arrow is reattached to the head of the limiting step in A_i^m)

C. Cycle averaging in stochastic linear chemical networks

The Markovian stochastic dynamics of a single molecule in a linear reaction network is given by the probability $p(j, t)$ that the molecule is in A_j at the time t . We can easily show that the master equation for $p(j, t)$ is the same as the deterministic kinetic equation (1). Considering only one molecule does not restrict generality because when several molecules are present in a linear network, these behave independently. Thus, the simplification method proposed for deterministic networks [3], [2] can be also applied to stochastic networks.

Simplified stochastic models will represent pre-conditioned models used in order to reduce simulation time. Instead of searching for a multiscale approximation, our purpose here is to find a reduced model that is computationally effective and which captures dynamics on time scales or order τ or slower. τ could be for instance the experimental time resolution.

In order to present the simplification algorithm let us use two simple examples.

First, let us consider a chain of molecular reactions $A_1 \rightarrow A_2 \rightarrow \dots \rightarrow A_m$. The reaction rate constant for $A_i \rightarrow A_{i+1}$ is k_i . All rate constants are considered well separated, i.e. either $k_i \ll k_j$ or $k_i \gg k_j$ for any $i \neq j$. The smallest rate constant in the chain is denoted by k_{lim} . If $k_{\text{lim}} \gg 1/\tau$ (rapid chain), then within the timescale τ all molecules A_1 are transformed into molecules A_m . We

can thus ignore the chain reactions and consider that the entire initial mass of the chain is in A_m . This is equivalent to considering the chain at quasi-stationarity because the steady state probability distribution of a chain is a Dirac delta measure localized at the end of the chain. However, if we do not simplify chains, then simulating them by Gillespie's SSA [1] will not be computationally expensive because the mass of the chain is transferred to the end of the chain A_m in a number of steps that is relatively small.

As a second example, let us consider the cycle C be the following sequence of mono-molecular reactions $A_1 \rightarrow A_2 \rightarrow \dots A_m \rightarrow A_1$. Let all rate constants be well separated and the smallest one be k_{lim} like before. We add to the cycle one branching reaction; this transforms A_j a component of the cycle into B a component exterior to the cycle. We consider the following distinct situations: (I) the branching reaction is $A_j \rightarrow B$ of rate constant k and $k \ll k_j$, (II) the branching reaction is $A_j \rightarrow B$ and $k \gg k_j$, (III) the branching reaction is $A_j \rightarrow A_j + B$, or (IV) the branching reaction is $A_j \rightarrow A_{j+1} + B$ of rate constant k_j . In the situation (I) the exit reaction is faster and dominates the cycling reaction $A_j \rightarrow A_{j+1}$. According to the rule for auxiliary networks in this case (that we call "broken" cycle) the cycle can be opened (by eliminating the cycling reaction $A_j \rightarrow A_{j+1}$) and the resulting multiscale dynamics is the one of a chain; we recover the previous example and in this case we can safely decide to do nothing. In the situation (II) the exit reaction is much slower than the cycling reaction. In this case the molecules inside the cycle have rapid transformations and the mass distribution inside the cycle can be considered to reach quasi-stationary distribution. As discussed in [4], [3], [2], the relaxation time of a cycle with separated constants is the inverse of the second slowest rate constant $k^{(2)} \gg k^{(1)} = k_{lim}$. To understand this, one should consider the two possible paths to equilibrate a cycle, one passing through the slowest step and the quicker one passing through the second slowest step: the quicker short-cuts the first one. Thus, a cycle can be considered quasi-stationary if $k^{(2)} \gg 1/\tau$. A non-averaged fast cycle could be computationally expensive in SSA, because a molecule can perform a huge number of steps along the cycle on the timescale τ . The corresponding condition involves the quasi-stationary flux (not the relaxation time) and reads $k^{(1)} \gg 1/\tau$.

From a quasi-stationary cycle, the mass is lost stochastically, but slowly by the branching reaction. The intensity of the loss process can be calculated by replacing X_j by its average with respect to the quasi-stationary distribution of the cycle. The average of X_j is $\bar{X}_j = N(t)k_{lim}/k_j$, where $N(t)$ is the total mass inside the cycle $N = \sum_{j=1}^m N_j$. We obtain the average intensity $\bar{\lambda} = k\bar{X}_j = N(t)kk_{lim}/k_j$. In the situations (III) or (IV) the average intensities of the branching reactions are $k\bar{X}_j = N(t)kk_{lim}/k_j$ and $k_j\bar{X}_j = N(t)k_{lim}$, respectively.

The result of the cycle averaging can be represented as a simplification of the mechanism (cycle glueing), applied only to non-broken cycles:

- "glue" the cycle into a single node C having the total mass N
- replace the exit reaction of the type i) $A_j \rightarrow B$ of rate constant k by a reaction $C \rightarrow B$ of effective constant $k' = kk_{lim}/k_j$.
- replace the reaction of the type ii) $A_j \rightarrow A_j + B$ of rate constant k by a reaction $C \rightarrow C + B$ of effective constant $k' = kk_{lim}/k_j$.
- replace the reaction of the type iii) $A_j \rightarrow A_{j+1} + B$ of rate constant k_j by a reaction $C \rightarrow C + B$ of effective constant $k' = k_{lim}$.

As a possible design rule, notice that, unless k_j is the limiting step in the cycle, one has $k_{lim}/k_j \ll 1$. Then, the average intensity of the exit reaction of the type i) or ii) is weak and could represent a source of intermittence in the system. This situation should be avoided for less noise in the system, or created when noise is wanted.

III. APPLICATIONS

A. NF κ B oscillations

The transcription factor NF- κ B is involved in a wide diversity of domains such as the immune and inflammatory responses, cell survival and apoptosis, cellular stress and neuro-degenerative diseases, cancer and development. NF- κ B is sequestered in the cytoplasm by inactivating proteins named I κ B. Upon signalling, I κ B molecules are phosphorylated by a kinase complex, then ubiquitinated, and finally degraded by the proteasomal complex. NF- κ B released from I κ B molecules is then transported to the nucleus to activate its target genes, among which its inhibitor I κ B. The produced I κ B enters the nucleus, binds to, back-translocates and re-sequester NF- κ B in the cytosol. This delayed negative feed-back is responsible for oscillations of NF- κ B activity.

The biochemical models for NF κ B signalling discussed in [2] contain linear sub-networks that were simplified using the algorithm described in sub-section IIA. After simplification, a mapping has been constructed between parameters of the initial model and the parameters of the simpler model. This mapping allowed us to find the critical parameters and to assess their influence on the capacity of the system to undergo sustained oscillations. Thus, many reactions are dominated and not critical. The precise values of their constants are not important for the dynamics, although their relative order matters. The details of this analysis can be found in [2].

B. Stochastic bursting of repressed operon

To illustrate reduction of stochastic models, we present here a new application.

Under strong repression, protein production from a bacterium operon undergoes stochastic bursting. The phenomenon has been modelled by [5], see Fig.1. In this model the bacterium is considered to be in exponential growth phase, increasing size and dividing normally. Cell growth is simulated by a linear increase of the volume in time. During replication the nuclear material doubles (variables D,D.R,DRNAP). At fission the nuclear material

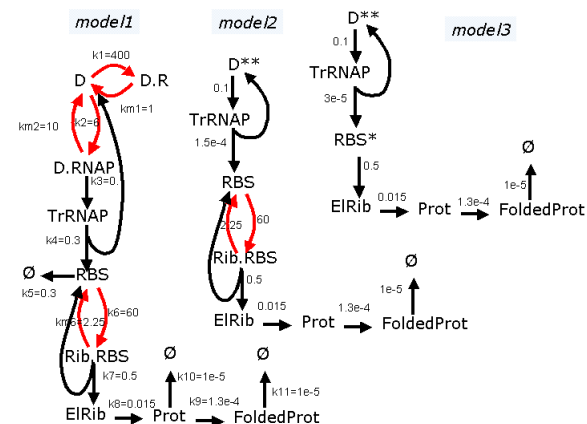


Fig. 1. Repressed operon models. The averaged cycles are in red.

is halved and all other components are divided among daughter cells according to a binomial distribution.

The cycle averaging procedure can be applied three times:

1.1 The cycle $D, D.R$ is not-broken. It is glued to the node D^* whose total mass is equal to the mass of D and $D.R$.

1.2 The limiting step of the cycle is $k_{lim} = k_{m1} \ll k_1$.

1.3 The branching reaction $D \rightarrow D.RNAP$ is replaced by $D^* \rightarrow D.RNAP$ of effective constant $k'_2 = \frac{k_{m1}}{k_1} k_2$.

2.1 The cycle $D^*, D.RNAP$ is not-broken. It is glued to the node D^{**} whose total mass is equal to the mass of D and $D.R$ and $D.RNAP$.

2.2 We have $k'_2 \ll k_{m2}$ hence the limiting step of the cycle is k'_2 .

2.3 The branching reaction $D.RNAP \rightarrow TrRNAP$ is replaced by $D^{**} \rightarrow TrRNAP$ of effective constant $k'_3 = \frac{k_{m1} k_2 k_3}{k_{m2} k_1}$.

3.1 The cycle $RBS, Rib.RBS$ is not-broken. It is glued to the node RBS^* whose total mass is the one of RBS and of $Rib.RBS$.

3.2 The limiting step is $k_{m6} \ll k_6$.

3.3 The branching reaction $Rib.RBS \rightarrow EIRib + RBS$ is replaced by the reaction $RBS^* \rightarrow EIRib + RBS^*$ of effective constant $k7^* \approx k_7$.

Notice that a loss of accuracy should be expected from the application of the third averaging step. The separation of the branching and cycling reactions is not that good. Indeed, $k_7/k_{m6} \approx 0.22$ while in theory we need $k_7/k_{m6} \ll 1$. The trajectories obtained by SSA (Fig.2) show the bursting phenomenon that can be now understood by the resulting low intensity of the reaction $TrRNAP \rightarrow RBS$. The reduced models reproduce the same behavior (with good accuracy for model 2, only qualitatively for model 3).

In order to compare the performance of the models (in terms of time complexity) we have represented the total jump intensities for three models (exact SSA, second and third averaged steps models) as functions of time on a trajectory. The model that demands the least computer time is the one with the smallest jump intensity. In Fig.3, we notice a decrease of several orders of magnitudes of

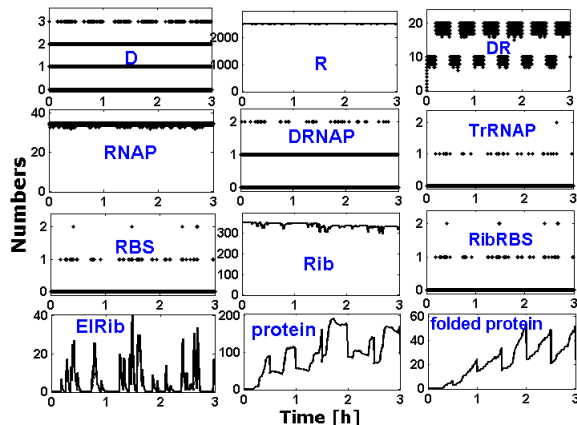


Fig. 2. Trajectories obtained by SSA

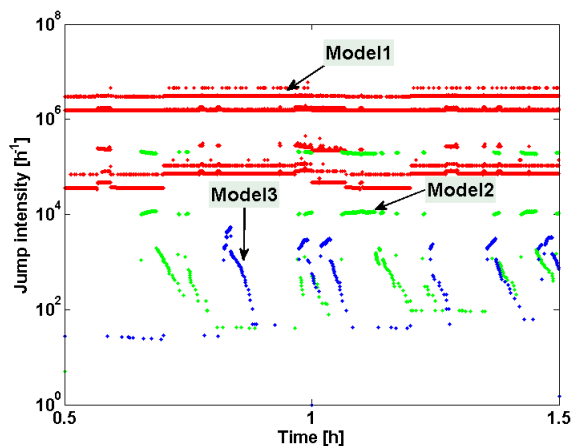


Fig. 3. Jump intensities for the 3 models.

the total intensity from exact SSA to the second and third averaging steps.

REFERENCES

- [1] D.T. Gillespie, "A General Method for Numerically Simulating the Stochastic Time Evolution of Coupled Chemical Reactions", *J.Comput.Phys.*, vol.22, p.403, 1976.
- [2] O. Radulescu, A.N. Gorban, A. Zinovyev and A. Lilienbaum, "Robust simplifications of multiscale biochemical networks", *BMC Systems Biology*, vol.2, p.86, 2008.
- [3] A.N. Gorban, O. Radulescu, "Dynamic and static limitation in multiscale reaction networks, revisited", In *Advances in Chemical Engineering*, vol. 34, G. Marin, D. West and G. Yablonsky, Eds., Academic Press 2008, pp. 103-173. E-print: arXiv:physics/0703278v4 [physics.chem-ph].
- [4] A.N. Gorban and O. Radulescu, "Dynamical robustness of biological networks with hierarchical distribution of time scales", *IET Systems Biology*, vol. 1, pp. 238-246, 2007.
- [5] S. Krishna, B. Banerjee, T. Ramakrishnan and G. Shivashankar, "Stochastic simulations of the origins and implications of long-tailed distributions in gene expression", *PNAS*, vol. 102, pp. 4771-4776, 2005.
- [6] M.D. Kruskal, "Asymptotology", In *Mathematical Models in Physical Sciences*, S. Dobrot, Eds., New Jersey: Prentice-Hall, 1963, pp. 17-48.

Flamelet Generated Manifolds for Chemistry Representation in Partially-Premixed Flames

W.J.S. Ramaekers*, J.A. van Oijen*, L.P.H. de Goey*

*Eindhoven University of Technology (TUE), Department of Mechanical Engineering, Eindhoven, The Netherlands

Abstract—In this article it will be assessed how well partially-premixed one-dimensional flames are represented using premixed and non-premixed flamelet-based Flamelet Generated Manifold (FGM) databases. A procedure is introduced which enables combination of both types of FGM databases as a function of local conditions. This allows a more accurate description of detailed chemical kinetics while the considerable speedup of computations enabled by the FGM reduction method is retained.

I. INTRODUCTION

In LES and DNS simulations of turbulent reacting flows the high computational cost associated with the large system of stiff differential equations can become limiting or even prohibitive for moderate and high Reynolds numbers. To reduce the required efforts reduction methods are commonly used. The Flamelet Generated Manifold (FGM) [8], also known as Flamelet Prolongated ILDM (FPI) [6], tabulates thermochemical variables originating from one-dimensional laminar flame structures: *flamelets*. The FGM reduction method assumes that in (turbulent) three-dimensional flames locally flame structures can be identified which closely resemble flamelets in composition space; the FGM reduction method can therefore be considered to be a combination of classic flamelet- and manifold methods. Any thermochemical variable is now parameterized by a small number of control variables. FGM databases can be generated using either premixed or non-premixed flamelets. The question which is addressed in this work is how well partially-premixed flames are reproduced when premixed and non-premixed flamelet-based FGM databases are used to represent combustion chemistry. Bongers *et al.* [3] showed that a FGM database based on premixed flamelets can accurately describe the premixed part of partially-premixed counterflow flames. However, in this study the considered range in mixture fraction was limited since the fuel stream had the same composition as a premixed system at the upper flammability limit. Previous work from Fiorina *et al.* [5] showed that (premixed flamelet-based) FPI databases could not accurately predict combustion parameters in partially-premixed and non-premixed flamelets. A flame-index was introduced to distinguish between premixed and non-premixed combustion and in case of non-premixed combustion the chemical source term for the reaction progress variable was assumed to equal diffusive transport [1]. In other words, no detailed chemistry was used for the non-premixed combustion mode. From these two references it can be concluded that a premixed flamelet-based FGM

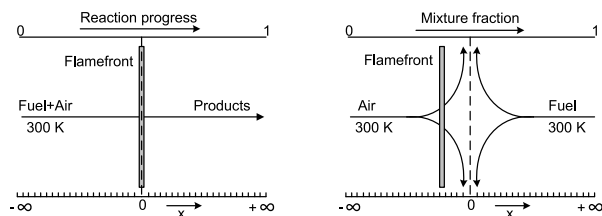


Fig. 1. Two flamelet types used for this study: premixed (left) and partially-/non-premixed (right) flamelets.

database can be used to describe partially-premixed combustion provided that the gradient in mixture fraction is kept small.

The novelty of this article is the use of detailed chemistry for both the premixed and non-premixed combustion mode, including a switch-function to distinguish (locally) between the two different modes of combustion and thereby enabling the determination of the most appropriate type of FGM database. It will be discussed whether the switch should be based on mixture fraction and reaction progress variable gradients or using an additional control variable.

In the next section it will be explained how individual flamelets are computed and, subsequently, how FGM databases are generated from these individual flamelets. In the third section need to use an appropriate FGM database to describe chemical kinetics is outlined. In the last section a brief description of the work in progress is given.

II. FLAMELET GENERATED MANIFOLDS

FGM databases are composed of many individual flamelets, each flamelet having slightly different boundary conditions. Boundary conditions, above all, determine the type of flamelet: premixed or non-premixed. Schematic representations of these flamelets types are shown in figure 1. The main difference between these two types is the direction of diffusion in composition space. In premixed flamelets diffusion is only allowed along iso-mixture fraction contours while in non-premixed flamelets diffusion mainly takes place perpendicular to these iso-contours.

For this study, partially-premixed combustion parameters are mapped on two control variables describing mixing (mixture fraction Z) and reaction progress (reaction progress variable \mathcal{Y}):

$$\psi = \psi(Z, \mathcal{Y}) \quad (1)$$

in which ψ can denote any thermo-chemical variable. The mixture fraction Z is defined by Bilger [2] and the reaction progress variable, which has to be monotonous in both lean and rich mixtures in order to facilitate an unambiguous determination of dependent variables, is defined as:

$$\mathcal{Y} = \frac{Y_{\text{CO}_2}}{M_{\text{CO}_2}} + \frac{Y_{\text{H}_2\text{O}}}{M_{\text{H}_2\text{O}}} + \frac{Y_{\text{H}_2}}{M_{\text{H}_2}} \quad (2)$$

in which Y_i and M_i denote a species mass fraction and a species its molar mass respectively.

A. Flamelet equations

The flamelet equations [8] form a set of specific transport equations for one-dimensional reacting flows describing conservation of mass, species and enthalpy. When unit Lewis numbers are assumed for all species the set of equations reduces to:

$$\frac{\partial(\rho)}{\partial t} + \frac{\partial(\rho u)}{\partial x} = -\rho K \quad (3)$$

$$\frac{\partial(\rho Y_i)}{\partial t} + \frac{\partial}{\partial x} \left(\rho u Y_i - \frac{\lambda}{c_p} \frac{\partial Y_i}{\partial x} \right) = -\rho K Y_i + \dot{\omega}_i \quad (4)$$

$$\frac{\partial(\rho h)}{\partial t} + \frac{\partial}{\partial x} \left(\rho u h - \frac{\lambda}{c_p} \frac{\partial h}{\partial x} \right) = -\rho K h \quad (5)$$

in which x , ρ , u , K denote the physical coordinate perpendicular to the flame, the mixture density, the velocity of the gas mixture and the flame stretch [7] respectively. Y_i , \mathbf{V} , $\dot{\omega}$, λ , c_p , μ and h denote the mass fraction of species i , the diffusion velocity, the chemical production rate, the thermal conductivity, the specific heat at constant pressure, the dynamic viscosity and the total enthalpy, respectively. N_s denotes the total number of species present in the used reaction mechanism and subscript 2 refers to the oxidizer stream. The low-Mach approximation is applied to the equation of state to prohibit acoustic waves propagating through the computational domain. For counterflow diffusion flames an additional transport equation for the unknown stretch field K has to be solved:

$$\frac{\partial(\rho K)}{\partial t} + \frac{\partial}{\partial x} \left(\rho u K - \mu \frac{\partial K}{\partial x} \right) = -\rho K^2 + \rho_2 a^2 \quad (6)$$

in which a denotes the applied strain rate at the oxidizer side. This transport equation has been derived by Dixon-Lewis [4]; here the formulation for two-dimensional cartesian geometries has been adopted. The set of governing equations describing either premixed or non-premixed flamelets is solved by the fully implicit solver CHEM1D [9] developed at TUE.

B. Boundary conditions for the flamelet equations

When FGM databases are to be constructed from unstrained steady premixed flamelets, equations 3, 4 and 5 are solved. K equals zero everywhere and equation 6 thereby is redundant. The equation of state closes the system of equations. Boundary conditions for premixed flamelets are:

$$\begin{aligned} u(x \rightarrow -\infty) &= s_L(Z_u) \\ Y_i(x \rightarrow -\infty) &= Z_u Y_{i,1} + (1 - Z_u) Y_{i,2} \\ h(x \rightarrow -\infty) &= Z_u h_1 + (1 - Z_u) h_2 \end{aligned}$$

in which subscript u denotes the unburnt mixture, s_L denotes the adiabatic flame propagation velocity and is an eigenvalue of the system. Subscripts 1 and 2 refer to the fuel- and oxidizer stream, respectively. The parameter of this system is the stoichiometry of the fresh mixture denoted by the mixture fraction Z_u . Beyond flammability limits thermo-chemical variables are linearly interpolated between the leanest flamelet and pure oxidizer and the richest flamelet and pure fuel, respectively. Chemical equilibrium has been explicitly added to all flamelets. When FGM databases are constructed from strained counterflow diffusion flamelets, equations 3, 4, 5 and 6 are solved. The equation of state again closes the system of equations. Boundary conditions for strained counterflow diffusion are:

$$\begin{aligned} Y_i(x \rightarrow -\infty) &= Y_{i,1} \\ h(x \rightarrow -\infty) &= h_1 \\ Y_i(x \rightarrow +\infty) &= Y_{i,2} \\ h(x \rightarrow +\infty) &= h_2 \\ K(x \rightarrow +\infty) &= a(t) \end{aligned}$$

in which subscripts 1 and 2 again refer to the fuel- and oxidizer stream, respectively. The parameter of this system is the applied strain rate a , which can be a function of time in case of unsteady computations, and is defined at the oxidizer side ($x = \infty$). Solving the unsteady equations for conservation of mass, species mass fractions and enthalpy results in a natural continuation of the profiles in Z - \mathcal{Y} space beyond the extinction strain rate. The time-dependent solution of the unsteady equations, which is treated as a family of solutions, is tracked until the solution equals the mixing limit starting from a steady solution with a strain rate equal to unity.

III. FGM VERSUS DETAILED CHEMISTRY

Laminar, one-dimensional CH₄/air (21% O₂ and 79% N₂ by volume) flames are simulated in a counterflow setup. The boundary conditions will be varied from premixed to fully non-premixed resulting in realizations ranging from a premixed double flame, via a triple-flame structure to a (single) diffusion flame structure. All setups are simulated at ambient conditions ($p = 1.01325 \times 10^5$ Pa and $T = 300$ K) and Lewis numbers are set to unity for all species. The GRI 3.0 reaction mechanism [10] is used to represent combustion chemistry.

For the FGM database based on unstrained, steady premixed flamelets, 400 flamelets with $Z \in [0.25Z_{st}, 2.0Z_{st}]$ have been used. For a given inlet composition, determined by Z , \mathcal{Y} is tracked. Equation 6 is removed from the system of equations since K equals zero everywhere. Beyond the flammability limits linear extrapolation between the leanest flamelets and pure oxidizer, and the richest flamelet and pure fuel respectively, has been applied. The resulting database has been interpolated onto an equidistant grid with 375 points in both Z and \mathcal{Y} direction. For the FGM database based on non-premixed flamelets, 600 flamelets with increasing strain rate have been used. The unsteady

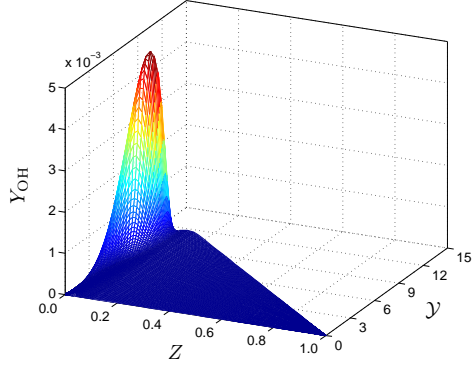


Fig. 2. OH mass fraction, which is a function of Z and \mathcal{Y} , originating from the non-premixed flamelet-based Flamelet Generated Manifold database. OH is a typical indicator of combustion chemistry activity.

flamelet equations, equation 3, 4, 5 and 6 are solved while the strain rate at the oxidizer side is increased by 1 s^{-2} on average using a Wiebe function, starting with a strain rate equal to unity. For each solution, dependent on time, \mathcal{Y} is recalculated at each point according to equation 2 while for Z a transport equation is solved. The steady, slow increase in strain rate implies that the flamelet will extinguish at a given moment: the (extinguishing) flamelet is tracked until it equals the mixing limit. By this means the entire composition space between (near) chemical equilibrium and the mixing limit can be spanned. The resulting database has again been interpolated onto an equidistant grid with 375 points in both Z and \mathcal{Y} direction. In figure 2 the OH variables Z and \mathcal{Y} , is shown as an example.

When the FGM databases are used in flamelet computations equations 4 and 5 are replaced by transport equations for the two control variables only:

$$\frac{\partial(\rho Z)}{\partial t} + \frac{\partial}{\partial x} \left(\rho u Z - \frac{\lambda}{c_p} \frac{\partial Z}{\partial x} \right) = -\rho K Z \quad (7)$$

$$\frac{\partial(\rho \mathcal{Y})}{\partial t} + \frac{\partial}{\partial x} \left(\rho u \mathcal{Y} - \frac{\lambda}{c_p} \frac{\partial \mathcal{Y}}{\partial x} \right) = -\rho K \mathcal{Y} + \dot{\omega}_{\mathcal{Y}} \quad (8)$$

The chemical source term for \mathcal{Y} ($\dot{\omega}_{\mathcal{Y}}$) is retrieved from the FGM database using linear interpolation; when the solutions for Z and \mathcal{Y} have converged all species mass fractions are retrieved from the FGM database in the same way.

A. The need for using the appropriate FGM database

When premixed flamelets are computed using a premixed flamelet-based FGM and when non-premixed flamelets are computed using a non-premixed flamelet-based FGM it can be seen from figure 3 that combustion chemistry and diffusive transport are well described by the FGM database. However, if the non-appropriate type of FGM database is used, i.e. premixed flamelets are computed using a non-premixed flamelet-based FGM or non-premixed flamelets are computed using a premixed flamelet-based FGM, it can be seen from figure 4 that errors appear when predictions using FGM databases

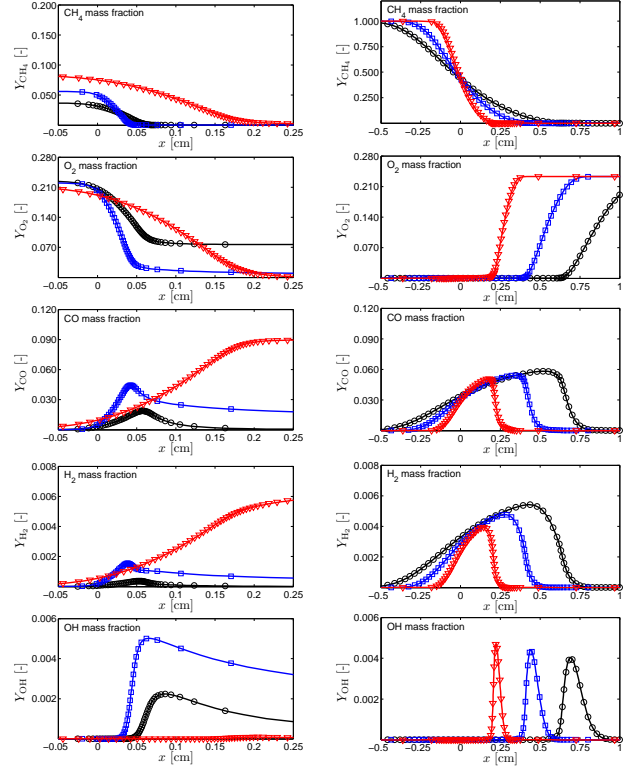


Fig. 3. Results for steady premixed flamelets using a premixed flamelet-based FGM (left) and steady non-premixed flamelets using a non-premixed flamelet-based FGM (right). For the premixed flamelets black lines with circle markers denote a flamelet with $Z = 0.67Z_{st}$, blue lines with square markers denote a flamelet with $Z = Z_{st}$ and red lines with triangle markers denote a flamelet with $Z = 1.5Z_{st}$. For the non-premixed flamelets black lines with circle markers denote a flamelet with $a = 10 \text{ s}^{-1}$, blue lines with square markers denote a flamelet with $a = 25 \text{ s}^{-1}$ and red lines with triangle markers denote a flamelet with $a = 100 \text{ s}^{-1}$. In all figures solid lines denote detailed chemistry solutions while the markers (circles, squares or triangles) denote solutions using FGM databases. Figures from top to bottom represent CH_4 mass fractions, O_2 mass fractions, CO mass fractions, H_2 mass fractions and OH mass fractions.

are compared to detailed chemistry. These errors are most significant for CO and H_2 which are formed under rich conditions but in non-premixed flamelets can diffuse towards the reaction layer near the stoichiometric mixture fraction where they are consumed again. When premixed flamelets are considered this is not possible; this results in higher CO and H_2 under rich conditions. In figure 4 this effect is most visible in CO and H_2 mass fraction predictions in non-premixed flames using a premixed flamelet-based FGM database. For OH it is observed that errors using the wrong type of FGM database are not as significant as for CO and H_2 . It will be examined whether this can be attributed to the dominance of chemistry over (convective and diffusive) transport.

It can be concluded that it is important to use the appropriate FGM database when accurate predictions of species are desired, especially when CO and H_2 are concerned.

B. Partially-premixed flamelets

For partially-premixed flamelets FGM databases which are based on either premixed or non-premixed flamelets are not sufficient. It will be examined whether the local

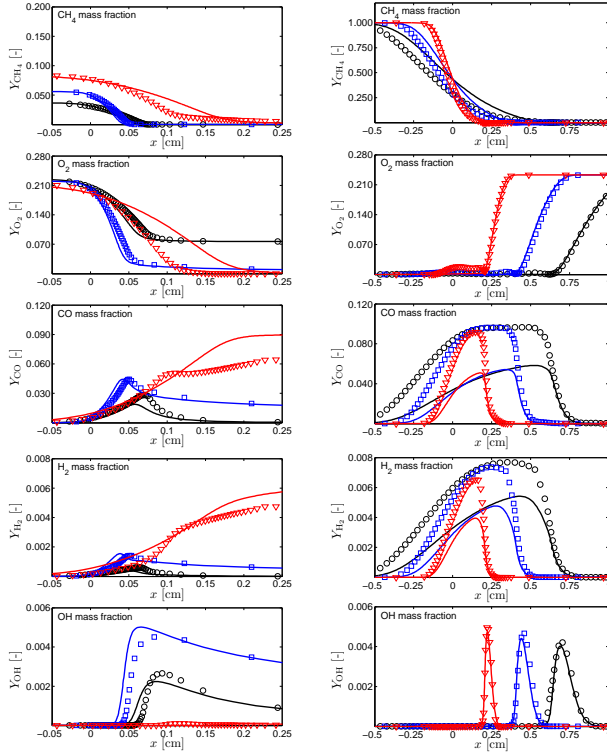


Fig. 4. Results for premixed flamelets using a non-premixed FGM (left) and non-premixed flamelets using a premixed FGM (right). Identical symbols have been used as in figure 3.

source term for \mathcal{Y} can be defined as a linear combination of the source term in premixed and non-premixed flamelets for the same values for Z and \mathcal{Y} :

$$\dot{\omega}_{\mathcal{Y}}(Z, \mathcal{Y}) = \alpha \dot{\omega}_{\mathcal{Y}}^{\text{P}}(Z, \mathcal{Y}) + (1 - \alpha) \dot{\omega}_{\mathcal{Y}}^{\text{NP}}(Z, \mathcal{Y}) \quad (9)$$

To determine the weight factor α several methods have been proposed starting with the flame index method proposed by Yamashita *et al.* [11], for which a modified version for the use with FPI-databases was introduced by Fiorina *et al.* [5]; nevertheless for one-dimensional flames these indices exhibit a non-continuous behavior. Another switch function formulation which will be examined reads:

$$\alpha = \tanh \left[\log \left(\frac{\vec{\nabla} \mathcal{Y} \cdot \vec{\nabla} \mathcal{Y}}{\vec{\nabla} Z \cdot \vec{\nabla} Z} \right) \right] \quad (10)$$

which should exhibit a continuous and smooth behavior throughout the entire domain.

IV. WORK IN PROGRESS

It will be examined whether a switch function as defined in the previous section yields an increase in accuracy of predictions when FGM databases are used to replace expensive detailed chemistry computations. The switch function will be compared to the use of an additional control variable, e.g. H_2 mass fraction, for which an additional transport equation has to be solved.

REFERENCES

[1] R.W. Bilger, “The structure of diffusion flames,” *Comb. Sci. Tech.*, vol. 13, pp. 155–170, 1976.

[2] R.W. Bilger, “On reduced mechanisms for methane-air combustion in non-premixed flames,” *Comb. Flame*, vol. 80, pp. 135–149, 1990.

[3] H. Bongers, J.A. van Oijen and L.P.H. de Goeij “The Flamelet Generated Manifold method applied to steady planar partially-premixed counterflow flames,” *Comb. Sci. Tech.*, vol. 177(12), pp. 2373–2393, 2005.

[4] G. Dixon-Lewis, “Structure of laminar flames,” *Proc. Comb. Inst.*, vol. 23, pp. 305–324, 1990.

[5] B. Fiorina, O. Gicquel, L. Vervisch, S. Carpentier and N. Darabiha, “Approximating the chemical structure of partially premixed and diffusion counterflow flames using FPI flamelet tabulation,” *Comb. Flame*, vol. 140, pp. 147–160, 2005.

[6] O. Gicquel, N. Darabiha and D. Thevenin, “Laminar premixed hydrogen/air counterflow flame simulations using Flame Prolongation of ILDM with differential diffusion,” *Proc. Comb. Inst.*, vol. 28, pp. 1901–1908, 2000.

[7] L.P.H. de Goeij and J.H.M. Ten Thije Boonkkamp, “A mass based definition of flame stretch for flames with finite thickness,” *Comb. Sci. Tech.*, vol. 122, pp. 399–405, 1997.

[8] J.A. van Oijen and L.P.H. de Goeij, “Modelling of premixed laminar flames using Flamelet Generated Manifolds,” *Comb. Sci. Tech.*, vol. 161, pp. 113–137, 2000.

[9] L.M.T. Somers, *The simulation of flat flames with detailed and reduced chemical models*. PhD Thesis: Eindhoven University of Technology, 1994.

[10] G.P. Smith, D.M. Golden, M. Frenklach, N.W. Moriarty, B. Eiteeneer, M. Goldenberg, C.T. Bowman, R.K. Hanson, S. Song, W.C. Gardiner Jr., V.V. Lissianski and Z. Qin, *GRI mech 3.0 reaction mechanism*. Sandia National Laboratories, 2000.

[11] H. Yamashita, M. Shimada and T. Takeno, “A numerical study on flame stability at the transition point of jet diffusion flames,” *Proc. Comb. Inst.*, vol. 26, pp. 27–34, 1996.

Extending the Tools of Chemical Reaction Engineering to the Molecular Scale

Author: James B. Rawlings
Department of Chemical and Biological Engineering
University of Wisconsin

In classical continuum chemical kinetics, two primary physical situations result in model reduction. The first case is the presence of fast and slow reactions. In this case, the fast reactions are assumed to be in equilibrium and one expresses a slow-time scale evolution of all the species concentrations due to the slow reactions. In the second case, highly reactive intermediates rapidly approach and maintain a low quasi-steady-state concentration. In this case, one can express a simplified evolution equation for the large concentration species (reactants and products). These two cases arise frequently in applications and are a standard part of the classical reaction engineering toolkit. Examples include Michaelis-Menten kinetics and Langmuir-Hinshelwood or Hougen-Watson reaction mechanisms on catalytic surfaces.

But when reactions are considered at small length scales (small catalyst particles, inside living cells, etc.), the concentrations are small enough that the stochastic fluctuations cannot be neglected. In this regime, we often use kinetic Monte Carlo (KMC) methods to simulate the reaction networks of interest. But when confronted with large separations in reaction rates or large separations in species concentrations, the computation time for the standard KMC simulation method becomes excessive, and standard KMC is no longer useful for simulating the reaction network of interest.

This talk presents recent results for extending kinetic model reduction methods to handle this stochastic, molecular regime. The resulting reduced chemical mechanisms can be quite different from what one expects based on knowledge of the results for only the macroscopic, deterministic setting. The model reduction methods will be illustrated by application to a set of illustrative chemical kinetic mechanisms.

Spectral Representation and Reduced Order Modeling of Stochastic Reaction Networks

Khachik Sargsyan, Bert Debuschere, Habib Najm

Sandia National Laboratories, 7011 East Ave., MS 9051, Livermore, CA 94550, USA

{ksargsy,bjdebus,hnnajm}@sandia.gov

Abstract—For many biochemical phenomena in cells the molecule count is low, leading to stochastic behavior that causes deterministic macroscale reaction models to fail. The main mathematical framework representing these phenomena is based on continuous-time, discrete-state Markov processes that model the underlying *stochastic reaction network*. Conventional dynamical analysis tools do not readily generalize to the stochastic setting due to non-differentiability and absence of explicit state evolution equations. We developed a reduced order methodology for dynamical analysis that relies on the Karhunen-Loève decomposition and polynomial chaos expansions. The methodology relies on adaptive data partitioning to obtain an accurate representation of the stochastic process, especially in the case of multimodal behavior. As a result, a mixture model is obtained that represents the reduced order dynamics of the system. The Schlögl model is used as a prototype bistable process that exhibits time-scale separation and leads to multimodality in the reduced order model.

I. INTRODUCTION

The simplest description of chemical reaction processes is based on *rate equations*, i.e. ordinary differential equations (ODEs) for species concentrations. This macroscopic setting fails when the relevant volume or the species numbers are small because of the increased significance of stochastic noise due to random molecular collisions [9], [22]. *Stochastic reaction networks* (SRNs) account for intrinsic stochastic noise, and provide a general framework for chemical reaction models at the microscopic, molecular level. SRNs are generally governed by the Chemical Master Equation [7] (CME), which is a differential equation governing the time evolution of the Probability Density Function (PDF) of species numbers. The chemical master equation is obtained by modeling a SRN as a jump Markov process [23], [6], i.e. discrete-state, continuous-time stochastic processes with no memory. Since computing direct numerical solutions for CMEs is still challenging (for recent efforts, see [15] and references therein), simulation-based methods become the main analytical tools. In particular, Gillespie’s Stochastic Simulation Algorithm [4], [5] (SSA) provides a simulation mechanism for the time-evolution of species numbers at the microscopic scale, thereby effectively sampling the CME solution. This allows determining useful statistical properties of the system by averaging *without* solving the CME itself.

In this work, we rely on Karhunen-Loève (KL) expansions [10], [14], [2] that represent the underlying stochastic processes in terms of orthonormal random

variables, truncated to a reduced order model. This low-order representation is constructed based on the observed statistics of the stochastic process over a given period of time. With a truncated KL expansion, each realization of a stochastic process corresponds to a finite number of uncorrelated random variables, with non-standard distributions determined by the data. As a result, it is desirable to represent these random variables with polynomial chaos (PC) expansions [25] that enable computationally efficient estimation of system properties.

However, a global PC representation with a finite order and dimensionality does not accurately capture random variables that exhibit strong multimodalities [18]. Adaptive multi-wavelet [11], [12], [13] or PC [24] bases, both relying on stochastic domain decomposition, enable efficient analysis of such processes in the continuous deterministic setting. In this work, we extend the methodology proposed in [18] to obtain an adaptive, data-driven partitioning that captures the structure and modalities of intrinsic stochasticity. Our data partitioning algorithm, which involves a combination of clustering and data range bisection, leads to a mixture of PC expansions that properly represents multimodal distributions by taking advantage of the underlying data structure.

II. REDUCED ORDER MODELING VIA KARHUNEN-LOÈVE DECOMPOSITION

As a reduced order model for a stochastic process $X(t, \theta)$, consider the L -truncated *Karhunen-Loève* (KL) expansion [10], [14]

$$X(t, \theta) \approx X_{KL}(t, \theta) = \bar{X}(t, \theta) + \sum_{i=1}^L \sqrt{\lambda_i} f_i(t) \xi_i, \quad (1)$$

where $\bar{X}(t, \theta)$ denotes the expectation with respect to the sample space element θ . In the above KL expansion, the λ_i are the eigenvalues of the covariance kernel with corresponding orthogonal eigenfunctions $f_i(t)$. The random vector $\xi = (\xi_1, \dots, \xi_L)$ consists of L jointly distributed and uncorrelated (but not independent) random variables. Essentially, the dynamics of the full process $X(t)$ is captured by a single random vector ξ (we will drop the argument θ for clarity, unless there is a need to put an emphasis on the intrinsic randomness).

As a benchmark process that exhibits a bimodal behavior, consider the Schlögl model [19], [6], [18], which is a SRN involving two reversible reactions and three species

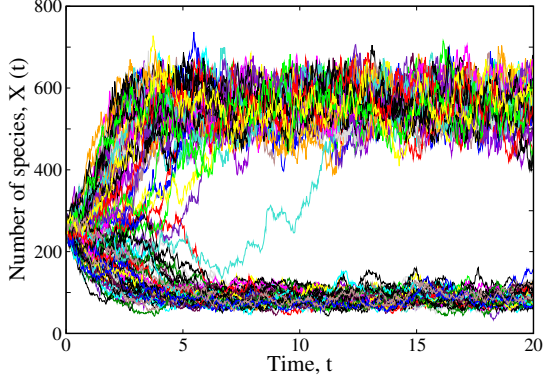


Fig. 1. Hundred SSA realizations of the Schlögl model with the nominal parameter set [17].

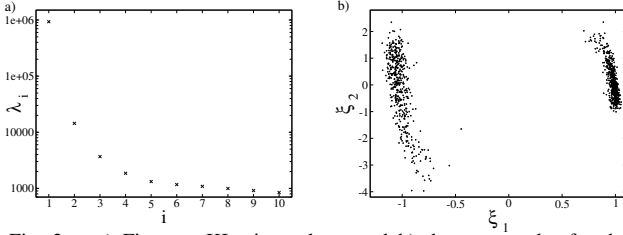


Fig. 2. a) First ten KL eigenvalues, and b) the scatter plot for the first two KL random variables for the Schlögl model with the nominal parameter set [17].

X , A and B , but with A and B assumed to be present in large and fixed numbers. We are interested in the number of species $X(t)$. With $X(0) = 250$ and the nominal set of rate constants, the system exhibits bistable behavior over a time window $t \in [0, 20]$, see Fig. 1. Furthermore, Fig. 2 illustrates the corresponding eigenvalue spectrum and the scatter plot of the projected samples of ξ_1 and ξ_2 . The huge gap between the first two eigenvalues and bimodality along the ξ_1 -dimension are direct results of the bimodality of the time-dependent process itself. Although the random vector ξ has uncorrelated components, it may have a complicated structure that is not known beforehand. We then turn to spectral expansions in order to properly represent the random vector ξ .

III. POLYNOMIAL CHAOS EXPANSION OF THE REDUCED ORDER MODEL

We seek to approximate ξ with a random variable represented by a d -th order, L -dimensional PC expansion

$$\xi = \sum_{k=0}^P c_k \Psi_k(\zeta_1, \dots, \zeta_L) \equiv \mathbf{g}(\zeta; \mathbf{C}), \quad (2)$$

with the number of terms $P+1 = \frac{(d+L)!}{d!L!}$ and multivariate orthogonal polynomials $\Psi_k(\zeta)$. The components of the random vector ζ are standard i.i.d. random variables. In this work, we have used Hermite polynomials that are orthogonal with respect to the PDF of a standard normal

random variable. Namely,

$$\begin{aligned} \langle \Psi_j(\zeta) \Psi_k(\zeta) \rangle &\equiv \int \Psi_j(\zeta) \Psi_k(\zeta) \frac{e^{-\frac{\zeta^T \zeta}{2}}}{\sqrt{2\pi}} d\zeta \\ &= \langle \Psi_k^2(\zeta) \rangle \delta_{jk}. \end{aligned} \quad (3)$$

The above orthogonality relation leads to the projection formulas

$$c_k = \frac{\langle \xi \Psi_k(\zeta) \rangle}{\langle \Psi_k^2(\zeta) \rangle}. \quad (4)$$

However, in order to compute the stochastic projection integral $\langle \xi \Psi_k(\zeta) \rangle$, one needs an one-to-one correspondence between samples of ξ and ζ . To resolve this, we employ the *Rosenblatt transformation* [16], [17] that enables the projection (4) in the same, ζ -space. Finally, the full representation can be written as

$$\begin{aligned} X(t, \theta) &\approx X_{KLPC}(t, \theta) = \\ &= \bar{X}(t, \theta) + \sum_{i=1}^L \left(\sum_{k=0}^P c_{ik} \Psi_k(\zeta) \right) \sqrt{\lambda_i} f_i(t), \end{aligned} \quad (5)$$

i.e. the process $X(t, \theta)$ is described in terms of *deterministic* matrix elements c_{ik} and a random vector $\zeta = (\zeta_1, \dots, \zeta_L)$ of standard normal i.i.d. random variables. However, as shown in [18], the global PC representation is challenged if the random vector ξ has a multimodal character, which is certainly the case for the Schlögl model, see Fig. 2b.

IV. ADAPTIVE DATA PARTITIONING ALGORITHM

In order to tackle multimodalities, we analyzed various approaches of partitioning the data set of samples of ξ , and introduced a novel, hybrid and adaptive strategy that involves approximate k -center clustering [8] to detect the bimodalities, followed by data-range bisection. The algorithm adaptively partitions the data set into subsets that are simpler to represent with low-order PC, until this representation is satisfactory in terms of the *Kullback-Leibler (K-L) divergence* or *relative entropy* [3], [1] between the PDFs of the data samples and the samples of the corresponding representation (i.e., $P(\cdot)$ and $Q(\cdot)$, respectively)

$$d(P||Q) = \int P(\mathbf{x}) \log \frac{P(\mathbf{x})}{Q(\mathbf{x})} d\mathbf{x}. \quad (6)$$

Exact computation of the K-L divergence requires an integration that is extremely costly in multiple dimensions. Nevertheless, it can be estimated by Monte-Carlo integration in terms of the data samples that are available. Namely,

$$\begin{aligned} d(P||Q) &\approx \frac{1}{N} \sum_{n=1}^N \log \frac{P(\xi^{(n)})}{Q(\xi^{(n)})} \\ &= \frac{1}{N} \left(\sum_{n=1}^N \log P(\xi^{(n)}) - \sum_{n=1}^N \log Q(\xi^{(n)}) \right), \end{aligned} \quad (7)$$

where $\xi^{(n)}$ for $n = 1, 2, \dots, N$ are the samples drawn from the distribution $P(\cdot)$, i.e. exactly the data samples

that are to be PC-represented. This approximation of the K-L divergence allows simple intuitive interpretation: the second sum is the log-probability of having the particular data set $\{\xi^{(n)}\}_{n=1}^N$ given a model that leads to the PDF $Q(\cdot)$ (in other terms, the *likelihood* of the model), while the first sum is the likelihood *if* the model had the exact same PDF as the original data set (in a sense, a *target likelihood*). The PDFs in (7) are computed by standard KDE techniques [21], [20].

We have analyzed various data partitioning schemes and found that the domain-based bisection approaches (specifically, data range bisection, data median bisection and data size bisection, see [17]) blindly split the data without detecting the modalities. Therefore, we enhanced the methodology with an initial clustering step (namely, an approximate version of the k -center clustering is implemented) that detects the modalities present in the data structure. After this initial step, it is shown that the data range bisection works better than the other approaches. It consists of finding and bisecting the data range in each direction simultaneously.

In order to find out whether an initial clustering is needed and what the optimal number of clusters is, we employ the *explained variance criterion*. The explained variance for a specific clustering is a variance of a data set that is obtained from the initial data set by replacing each sample with the mean of its cluster. The fraction of the explained variance over the total variance vanishes if there is only one cluster (the set itself) and is equal to one, if the number of clusters is the same as the number of data samples. We run several trial clustering cases for various fixed number of clusters and check the graph of the explained variance fraction versus the cluster number. This graph is generally increasing and concave down. If there is a well-seen ‘elbow’ in the graph, then its location corresponds to the optimal number of clusters. Otherwise, there is no need to proceed with the clustering, and the data is considered sufficiently unimodal [17].

The adaptive PC representation algorithm then proceeds as follows:

0. Obtain N SSA realizations $X(t)$.
1. Perform KL decomposition up to the eigenmode (dimension) L .
 - 1a. As a result, obtain a set of N data samples of the random vector $\xi = (\xi_1, \dots, \xi_L)$ and call it the current data set $S = \{\xi^{(1)}, \xi^{(2)}, \dots, \xi^{(N)}\}$.
 - 1b. *If* the explained variance criterion [17] detects modalities, cluster the data into the optimal number of clusters and proceed considering each cluster as a new data set. *Otherwise* proceed to Step 2.
2. Use the Rosenblatt transformation and quadrature evaluation of the projection integrals (4) to find a finite order PC representation for the current data samples: $\xi_i = \sum_{k=0}^P c_{ik} \Psi_k(\zeta)$, for $i = 1, 2, \dots, L$.
 - 2a. Compute the K-L divergence between the data and the PC model using (7).

3. *If* the number of samples in the current data set exceeds the threshold N_{thr} *and* the K-L divergence is larger than the threshold d_{thr} , partition the current data set according to data range bisection, and recursively return to Step 2 for each new data set. *Else* keep the current PC representation and move to the next untreated data set.

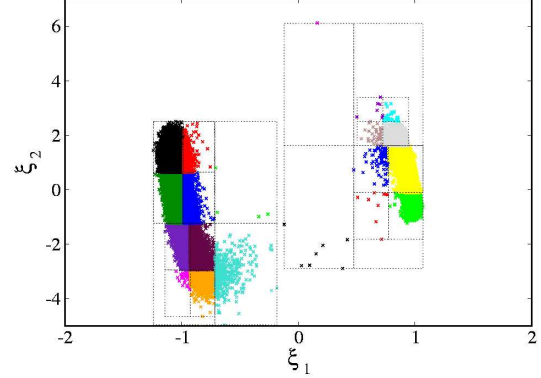


Fig. 3. The data partitions for the first two KL variables obtained from a KL projection of $N = 10^5$ realizations of the Schlögl process.

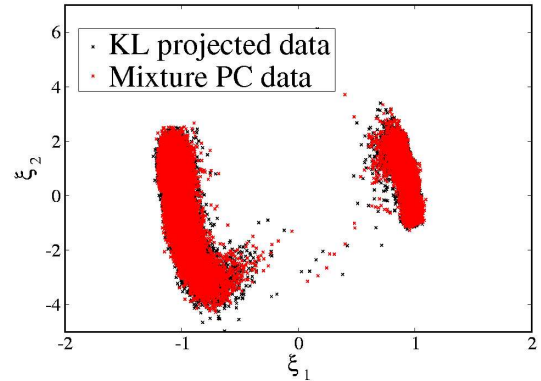


Fig. 4. The scatter plot of the original data set and the samples obtained from the mixture PC representation.

The final representation then corresponds to a PDF that is a *mixture* of PDFs of PC representations of each of the K subsets. Namely,

$$PDF_{\xi_{PC}}(\mathbf{y}) = \sum_{j=1}^K p_j PDF_{\mathbf{g}(\zeta; \mathbf{C}^{(j)})}(\mathbf{y}), \quad (8)$$

where p_j is the fraction of data samples in the j -th partition.

Fig. 3 shows the final partitions for a two-dimensional data set for a random vector $\xi = (\xi_1, \xi_2)$ that is obtained by a KL projection of $N = 10^5$ realizations of the Schlögl process. The data set itself and the samples of its third order mixture PC model representation are shown in Fig. 4. The K-L convergence analysis of our hybrid methodology and other data partitioning strategies is illustrated in Fig. 5. Although for this particular data set - it is bimodal along the first dimension only - the plain

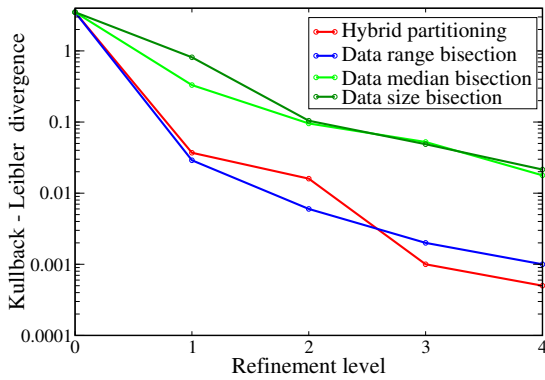


Fig. 5. Convergence of the mixture PC representation as the partitioning refinement level increases. Various data partitioning strategies are compared [17]. The zeroth refinement levels correspond to the global representation, while the first level is simply the clustering for the hybrid partitioning. The third refinement levels correspond to the illustration from Fig. 3.

data range bisection is as efficient as the hybrid approach, it is shown [17] that the hybrid methodology is more robust for *general* data sets with no *a priori* knowledge of the data structure available.

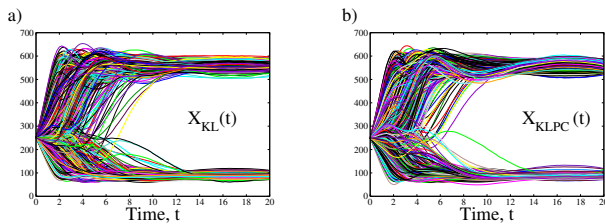


Fig. 6. a) The 5-mode KL truncated sum for the Schlögl process. b) The final representation obtained from mixture PC expansions of the underlying five-dimensional KL random vector. Both expansions are obtained with $N = 10^9$ realizations with only every hundredth realization shown for illustration purposes.

Finally, Fig. 6 illustrates the 5-mode KL-truncated sum

$$X_{KL}(t) = \bar{X}(t) + \sum_{i=1}^5 \xi_i \sqrt{\lambda_i} f_i(t) \quad (9)$$

of the underlying Schlögl process as well as the process, recovered from the third order mixture PC representation of the KL-projected variables, i.e.

$$X_{KLPC}(t) = \bar{X}(t) + \sum_{i=1}^5 (\xi_{PC})_i \sqrt{\lambda_i} f_i(t). \quad (10)$$

Clearly, the stochastic process $X(t)$, first reduced to $X_{KL}(t)$ (described by a random vector ξ) by the KL projection, is further reduced to $X_{KLPC}(t)$ (described by a set of deterministic matrices $\{C^{(j)}\}_{j=1}^K$, one for each partition of the data samples of ξ) by our mixture PC representation while preserving the skeleton of the dynamics of the original process for further analysis of the system, or as a reduced order model.

ACKNOWLEDGMENT

This work was supported by the U.S. Department of Energy Office of Science through the Applied Math-

ematics program in the Office of Advanced Scientific Computing Research (ASCR) under contract 07-012783 with Sandia National Laboratories. Sandia National Laboratories is a multiprogram laboratory operated by Sandia Corporation, a Lockheed Martin Company, for the U.S. Department of Energy under contract No. DE-AC04-94-AL85000.

REFERENCES

- [1] M. Arnst and R. Ghanem. Probabilistic equivalence and stochastic model reduction in multiscale analysis. *Comput. Methods Appl. Mech. and Engrg.*, 197:3584–3592, 2002.
- [2] R. Ghanem and P. Spanos. *Stochastic Finite Elements: A Spectral Approach*. Springer Verlag, New York, 1991.
- [3] A. Gibbs and F. Su. On choosing and bounding probability metrics. *International Statistical Review*, 70:419–436, 2002.
- [4] D. Gillespie. A general method for numerically simulating the stochastic time evolution of coupled chemical reactions. *J. Comput. Phys.*, 22:403–434, 1976.
- [5] D. Gillespie. Exact Stochastic Simulation of Coupled Chemical Reactions. *Journal of Physical Chemistry*, 81(25):2340–2361, 1977.
- [6] D. Gillespie. *Markov Processes: An Introduction for Physical Scientists*. Academic Press, San Diego, CA, 1992.
- [7] D. Gillespie. A rigorous derivation of the chemical master equation. *Phys. A*, 188:404–425, 1992.
- [8] T. Gonzalez. Clustering to minimize the maximum intercluster distance. *Theor. Comp. Science*, 38:293–306, 1985.
- [9] W. Horsthemke and R. Lefever. *Noise-Induced Transitions*. Springer-Verlag, Berlin, 1984.
- [10] K. Karhunen. Zur spektraltheorie stochastischer prozesse. *Ann. Acad. Sci. Fennicae*, 37, 1946.
- [11] O. Le Maître, R. Ghanem, O. Knio, and H. Najm. Uncertainty propagation using Wiener-Haar expansions. *J. Comput. Phys.*, 197(1):28–57, 2004.
- [12] O. Le Maître, H. Najm, R. Ghanem, and O. Knio. Multi-resolution analysis of Wiener-type uncertainty propagation schemes. *J. Comput. Phys.*, 197:502–531, 2004.
- [13] O. Le Maître, H. Najm, P. Pébay, R. Ghanem, and O. Knio. Multi-resolution-analysis scheme for uncertainty quantification in chemical systems. *SIAM J. Sci. Comput.*, 29(2):864–889, 2007.
- [14] M. Loève. *Probability Theory*. Van Nostrand, Princeton, NJ, 1955.
- [15] S. MacNamara, A. Bersani, K. Burrage, and R. Sidje. Stochastic chemical kinetics and the total quasi-steady-state assumption: application to the stochastic simulation algorithm and chemical master equation. *Journal of Chemical Physics*, 129(9):095105–1–13, 2008.
- [16] M. Rosenblatt. Remarks on a multivariate transformation. *Annals of Mathematical Statistics*, 23(3):470 – 472, 1952.
- [17] K. Sargsyan, B. Debusschere, H. Najm, and O. L. Maître. Spectral representation and reduced order modeling of the dynamics of stochastic reaction networks via adaptive data partitioning. *SIAM Journal on Scientific Computing*, submitted.
- [18] K. Sargsyan, B. Debusschere, H. Najm, and Y. Marzouk. Bayesian inference of spectral expansions for predictability assessment in stochastic reaction networks. *Journal of Computational and Theoretical Nanoscience*, in press.
- [19] F. Schlögl. On thermodynamics near a steady state. *Z. Phys.*, 248:446–458, 1971.
- [20] D. Scott. *Multivariate Density Estimation. Theory, Practice and Visualization*. Wiley, New York, 1992.
- [21] B. Silverman. *Density Estimation*. Chapman and Hall, London, 1986.
- [22] R. Srivastava, L. You, J. Summers, and J. Yin. Stochastic vs. deterministic modeling of intracellular viral kinetics. *Journal of Theoretical Biology*, 218(3):309 – 321, 7 2002.
- [23] N. van Kampen. *Stochastic Processes in Physics and Chemistry*. Elsevier Science, Amsterdam, 1992.
- [24] X. Wan and G. E. Karniadakis. An adaptive multi-element generalized polynomial chaos method for stochastic differential equations. *J. Comput. Phys.*, 209:617–642, 2005.
- [25] N. Wiener. The homogeneous chaos. *Am. J. Math.*, 60:897–936, 1938.

Reduction of detailed chemical models with controlled uncertainty

David A. Sheen^{*}, Terese Løvås[†] and Hai Wang^{*}

^{*} University of Southern California, Los Angeles, USA

[†] University of Tromsø, Tromsø, Norway

Abstract— Previously we proposed a method of uncertainty minimization by polynomial chaos expansion (MUM-PCE) to quantify and constrain the uncertainty in detailed chemical kinetic models. Here we extend this method to include its application in reaction model reduction using the Level-of-Importance (LOI) method. In particular, we demonstrate that the uncertainty introduced by the reduction process may be defined in conjunction with the MUM-PCE method. Coupled with the overall uncertainty of the detailed chemical model as determined by MUM-PCE, the kinetic uncertainty of a reduced chemical model may be quantified, both in terms of the uncertainty in the detailed model and that due to model reduction. Additionally, the same multi-parameter, comprehensive optimization approach used in MUM-PCE may be employed to constrain the uncertainty of a reduced model.

I. INTRODUCTION

The approach to developing detailed chemical kinetic models for fuel combustion involves compiling a set of elementary reactions whose rate parameters are determined from individual rate measurements, reaction-rate theory, or, in many cases, estimations from analogous reactions. As chemical models become larger, the number of parameters that must be estimated and species that must be considered increases. The number of scalars is usually too large to allow computation of realistic combusting flows, which are often turbulent, using detailed chemical kinetic models [1]. A rigorous means of reducing the complexity of the reaction model is therefore needed.

Traditionally, the accuracy of a reduced or skeletal model is ensured by comparing its performance against a detailed model [e.g., 2-5]. Without considering the uncertainty in the detailed model, this comparison can over-constrain the reduction criteria. In fact, a reduced model can be said as accurate so long as it reproduces the detailed model within its uncertainty bound. Of course, to make this comparison, the uncertainty bounds of both the detailed model and the reduced model need to be rigorously quantified.

This paper summarizes the Method of Uncertainty Minimization by Polynomial Chaos Expansion (MUM-PCE) [6], and details a method for developing a reduced chemical kinetic model from a detailed model with quantifiable uncertainties. The PCE method is based on a series of earlier work of Najm, Ghanem and coworkers [7-9]. First, a set of combustion conditions is chosen against which the model will be reduced. An optimization study is performed on the detailed model, using ethylene combustion as a test case [6]. This optimized model is then reduced using the automated level-of-importance method (LOI) [3]. To assess the predictive capacity of the reduced model, the error introduced by the reduction is calculated and used to compare the reduced model predictions to those of the detailed model. The method of uncertainty estimation is described here, and is similar to the quasi-steady-state approximation (QSSA) error found in [10].

II. METHODOLOGY

A. Uncertainty propagation

A set of fundamental combustion data is chosen as simulation targets to cover as wide a range of combustion conditions as possible. Active parameters for each experiment are identified by a local sensitivity analysis of the observables with respect to the reaction Arrhenius pre-factors. It is then assumed that the chemical model response η_r can be expressed as a polynomial response surface with respect to active parameters expressed as factorial variables. For N uncertain rate parameters, the response can be described by

$$\eta_r(\mathbf{x}) = \eta_{r,0} + \sum_{i=1}^N a_i x_i + \sum_{i=1}^N \sum_{j \geq i}^N b_{ij} x_i x_j, \quad (1)$$

where x_i is a factorial rate parameter variable ($-1 \leq x_i \leq 1$). The response surface coefficients a_i and b_{ij} can be determined as described in [11, 12]. Uncertainty in the model prediction due to the rate coefficients can be determined by treating each of them as a lognormally-distributed random variable, independent of all the others, with 2σ -uncertainty defined by the uncertainty factor f_i . This is equivalent to

$$x_i = \frac{1}{2} \xi_i, \quad (2)$$

where ξ_i is a unit-normal random variable. If a more sophisticated description of the rate parameters is desired, \mathbf{x} can be described as a polynomial in $\boldsymbol{\xi}$,

$$\mathbf{x} = \mathbf{x}^{(0)} + \sum_{i=1}^M \boldsymbol{\alpha}_i \xi_i, \quad (3)$$

which can be propagated into (1) to yield a stochastic representation of η_r ,

$$\eta_r(\boldsymbol{\xi}) = \eta_r(\mathbf{x}_0) + \sum_{i=1}^M \hat{\boldsymbol{\alpha}}_{r,i} \xi_i + \sum_{i=1}^M \sum_{j=i}^M \hat{\boldsymbol{\beta}}_{r,ij} \xi_i \xi_j, \quad (4)$$

where the coefficient vector $\hat{\boldsymbol{\alpha}}$ and $\hat{\boldsymbol{\beta}}$ can be calculated from the response surface equation. Equation (4) can then be used to calculate the predicted uncertainty by taking its expected value. Therefore, if the variation of the factorial variables is prescribed, then the solution mapping method can be used to explicitly calculate of the uncertainty in model predictions.

B. Optimization

The difference between the model response and experimental observations is minimized as detailed in [6]. Explicitly, this minimization is done with least-squares

optimization that best fits the experimental data given to it.

It is expected that some of the experimental data chosen for validation will not be consistent with the optimized model, and therefore a consistency measure may be used to determine which of the reduction targets should be removed. When a final optimized model has been determined, the remaining uncertainty is calculated. It is assumed that all experiments are independent of each other and a distribution is defined, termed the target distribution, where each target has its own ξ_i , as

$$\eta_r(\xi) = \eta_r^{\text{obs}} + \sigma_r^{\text{obs}} \xi_r \quad (5)$$

The optimized model uncertainty is described by an expansion similar to (3) that minimizes the difference between the predicted distribution (4) and the target distribution (5); obtaining this expansion is described in detail in [6]. The result is therefore an optimized model along with a rigorously-calculated uncertainty.

C. Model Reduction

The model optimization procedure detailed above produced a chemical kinetics model optimized for ethylene combustion. However, because the model contains over 100 species, it is unsuitable for use in computational fluid dynamics applications. As such, a reduced form of the model must be developed. The LOI method [3] is used to determine the species that must be retained in the reduced mechanism. In this method, a non-dimensional lifetime \mathcal{S}_i is defined for each species such that those species that have short lifetimes relative to the mean convective time will have very small \mathcal{S}_i , whereas those with long lifetimes will have \mathcal{S}_i close to unity. This lifetime parameter is combined with a calculation of the sensitivity of each observable to the species concentration; the result is the LOI index, L_i . Species with large L will have long lifetimes and large sensitivities and so must be explicitly included in the reduced model. It should be noted that LOI reduction is used here as an example, and MUM-PCE could be just as easily applied for any other model reduction methods.

D. Reduced Model Uncertainty Estimate

As stated above, the uncertainty estimation procedure is similar to the QSSA error discussed in [10]. Consider a general dynamical model L ,

$$L[\boldsymbol{\varphi}(\mathbf{x}, t), \mathbf{x}, t] = f(\mathbf{x}, t), \quad (6)$$

where $\boldsymbol{\varphi}$ is the solution of L and \mathbf{x} is the spatial coordinate. We define two solutions, $\boldsymbol{\varphi}^{(D)}$ and $\boldsymbol{\varphi}^{(r)}$, which are the steady-state solutions to the detailed and reduced models, respectively. In [10], the error introduced by the QSSA, $\Delta\boldsymbol{\varphi}$, evolves according to

$$\frac{d\Delta\boldsymbol{\varphi}}{dt} = \mathbf{J}\Delta\boldsymbol{\varphi}, \quad (7)$$

where \mathbf{J} is the Jacobian of the detailed model. This can be thought of as using $\boldsymbol{\varphi}^{(r)}$ as the initial guess for the detailed model and, in the long-time limit, should be equal to the difference between $\boldsymbol{\varphi}^{(D)}$ and $\boldsymbol{\varphi}^{(r)}$. For a steady state problem such as stationery, premixed flames or combustion in a perfectly stirred reactor, it is not desirable

to integrate (7), and so the QSSA error can be estimated by calculating the rate-of change vector $\mathbf{F} \mathbf{p} \mathbf{f}$ the detailed model, and then estimating $\boldsymbol{\varphi}^{(D)}$ using a single Newton step,

$$\Delta\boldsymbol{\varphi} = -\mathbf{J}^{-1} \mathbf{F}(\boldsymbol{\varphi}^{(r)}). \quad (8)$$

This then gives a robust criterion for comparing the detailed and reduced model, when coupled with the uncertainty analysis performed in section B. At this point, if the predictions of the reduced model do not agree with those of the detailed model, the reduced model may be re-optimized as described in section B, thus ensuring its predictive capacity.

ACKNOWLEDGMENT

The work at USC was sponsored by the U.S. Air Force Office of Scientific Research (AFOSR) (Grant No. FA9550-07-1-0168) and by the Strategic Environmental Research and Developmental Program (SERDP).

REFERENCES

- [1] U. Maas and S.B. Pope, "Simplifying chemical kinetics: Intrinsic low-dimensional manifolds in composition space." *Combust. Flame*, vol 88, pp. 239-264. 1992
- [2] H. Wang and M. Frenklach, "Detailed reduction of reaction mechanisms for flame modeling." *Combust. Flame*, vol 87, pp. 365-370. 1991
- [3] T. Lovas, D. Nilsson, and F. Mauss, "Automatic reduction procedure for chemical mechanisms applied to premixed methane/air flames." *Proc. Combust. Inst.*, vol 28, pp. 1809-1815. 2000
- [4] T. Lovas, P. Amneus, F. Mauss, and E. Mastorakos, "Comparison of automatic reduction procedures for ignition chemistry." *Proc. Combust. Inst.*, vol 29, pp. 1387-1393. 2002
- [5] T. Lovas, F. Mauss, C. Hasse, and N. Peters, "Development of adaptive kinetics for application in combustion systems." *Proc. Combust. Inst.*, vol 29, pp. 1403-1410. 2002
- [6] D.A. Sheen, X. You, H. Wang, and T. Lovas, "Spectral uncertainty quantification, propagation and optimization of a detailed kinetic model for ethylene combustion." *Proc. Combust. Inst.*, vol 32, pp. 535-542. 2009.
- [7] M.T. Reagan, H.N. Najm, R.G. Ghanem and O.M. Kiono. "Uncertainty quantification in reacting flow simulations through non-intrusive spectral projection. Combustion and Flame." *Combust. Flame* 132 pp. 545-555, 2003.
- [8] M.T. Reagan, H.N. Najm, B.J. Debusschere, O.P. Le Maitre, O.M. Kiono and R.G. Ghanem. "Spectral stochastic uncertainty quantification in chemical systems." *Combust. Theory Model.* 8 pp. 607-632 (2004).
- [9] M.T. Reagan, H.N. Najm, P.P. Pépey, O.M. Kiono, R.G. Ghanem. "Quantifying uncertainty in chemical systems modeling." *Int. J. Chem. Kinet.* 37, pp. 368-382 (2005).
- [10] T. Turanyi, A.S. Tomlin, and M.J. Pilling, "On the error of the quasi-steady-state approximation." *J. Phys. Chem.*, vol 97, pp. 163-172. 1993
- [11] G.E.P. Box, W.G. Hunter, and J.S. Hunter, *Statistics for Experimenters: Introduction to Design, Data Analysis, and Model Building*. 1978, New York, NY: Wiley.
- [12] S.G. Davis, A.B. Mhadeshwar, D.G. Vlachos, and H. Wang, "A new approach to response surface development for detailed gas-phase and surface reaction kinetic model optimization." *Int. J. Chem. Kinet.*, vol 36, pp. 94-106. 2004

Geometric criteria for model reduction in chemical kinetics via optimization of trajectories

Dirk Lebiedz*, Volkmar Reinhardt†, Jochen Siehr†

* Modeling and Scientific Computing Group, ZBSA, University of Freiburg, Germany

† Interdisciplinary Center for Scientific Computing, University of Heidelberg, Germany

Abstract—In previous work we proposed an approach for the approximation of slow invariant manifolds by computing trajectories as solutions of an optimization problem with respect to their initial values. The objective functional of the optimization problem is supposed to represent the extent of relaxation of chemical forces. Following these ideas we discuss this approach on the basis of results for three example models of chemical reaction mechanisms.

I. INTRODUCTION

The need for reduced chemical kinetics is motivated by the fact that the computational effort for a full simulation of reactive flows, e.g. of fluid transport involving combustion processes, is computationally extremely expensive.

For getting useful approximations of the full mechanism, we are convinced, that global information on phase space dynamics should be used to determine the reduced kinetics. As reaction kinetics are usually modeled by ordinary differential equations (ODE), trajectories in phase space that are solutions of these ODE bear global information of the system dynamics. This information can be exploited within a trajectory optimization framework for identifying suitable reaction trajectories approximating slow attracting manifolds, where – after a short initial time – the system dynamics take place.

A suitable formulation of the computation of reduced models as an optimization problem assures the existence of a solution irrespective of assumptions on the time scale structure and sophisticated optimization software can be used for the numerical solution of these problems.

The optimization criterion for the identification of suitable trajectories should represent the assumption that chemical forces are maximally relaxed along these trajectories. Various approaches for the formulation of optimization criteria are conceivable.

II. METHODOLOGY

A. General Problem Formulation

In our approach the general trajectory-based optimization problem can be written as

$$\min_c \int_0^{t_f} \Phi(c(t)) dt \quad (1a)$$

The authors thank the German Research Foundation (DFG) for funding, in particular in the Special Research Area (SFB) 568.

subject to

$$\frac{dc(t)}{dt} = f(c(t)) \quad (1b)$$

$$0 = g(c(0)) \quad (1c)$$

$$c_k(0) = c_k^0, \quad k \in I_{\text{fixed}}. \quad (1d)$$

Here the nonlinear function f describes the chemical reaction kinetics for the chemical species vector $c(t)$. The element mass conservation is collected in g . I_{fixed} is the index set of reaction progress variables chosen for parameterization of the reduced model. These can in principle be selected without restriction from the list of all species and are fixed at $t = 0$ in (1d). All other species concentrations at $t = 0$ are free variables and subject to optimization. Thus the solution of the optimization problem is equivalent to species reconstruction. The computed full composition should represent a point on the slow invariant manifold. The final time t_f is chosen as large as necessary for approximately reaching the chemical equilibrium point. The central issue to be addressed is how to choose the objective function Φ in (1a). This will be discussed in the following.

B. Entropy-Based Criteria

In previous work (including the first workshop on model reduction in reacting flows, Rome 2007) the entropy production rate was suggested as an optimization criterion. Entropy production is related to the relaxation of chemical forces and the development of partial equilibria [1].

The formula for the entropy production rate with the forward and backward reaction rates $R_{j,\rightarrow}$ and $R_{j,\leftarrow}$, respectively, is

$$\frac{dS_j}{dt} = R(R_{j,\rightarrow} - R_{j,\leftarrow}) \log\left(\frac{R_{j,\rightarrow}}{R_{j,\leftarrow}}\right) \quad (2)$$

for the j -th elementary reaction in the kinetic mechanism. Here R is the gas constant. With (2) a relaxation criterion for the objective function (1a) can be formulated

$$\Phi(c(t)) = \sum_{j=1}^m \frac{dS_j}{dt}. \quad (3)$$

This criterion was studied in [1] and [2]. The results and the concept of the approach look promising but do not provide a sufficiently accurate approximation of the slow attracting manifold, in particular far from equilibrium. In the following, alternative criteria have been investigated.

C. Geometric Criteria

As stated above, a suitable reduction criterion $\Phi(c(t))$ should characterize the relaxation of “chemical forces”. From a physical point of view, curvature (in the sense of the rate of change in velocity) is closely related to the geometric interpretation of force. The aim of [3], [4], [5], [6] was to make an attempt to transfer that relation to the field of reaction kinetics in a way suitable to model reduction via problem formulations such as in (1).

In chemical systems, dissipative forces are active. The different time scales of dynamic modes result in an anisotropic force relaxation in phase space. We consider the tangent (reaction velocity) vectors $\dot{c}(t) = f(c(t))$ of reaction trajectories. The relaxation of chemical forces results in a change of $\dot{c}(t)$ along a trajectory on its way towards chemical equilibrium. This change along the trajectory may be characterized by taking the directional derivative of the tangent vector of the curve $c(t)$ with respect to its own direction $v := \frac{\dot{c}}{\|\dot{c}\|_2}$.

Mathematically that can be formulated as

$$D_v \dot{c}(t) := \frac{d}{d\alpha} (\dot{c}(t) + \alpha v) \Big|_{\alpha=0} = J_c f \cdot \frac{f}{\|f\|_2},$$

with $J_c f$ being the Jacobian of the right hand side f evaluated at $c(t)$ and $\|\cdot\|_2$ denoting the Euclidian norm. Hence, we may choose the optimization criterion

$$\Phi(c) = \frac{\|J_c f \cdot f\|_2}{\|f\|_2}. \quad (4)$$

The natural way for the evaluation of this criterion would be a path integral along the trajectory towards equilibrium

$$\int_{l(0)}^{l(c^{\text{eq}})} \Phi(c(l(t))) dl(t),$$

where $l(t)$ is the length of the curve $c(t)$ at time t given by

$$l(t) = \int_0^t \|\dot{c}(\tau)\|_2 d\tau.$$

This results in the reparametrization

$$dl(t) = \|\dot{c}(t)\|_2 dt. \quad (5)$$

The objective used in (1a) would be

$$\min_c \int_0^{t_f} \|J_c f \cdot f\|_2 dt. \quad (6)$$

However, an alternative norm for the evaluation of $\|J_c f \cdot f\|$ might be taken into account, which has already been used in [7] and is motivated from thermodynamics. In this norm the criterion adapted from (4) can be written as

$$\frac{\|J_c f \cdot f\|_W}{\|f\|_W} = \frac{(f^T \cdot (J_c f)^T \text{diag}(1/c_i) J_c f \cdot f)^{1/2}}{\|f\|_W} \quad (7)$$

with $W = \text{diag}(1/c_i)$ being the diagonal matrix with diagonal elements $1/c_i$. This criterion brings thermodynamic considerations into play and represents the Riemannian metric induced by the second differential of Gibbs

free enthalpy G

$$G = \sum_{i=1}^n c_i [\ln(c_i/c_i^{\text{eq}}) - 1], \quad W = \text{Hess}(G).$$

The corresponding metric has been discussed in the context of an entropic scalar product [8]. The corresponding optimization problem is

$$\min_c \int_0^{t_f} \|J_c f \cdot f\|_W dt. \quad (8)$$

In the following results for both criteria (6) and (8) are presented.

D. Numerical Methods

Problem (1) together with a suitable choice of $\Phi(c(t))$ can be numerically solved with an appropriate solver for nonlinear programming problems (NLP) coupled to a numerical integrator. For our results MUSCOD-II [9], [10] is used. This software package is based on a multiple shooting discretization of trajectories and sequential quadratic programming (SQP) for the resulting finite-dimensional NLP. For numerical integration on the multiple shooting intervals DAESOL [11], [12] is used, which is an integrator based on backward differentiation formulae.

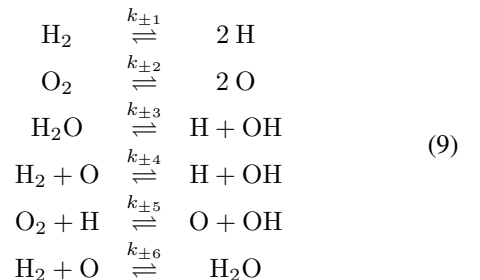
The computation of optimal trajectories for neighboring fixed initial values for the reaction progress variables in order to span higher-dimensional manifolds by families of trajectories can be significantly accelerated by the use of continuation methods embedding the problem into a parametric family of optimization problems. Diehl et al. describe an efficient numerical implementation of an initial value embedding strategy in [13]; this strategy is used for the computations presented below.

III. RESULTS

Here we present the application of the method described above for three example problems. First a temperature-independent six species hydrogen combustion process is analyzed, then we study the benchmark Skodje-Davis system and finally we discuss a temperature dependent ozone mechanism involving oxygen as only chemical element.

A. Example Mechanism: Hydrogen Combustion

In this section we consider a small test mechanism taken from [8], that we already used for previous work:



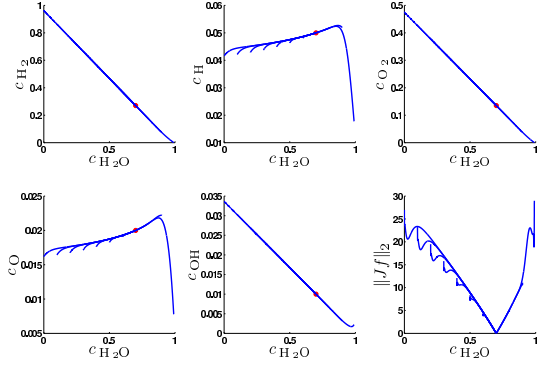


Fig. 1. Solution of (1) with (4) as relaxation criterion for the hydrogen combustion mechanism (9).

with the rate constants

$$\begin{aligned}
 k_1 &= 2.0, & k_{-1} &= 216.0 \\
 k_2 &= 1.0, & k_{-2} &= 337.5 \\
 k_3 &= 1.0, & k_{-3} &= 1400.0 \\
 k_4 &= 1000.0, & k_{-4} &= 10800.0 \\
 k_5 &= 1000.0, & k_{-5} &= 33750.0 \\
 k_6 &= 100.0, & k_{-6} &= 0.7714.
 \end{aligned}$$

Together with the conservation relations

$$\begin{aligned}
 2c_{\text{H}_2} + 2c_{\text{H}_2\text{O}} + c_{\text{H}} + c_{\text{OH}} &= C_1 \\
 2c_{\text{O}_2} + c_{\text{H}_2\text{O}} + c_{\text{O}} + c_{\text{OH}} &= C_2
 \end{aligned}$$

this mechanism yields a system with four degrees of freedom. For the computations with this mechanism mass relations with $C_1 = 2.0$ and $C_2 = 1.0$ were chosen.

In Fig. 1 the results with the Euclidian norm criterion (6) as objective functional are depicted. We analyze the approximation accuracy of the slow manifold via checking consistency (invariance) by restarting the solution of the optimization problem from a later time point on the earlier computed trajectory. If the slow invariant manifold has been identified correctly, the solution of the second optimization problem should be exactly on the trajectory computed before, a property that we denote consistency. The results are not too bad but can be improved.

The weighted norm proposed in (8) is used as a criterion for the results presented in Fig. 2. The results demonstrate that this criterion can be regarded to be nearly consistent. These results encourage to test the criterion (7) for the Davis-Skodje problem in the next section.

B. Davis-Skodje Problem

The well-known Davis-Skodje mechanism is our second test case.

$$\begin{aligned}
 \frac{dy_1}{dt} &= -y_1 \\
 \frac{dy_2}{dt} &= -\gamma y_2 + \frac{(\gamma - 1)y_1 + \gamma y_1^2}{(1 + y_1)^2},
 \end{aligned}$$

where $\gamma > 1$ is a measure for the spectral gap or stiffness respectively of the system. Results are shown in Fig. 3. For large values of γ , representing a large gap in time scales between fast and slow modes, the results are acceptable. For small values of γ the approximation is getting worse.

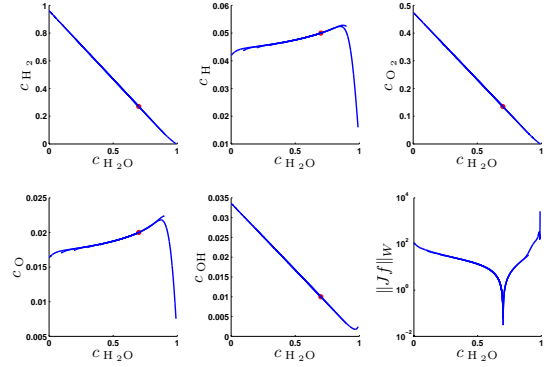


Fig. 2. Solution of (1) with (7) as relaxation criterion for the hydrogen combustion mechanism (9). The results look promising.

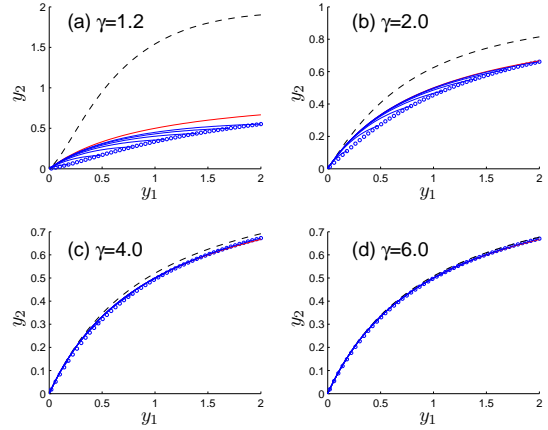


Fig. 3. Results for the Davis-Skodje problem with (8) as relaxation criterion. Results for different values of γ are shown. The red curve is the analytically computed SIM (slow invariant manifold). The black dashed curve represents the analytic Maas-Pope-ILDM. The blue curves are trajectories integrated from solution points of our optimization problem.

C. Example Mechanism: Ozone

The last test case is a three component ozone mechanism shown in Table I taken from [14]. It is chosen to demonstrate the performance of our method taking temperature dependence into account. Many approaches based on time scale separation fail when the spectral gap becomes too small. Together with the element conservation

$$c_{\text{O}} + 2c_{\text{O}_2} + 3c_{\text{O}_3} = C$$

this mechanism yields a system with two degrees of freedom. We use without loss of generality $C = 1$.

TABLE I
OZONE DECOMPOSITION MECHANISM FROM [14]. RATE COEFFICIENT $k = AT^b \exp(-E_a/RT)$. COLLISION EFFICIENCIES IN REACTIONS INCLUDING M: $f_{\text{O}} = 1.14, f_{\text{O}_2} = 0.40, f_{\text{O}_3} = 0.92$.

Reaction	A (cm, mol, s)	b	E_a (kJ/mol)
$\text{O} + \text{O} + \text{M} \rightarrow \text{O}_2 + \text{M}$	2.90×10^{17}	-1.0	0.0
$\text{O}_2 + \text{M} \rightarrow \text{O} + \text{O} + \text{M}$	6.81×10^{18}	-1.0	496.0
$\text{O}_3 + \text{M} \rightarrow \text{O} + \text{O}_2 + \text{M}$	9.50×10^{14}	0.0	95.0
$\text{O} + \text{O}_2 + \text{M} \rightarrow \text{O}_3 + \text{M}$	3.32×10^{13}	0.0	-4.9
$\text{O} + \text{O}_3 \rightarrow \text{O}_2 + \text{O}_2$	5.20×10^{12}	0.0	17.4
$\text{O}_2 + \text{O}_2 \rightarrow \text{O} + \text{O}_3$	4.27×10^{12}	0.0	413.9

The results for the Euclidian criterion (4) shown in Fig. 4 appear to become worse in particular for low temperatures. In contrast the weighted criterion (7) gives much better results as illustrated in Fig. 5.

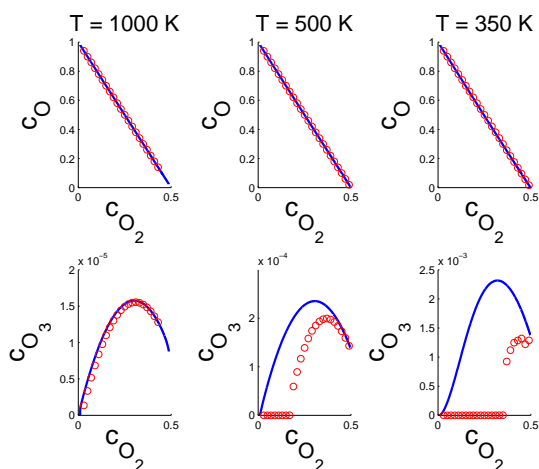


Fig. 4. Solution of (1) with (6) as objective function for the ozone mechanism as in Table I. Here red dots denote the solution for different values of the progress variable c_{O_2} . The blue trajectory can be regarded as relaxed to the one-dimensional SIM after a short integration time.

IV. CONCLUSION

Here we present an extension of the model reduction approach discussed at the first workshop in Rome and in [5]. Various geometric criteria are investigated. In many cases the results demonstrate a good quality of the approximation of the slow attracting manifold. The SIM can even be approximated with sufficient accuracy for the ozone mechanism in the case of low temperatures.

To summarize, this approach looks promising for application to realistic and large-scale detailed combustion mechanisms. Even though a detailed and systematic investigation of the different criteria with a focus on theoretical analysis, approximation accuracy and (numerical) applicability remains a challenging task for our future work.

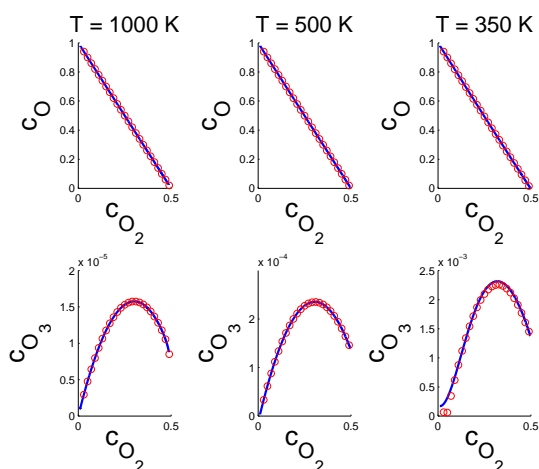


Fig. 5. Solution of (1) with (7) as relaxation criterion for the ozone mechanism as in Fig. 4. The results look much better even for low temperature.

ACKNOWLEDGMENT

The authors thank the Interdisciplinary Center for Scientific Computing Heidelberg, Germany, in particular Prof. Dr. Dr. h.c. H.G. Bock for providing the MUSCOD-II-package, Prof. Dr. Moritz Diehl (now at K.U. Leuven, Belgium) for the initial value embedding add-on for MUSCOD-II.

REFERENCES

- [1] D. Lebiez, "Computing minimal entropy production trajectories: An approach to model reduction in chemical kinetics," *J. Chem. Phys.*, vol. 120, pp. 6890–6897, 2004.
- [2] D. Lebiez, V. Reinhardt, and J. Kammerer, "Novel trajectory based concepts for model and complexity reduction in (bio)chemical kinetics," in *Model reduction and coarse-graining approaches for multi-scale phenomena*, A.N. Gorban, N. Kazantzis, I.G. Kevrekidis, H.C. Öttinger, C. Theodoropoulos, Eds. Heidelberg: Springer, 2007, pp. 343–364.
- [3] D. Lebiez, "Optimal Control, Model- and Complexity-Reduction of Self-Organized Chemical and Biochemical Systems: A Scientific Computing Approach," *Habilitation thesis, University of Heidelberg*, 2006.
- [4] M. Winckler, "Towards optimal criteria for trajectory-based model reduction in chemical kinetics via numerical optimization," *Diploma thesis, University of Heidelberg*, 2007.
- [5] V. Reinhardt, M. Winckler, and D. Lebiez, "Approximation of Slow Attracting Manifolds in Chemical Kinetics by Trajectory-Based Optimization Approaches," *J. Phys. Chem.*, vol. 112, pp. 1712–1718, 2008.
- [6] V. Reinhardt, "On the Application of Trajectory-based Optimization for Nonlinear Kinetic Model Reduction," *PhD thesis, University of Heidelberg*, 2008.
- [7] F. Weinhold, "Metric geometry of equilibrium thermodynamics," *J. Phys. Chem.*, vol. 63, pp. 2479–2483, 1975, and his following publications.
- [8] A.N. Gorban and I.V. Karlin and A.Yu. Zinovyev, "Constructive methods of invariant manifolds for kinetic problems," *Phys. Rep.*, vol. 396, pp. 197–403, 2004.
- [9] H.G. Bock and K.J. Plitt, "A multiple shooting algorithm for direct solution of optimal control problems," in *Proceedings of the Ninth IFAC World Congress, Budapest*, 1984.
- [10] D.B. Leineweber, I. Bauer, H.G. Bock, and J.P. Schlöder, "An Efficient Multiple Shooting Based Reduced SQP Strategy for Large-Scale Dynamic Process Optimization," *Comput. Chem. Eng.*, vol. 27, pp. 157–174, 2003.
- [11] I. Bauer, F. Finocchi, W.J. Duschl, H.-P. Gail, and J.P. Schlöder, "Simulation of chemical reactions and dust destruction in protoplanetary accretion discs," *Astron. Astrophys.*, vol. 317, pp. 273–289, 1997.
- [12] J. Albersmeyer, "Efficient sensitivity generation in an adaptive BDF method," *Diploma thesis, University of Heidelberg*, 2005.
- [13] M. Diehl, H.G. Bock, J. Schlöder, R. Findeisen, Z. Nagy and F. Allgöwer, "Real-time optimization and nonlinear model predictive control of processes governed by differential-algebraic equations," *J. Process Contr.*, vol. 12, pp. 577–585, 2002.
- [14] U. Maas and J. Warnatz, "Simulation of Thermal Ignition Processes in Two-Dimensional Geometries," *Z. Phys. Chem. NF*, vol. 161, pp. 61–81, 1989.

Mechanism Reduction Based on Simulation Error Minimization

Tibor Nagy and Tamás Turányi*

Institute of Chemistry, Eötvös University (ELTE), Budapest, Hungary

Abstract—A new species reduction method called the Simulation Error Minimization Connectivity Method (SEM-CM) was developed. According to the SEM-CM algorithm, a mechanism building procedure is started from the important species. Strongly connected sets of species, identified on the basis of the normalized Jacobian, are added and several consistent mechanisms are produced. The model is simulated with each of these mechanisms and the mechanism causing the smallest error (i.e. deviation from the model that uses the full mechanism), considering the important species only, is selected. Then, in several steps other strongly connected sets of species are added, the size of the mechanism is gradually increased and the procedure is terminated when the error becomes smaller than the required threshold. A new method for the elimination of redundant reactions is also presented, which is called the Principal Component Analysis of Matrix F with Simulation Error Minimization (SEM-PCAF). According to this method, several reduced mechanisms are produced by using various PCAF-thresholds. The reduced mechanism having the least CPU time requirement among the ones having almost the smallest error is selected. Application of SEM-CM and SEM-PCAF together provides a very efficient way to eliminate redundant species and reactions from large mechanisms. The suggested approach was tested on a mechanism containing 6874 irreversible reactions of 345 species that describes methane partial oxidation to high conversion. The aim is to accurately reproduce the concentration–time profiles of 12 major species with less than 5% error at the conditions of an industrial application. The reduced mechanism consists of 246 reactions of 47 species and its simulation is 116 times faster than using the full mechanism. The SEM-CM was found to be more effective than the classic Connectivity Method, and also than the DRG, two-stage DRG, DRGASA, basic DRGEP and extended DRGEP methods.

I. INTRODUCTION

Almost all published detailed reaction mechanisms contain redundant species and reactions [1]. Elimination of redundant species and reactions from a large reaction mechanism allows a significant decrease of simulation time. Also, other mechanism reduction methods, based for example on time scale analysis [2-4] or lumping [5] may be more efficient if the starting mechanism is smaller. Several reviews have dealt with the problem of mechanism reduction [1] [6-7].

Frenklach et al. [8] suggested a method for the elimination of species and reactions from a detailed

mechanism, when the aim was the reproduction of ignition delay times and temperature profiles. The first general systematic method for species reduction, which is called here the Connectivity Method, was suggested by Turányi [9] and since then several other methods have been published for this task [10-23].

In this paper algorithms Simulation Error Minimization Connectivity Method (SEM-CM) and Principal Component Analysis of Matrix F with Simulation Error Minimization (SEM-PCAF) are described briefly. More details can be found in our recent article [23].

II. SIMULATION ERROR MINIMIZATION CONNECTIVITY METHOD (SEM-CM)

A. Definitions

The aim of simulations is to reproduce the concentration profiles of the *important species* or to reproduce some important features. The mechanism reduction methods select further species to the group of important species to ensure the good agreement between the simulation results obtained using the full and the reduced mechanisms. A *complementary set* consists of those species that are not yet selected but would yield at least one additional selected reaction if these were introduced to the current group of selected species. Note that according to this definition, unions of complementary sets are also complementary sets.

A species is designated a *living species* if its initial concentration is non-zero or it has an inflow term (e.g. non-zero inlet concentration in a PSR) or if it is formed in chemical reactions. The list of living species depends on the mechanism and also on the initial (or boundary) conditions. A mechanism is called *consistent*, if each of its species is living at least at one condition.

B. The algorithm

Connection of a complementary set to the group of currently selected species can be assessed by the following measure:

$$C_k = \frac{1}{n_k} \sum_{i \in \text{set}} B_i = \frac{1}{n_k} \sum_{i \in \text{set}} \sum_{j \in \text{group}} \bar{J}_{ij}^2,$$

where $\bar{J}_{ij} = (c_i/f_j)(\partial f_j/\partial c_i)$ is an element of the normalized Jacobian.

The Simulation Error Minimization Connectivity Method (SEM-CM) can be summarized as follows.

The work was supported by OTKA fund T68256.

Starting from the group of n_{imp} important species, complementary sets strongly connected to them are added at each time and the formed reduced mechanisms are made consistent if necessary. Depth level m means that the first m complementary sets with the highest C_k values are considered. The complex model is simulated with each of these mechanisms and their sets of species with their errors are stored in a database. The reduced mechanism that has $n_{\text{imp}}+1$ species and has the smallest error is identified in the database, and the previous procedure is repeated. If no such a mechanism exists, mechanism with species number $n_{\text{imp}}+2$, $n_{\text{imp}}+3$, *etc.* is looked for. The mechanism building is terminated when the simulation error, using the reduced mechanism, becomes smaller than a required threshold. This way, a series of consistent reduced mechanisms are produced, usually with continuously decreasing error.

While the SEM-CM procedure effectively reduces the number of species, the reduced mechanisms may still contain redundant reactions.

III. PRINCIPAL COMPONENT ANALYSIS OF MATRIX F WITH SIMULATION ERROR MINIMIZATION (SEM-PCAF)

A. The algorithm

The procedure above results in a series of consistent reduced mechanisms with different number of necessary species. These mechanisms can be reduced further via the elimination of the redundant reactions. This may lead to a reduced mechanism that can be simulated much faster, while the error of simulation remains essentially the same.

The identification of the redundant reactions is carried out using the principal component analysis (PCA) of the normalized rate sensitivity matrix \bar{F} [24]. This matrix is defined as $\bar{F}_{ij} = (k_i/f_j)(\partial f_j/\partial k_i)$. This method has been encoded as the PCAF option of KINALC [25]. In this program the user has to suggest one or several thresholds for the eigenvalues and the eigenvector elements.

Increasing the threshold values of PCAF in small steps results in the elimination of further reactions, and it causes small, but non-monotonic changes in the error of important species. Therefore, it is impossible to find the optimum threshold values based on a systematic search. Thus, the PCAF procedure is adapted here in such a way, that many different thresholds are tried automatically. Initially, low thresholds for the eigenvalues and eigenvectors are selected, leading to the elimination of few reaction steps. Then, both thresholds are changed independently, resulting in several different, smaller reduced mechanisms. Each of the obtained reduced mechanisms is investigated for consistency. If a mechanism is found not to be consistent, then the corresponding thresholds are considered to be too high, and this mechanism is discarded.

B. Optimization for simulation time

Simulations are carried out with all consistent mechanisms, and the errors and CPU times are recorded. Many different reduced mechanisms may have an error that is very close to the smallest error found. However, these mechanisms may have significantly different numbers of reactions, thus the required computing times for the simulations may vary considerably. The aim is to

find the fastest one among all reduced mechanisms having similarly small errors. Mechanisms having errors not more than a few percent higher than the smallest error are investigated further. From all these mechanisms, the one having the smallest CPU time is accepted as the recommended reduced mechanism.

IV. EXAMPLE

Anthony Dean and his co-workers developed a large elementary reaction mechanism [26] in order to describe the homogeneous gas-phase chemistry in the anode channel of natural gas fuelled solid-oxide fuel cells (SOFCs). At the operation of the fuel cell, air is added to the natural gas to prevent deposit formation. Thus, the mechanism has to describe the partial oxidation of methane up to high conversion. The full reaction mechanism includes 345 species and 6874 irreversible reactions. This mechanism, due to its large size, cannot be used in reacting flow models for the optimization of fuel cell geometry and operating conditions. Our goal was to produce a reduced mechanism, which reproduces the simulation results of the original mechanism for all large concentration species within a few percent of error.

The selected initial parameters were representative for the SOFC operation, that is temperature and pressure were chosen to be 900 °C (1173.15 K) and 1 atm (101325 Pa), respectively. The simulations were carried out at isothermal and isobaric conditions. The composition of the initial mixture was 30.0 % v/v methane and 70.0 % v/v air.

Home-made Fortran codes were developed for the SEM-CM and SEM-PCAF calculations. Another series of Fortran codes were produced for the application of the various DRG and DRGEP methods, including the original DRG method [15], and also later improvements like linear time reduction [16], two-stage reduction (restart) [16] and DRGASA [18]. The applied DRGEP method included as options scaling and group-based coefficients [21]. The Connectivity Method was applied using a modified version of KINALC [25].

Species CH₄, N₂, O₂, H₂, H₂O, CH₂O, CO, CO₂, C₂H₂, C₂H₄, C₂H₆ and benzene (C₆H₆) were considered important. The mole fraction of these species exceeded 0.001 during the 1000 s simulation time.

Fig. 1 compares the best versions of all investigated methods. Considering the maximum errors as a function of the number of species, the classic Connectivity Method has the worst performance. At 5% required error, it leaves 139 species in the reduced mechanism by eliminating 206 species. DRGEP is usually better than the two-stage DRG (DRG restart). Using DRGASA, the error is increasing by eliminating more and more species, and this method results in a small mechanism of 57 species at 5% error. SEM-CM using depth level 1 gives a reduced mechanism of similar size. However, SEM-CM using high depth level (in this case up to depth level 256) is the best of all these methods, since it provided a 47-species reduced mechanism.

In the DRG method, it is generally assumed that the simulation error decreases monotonically when threshold ε is lowered, provided that threshold ε is small (e.g. less than 0.2). It is true for the error of flux calculation, but not for the simulation error of the concentration profiles. Fig. 2 shows that by decreasing epsilon the simulation error

decreases in large steps and also non-monotonically, while the number of species in the reduced mechanism increases in a monotonic way. The result is that almost the same simulation error can be obtained with mechanisms of very different size using the DRG method. This shows that in the DRG method several epsilon values should be tried and the resulting mechanisms should be checked by simulations.

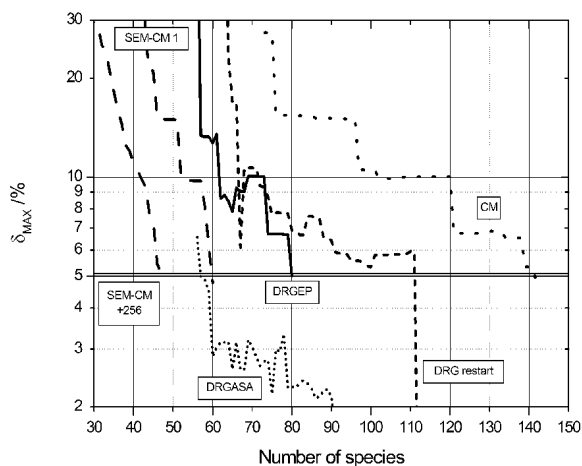


Fig. 1. Maximal simulation errors of the mechanisms as function of species number, obtained by the Connectivity Method (CM), DRG with restart, the basic DRGEP, DRGASA-improved results of the DRG-restart method, and SEM-CM (depth levels 1+4+...+256).

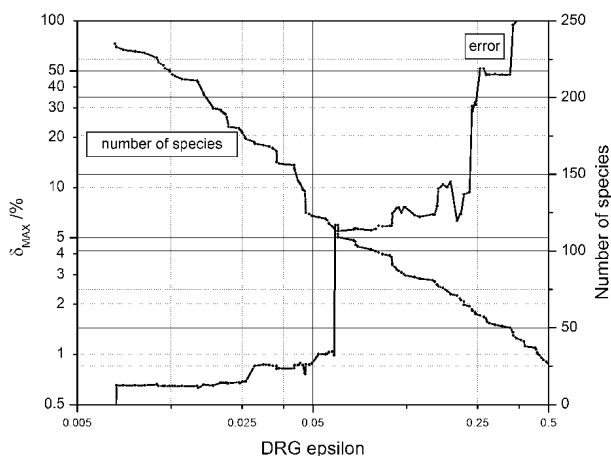


Fig. 2. Maximal simulation error and the number of species as a function of epsilon using the original DRG method.

Table I shows the numerical results for the best versions of the DRG, DRGEP, CM and SEM-CM methods. DRGEP and CM required about 1 minute CPU time. Both DRGASA and SEM-CM (depth level 1) required about 10 minutes. SEM-CM (depth level 1+4+...+256) required about 10.5 hours on a desktop PC, but provided far the smallest reduced mechanism of 47 species and 613 irreversible reactions. When SEM-PCAF was applied on the result of the SEM-CM reduction, the number of irreversible reactions could be reduced to 297. If the SEM-PCAF method is applied again on the mechanism obtained as the result of the combined SEM-CM and

SEM-PCAF methods, then an even smaller mechanism is obtained, that consists of 246 reactions.

The Table also indicates the speed-up of simulations as a result of mechanism reduction. SEM-CM (1+4+...+256) alone gave 58.4 times speed-up, while the increase of simulation speed is 103 times if the SEM-CM and SEM-PCAF methods are combined. The simulation of the final reduced mechanism having 47 species and 246 reactions is 116 times faster, than that of the initial mechanism of 345 species and 6874 reactions.

TABLE I.
PERFORMANCE OF THE MECHANISMS FOR THE REQUIRED 5% MAXIMUM ERROR WITH THE SMALLEST POSSIBLE NUMBER OF SPECIES THAT CAN BE ACHIEVED BY EACH METHOD.

method	DRG+restart +DRGASA	DRGEP basic method	CM	SEM-CM depth level 1	SEM-CM depth level 1+4+...+256	+SEM-PCAF	+SEM-PCAF +restart
time to develop the reduced mechanism (hh:mm)	00:10	00:01	01:05	00:12	10:29	+ 00:30	+ 00:42
Size	Species (originally 345)	57	80	139	60	47	47
	irreversible reactions (originally 6874)	821	1172	2494	962	613	297
Simulation time (s)	0.720	1.32	4.87	0.875	0.465	0.263	0.233
speed-up (xtimes)	37.7	20.5	5.57	31.0	58.4	103	116

V. DISCUSSION

Previously published methods for species reduction include the Directed Relation Graph (DRG) method [15-19], the DRG with Error Propagation (DRGEP) method [20-21] and the Connectivity Method [9]. These methods investigate the system of kinetic differential equations (or the reaction graph, which is an equivalent form) for the detection of redundant species and reactions in a large reaction mechanism. The size of the obtained reduced mechanism is controlled by a threshold, which cannot be related directly to the error of reduction, that is the deviation between the simulation results obtained by full and the reduced mechanisms. A range of reduced mechanisms can be obtained by systematically changing this threshold.

In the mechanism reduction approach used in this paper, several thousands of reduced mechanisms are produced based on the investigation of the kinetic differential equations. Using the results of simulations, the best one is selected for a given level of error. This approach was implemented for the elimination of both the

redundant species (SEM-CM) and the redundant reactions (SEM-PCAF).

Similar approaches have been published in the literature. Turányi [9] recommended the elimination of all consuming reactions of each species, one by one, and considering those species as redundant for which the simulation results of these reduced mechanisms remained within an error limit for the important species and/or important reaction features. This method could not predict the effect of the simultaneous elimination of species groups. Petzold and Zhu [11] generated reduced mechanisms using a nonlinear integer programming approach. The simulation error was calculated and used for the optimization process. The method worked well for few-step mechanisms, but for large mechanisms it was applicable only with many extensions and human decisions, like grouping of the reactions and pre-selection of the most important reactions.

DRGASA [18] also has a similar reduction philosophy. Like in the Simulation Error Minimization Connectivity Method used in this paper, another method (DRG) is used as a guideline, reduced mechanisms are produced, and the final reduced mechanism is selected on the basis of the

simulation results. This is the reason why DRGASA performs much better than the other DRG-based methods.

According to the Simulation Error Minimization Connectivity Method (SEM-CM), a mechanism building procedure is initiated by creating a small consistent mechanism comprising the important species and their reactions with other species, extracted from the full mechanism on the basis of the normalized Jacobian.

According to the PCAF method with Simulation Error Minimization (SEM-PCAF), several consistent reduced mechanisms are produced using the PCAF method [24] with various thresholds; then simulations are carried out with all the candidate mechanisms. The reduced mechanism having the least CPU time requirement is selected from the ones related to small errors of reduction. Application of the SEM-PCAF method after the SEM-CM halved the number of reactions and almost doubled the simulation speed.

The suggested mechanism reduction methods were programmed in Fortran 90 and made fully automatic, thus these are readily applicable for the reduction of other reaction mechanisms. The code is available from our Web site [25].

REFERENCES

- [1] A. S. Tomlin, T. Turányi, and M. J. Pilling, "Mathematical tools for the construction, investigation and reduction of combustion mechanisms," in *Low temperature combustion and autoignition*, Amsterdam, Elsevier, 1997, pp. 293–437.
- [2] U. Maas and S. Pope, "Simplifying chemical kinetics - intrinsic low-dimensional manifolds in composition space," *Combust. Flame*, vol. 88, pp. 239–264, March 1992.
- [3] T. Turányi, A. S. Tomlin, and M. J. Pilling, "On the error of the quasi-steady-state approximation," *J. Phys. Chem.*, vol. 97, pp. 163–172, January 1993.
- [4] S. Lam and D. Goussis, "The CSP method for simplifying kinetics," *Int. J. Chem. Kinet.*, vol. 26, pp. 461–486, April 1994.
- [5] H. Huang, M. Fairweather, J. F. Griffiths, A. S. Tomlin, and R. B. Brad, "A systematic lumping approach for the reduction of comprehensive kinetic models," *Proc. Combust. Inst.*, vol. 30, pp. 1309–1316, 2005.
- [6] M. S. Okino and M. L. Mavrouniotis, "Simplification of mathematical models of chemical reaction systems," *Chem. Rev.*, vol. 98, pp. 391–408, March 1998.
- [7] C. K. Law, "Combustion at a crossroads: Status and prospects," *Proc. Combust. Inst.*, vol. 31, pp. 1–29, 2007.
- [8] M. Frenklach, K. Kailasanath, and E. S. Oran, "Systematic development of reduced reaction mechanisms for dynamic modeling," *Progress in Astronautics and Aeronautics*, vol. 105, pp. 365–376, 1986.
- [9] T. Turányi, "Reduction of large reaction mechanisms," *New J. Chem.*, vol. 14, pp. 795–803, 1990.
- [10] H. Wang and M. Frenklach, "Detailed Reduction of Reaction Mechanisms for Flame Modeling," *Combust. Flame*, vol. 87, pp. 365–370, 1991.
- [11] L. Petzold and W. J. Zhu, "Model reduction for chemical kinetics: an optimization approach," *AIChE Journal*, vol. 45, pp. 869–886, April 1999.
- [12] H. S. Soyhan, F. Mauss, and C. Sorousbay, "Chemical kinetic modeling of combustion in internal combustion engines using reduced chemistry," *Combust. Sci. Tech.*, vol. 174, pp. 73–91, November 2002.
- [13] J. Luche, M. Reuillon, J.-C. Boettner, and M. Cathonnet, "Reduction of large detailed kinetic mechanisms: application to kerosene/air combustion," *Combust. Sci. Tech.*, vol. 176, pp. 1935–1963, 2004.
- [14] M. Valorani, F. Creta, D. Goussis, J. Lee, and H. Najm, "An automatic procedure for the simplification of chemical kinetic mechanisms based on CSP," *Combust. Flame*, vol. 146, pp. 29–51, 2006.
- [15] T. Lu and C. K. Law, "A directed relation graph method for mechanism reduction," *Proc. Comb. Inst.*, vol. 30, pp. 1333–1341, 2005.
- [16] T. Lu and C. Law, "Linear time reduction of large kinetic mechanisms with directed relation graph: n-heptane and iso-octane," *Combust. Flame*, vol. 144, pp. 24–36, January 2006.
- [17] T. Lu and C. Law, "On the applicability of directed relation graphs to the reduction of reaction mechanisms," *Combust. Flame*, vol. 146, pp. 472–483, August 2006.
- [18] X. L. Zheng, T. F. Lu, and C. K. Law, "Experimental counterflow ignition temperatures and reaction mechanisms of 1,3-butadiene," *Proc. Combust. Inst.*, vol. 31, pp. 367–375, 2007.
- [19] T. Lu and C. Law, "Strategies for mechanism reduction for large hydrocarbons: n-heptane," *Combust. Flame*, vol. 154, pp. 153–163, 2008.
- [20] P. Pepiot and H. Pitsch, "Systematic Reduction of Large Chemical Mechanisms," *4th Joint Meeting of the U.S. Sections of the Combustion Institute*, Philadelphia, PA, 2005.
- [21] P. Pepiot-Desjardins and H. Pitsch, "An efficient error-propagation-based reduction method for large chemical kinetic mechanisms," *Combust. Flame*, vol. 154, pp. 67–81, 2008.
- [22] I. Gy. Zsély and T. Turányi, "The influence of thermal coupling and diffusion on the importance of reactions: The case study of hydrogen-air combustion," *PCCP*, vol. 5, pp. 3622–3631, 2003.
- [23] T. Nagy and T. Turányi, "Reduction of very large reaction mechanisms using methods based on simulation error minimization," *Combust. Flame*, vol. 156, pp. 417–428, February 2009.
- [24] T. Turányi, T. Bérces, and S. Vajda, "Reaction rate analysis of complex kinetics systems," *Int. J. Chem. Kinet.*, vol. 21, pp. 83–99, 1989.
- [25] <http://garfield.chem.elte.hu/Combustion/Combustion.html>
- [26] G. Gupta, E. S. Hecht, H. Zhu, A. M. Dean, and R. J. Kee, "Gas-phase reactions of methane and natural gas with air and steam in non-catalytic regions of a solid-oxide fuel cell," *Journal of Power Sources*, vol. 156, pp. 434–447, 2006.

Recent Developments in Detailed Chemical Kinetic Mechanisms

Charles K. Westbrook, William J. Pitz and Marco Mehl

Lawrence Livermore National Laboratory, Livermore, CA 94551 USA

Abstract—Mechanism reduction must work for the mechanisms being used in current kinetics research. Recent mechanisms and their uses in combustion research are reviewed, attempting to quantify and limit the needs of new mechanism reduction techniques. These mechanisms also provide an ongoing challenge to reduction practitioners.

I. INTRODUCTION

Chemical kinetic reaction mechanisms have become essential parts of computational models for many types of practical combustion systems, ranging from flames and shock tubes to internal combustion engines, gas turbines and industrial furnaces. Most practical combustors have complex geometries, are essentially three dimensional and must be modeled with 2D or 3D fluid mechanics, and many such systems also feature other complex physics processes in addition to chemical kinetics. In the past, most of the computer resources would be given to the CFD simulation, with sharply reduced or simplified treatments of most or all of the major physics and chemistry submodels. However, in recent years, modeling approaches have become unwilling to sacrifice so much realism and accuracy in these submodels and have addressed problems in which one or more of these submodels provide important and complex interactions with the fluid mechanics.

In this paper, one class of those submodels is discussed in detail, that of the detailed chemical kinetics of practical hydrocarbon fuels. The focus will be not only on the complexity of the fuel combustion model but also on the features of some of the combustion problems of current importance and on the demands these problems place on the kinetics model. Systematic reduction of the kinetics submodels must retain the ability to reproduce those essential features that were in the original kinetic model.

II. SURROGATES FOR PRACTICAL FUELS

Current attention has been focused on developing kinetic mechanisms for practical, largely transportation fuels. A recent publication by the US DOE [1] on Basic Research Needs for Clean and Efficient Combustion of 21st Century Transportation Fuels noted that gasoline, diesel fuel, jet fuel, natural gas, and related transportation fuels consist of complex mixtures of hundreds or thousands of different chemical species, almost all of

which have never had detailed kinetic mechanisms developed for them. The most common strategy to deal with this dilemma is based on the observation that most of the chemical components in these practical fuels can be placed into one of a small number of structural classes, such as n-alkanes, olefins, aromatics, branched alkanes, and cyclic alkanes. For example, one such analysis of samples of gasoline, jet fuel and diesel fuel is summarized in Figure 1.

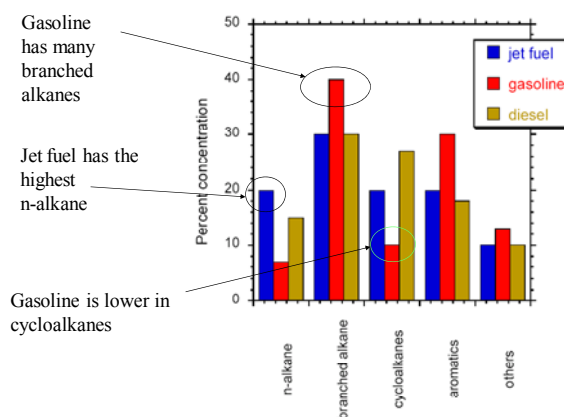


Fig.1. Compositions of some transportation fuels, sorted by structural classes

Over the years, kinetic mechanisms have been developed and validated for one or more hydrocarbon species from each of these classes, and in some classes, especially that of n-alkanes and branched alkanes, mechanisms from many different species have been developed. Some recent examples from our LLNL library include n-alkanes including n-heptane [2] and all of the n-alkanes from n-octane through n-hexadecane [3], branched alkanes including iso-octane [4], the 5 structural isomers of hexane [5] and the 9 structural isomers of heptane [6], cyclic paraffins including cyclohexane [7] and methyl cyclohexane [8], aromatics such as toluene [9], and large olefins such as di-isobutylene [10] and the isomers of hexene [11]. There are many other mechanisms from different researchers that have comparable features. Many other smaller examples of detailed mechanisms for species from most of these classes in the range of C₂-C₅ also exist within larger detailed mechanisms. These all provide an extensive

alkylperoxy radical isomerization reaction paths [15]. The kinetic description of this region has been shown to be the source of such features as octane and cetane numbers for hydrocarbon ignition [16] and reproduction of these features requires a model to include all of the key reaction sequences, most of which are strongly dependent on the molecular structure of the fuel molecule. It is very challenging to devise a mechanism reduction algorithm that can reproduce all of these features. The features are rather subtle and change the amounts of low temperature heat release by only a few degrees of temperature, but these small features make a large difference in the amounts of low temperature heat release that is observed and in the onset of ignition under practical conditions [17].

For example, a commonly used set of experiments that are used to validate hydrocarbon oxidation over a wide range of conditions are the shock tube experiments of Adomeit et al. [18,19] at Aachen in Germany. In these experiments, stoichiometric mixtures of fuel and air are ignited at elevated pressures (i.e., 13.5 and 40 bar). The ignition delay times depend on the initial temperature in a highly non-linear manner, as shown in Fig. 4.

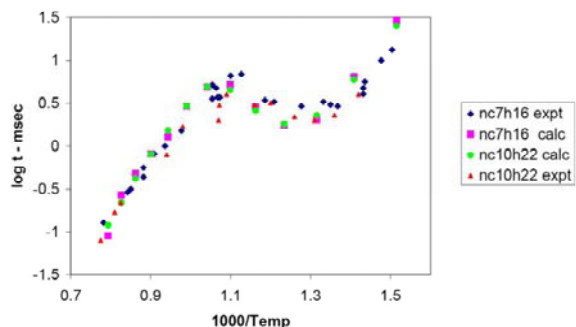


Fig. 4. Shock tube ignition delay times for n-heptane and n-decane, from experiments [18,19] and model [3].

This behavior may seem outrageously academic and unimportant, but it is actually the key to understanding and predicting octane and cetane numbers and predicting ignition in HCCI engines. For example, if two different fuels are used in a modern HCCI engine [20], the experimental and computed rates of heat release for those two fuels are shown in Fig. 5.

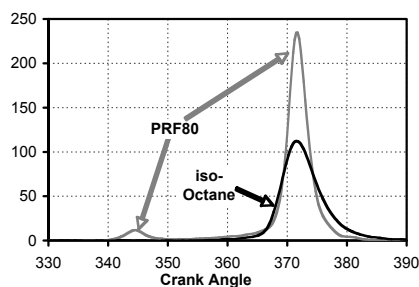
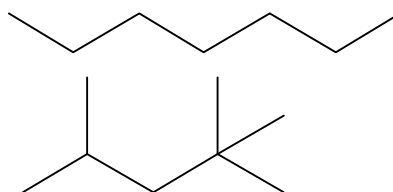


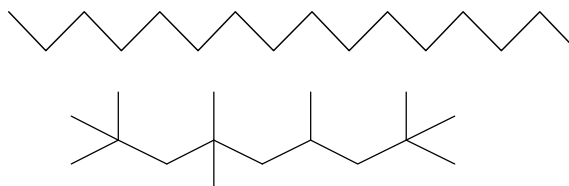
Fig. 5. Heat release rate as a function of crank angle in an HCCI engine for two fuels with different octane ratings.

The fuel with lower octane, PRF80, releases heat at early times which advances ignition, while the iso-octane fuel, with a higher octane, does not have the same low temperature heat release and needs a higher intake temperature to ignite at the same temperature as the PRF80 fuel. This behavior is important to the engine designer and must be reproduced in the detailed and in the reduced reaction mechanism.

Current kinetic mechanisms also can describe the limits of ignition properties in gasoline and diesel engines. The metric commonly used in gasoline is the octane number, and the primary reference fuels for octane number are n-heptane and iso-octane, one of which, n-heptane, indicates easy ignition and an octane number of zero, and iso-octane, which is very difficult to ignite and has an octane number of 100. These fuels can be represented as follows



At the same time, the reference fuels for cetane number, which measures ignition quality under diesel conditions, are n-hexadecane for the easily ignited fuel, and heptamethyl nonane, the difficult to ignite component



The differences in ignition quality are due to structural differences that are, in turn, reflected in nuances in reaction rates that must be retained in a reduced mechanism that is derived from the fully detailed mechanism.

V. CONCLUSIONS

Historically, mechanism reduction has focused on larger scale phenomena in combustion phenomena, and on smaller hydrocarbon fuel molecules. Recent advances in kinetic modeling have provided a much more detailed description of hydrocarbon combustion, with much larger mechanisms, and requiring description of much more detailed and more refined experimental phenomena. Both of these trends create much greater demands on the process of mechanism reduction.

VI. ACKNOWLEDGMENTS

This work was supported by the U.S. Department of Energy, Office of Freedom CAR and Vehicle Technologies, Gurpreet Singh and Kevin Stork, program managers, and was performed under the auspices of the U.S. Department of Energy by the Lawrence Livermore National Laboratory under Contract DE-AC52-07NA27344.

REFERENCES

- [1] "Basic Research Needs for Clean and Efficient Combustion of 21st Century Transportation Fuels", U.S. Department of Energy, Office of Science, 2006. Available at http://www.sc.doe.gov/bes/reports/files/CTF_rpt.pdf.
- [2] H.J. Curran, P. Gaffuri, W.J. Pitz, C.K. Westbrook, "A Comprehensive Modeling Study of n-Heptane Oxidation", *Combust. Flame*, vol. 114, pp. 149-177, 1998.
- [3] C.K. Westbrook, W.J. Pitz, O. Herbinet, H.J. Curran, E. J. Silke, "A comprehensive detailed chemical kinetic reaction mechanism for combustion of n-alkane hydrocarbons from n-octane to n-hexadecane", *Combust. Flame*, vol. 156, pp. 181-199, 2009.
- [4] H. J. Curran, P. Gaffuri, W.J. Pitz, C. K. Westbrook, "A Comprehensive Modeling Study of iso-Octane Oxidation", *Combust. Flame*, vol. 129, pp. 253-280, 2002.
- [5] H. J. Curran, P. Gaffuri, W.J.Pitz, C.K. Westbrook, W.R. Leppard, "Autoignition Chemistry in a Motored Engine: An Experimental and Kinetic Modeling Study", *Proc. Combust. Inst.*, vol. 26, pp. 2669-2677, 1996.
- [6] C.K. Westbrook, W.J. Pitz, J.E. Boercker, H.J. Curran, J.F. Griffiths, C. Mohamed, M. Ribaucour, "Detailed Chemical Kinetic Reaction Mechanisms for Autoignition of Isomers of Heptane Under Rapid Compression", *Proc. Combust. Inst.*, vol. 29, 1311-1319, 2002.
- [7] E.J. Silk, W.J. Pitz, C.K. Westbrook, M. Ribaucour, "Detailed Chemical Kinetic Modeling of Cyclohexane Oxidation", *J. Phys. Chem. A*, vol. 111, pp. 3761-3775, 2007.
- [8] W.J. Pitz, C.V. Naik, T.N. Mhaolduin, C.K. Westbrook, H.J. Curran, J.P. Orme, J.M. Simmie, "Modeling and Experimental Investigation of Methylcyclohexane Ignition in a Rapid Compression Machine", *Proc. Combust. Inst.*, vol. 31, pp. 267-275, 2007.
- [9] Y. Sakai, A. Miyoshi, M. Koshi, W.J. Pitz, "A kinetic modeling study on the oxidation of primary reference fuel-toluene mixtures including cross reactions between aromatics and aliphatics", *Proc. Combust. Inst.*, vol. 32, 2009.
- [10] W.K. Metcalfe, W.J. Pitz, H.J. Curran, J.M. Simmie, C.K. Westbrook, "The Development of a Detailed Chemical Kinetic Mechanism for Diisobutylene and Comparison to Shock Tube Ignition Times", *Proc. Combust. Inst.*, vol. 31, pp. 377-384, 2007.
- [11] M. Mehl, G. Vanhove, W.J. Pitz, E. Ranzi, "Oxidation and combustion of the n-hexene isomers: A wide range kinetic modeling study", *Combust. Flame*, in press, 2009.
- [12] J.T. Farrell, N.P. Cernansky, F.L. Dryer, D.G. Friend, C.A. Hergart, C.K. Law, R.M. McDavid, C.J. Mueller, A.K. Patel, H. Pitsch, "Development of an Experimental Database and Kinetic Models for Surrogate Diesel Fuels", Society of Automotive Engineers paper SAE-2007-01-0201, 2007.
- [13] W.J. Pitz, N.P. Cernansky, F.L. Dryer, F.N. Egolopoulos, J.T. Farrell, D.G. Friend, H. Pitsch, "Development of an Experimental Database and Kinetic Models for Surrogate Gasoline Fuels", Society of Automotive Engineers paper SAE-2007-01-0175, 2007.
- [14] M. Colket, T. Edwards, S. Williams, N.P. Cernansky, D.L. Miller, F. Egolopoulos, P. Lindstedt, K. Seshadri, F.L. Dryer, C.K. Law, D. Friend, D.B. Lenhart, H. Pitsch, A. Sarofim, M. Smooke, W. Tsang, "Development of an Experimental Database and Kinetic Models for Surrogate Jet Fuels", AIAA paper AIAA-2007-0770, 2007.
- [15] R.T. Pollard in: C.H. Bamford, C.F.H. Tipper, Eds., *Comprehensive Chemical Kinetics*, vol. 17, Elsevier, New York, 1977.
- [16] C.K. Westbrook W.J. Pitz, W.R. Leppard, "The Autoignition Chemistry of Paraffinic Fuels and Pro-Knock and Anti-Knock Additives: A Detailed Chemical Kinetic Study", *Soc. Auto. Eng. Trans.*, Vol. 100, pp. 605-622, 1991.
- [17] C.K. Westbrook, "Chemical Kinetics of Hydrocarbon Ignition in Practical Combustion Systems", *Proc. Combust. Inst.*, vol. 28, pp. 1563-1577, 2000.
- [18] U. Pfahl, K. Fieweger, G. Adomeit, "Self-Ignition of Diesel-Relevant Hydrocarbon-Air Mixtures Under Engine Conditions", *Proc. Combust. Inst.*, vol. 26, pp. 781-789, 1996.
- [19] H.K. Ciezki, G. Adomeit, "Shock-Tube Investigation of Self-Ignition of n-Heptane-Air Mixtures Under Engine Relevant Conditions", *Combust. Flame*, vol. 93, pp. 421-433, 1993.
- [20] M. Sjoberg, J.E. Dec, "Comparing Late-Cycle Autoignition Stability for Single- and Two-Stage Ignition Fuels in HCCI Engines", *Proc. Combust. Inst.*, vol. 31, pp. 2895-2902, 2007.

Center for Applied Mathematics

2009 Nieuwland Lecture Series

Dr. Charles Westbrook

Lawrence Livermore National Laboratory (ret.)

“The Role of Combustion in Future Energy Scenarios”

Wednesday, April 1, 2009

3:30pm

McKenna Hall Auditorium

Combustion of hydrocarbon fuels provides 85% of all power production in the United States and close to 95% of American transportation power. Modern society now realizes the central role that combustion plays in atmospheric air pollution and production of greenhouse gases that lead to global climate change, and growth in the economies of the so-called third world is being fueled by hydrocarbon fuels, including a great deal of heavily polluting coal. As a result, combustion is both the curse and the salvation of modern society. The technical world is trying to identify and develop alternatives to hydrocarbon fuels, such as solar, nuclear, wind and other technologies, but none of these are ready to supplant petroleum and other hydrocarbon fuel combustion on the world stage. Realistic projections indicate that there may be 100 years of remaining petroleum reserves worldwide, and that is the same timeline that is likely to be required to develop a broad set of alternative energy supplies. It is the responsibility of combustion science to bridge this time period in a responsible and technically sound way to minimize the damage to the environment and maximize the efficiency of those fuels that remain. Some combustion applications may continue to be important for extremely long times. Practical hydrocarbon fuels in internal combustion and gas turbine engines are complex mixtures of many hundreds of large hydrocarbon fuel molecules. At the same time, fuels for these engines are being produced from new sources in addition to petroleum, including coal, oil sands, agricultural oils and bioengineered algae whose combustion properties have never been studied in detail. This diversity in fuel sources is very likely to continue for as long as civilization produces energy from combustion, and it is essential to understand the ways that each type of fuel contributes to energy efficiency, pollutant emissions and global climate change. New types of engines are also being developed to increase combustion efficiency, which will reduce the level of pollutant emissions while extending the time period during which existing fuels will be available. This presentation will show new results in chemistry of conventional fuels and in biodiesel fuel molecules. Recent studies have provided new insights with implications for the combustion of many other types of fuels, and we will use a historical framework to try to predict the role of combustion in the future.